Università degli Studi di Siena

DIPARTIMENTO DI SCIENZE FISICHE DELLA TERRA E DELL'AMBIENTE

SEZIONE DI FISICA

Low Frequency Optimization and Performance of Advanced Virgo Seismic Isolation System

TESI DI DOTTORATO DI RICERCA IN FISICA SPERIMENTALE

In Partial Fulfillment of the Requirements for the Ph.D. Degree in Experimental Physics

CANDIDATE:
Lucia Trozzo

THESIS ADVISOR:
Dr. **Franco Frasconi**

TUTOR:
Prof. **Pier Simone Marrocchesi**

Ciclo di Dottorato XXX

Acknowledgements

Se qualcuno mi chiedesse: “come è stato il tuo PhD? ” Risponderei di sicuro: “ Il mio PhD è stata un’avventura singolare che mi ha fatto crescere come Fisico e come Persona!”

In quest’avventura mi hanno accompagnato e supportato molte persone che meritano di essere ringraziate. Andando a ritroso, la prima persona che sin dall’inizio ha creduto in me e che mi ha spronato ed incoraggiato a a fare il PhD è Enrico Calloni: Enrico grazie di cuore per la tua fiducia!

Ringrazio il Prof. Pier Simone Marrocchesi per avermi seguito durante questi tre anni di Dottorato, Giancarlo Cella e Franco Frasconi per tutti i preziosi consigli ed il supporto che mi hanno dato in questi anni.

Il Gruppo INFN Pisa che mi ha ospitato e dato la possibilità di lavorare sul Superattenuatore. Un particolare ringraziamento va a Roberto Passaquieti che mi ha permesso di mettere fisicamente le mani sui vari pezzi meccanici del sistema. Ringrazio Valerio Boschi per i preziosi consigli sul filtro di Kalman e sull’ Optimal control.

Ringrazio Ettore Majorana che sin dall’inizio ha creduto in me e che durante il commissioning di Virgo mi ha schierata in prima linea dandomi la possibiltà di vederlo funzionare in diretta step by step: Ettore grazie mille per la stima e la fiducia riposta in me, spero sinceramente di essermele meritate!

Ringrazio Paolo Ruggi che con grande pazienza mi ha iniziata al magico mondo delle sospensioni e guidata attraverso le sue insidie e le sue bellezze permettendomi di affiancarlo durante le attività di commissiong. Grazie per tutti i consigli, gli insegnamenti e il supporto, sia tecnico che morale, che mi hai sempre dato durante questo Dottorato. Grazie per avermi fatto da guida e per avermi dato l’onore e la possibilità di affiancarti in modo da poter apprendere i trucchi del mestiere, spero di esserne stata all’altezza: A te Paolo vanno la mia profonda stima e gratitudine!

Ringrazio Annalisa ed Antonino per avermi scarrozzato tutti i giorni da Pisa a Cascina e avermi dimostrato, giorno dopo giorno, la loro più sincera amicizia. Grazie per la simpatia e la disponibiltà e soprattutto grazie per avermi sempre ascoltata ed incoraggiata anche nei periodi più bui del mio Dottorato.

Come non ringraziare tutte le altre persone coinvolte nelle attività di commissioning di

Virgo: ringrazio Federico Paoletti, Flavio Nocera ed Irene Fiori per le dritte e i consigli che mi sono sempre stati utili. Maddalena, Julia, Diego, Gianmatteo, Federico, Fabio, Francesco, Perci, Beatrice, Giulio, Franco, Henrich, Valeria, Ilaria, Imran, Jose, Eric, Gabriel, Bas, Matthieu, Giovanni, Lorenzo, Gary e tante altre persone (troppe per menzionarle tutte, ma non troppe per ricordarle tutte) per aver contribuito ciascuno a suo modo a questa splendida avventura. Come non ricordare gli amici a lontani che nonostante tutto mi sono stati vicini: Adriana, Teresa, Elsa, Fulvio, Dario, Manuela, Chiara... Infine ma non per ultimi gli zii e cugini di Pisa.

Ma i ringraziamenti più grandi vanno a mio nonno Vincenzo il cui ricordo è sempre con me e a mia mamma che mi ha sempre sostenuta ed incoraggiata a modo suo... Mamma questa tesi è dedicata a te!

Should anyone ask me "How was your PhD?" I would surely answer: "It has been a peculiar adventure, something which made me progress both as a Physicist and a Person!"

Many people supported and accompanied me during this journey, they deserve my acknowledgment and gratitude. Going backward, the first person who trusted me since the very beginning was Enrico Calloni. He encouraged me and pushed me to start this PhD: Enrico, a wholehearted thank you for your trust!

I wish to thank prof. Pier Simone Marrocchesi for following me during these three years of PhD program, Giancarlo Cella and Franco Frasconi for their precious advice and all the support they provided me during these years.

INFN Pisa group for hosting me and for giving me the chance to work with the Superattenuator. A special thank to Roberto Passaquieti who allowed me to physically work on the mechanical parts of the system. I thank Valerio Boschi for the valuable advice about Kalman filter and Optimal Control.

I would like to thank Ettore Majorana, which believed in me from the beginning and put me on the forefront of the commissioning activities. This allowed me to see the step-by-step process of setting up the system: Ettore, many thanks for your appreciation and trust, I sincerely hope to deserve both!

I thank Paolo Ruggi, who introduced me with patience to the magic world of suspensions and led me through the troubles and beauty of this realm, by allowing me to stay at his side during the commissioning activities.Thank you for your advice, your precious teaching and the support, both technical and moral, you always gave me during this PhD. Thank you for being my guide and for giving me the chance and the honor to be at your side so that I could learn your tricks: I hope I lived up to your dedication. To you my deep appreciation and gratitude!

I thank Annalisa and Antonino for riding me every single day from Pisa to Cascina (and back!) and for showing me, day by day, their true friendship. Thank you both for being so nice with me, for your willingness to help and, most of all, thank you for listening to me even in the

darkest moments of this PhD.

How not to thank all the other people involved in the Virgo commissioning: thanks to Federico Paoletti, Flavio Nocera ed Irene Fiori for the always useful suggestions and advice. Maddalena, Julia, Diego, Gianmatteo, Federico, Fabio, Francesco, Perci, Beatrice, Giulio, Franco, Henrich, Valeria, Ilaria, Imran, Jose, Eric, Gabriel, Bas, Matthieu, Giovanni, Lorenzo, Gary and many others (too many to mention all of them, not too many to remind all of them) for contributing, each one his way, to this splendid journey. How not to remember all the friends who stay far but notwithstanding remained close to me: Adriana, Teresa, Elsa, Fulvio, Dario, Manuela, Chiara... Last but not least my uncles and cousins in Pisa.

But the biggest thank you is for my grandfather Vincenzo, whose memory is always with me, and to my Mother which always encouraged and supported me, in her own way... Mummy, this thesis is dedicated to you!

Contents

Introduction

The existence of Gravitational Waves is predicted from the General Relativity: any accelerated body loses energy as gravitational radiation that can be interpreted as a distortion of the space-time fabric. Gravitational Waves were predicted in 1916 by A. Einstein and confirmed by indirect observations by Hulse and Taylor in 1981 [40]. Anyhow, the world-wide quest for the direct observation of Gravitational Waves went on for decades even in the absence of detection, thanks to the continuous effort spent by visionary researchers. Indeed, despite the extreme difficulty of the task, the promise of completely new Astronomy using gravitational waves as a messenger – instead of Electromagnetic Radiation – was so exciting to devote entire careers to this goal.

This quest involved mainly two kinds of antennas: resonant bars and kilometer-scale laser-based Michelson interferometers, with the latter demonstrating a more promising technology to reach the needed sensitivity. It was soon understood that the likelihood of a detection was linked to the creation of a network of antennas operating in coincidence. Three kilometer-scale interferometers were built and operated at beginning of 2000s: the two LIGOs in the USA (LIGO Collaboration) and the French-Italian Virgo interferometer in Cascina (Italy) by the Virgo collaboration. It is remarkable that the building of these devices begun more or less one century after Einstein's interpretation of Michelson experiment, leading to Special Relativity.

The first few-year-long cycle of data takings ended up in 2011. Those early instruments demonstrated a reliable and promising technology, an observing duty cycle up to 80% and a satisfactory stationarity of noise [81], and, probably the most important outcome, they provided an excellent knowledge of limiting noise sources. No detections were recorded during the first generation antennas science runs, nor was it really hoped to have any when the expected detection rate of ~ 0.01 events per year is considered. Despite this huge limitation, non-negligible Astrophysics results (examples in [2]) and of instrument development were made possible thanks to the experience of early generation. Overall, thanks to the first generation of interferometric antennas, a clear path towards second generation antennas was developed. Moreover, a solid collaboration and exchange of data and experience was put in place between the Virgo and LIGO collaborations.

A five-years upgrade was started to increase the sensitivity of the antennas by one order of magnitude, and the volume of explored Universe, in turn, by a factor one thousand. At the end of the upgrade, the horizon of the instruments would have included the whole Virgo cluster of Galaxies and the rate of events would have risen to some per years.

The last upgrade was done in the framework of second generation detectors through advanced LIGO (aLIGO) and advanced Virgo (AdV) projects. LIGO started the upgrade earlier and so aLIGO was set in operation two years earlier than AdV. In fall 2015, on September the 14th, the first observation of Gravitational Waves was achieved by the collaboration LIGO-Virgo.

Other few events were detected using the two LIGO detectors and proved that it is possible to do astrophysical observations using ground-based detectors. Finally, AdV commissioning was completed and the French-Italian detect or joined the network in the last part of the observational run O2, on August 1st 2017. The run was set to last just one more month, but despite this short time AdV strongly contributed to two triple-coincidence observations: one BBH and one BNS, opening the new era of multi-messenger Astrophysics using Gravitational Waves.

The Gravitational Waves are perturbations of the metric of the space-time. Their effect on free falling masses is to alter their distance. If we consider the typical order of magnitude of the gravitational wave signal (for kilometer-scale distances, it is around $10^{-18}\,m$ we can well realize the difficulties encountered by the pioneers of this research and the reason why it was chosen to exploit the precision allowed by laser optics and symmetric interferometric detection for these devices. Since present interferometers are ground-based, the mirror suspension attenuation system, as well as its control strategy, is fundamental. Virgo detector was designed not to be limited by seismic noise starting from 10 Hz. To this purpose the INFN-Pisa Group developed and built a sophisticated system, the so-called Superattenuator, allowing to consider the mirror test masses as free-falling from few Hz. The detector is operated at nearly dark fringe, namely a nearly perfect destructive interference is achieved between the two beams reflected by the interferometer arms. To reach and remain stable in this working condition several control loops must be engaged, without which the residual motion of the free falling mass would be unacceptably large. In order to be compatible with the amplitude of the gravitational signal to be detected, a hierarchical control scheme for the suspensions must be implemented.

The main control implemented, applied to the Superattenuator top-stage is the active mode damping, the so-called Inertial Damping. The sophisticated mechanical design of the overall suspension and the performance of the Inertial Damping are among the key features of Virgo. The target of this thesis is the reduction of the impact of this control on the actual AdV sensitivity and the study of possible alternative developments, as Kalman filtering and Optimal control

approach. Both studies required not only commissioning work but also adequate simulations to provide a deeper understanding of experimental data. In this document, modeling and simulation studies based upon actual data are presented in the context of AdV commissioning works.

This document can be sectioned in three main parts:

PART I This part concerns the basic theoretical concept of the physics of gravitational waves and the ground based detectors. The physics of the Gravitational Waves and the most interesting sources are presented in Chapter 1. The detection principle on Earth based on kilometer-scale Michelson interferometer is described in Chapter 2, together with the optical configuration of the detector that maximizes the sensitivity and the and minimizes the impact of noise sources. The experimental results related to the observation of detection gravitational waves are presented in Chapter 3.

PART II The second part has as its specific subject the Superattenuator and the seismic noise reduction strategy adopted by AdV. The characteristic micro-seismic condition at the European Gravitational Observatory (Cascina, PI), where Virgo is installed, are presented in Chapter 4. In Chapter 5 the experimental set-up of the apparatus and its various components are explained, describing for each one purpose and operating principle. In this chapter, I briefly describe also the interface stages between the Superattenuator and the test masses of Virgo, i.e. the main mirrors of the detector. It is crucial to include the description of those stages in the overall modeling of the system. In Chapter 6 the modeling of Superattenuator and overall suspension system using the impedance matrix approach are presented.

PART III The results of the experimental work done in the Commissioning phase of AdV are shown in the final part. In Chapter 7 the experimental configuration of the sensors and actuators located on the suspension top stage and the diagonalization procedure adopted to pass from the “sensors reference frame” to “AdV reference frame” are presented. In this chapter the noise budget of the diagonalized sensors are presented. In Chapter 8 a detailed description of the implementation of AdV top stage suspension control is given and its performances are analyzed. In Chapter 9, the first implementation of Kalman filter and Optimal control, focused on the vertical d.o.f of a long superattenuator and aimed to possible future developments, are presented in perspective. In Chapter 10 the procedure to calculate the impact on AdV sensitivity of the suspension control, in the micro-seismic bandwidth and related experimental results are presented.

I wish you have a good trip in the magic world of the AdV suspension!

Part I

Gravitational Waves

Chapter 1

Physics of Gravitational Waves

At the base of every scientific discipline there is observation. The need to observe the universe, to get into possession of increasingly complex and articulated notions, has accompanied man from the dawn of the times. Thanks to this innate need, today we know that astrophysical objects emit radiation over the whole EM spectrum. It allows to take pictures of the universe at multiple wavelengths, ranging from Gamma-rays to Radio waves, and each picture gives us a different kind of information about the universe composition.

But if there was a way to see the whole universe, and not just the small portion offered by stellar light? If one could access the information of any object in the cosmos simply by analyzing the imprint that it leaves on the space-time? Gravitational waves could give a new picture of the Universe. The detection of Gravitational Waves is first of all an additional confirmation to the Theory of General Relativity, but could also tell us about the dynamics of large-scale events in the Universe like death of stars and birth of black holes, giving us the possibility to understand physical mechanisms in strong gravity regimes which can't be still fully foreseen by the theory.

1.1 General Relativity and Einstein Field Equation

This gravitation theory took shape in the conceptual picture of relativistic mechanics introduced by Albert Einstein in 1905. The extension of the Galilean relativity principle to the electrical phenomena requires the invariance in form, under appropriate coordinates transformations, of the theory's equations.

This request of invariance means that the time coordinate is treated as the spatial coordinates, and the transformations that have this property are *The Lorentz Transformations.* In this new contest, it makes not sense to consider space and time as absolute and separated entities, but

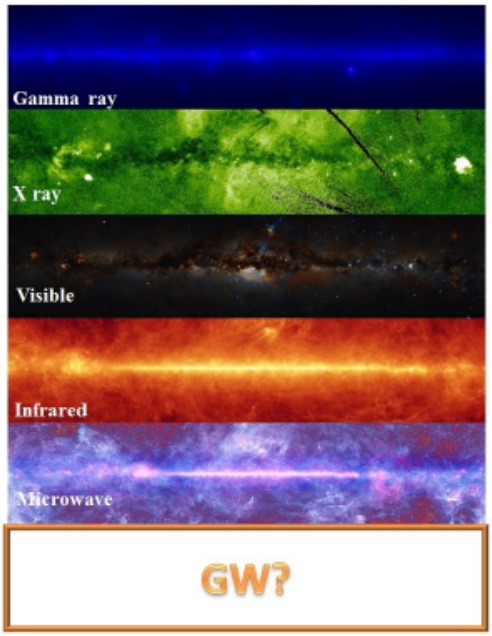

Figure 1.1: Sight of the Universe at different wavelengths in the EM spectrum.

they depend on the reference frame and they are united in a new entity called *'Space-Time'*. In this way, a new physical quantity ds^2 (space-time interval) has a fundamental role for the estimation of distance between two event in *Space-Time [3, 46]* :

$$\begin{aligned} ds^2 &= -c^2dt^2 + dx^2 + dy^2 + dz^2 \\ &\downarrow \\ ds^2 &= \eta_{\mu\nu} dx^\mu dx^\nu \end{aligned} \tag{1.1}$$

The second equation is the tensorial expression of ds^2 and

$$\eta_{\mu\nu} = \begin{pmatrix} -1 & 0 & 0 & 0 \\ 0 & 1 & 0 & 0 \\ 0 & 0 & 1 & 0 \\ 0 & 0 & 0 & 1 \end{pmatrix} \tag{1.2}$$

is the Minkowski tensor metric.

This expression is true if the reference frame is inertial and the space-time is flat. The extension of this mathematical formulation at all kind of reference frames is realized in '*General Relativity Theory,* ten years later by Albert Einstein [19].

Einstein introduces a new definition of inertial reference frame. He considers a test mass in free motion under the gravitational attraction of matter. The trajectory traveled by the body

(whatever the body under observation) do not depend on their intrinsic properties, but it depends only on its initial mechanical state (position and speed). From a reference frame fixed to this trajectory the body appears at rest. Moreover, if we exclude the presence of other interactions in addition to the gravitational one, and we consider a limited neighborhood region of space-time, the motion of any other body appears rectilinear and uniform. The reference frame has therefore the characteristics of an inertial system, because in it there is not evidence of interactions. In this reasoning, it is necessary that the region of space-time is small and we have been assumed that the interval between events can be calculated by the equation (1.1).

In *General Relativity* one extends the principle of relativity to this class of reference frames, and those that are obtained by applying to them the Lorentz transformations. In a reference frame that covers a large region of space-time, the effects of the force of gravity become obvious: the trajectories of the falling bodies tend to curve, according to geometries dependent by the distribution of attraction sources. In this way, the use of inertial coordinates and the metric relationship becomes totally arbitrary.

In a 'global' reference frame, the space-time interval is calculated starting from:

$$ds^2 = g_{\mu\nu} dx^\mu dx^\nu \tag{1.3}$$

where $g_{\mu\nu}$ is the symmetric tensor metric and $dx^\mu = (dx^0, \vec{dx})$ is a infinitesimal vector in the coordinates frame. The coefficients that appear in the definition of a time-space interval, in this case, are the functions depending by the coordinates, which have their temporal evolution, interconnected with those of the matter. Starting from a masses distribution, in principle, it's possible to determine the metric tensor $g_{\mu\nu}$.

The relationship between space-time geometry and masses distribution is expressed by Einstein's Field Equations:

$$G_{\mu\nu} = \frac{8\pi G}{c^4} T_{\mu\nu} \tag{1.4}$$

where $G_{\mu\nu}$ is the Einstein tensor, G is the Newton constant, c the vacuum speed of light and $T_{\mu\nu}$ is the stress-energy tensor that takes into account the mass-energy distribution[1].

[1] In a relativistic theory, the four momentum vector for a particle of mass m is defined as $P_\mu = \int d^3x T_{\mu 0} \equiv (\frac{E}{c}, \vec{p})$, where E and p are respectively the energy and the momentum of the particle.The module of this four-vector ,in the Minkowski's space-time , is a Lorentz's invariant and in particular for the four-momentum, we have $P_\mu P^\mu = (E^2 + p^2c^2) = m^2c^4$. From last relationship it's possible to obtain the expression of the relativistic energy of a particle $E = \sqrt{p^2c^2 + m^2c^4}$ which is reduced in this form $E = mc^2$ when the particle is at rest ($p = 0$). This relationship in known as mass–energy equivalence formula; that is anything having mass has an equivalent amount of energy and vice versa.

The Einstein's tensor is defined as:

$$G_{\mu\nu} = R_{\mu\nu} - \frac{1}{2} R g_{\mu\nu} \tag{1.5}$$

where $R_{\mu\nu}$ is the *tensor of Ricci* and R is the *scalar curvature ($R = g^{\mu\nu} R_{\mu\nu}$).*

The Ricci tensor describes space-time curvature in every reference frame and it is obtainable as contraction of Riemann tensor (4th order tensor), given by

$$R^{\mu}{}_{\nu\rho\sigma} = \partial_\rho \Gamma^{\mu}_{\nu\sigma} - \partial_\sigma \Gamma^{\mu}_{\nu\rho} + \Gamma^{\mu}_{\alpha\rho} \Gamma^{\alpha}_{\nu\sigma} - \Gamma^{\mu}_{\alpha\sigma} \Gamma^{\alpha}_{\nu\rho} \tag{1.6}$$

The quantities $\Gamma^{\mu}_{\alpha\rho}$ are the *Christoffel Symbols,* which are functions of the metric tensor:

$$\Gamma^{\mu}_{\nu\rho} = \frac{1}{2} g^{\mu\sigma} (\partial_\rho g_{\sigma\nu} + \partial_\nu g_{\sigma\rho} - \partial_\sigma g_{\nu\rho}) \tag{1.7}$$

In this perspective, the motion of a body in the gravitational field is a particular sequence of events immersed in metric space created by a distribution of matter. The trajectories followed by falling bodies are curves defined by the geometrical properties of space-time: the geodesic, id est the extremal space-time curves joining two given events. The equation that describes these curves is the natural generalization to any spaces of the equation of motion in the absence of force, that is, the condition of the absence of acceleration. It can be said, adopting a suggestive point of view, that the freely gravitating bodies follow trajectories curved to accommodate the 'curved profile' of space-time.

1.2 Propagation of Gravitational Field and Gravitational Waves

Einstein's equations have a tensorial nature, thus they are invariant in form under general coordinates transformations (covariance) and then are valid in all reference systems. The mass-energy distribution determines the spacetime geometry, and the geometry itself determines the motion of the masses. Consequently, the gravitational interaction is the manifestation of the geometrical properties of space-time and it is natural to identify his intermediary with the metric tensor. This field of interaction can propagate the information related to the state of the source in the space at a finite speed, and this speed can not be higher than the speed of light. Since Einstein's Equations are non-linear, it is not possible to find a solution that is general and exact at the same time. In fact, their non-linear nature makes difficult the exact description of the gravitational field propagation. In some case there are exact, but not general, solutions of Einstein's Equations that were found conjecturing a high level of symmetry (like Schwarzschild solution) and some approximated solutions that are general, but not exact.

1.2.1 Linearized gravity and weak field approximation

Linearized gravity is an approximation scheme used to simplify the general relativity equations. In this scheme the nonlinear contributions of the metric of space-time are ignored [69, 87]. In fact the metric tensor of spacetime $g_{\mu\nu}$ is treated as the sum of a solution of Einstein's equations and a perturbation $h_{\mu\nu}$:

$$g_{\mu\nu} = \overline{g}_{\mu\nu} + h_{\mu\nu} \tag{1.8}$$

where $\overline{g}_{\mu\nu}$ is the background metric , and $h_{\mu\nu}$ represents the deviation of the true metric from $\overline{g}_{\mu\nu}$. This perturbation scheme allows linearized Einstein field equations to be obtained: these equations are linear in the perturbation , and the sum of two solutions is also a solution.

When the background metric is the Minkowski one in (1.2) (i.e., $\overline{g}_{\mu\nu} = \eta_{\mu\nu}$) and $h_{\mu\nu}$ is a small perturbation ($\left|h_{\mu\nu}\right| \ll 1$) we are working on *Weak field approximation.* . In this picture imposing the following coordinates transformation[2]:

$$x'^{\mu} = x^{\mu} + \xi^{\mu}(x) \qquad |\, \partial_{\nu}\xi^{\mu} \,| \ll 1 \tag{1.9}$$

$$\Lambda^{\mu}_{\nu} \equiv \frac{\partial x^{\mu}}{\partial x'^{\nu}} = \delta^{\mu}_{\nu} - \partial_{\nu}\xi^{\mu} + \circ(|\, \partial_{\nu}\xi^{\mu} \,|^2) \tag{1.10}$$

we obtain a metric tensor expressed by:

$$g'_{\mu\nu} = \Lambda^{\rho}_{\mu}\Lambda^{\sigma}_{\nu} g_{\rho\sigma} = \eta_{\mu\nu} + h_{\mu\nu} - \partial_{\nu}\xi_{\mu} - \partial_{\mu}\xi_{\nu} \tag{1.11}$$

Using the (1.8), at first order, the Riemann tensor is given by:

$$R_{\mu\nu\rho\sigma} = \frac{1}{2}(\partial_{\nu}\partial_{\rho}h_{\mu\sigma} + \partial_{\mu}\partial_{\sigma}h_{\nu\rho} - \partial_{\mu}\partial_{\rho}h_{\nu\sigma} - \partial_{\nu}\partial_{\sigma}h_{\mu\rho}) \tag{1.12}$$

and in term of this approximation, the *linearized field equations* are:

$$\Box\overline{h}_{\mu\nu} + \eta_{\mu\nu}\partial^{\rho}\partial^{\sigma}\overline{h}_{\rho\sigma} - \partial^{\rho}\partial_{\nu}\overline{h}_{\mu\rho} - \partial^{\rho}\partial_{\mu}\overline{h}_{\nu\rho} = -\frac{16\pi G}{c^4}T_{\mu\nu} \tag{1.13}$$

where $\overline{h}_{\mu\nu}$, h , and $\Box$ (Dalambertian operator) are given by:

[2] The transformations (1.9) are called infinitesimal diffeomorphisms or gauge transformations.

$$\begin{aligned} \bar{h}_{\mu\nu} &= h_{\mu\nu} - \frac{1}{2}\eta_{\mu\nu}h \\ h &= \eta^{\mu\nu}h_{\mu\nu} \\ \Box = \partial^{\alpha}\partial_{\alpha} &= \eta^{\mu\nu}\partial_{\mu}\partial_{\nu} = -\frac{1}{c^2}\frac{\partial^2}{\partial t^2} + \sum_{i=1}^{3}\frac{\partial^2}{\partial x_i^2} \end{aligned} \tag{1.14}$$

1.2.2 Gravitational waves

The distribution of matter and energy in space time determines the bending of space time. This distribution is the source of the gravitational field. Far from it, its effects can be treated through a linearized weak field and viewed as a perturbation of the metric (Eq. 1.8). In a certain sense, $h_{\mu\nu}$ has the task of organizing the space-time structure of each event: $h_{\mu\nu}$ represents a change in the gravitational field from the standard situation.

Now, in order to simplify the expression (1.13), we can take advantage of the gauge invariance of equations 1.9. In fact, for any field $\bar{h}_{\mu\nu}$, exists another one $\bar{h}'_{\mu\nu}$, obtainable applying the following gauge transformation to $\bar{h}_{\mu\nu}$:

$$\bar{h}'_{\mu\nu} = \bar{h}_{\mu\nu} - \partial_{\nu}\xi_{\mu} - \partial_{\mu}\xi_{\nu} + \eta_{\mu\nu}\partial_{\alpha}\xi^{\alpha} \tag{1.15}$$

and satisfying the gauge condition called *Lorentz gauge:*

$$\partial^{\nu}\bar{h}'_{\mu\nu} = 0 \tag{1.16}$$

In this gauge, the Field equations are written as:

$$\Box\bar{h}_{\mu\nu} = -\frac{16\pi G}{c^4}T_{\mu\nu} \tag{1.17}$$

These are the **gravitational wave equations** that describes the propagation of the metric perturbation and a possible solution of (1.17) can be written as:

$$\bar{h}_{\mu\nu}(\vec{x},t) = \frac{4G}{c^4}\int\frac{d^3x'}{r}T_{\mu\nu}\left(\vec{x}',t-\frac{r}{c}\right) \quad \text{with} \quad r = \mid \vec{x} - \vec{x}' \mid \tag{1.18}$$

The last equation describes physical entities called **Gravitational Waves** (**GW**). They travel at speed of light, they carry energy and their amplitude is proportional to the inverse of the distance from the source.

With the aim to study the propagation of gravitational waves and their interaction with the detector, we must consider $T_{\mu\nu} = 0$, which physically corresponds to vacuum perturbations of

the gravitational field in the absence of matter:

$$\Box \overline{h}_{\mu\nu} = 0 \tag{1.19}$$

In this case a plane wave solution of Equation (1.13) can be written as:

$$\overline{h}_{\mu\nu}(x) = \alpha_{\mu\nu}\, e^{ikx} + \alpha^{*}_{\mu\nu}\, e^{-ikx} \tag{1.20}$$

where $\alpha_{\mu\nu}$ is a symmetric 4×4 matrix called the polarization tensor.

The solution (1.20) satisfies the wave equation (1.19) and must also meet the four gauge conditions (1.16), which reduces the number of independent components of $\alpha_{\mu\nu}$ to six. [3]

To further reduce the number of independent components of $\alpha_{\mu\nu}$ we can do another coordinate transformation and choose so a reference system in which our request is verified. The infinitesimal change of coordinates is given by $x'_{\mu} = x_{\mu} + \varepsilon_{\mu}(x)$ and preserve the Lorentz condition if

$$\begin{aligned} \partial^{\nu}\overline{h}'_{\mu\nu} &= \partial^{\nu}\left(\overline{h}_{\mu\nu} - \partial_{\nu}\xi_{\mu} - \partial_{\mu}\xi_{\nu} + \eta_{\mu\nu}\partial_{\alpha}\xi^{\alpha}\right) \\ &= -\Box\xi_{\mu} = 0 \end{aligned}$$

It is possible to show that with an appropriate ε_{μ} we can impose

$$\begin{aligned} h_{0\mu} &= 0 \\ h &= 0 \end{aligned}$$

a choice of coordinates which is called *transverse traceless gauge (TT)*.

The TT gauge leaves two independent physical polarizations, usually called plus and cross polarization. For a plane wave propagating along the z direction we can write for example

$$h^{TT}_{\mu\nu} = \begin{pmatrix} 0 & 0 & 0 & 0 \\ 0 & h_{+} & h_{\times} & 0 \\ 0 & h_{\times} & -h_{+} & 0 \\ 0 & 0 & 0 & 0 \end{pmatrix} e^{i\omega\left(t-\frac{z}{c}\right)} + \begin{pmatrix} 0 & 0 & 0 & 0 \\ 0 & h_{+} & h_{\times} & 0 \\ 0 & h_{\times} & -h_{+} & 0 \\ 0 & 0 & 0 & 0 \end{pmatrix}^{*} e^{-i\omega\left(t-\frac{z}{c}\right)} \tag{1.21}$$

The two complex amplitudes h_{+} and $h_{\times}$ are related to the amplitude and phase of plane waves with plus (h_{+}) and cross ($h_{\times}$) polarization.

[3] Owing to its symmetry $\alpha_{\mu\nu}$ has generally 10 independent components.

1.2.3 Gravitational Waves generation

In presence of sources, the gravitational waves equations (in the Lorentz gauge), can be written as:

$$\begin{cases} \Box \bar{h}_{\mu\nu} = -\frac{16\pi G}{c^4} T_{\mu\nu} \\ \\ \partial^{\mu} \bar{h}_{\mu\nu} = 0 \end{cases} \tag{1.22}$$

where $T_{\mu\nu}$ is the stress-energy tensor. Looking at these equations it seems that all the components of $h_{\mu\nu}$ are radiative, since they all satisfy the wave equations. A causal solution of Eq. (1.22) is the retarded one shown previously (Equation (1.18)).

In frequency domain this becomes

$$\tilde{\bar{h}}_{\mu\nu}(\vec{x},\omega) = \frac{4G}{c^4} \int d^3x' \frac{e^{i\omega \frac{|\vec{x}-\vec{x}'|}{c}}}{|\vec{x}-\vec{x}'|} \tilde{T}_{\mu\nu}\left(\vec{x}',\omega\right) \tag{1.23}$$

being $\vec{x}'$ and $\vec{x}$ the origin of the radiation source and the observation point respectively. $\tilde{T}_{\mu\nu}$ is the Fourier transform of the stress-energy tensor and it is different from zero only inside the source.

To understand what are the radiative components of the tensor $h_{\mu\nu}$ it useful to rewrite the kernel of the integral (1.23) by considering some approximations.

Let us consider a reference system whose origin is in the center of the source, and suppose that this source is contained in a sphere of radius L such that $|\vec{x}'| < L$. If the GW wavelength is greater than L ($\lambda_{GW} \gg L$) we can write:

$$\frac{2\pi c}{\omega_{GW}} \gg |\vec{x}'| \qquad \Rightarrow 2\pi c \gg \omega_{GW} |\vec{x}'| \simeq v_{source} \tag{1.24}$$

where ω_{GW} is the GW angular frequency, and v_{source} the source points speed. This implies that, for a bounded system, $v_{source} \ll c$. Using this *slow-motion approximation* and considering a point very far from the source we have:

$$|\vec{x}-\vec{x}'| \simeq |\vec{x}| - \hat{n}\cdot\vec{x}' + O\left(\frac{L^2}{|\vec{x}|}\right) \tag{1.25}$$

where $\hat{n} = \overrightarrow{x} / \mid \overrightarrow{x} \mid$. Thus we can approximate

$$\begin{aligned}\frac{e^{i\omega\frac{|\overrightarrow{x}-\overrightarrow{x}'|}{c}}}{\mid \overrightarrow{x}-\overrightarrow{x}' \mid} &\simeq \frac{e^{i\omega|\overrightarrow{x}|/c}}{\mid \overrightarrow{x} \mid}\exp\left[-i\left(\frac{\omega}{c}\right)\hat{n}\cdot\vec{x}'\right] \\ &\simeq \frac{e^{i\omega|\overrightarrow{x}|/c}}{\mid \overrightarrow{x} \mid}\left[1-i\left(\frac{\omega}{c}\right)\hat{n}\cdot\vec{x}'-\frac{1}{2}\left(\frac{\omega}{c}\right)^2\left(\hat{n}\cdot\vec{x}'\right)^2\right]\end{aligned}$$

Using this approximation we can rewrite the solution (1.23) as

$$\tilde{\bar{h}}_{\mu\nu}(\overrightarrow{x},\omega) = \frac{4G}{c^4}\frac{e^{i\omega|\overrightarrow{x}|/c}}{\mid \overrightarrow{x} \mid}\int d^3x'\tilde{T}_{\mu\nu}\left(\overrightarrow{x}',\omega\right)\left[1-i\left(\frac{\omega}{c}\right)\hat{n}\cdot\vec{x}'-\frac{1}{2}\left(\frac{\omega}{c}\right)^2\left(\hat{n}\cdot\vec{x}'\right)^2\right] \quad (1.26)$$

which is equivalent in the time domain to

$$\bar{h}_{\mu\nu}(\overrightarrow{x},t) = \frac{4G}{c^4}\frac{1}{\mid \overrightarrow{x} \mid}\int d^3x'\left[T_{\mu\nu}\left(\overrightarrow{x}',t_{ret}\right)-\frac{1}{c}\dot{T}_{\mu\nu}\left(\overrightarrow{x}',t_{ret}\right)\hat{n}\cdot\vec{x}'+\frac{1}{2c^2}\ddot{T}_{\mu\nu}\left(\overrightarrow{x}',t_{ret}\right)\left(\hat{n}\cdot\vec{x}'\right)^2\right] \quad (1.27)$$

with $t_{ret} = t - \mid \overrightarrow{x} \mid /c$. In this expression we can distinguish a **monopole** term:

$$\bar{h}^{(M)}_{\mu\nu}(t,\overrightarrow{x}) = \frac{4G}{c^4R}\int d^3x' T_{\mu\nu}(\overrightarrow{x}',t_{ret},) \quad (1.28)$$

a **dipole** term:

$$\bar{h}^{(D)}_{\mu\nu}(t,\overrightarrow{x}) = \frac{4G}{c^5R}n_i\int d^3x'[x'^i\dot{T}_{\mu\nu}(\overrightarrow{x}',t_{ret})] \quad (1.29)$$

and a **quadrupole** term:

$$\bar{h}^{(Q)}_{\mu\nu}(t,\overrightarrow{x}) = -\frac{4G}{c^4R}\frac{1}{2c^2}n_in_j\int d^3x'[x'^ix'^j\ddot{T}_{\mu\nu}(\overrightarrow{x}',t_{ret})] \quad (1.30)$$

Remember that the stress-energy tensor $T_{\mu\nu}$ satisfies the following conservation law:

$$\partial_\nu T^{\mu\nu} = 0 \quad (1.31)$$

It follows that the momentum quadrivector P^μ and the angular momentum tensor $M^{\mu\nu}$, defined by:

$$\begin{aligned}P^\mu &= \int d^3x'\tau^{\mu 0}(t,\overrightarrow{x}') \\ M^{\mu\nu} &= \int d^3x'[\tau^{0\mu}(t,\overrightarrow{x}')\cdot x'^\nu - \tau^{0\nu}(t,\overrightarrow{x}')\cdot x'^\mu]\end{aligned}$$

are time independent.

After this small parenthesis it is easy verify that only the time dependent components of the tensor expressed by Equation (1.30) contributes to the radiation. Other terms, proportional to the quadrimomentum components, being these conserved quantities are constant and then do not contribute to the gravitational radiation. Now we can finally verify which terms are radiative and which are not. Let us now analyze the monopole, the dipole and the quadrupole terms of $\overline{h}_{00}$, $\overline{h}_{0i}$ and $\overline{h}_{ij}$:

$$\overline{h}_{00}: \begin{cases} \overline{h}_{00}^{(M)} = constant \\ (non\ radiative\ term) \\ \\ \overline{h}_{00}^{(D)} = constant \\ (non\ radiative\ term) \\ \\ \overline{h}_{00}^{(Q)} \neq constant \\ (radiative\ term) \end{cases} \quad \overline{h}_{0i}: \begin{cases} \overline{h}_{0i}^{(M)} = constant \\ (non\ radiative\ term) \\ \\ \overline{h}_{0i}^{(D)} \neq constant \\ (radiative\ term) \end{cases} \quad \overline{h}_{ij}: \begin{cases} \overline{h}_{ij}^{(M)} \neq constant \\ (radiative\ term) \end{cases} \tag{1.32}$$

Introducing the quadrupole mass distribution of the source:

$$q^{ij}(t_{rit}) = \int d^3x' T_{00}(t_{rit}, x') x'^i x'^j \tag{1.33}$$

it is easy to verify that the the terms that contribute to the gravitational radiation can be written as:

$$\begin{cases} \overline{h}_{ij}^{(M)} = \frac{2G}{Rc^4} \ddot{q}^{ij}(t_{rit}) \\ \\ \overline{h}_{0i}^{(D)} = -\frac{2G}{Rc^3} n_j q^{ij}(t_{rit}) \\ \\ \overline{h}_{00}^{(Q)} = \frac{2G}{Rc^4} n_i n_j \ddot{q}^{ij}(t_{rit}) \end{cases} \tag{1.34}$$

In order to write the Equations (1.34) in the TT gauge, we introduce the *reduced transverse and traceless quadrupole momenta:*

$$Q_{ij} = q_{ij} - \frac{1}{2}\delta_{ij} q \tag{1.35}$$

The radiative part of h_{ij} is given by:

$$h_{ij}^{TT} = \frac{2G}{c^4 R}[\ddot{Q}_{ij} + \frac{1}{2}(n_i n_j + \delta_{ij})\ddot{Q}^{kl} n_k n_l - (n_i n^k \ddot{Q}_{kl} + n_j n^k \ddot{Q}_{ki})](t_{rit}) \tag{1.36}$$

known as **quadrupole radiation formula**. Introducing the transverse projectors

$$P_{ij} = \delta_{ij} - n_i n_j$$
$$P_{ij,k\ell} = P_{ik}P_{j\ell} - \frac{1}{2}P_{ij}P_{k\ell}$$

it is possible to simplify Equation (1.36) as:

$$h_{ij}^{TT} = \frac{2G}{c^4 R} P_{ij,k\ell}\ddot{Q}^{k\ell}(t_{rit}) \tag{1.37}$$

It easy to verify that h_{ij} is **transvers and traceless**:

$$n^i h_{ij}^{TT} = 0$$
$$\delta^{ij} h_{ij}^{TT} = 0$$

As we see, the gravitational wave production is proportional to the second time derivative of the transverse and traceless quadrupole moment of the source. This is the fundamental difference respect to the electromagnetic radiation, whose higher order term is proportional to the second time derivative of the electric dipole moment of the source. Another interesting observation is that a spherically symmetrical distribution of matter, whose transverse quadrupole moment is equal to zero at all times, does not emit, in agreement with the Birkhoff theorem, which states that all spherically symmetric solutions of the vacuum Einstein equations are static. This is analogue to the electromagnetic case in which Gauss theorem implies that the electric field of a spherically symmetric distribution of charge, outside the distribution, does not emit, being it equal to the Coulomb field of the total charge.

1.3 Gravitational waves sources

Being *GW* interaction with matter very weak, only astrophysical sources, characterized by a great mass and relativistic speed can emit detectable gravitational waves. Based on the temporal behavior of the signal they generate, it is possible to distinguish several kind of gravitational wave sources [69].

Periodic sources A periodic or quasi-periodic signal is a superposition of periodic components with a constant or quasi constant period. Examples of this kind of sources are

pulsar inspiralling neutron stars or black holes binaries

Chirp from coalescing compact binaries Examples of this kind of sources are inspiralling neutron stars or black holes binaries.

Impulsive sources A impulsive signal is characterized by a time duration shorter than the typical time of observation. Sources of this kind of signal are supernovae explosion and gamma ray bursts.

Stochastic background Signals with statistical fluctuations with a time duration longer than the typical observation time is classified as stochastic background. They can have astrophysical or a cosmological origin.

1.3.1 Pulsar

A pulsar is a highly magnetized rotating neutron star emitting a beam of electromagnetic radiation. Current models of stellar evolution predict the presence of approximately 10^9 neutron stars in our galaxy of which 10^5 are expected to be spinning and actively emitting radiation. Only about 1700 pulsars have been observed so far. This is due to the high variability in the intensity of the generated radiation [40, 44].

Assuming that the neutron stars are uniformly distributed in the galaxy and have a constant birthrate, the strongest expected signals will have an amplitude $h \approx 10^{-24}$.

In a ground-based detector, the frequency range of the GWs from pulsars is $[20H - 2kHz]$.

The amplitude of the wave depends on the momentum of inertia of the star along the spin axis I, on the distance from the Earth r and on the ellipticity ε.

The amplitude of the gravitational wave produced by a pulsar, depends on its rotation frequency, its distance from the earth, and by the amount of asymmetry [54]. Including, also the rotational period P , the typical gravitational wave amplitude for a Pulsar is:

$$h \sim 4.2\,10^{-24} \left(\frac{\mathrm{ms}}{P}\right)^2 \left(\frac{\mathrm{Kpc}}{r}\right) \left(\frac{I_3}{10^{38}\mathrm{Kg\,m^2}}\right) \left(\frac{\varepsilon}{10^{-6}}\right) \tag{1.38}$$

Even though the amplitude of the pulsar is slower than the amplitude of other source , can be observed for a longer time T and they are good source of detectable gravitational signal.

1.3.2 Coalescing binaries

Coalescing Binaries are the most promising sources of gravitational waves [31, 32, 40, 44]. A binary system composed by compact objects (two black holes, two neutron stars or a black hole and a neutron star) is expected to produce a detectable gravitational wave signal, since its

frequency, for a certain interval of masses, belongs to the frequency band in which ground based detectors are more sensitive. The binary coalescence process can be divided in three phases: inspiral, merger, ringdown. During the inspiral phase the two compact objects spiraling around each other and emits a chirp signal whose amplitude and frequency increase with time. This phase lasts until the orbits became unstable and it is the only one for which the gravitational waveform is known.

A first order the calculation of the characteristic parameters for these systems can be done using the Newtonian approximation [54]. The expected amplitude of the two polarization components of h are:

$$h_+(r,\theta,t) = \frac{4}{r}\left(\frac{GM_c}{c^2}\right)^{5/8}\left(\frac{\pi f_{gw}}{c}\right)^{2/3}\frac{1+\cos^2\theta}{2}\cos(2\pi f_{gw}t_{ret}+2\phi) \tag{1.39}$$

$$h_x(r,\theta,t) = \frac{4}{r}\left(\frac{GM_c}{c^2}\right)^{5/8}\left(\frac{\pi f_{gw}}{c}\right)^{2/3}\cos^2\theta\,\sin(2\pi f_{gw}t_{ret}+2\phi) \tag{1.40}$$

where

$$M_c = \frac{(m_1 m_2)^{3/5}}{(m_1+m_2)^{1/5}}$$

is the *chirp mass* of a binary system and f_{gw} is the gravitational wave frequency and r is the distance from the source.

If we assume that the motion of the sources is on a given circular keplerian orbit ,the estimated frequency f_{gw} of the gravitational signal amplitude is:

$$f_{gw} = 134\,Hz\cdot\left(1.21\frac{M_\odot}{M_c}\right)^{5/8}\left(\frac{1s}{\tau}\right)^{3/8} \tag{1.41}$$

where $\tau = (t_{coal}-t)_{ret}$ is defined as the retarded time at coalescence and as reference value for M_c we have taken $1.21M_\odot$. Under the assumption of circular orbits and for masses of order of $M_\odot$ we have that the Equations (1.39) and (1.40) become:

$$h_+(t) = \frac{1}{r}\left(\frac{GM_c}{c^2}\right)^{5/4}\left(\frac{5}{c\tau}\right)^{1/4}\frac{1+cos^2t}{2}cos(\Phi(\tau)) \tag{1.42}$$

$$h_x(t) = \frac{1}{r}\left(\frac{GM_c}{c^2}\right)^{5/4}\left(\frac{5}{c\tau}\right)^{1/4}cos^2t\,sin(\Phi(\tau)) \tag{1.43}$$

where $\Phi(\tau)$ is:

$$\Phi(\tau) = -2\left(\frac{5GM_c}{c^3}\right)^{-5/8}\tau^{5/8} + \Phi_0 \tag{1.44}$$

The equation (1.41), (1.42) and (1.43) show us that the amplitude and frequency of the gravitational wave increases as the coalescence is appreciate: this behavior is referred to a "chirping"

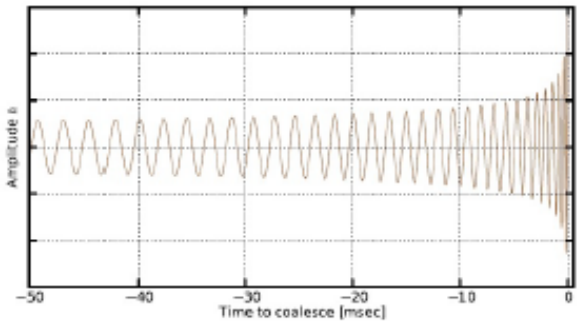

Figure 1.2: Chirp signal produced by NS-NS system.

In the next stage (*merger phase*) the binary system enters the regime of strong field and then becomes not possible to calculate its waveform in an analytic way. In particular, when in the binary system at least a neutron star is involved, during the merger, the violent shock produced, would generate *Gamma Ray Bursts* (GRB) that are flashes of gamma rays associated with very energetic explosions. The gravitational signal produced in this phase is *transient-like*. The last stage is the *ring-down* phase, being the signal analogue to a vibration of a bell. This signal can be decomposed in vibrational modes that dump in an exponential way. The frequency and the damping time depend only on the spin and the mass of the black hole formed by the complete merger of the two objects that compose the binary system.

1.3.3 Supernovae

Supernovae are of two types: Type I and Type II. A type I supernova originates from the gravitational collapse of a white draft star in a binary system; it increases its mass at the expense of its companion until it reaches the Chandrasekhar limit and then the collapse of its core. A type II supernova originates from aged massive star at the end of its evolution process when the nuclear reaction finishes, the outwards pressure due to the radiation is no longer able to balance gravitational force and matter starts to collapse. In both the cases, in a time of the

order of ms, the star core first implodes and then explodes, giving origin to a supernovae. If the implosion and the subsequent explosion happen without a spherical symmetry, during these phase, some fraction of energy is emitted as gravitational radiation is emitted [9]. The emitted gravitational wave amplitude is

$$h \sim 2.7\,10^{-20} \left(\frac{E_{gw}}{M_{\odot}c^2}\right)^{1/2} \left(\frac{1\text{kHz}}{f}\right) \left(\frac{10\text{Mpc}}{r}\right) \tag{1.45}$$

This signal is very rare, in fact in a period of two years it is possible to observe only one event at a distance of $3-5\,$Mpc from the Earth.

1.3.4 Stochastic background

Stochastic background is a relic from the early evolution of the universe which arises from a large number of random, independent events which can't be singularly resolved. A possible origin of a gravitational stochastic background is the superposition, in the time or frequency domain, of signals coming from many astrophysical events. We expect for example that the collapse of vast population of black holes could generate, depending on their mass distribution and formation time, signals with intensity and frequency that can be detected by the present experiments.

Another, particularly interesting stochastic background can be of cosmological origin [53]. This can be generated with several mechanisms at the beginning of universe.

In some cases the expected signal is very weak and is not detectable by the present detectors, but some promising possibilities also exists.

The intensity of a stochastic signal is usually characterized by a dimensionless quantity that is the normalized energy density of the gravitational radiation in the Universe per logarithmic interval of frequency

$$\Omega_{GW}(f) = \frac{1}{\rho_c}\frac{d\rho_{gw}}{d\log f} \tag{1.46}$$

where ρ_{gw} is the energy density of the background, f the spectrum frequency and ρ_c is the critical energy density value for a close Universe defined as

$$\rho_c = \frac{3H_0^2}{8\pi G} \tag{1.47}$$

where H_0 is the present value of the Hubble constant and G the Newtonian gravitational constant.

Chapter 2

Detectors of Gravitational Waves

In other fields of physics the experimentalist is faced with the problem of choosing the most important out of a large number of possible experiments. With gravitation the problem is different. In fact, there are so few possible experiments, and their importance is such, that any and all significant experiments should be performed. First experiments for gravitational wave detection are those performed in the 1960's by J.Weber using two resonant bars. They were aluminum cylinders with a particular resonance frequency which was expected to be excited by gravitational waves. In the resonant bars (the Italian experiments AURIGA, NAUTILUS, EXPLORER, ALTAIR, the experiments ALLEGRO and Niobe in Louisiana, USA and Australia respectively), the amplitude of normal modes of oscillation of a cylindrical metal mass is measured, cooled at cryogenic temperatures, using extremely sensitive magnetic sensors, called Superconducting Quantum Interference Devices (SQUIDs) [25, 69]. Despite the claims of Weber, no gravitational wave was ever detected using this device [86]. Today, the highest expectations of the scientific community are for another kind of instrument, based on interferometry.

2.1 Interferometric detection of Gravitational Waves

The effect of gravitational radiation is to change the distance between two free falling masses, the induced displacement being proportional to the gravitational wave amplitude and to the initial distance between them. In principle, to measure the amplitude of a GW the variation of the distance between two test-masses should be measured. The gravitational signal is very weak and the used device for the detection of such a little signal is an interferometer, that is very sensitive to the variation of the distance between its mirrors (test masses). In particular a Michelson interferometer with suspended mirrors is the most appropriate kind of interferometric device, since its optical configuration is good to detect little differential displacements between

its two arms. Being the strain sensitivity of the interferometer proportional to the optical path length of the laser beam, Fabry-Perot arm cavities are used. To increase the sensitivity the interferometer is further enhanced through power recycling, signal recycling. The detection bandwidth, for a ground-based interferometer, comes from roughly 10Hz to 10kHz. There are several ground-based gravitational wave detectors in the world: LIGO in USA (one in Hanford, Washington and another in Livingston, Louisiana) GEO600 in Germany (Hannover) and VIRGO in Italy (Cascina (PI)). Other detectors are under construction in Japan (KAGRA) and in India (LIGO-Indigo).

All these things will be discussed in detail throughout this chapter.

2.1.1 Effect of a gravitational wave on free falling masses

In order to understand the effect induced by a gravitational wave it can be helpful to write explicitly, in the TT coordinate system, the proper distance between two free falling mass.

In General Relativity, a free falling mass is an object whose motion is only due to the gravitational interaction, and then to the space-time geometry. It moves along a trajectory called *geodesic* with the following equation of motion:

$$\frac{d^2x^\mu}{d\tau^2} + \Gamma^\nu{}_{\nu\rho}\frac{dx^\nu}{d\tau}\frac{dx^\rho}{d\tau} = 0 \tag{2.1}$$

where τ is the proper time and Γ are the *Christoffel Symbols* defined in the previous chapter (see Eq.1.7).

If we consider two geodesics, each parameterized with its proper time, the quadrivector $L^\nu(\tau)$, connecting two points of the geodesics at the same τ, satisfies the equation:

$$\frac{D^2L^\mu}{D\tau^2} = -R^\mu{}_{\nu\rho\sigma}\frac{dx^\nu}{d\tau}\frac{dx^\sigma}{d\tau}L^\rho \tag{2.2}$$

called geodesic deviation equation. It is possible to demonstrate that the variation of the distance between two test masses is proportional to the initial distance (L_0^i) between them and the amplitude of the gravitational wave [87]:

$$\delta L_i = \frac{1}{2}h_{ij}^{TT}L_0^j. \tag{2.3}$$

For example, let's consider a pair of contemporary and aligned events along the x axis:

$$\mathbf{X_1} = (x_0, x, y, z) \qquad \mathbf{X_2} = (x_0, x+L, y, z) \tag{2.4}$$

The infinitesimal vector oriented along this segment has only the x component different from zero, $d\mathbf{x} = (0, dx, 0, 0)$. Assuming that is verified the condition $h \ll 1$ and therefore the

Einstein's equations reduce to wave equations far from the source, we obtain, for a plane wave with + polarization moving along the z direction,

$$ds = dx \cdot \left\{ 1 + \frac{h}{2} \cdot cos\left[\omega \left(t - \frac{z}{c} \right) \right] \right\} \tag{2.5}$$

Integrating this expression over whole the segment we get

$$s_{12} = L + \frac{Lh}{2} \cdot cos(\omega t + \varphi) \tag{2.6}$$

In short, it can be said that the passage of a gravitational wave changes the length of a segment located along an axis of polarization: this length changes at the passage of the gravitational wave with frequency ω . (Fig.2.1).

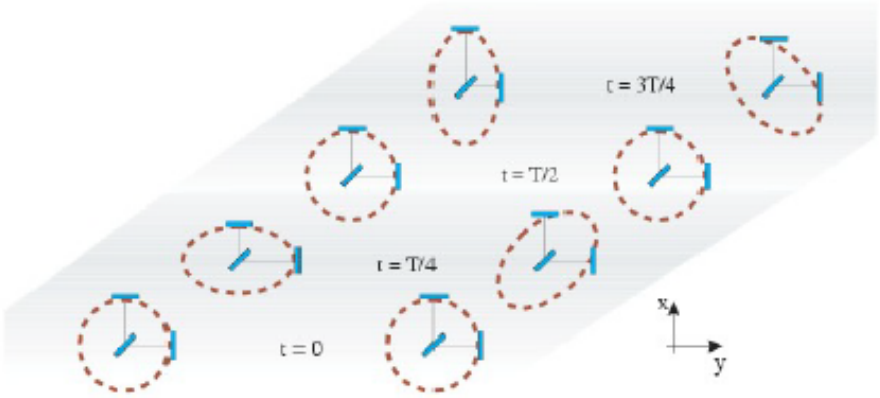

Figure 2.1: Effect of the two different polarization directions of a gravitational wave on a set of freely falling masses arranged on a circumference.

2.1.2 Michelson interferometer

The Michelson interferometer is the core of every GW interferometer. In this kind of interferometer, a beam coming from a light source is divided in two beams by a beamsplitter [6, 69]. The two beams travel along each of the interferometer arms, respectively. At the end of each arm is put a mirror which reflects the beam back towards its original direction. In this way, the beams coming from the two arms recombine at the beam splitter and interfere with each other. The output signal of the interferometer is detected by a photodiode placed at the output port of the interferometer. With this kind of device it is possible to measure the phase differences acquired by the two beams after their paths in the interferometer arms.

With some simple calculation, it is possible to show that what is detected at the interferometer output contains the information about the arms length difference.

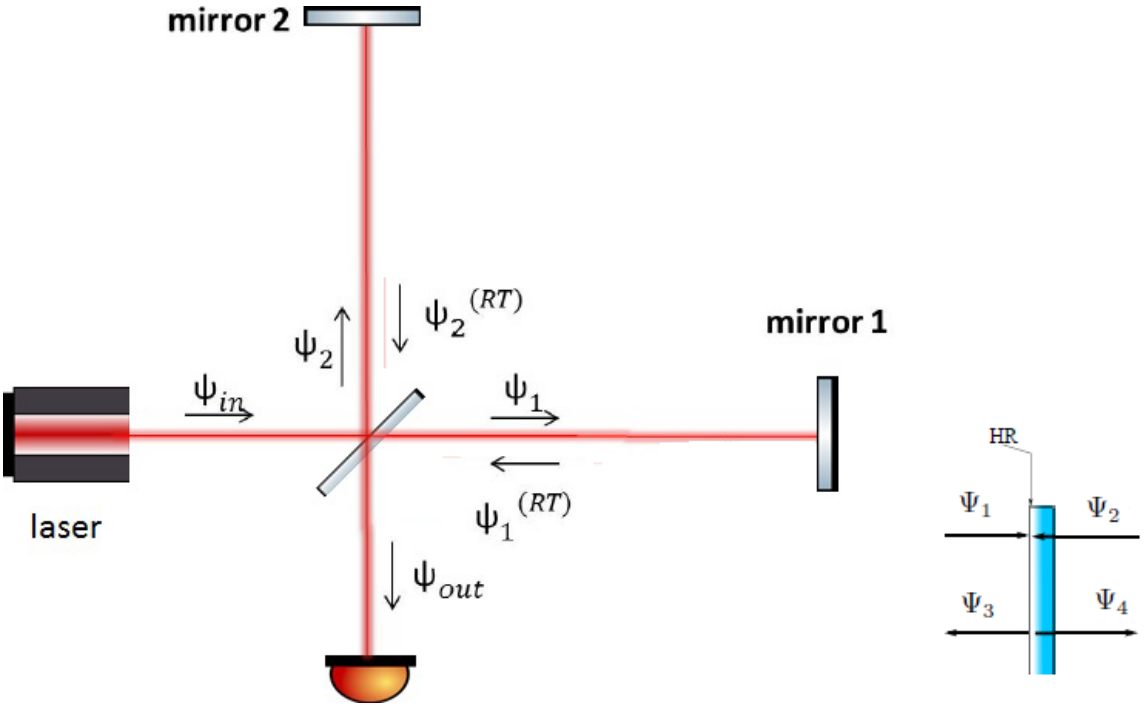

Figure 2.2: On the left, a schematic diagram of a Michelson interferometer. On the right, the sign convention used to evaluate the optical transfer functions.

Let ψ_{in} be the amplitude of the initial field, L_1 and L_2 the lengths of the two interferometer arms. The amplitudes of the transmitted beam, after the reflection by mirror 1 or mirror 2 (after a Round Trip), are [1]:

$$\begin{cases} \Psi_1^{(RT)} = -t_{BS}\, r_1\, e^{-2ikL_1}\, \psi_{in} \\ \\ \Psi_2^{(RT)} = -r_{BS}\, r_2\, e^{-2ikL_2}\, \psi_{in} \end{cases} \tag{2.7}$$

where r_{BS} and t_{BS} are the reflectivity and the transmissivity of the beam splitter mirror, respectively. These two fields recombine at the beam splitter. At the output port, in correspon-

[1] Referring to Figure 2.2, right we have: $\Psi_3 = -r\Psi_1 + t\Psi_2$, $\Psi_4 = r\Psi_2 + t\Psi_1$, where r is the mirror reflectivity. In our case for the end mirrors $r_{1,2} \simeq 1$ and $t_{1,2} \simeq 0$.

dence of which a photodetector is placed, the amplitude field is :

$$\begin{cases} \Psi_{out} = -r_{BS}\Psi_1^{(RT)} + t_{BS}\Psi_2^{(RT)} \\ \downarrow \\ \Psi_{out} = r_{BS}t_{BS}\, e^{-ik(L_1+L_2)} \left(r_1\, e^{-ik(L_1-L_2)} - r_2\, e^{ik(L_1-L_2)} \right) \psi_{in} \end{cases} \tag{2.8}$$

The beam power is proportional to the square modulus of the amplitude, so

$$P_{out} = r_{BS}^2 t_{BS}^2 \left[r_1^2 + r_2^2 - 2r_1 r_2 \cos 2k\,(L_1 - L_2) \right] P_{in} \tag{2.9}$$

This power depends on the difference of length of the arms. Defining the quantity $\phi = 2k\,(L_1 - L_2)]$ we can obtain P_{max} and P_{min} by changing the parameter ϕ

$$\begin{aligned} \phi = 0;\;\; P_{out} \to P_{min} = r_{BS}^2 t_{BS}^2 \,(r_1 - r_2)^2\, P_{in} \\ \phi = \pi;\;\; P_{out} \to P_{max} = r_{BS}^2 t_{BS}^2 \,(r_1 + r_2)^2\, P_{in} \end{aligned} \tag{2.10}$$

P_{out} depends on ϕ and then on the difference in lengths of the two interferometer arms. If this difference is due to the passage of a gravitational wave, and, therefore, to the gravitational wave amplitude, as shown in Eq. (2.3) we can detect a gravitational signal using P_{out}.

We use this property to compute the phase shift due to an incident gravitational wave. In addition we assume that the two interferometer arms have the same microscopic length $(L_1 = L_2 = L)$ and they are oriented along the x and y axis of a reference system, with the beam splitter placed in its origin.

Since the phase accumulated by the laser beam traveling along a path is proportional to the length of the $\Delta\phi = \frac{2\omega}{c}\Delta L$, any small difference with respect to the initial length in terms of phase will be:

$$\delta\phi = \frac{2\omega}{c}\delta L \tag{2.11}$$

Thanks to its configuration, a Michelson interferometer is particularly well suited for the GW detection purpose because of the geometry of the strains that the wave produces. Indeed, as described above, the effect of a gravitational wave propagating along z-direction is to change the distance between free-falling masses and the displacement is proportional to the amplitude of the GW:

$$\frac{\delta L}{L} = \frac{h}{2} \tag{2.12}$$

If we use the mirror at the end of each interferometer's arm as free-falling test mass, we can

write the length variation of the interferometer arm due to the gravitational wave in terms of phase variation

$$\delta\phi = \frac{\omega}{c} hL \tag{2.13}$$

2.1.3 Fabry-Perot Cavity

As discussed above the longer the interferometer arms the better the sensitivity. For this reason, the two arms of the simple Michelson interferometer are substituted with Fabry-Perot cavities.[78, 84]

These cavities are constituted by two plane mirrors, called the input and end mirrors, separated by a distance L and with reflectivities r_1 and r_2.

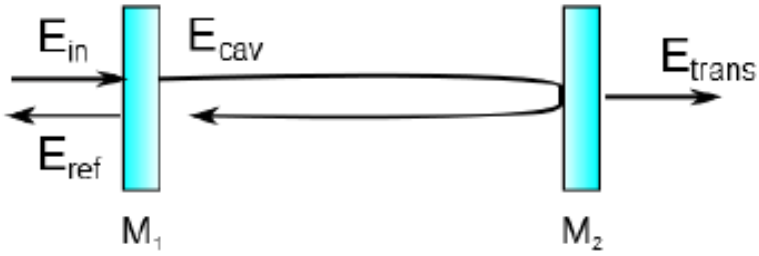

Figure 2.3: Schematic configuration of a Fabry-Perot cavity

Referring to Figure 2.3 and keeping in mind the sign convention defined in Fig. 2.2, we can compute the propagating fields which are given by:

$$\begin{aligned} E_{cav} &= t_1 E_{in} + r_1 r_2 e^{-2ikL} E_{cav} \\ E_{ref} &= r_1 E_{in} - t_1 r_2 e^{-2ikL} E_{cav} \\ E_{trans} &= t_2 e^{-ikL} E_{cav} \end{aligned} \tag{2.14}$$

Consequently, the expression for the cavity field and therefore for the intracavity power is given by

$$P_{cav} = \mid E_{cav} \mid^2 = \frac{t_1^2}{(1-r_1 r_2)^2 - 2r_1 r_2 \cos 2kL} P_i \tag{2.15}$$

The resonance condition occurs when $e^{-2ikL} = 1$ and the cavity gain is equal to

$$G_{cav} = \left(\frac{t_1}{1 - r_1 r_2} \right)^2 \tag{2.16}$$

The effect of a Gravitational Wave would induce a small detuning δL around the resonant position. Indeed if we consider a detuning δL around the resonant position we have that the power stored in the cavity is

$$P_{cav} = G_{cav} \frac{1}{1 + \frac{4}{\pi^2}\mathscr{F}^2 \sin^2 \frac{2\pi}{\lambda}\delta L} P_{in} \tag{2.17}$$

where $\mathscr{F} = \frac{\pi\sqrt{r_1 r_2}}{1-r_1 r_2}$ is the finesse of the cavity. It's possible to demonstrate that, the detuning from resonance that give half of the maximum power (half width at half maximum) is determined by

$$\delta L_{HWHM} = \frac{\lambda}{4\mathscr{F}} \tag{2.18}$$

It can be easily shown with some computations [78, 84], taking into account that the finesse is typically much larger than unity and total losses are small, that the slope around resonance is given by

$$\frac{d\phi}{dL} = \frac{8\mathscr{F}}{\lambda} \tag{2.19}$$

Another important aspect to consider is the cavity frequency response: indeed, the gravitational wave signal can be modeled as a sinusoidal signal shaking the mirrors at a certain frequency and for this reason we are interested to know the cavity response at that particular frequency.

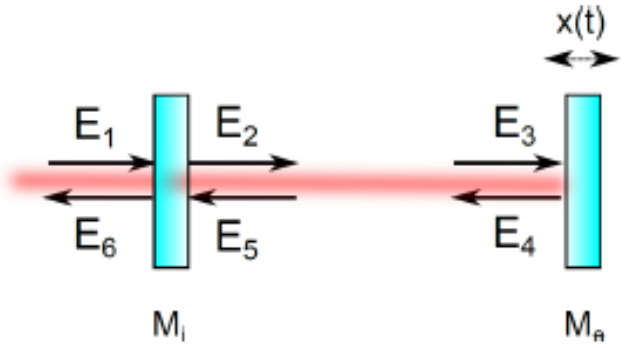

Figure 2.4: Schematic of the Fabry-Perot cavity and fields at each point of the cavity.

Considering the scheme showed in figure 2.4, we can model the relative motion between the two mirrors as a sinusoidal waveform applied only to the End mirror

$$x(t) = x_0 cos(\omega_s t) \tag{2.20}$$

The field reflected by the mirror Me gets an additional dephasing

$$E_4 = -r_e E_3 e^{-2ikx(t)} \tag{2.21}$$

If the displacement is very small with respect to the wavelength ($x_0 \ll \lambda$), we can expand the exponential and get

$$E_4 = -r_e E_3 - \frac{2\pi}{\lambda}(e^{-i\omega_s t} + e^{i\omega_s t})E_3 \tag{2.22}$$

Equation (2.22) shows that if the mirror is moved at a frequency ω_s, two signal sidebands at the frequency of the signal are created inside the cavity. These additional sidebands propagate inside the cavity and undergo interference.

The field reflected from the cavity at ω_s is

$$E_6(\omega_s) = -\frac{2\pi}{\lambda} r_e \frac{1}{(1+\frac{f_s}{\frac{c}{4LF}})} \frac{t_i^2}{(1-r_i r_e)^2} E_1 x_0 \tag{2.23}$$

This equation shows that the cavity response, as a function of the frequency, has a simple pole at a frequency given by

$$f_p = \frac{c}{4LF} \tag{2.24}$$

where $c/2L$ is the cavity free spectral range and F is the cavity finesse.

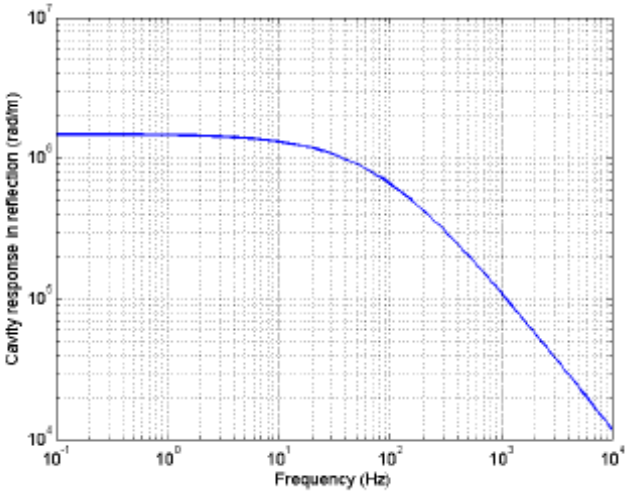

Figure 2.5: Frequency response of a Fabry-Perot cavity with a cavity pole at f_p = 80 Hz.

Therefore, any sideband at a frequency lower than the cavity pole, gets an additional gain,

while when its frequency is higher than the cavity pole, it is suppressed by the cavity filtering action.

2.2 Gravitational Waves Detectors: VIRGO experiment

VIRGO experiment was born as an international collaboration between the Italian INFN (Istituto Nazionale di Fisica Nucleare) and the French CNRS (Centre National de la Recherche Scientique). Its construction was completed in June 2003 and its first science run in May 2007.

To increase the power circulating into the interferometer and then to improve the sensitivity of the detector, a Power Recycling Mirror (PRM) is used [16]. This mirror is placed in front of the laser in a position such that light that come back towards the laser direction arrives in phase on it. In this way, together with the rest of the interferometer, it forms another cavity (recycling cavity) so that the beam power increases and in the Fabry-Peorot cavity reaches several tens of kilowatts. In addition to the Fabry-Perot cavities and the power recycling cavity, in the optical scheme of Virgo there are also two Mode Cleaner cavities: the Input one is placed before to inject the laser into the interferometer ensuring a good TEM00 mode entering the interferometer and the Output one is placed before the output photodiode, this is used to filter the signal and to improve the signal to noise ratio. The major challenge is to make the optics almost perfect and the mirror suspensions perfectly stable so that at the output port of the interferometer, only the light due to the mirror displacement, caused by the passage of a gravitational wave, could be detected.

To reach a very good stability the mirrors are suspended by an isolation system called **Superattenuator**. It allows to have a very good sensitivity also at low frequencies where the first generation of the others detectors in the world had a lower sensitivity . The Superattenuators performance will be the main topic of this thesis work.

2.2.1 Advanced VIRGO Design

With the aim to explore a volume of Universe 1000 times larger (increasing in this way by a factor 1000 the rate of sources) by improving the sensitivity by a factor 10, the Virgo collaboration did an upgrade of the Virgo interferometer. The goal of this upgrade is to construct an advanced detector, **called Advanced VIRGO (AdV) [16, 21, 22].** The main changes with respect to Virgo are:

1. **Introduction of a Signal Recycling (SR) mirror.** It is be placed between the beam splitter and the detection bench. This mirror, similarly to the PR mirror, forms a new cavity (recycling cavity) with the rest of the interferometer. By the tuning of the cavity

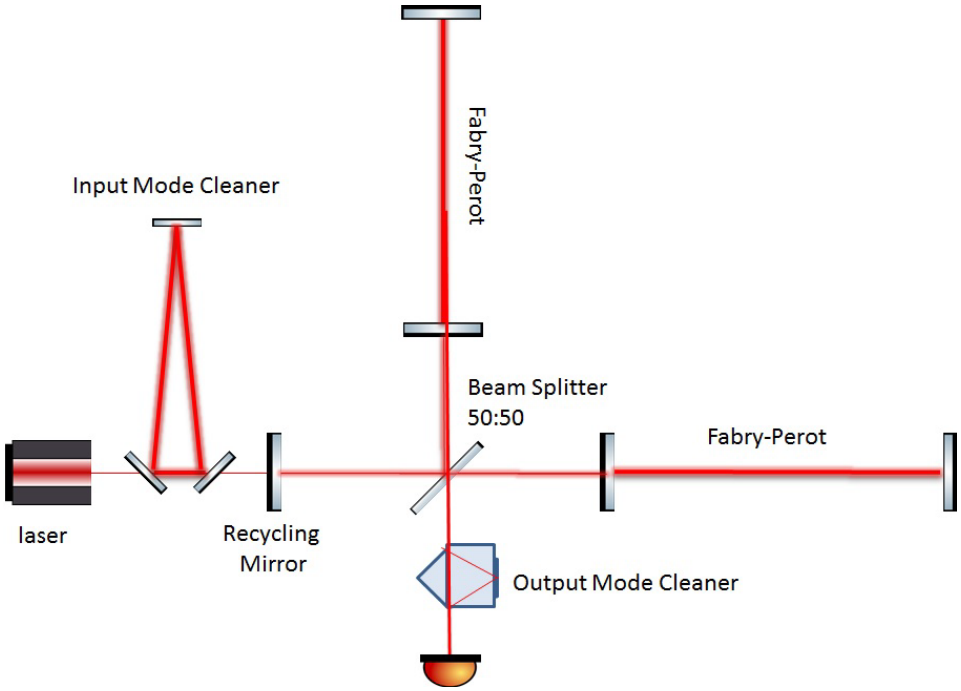

Figure 2.6: VIRGO experiment layout

Source	AdV detection rate $[\mathrm{yr}^{-1}]$	Virgo detection rate $[\mathrm{yr}^{-1}]$
NS-NS	17	4.5×10^{-3}
NS-BH	4.7	1.2×10^{-3}
BH-BH	7.6	1.9×10^{-3}

Table 2.1: Expected detection rates of compact binary coalescence for Advanced Virgo compared to that of Virgo

parameters it is possible to significantly increase the sensitivity detector in a certain frequency band and then to change the shape of the sensitivity curve. In this way the detector can be optimized for different astrophysical sources.

2. **increasing of the laser power**. After 2018 a 200 W laser, based on fiber amplifiers, will be installed. In the first years of operation the Virgo laser is used, that provide a power up to 60 W. A so high power requires specifically designed electrooptic modulators and Faraday isolators. Another problem is an increase of thermal aberration due to thermal lensing (also present in Virgo) and, in addition, to a thermo-elastic deformations of the mirrors. To cope with this problem a sophisticated new Thermal Compensation System (TCS) is used. Its sensing system includes includes a device, called phase camera, that measure the amplitude and phase of the beams, and a wavefront sensor, in particular a Hartmann sensor. The actuating system is based on a CO2 laser that provides a suitable

heating pattern by a double-axicon system and, for each mirror, a Compensation Plate (CP) and a Ring Heater (RH). To correct the thermal lensing, in Virgo, the heating pattern produced by the CO2 laser, was generated by a single-axicon and sent directly on the mirror, this makes possible a noise reduction by a factor of 10^2 ; in AdV a noise reduction by a factor of 10^3 is required. This laser has an intensity noise that worsens the detector sensitivity at low frequencies $(50-100Hz)$ where new generation of detectors are more sensitive. To limit this, a new transmissive optical (the CP) has been introduced between the laser and the mirror. Finally the RH, that is a circular resistor, is used to correct the radius of curvature of the mirrors.

3. **increase of the mirrors mass.** To reduce fluctuations due to thermal noise, the mirror masses are increased from 20 kg to 42 kg. For most critical optics fused silica substrates with low absorption and high homogeneity are used. These optics will have a very good level of polishing $(0:5nm\ rms)$ and coatings characterized by low-losses and low-absorption to limit the thermal noise and the optical losses.

4. **stray light control.** diaphragm baffles, either suspended around the mirrors, or ground connected inside the vacuum links, will be installed to reduce phase noise due to light backscattered into the interferometer. Main photodiodes are placed on suspended bench in vacuum to limit seismic and acoustic noise.

5. **payloads.** The mirror suspensions were improved with a new payload that is the last stadium of the Superattenuator. It must cope with the heavy of the mirror, the compensation plate and the baffle.

2.2.2 Detector sensitivity

The signal $s(t)$ output of the detector is given by the sum of a gravitational wave signal $h(t)$ and a noise $n(t)$: the detector sensitivity $\tilde{h}$ is actually defined in terms of the spectral density of this noise. Assuming that the noise is Gaussian and stationary, we can write the one-sided noise spectral density $S_n(f)$ as

$$\frac{1}{2}S_n(f) = \int e^{2\pi i f} C_n(t)dt \tag{2.25}$$

where $C_n(t)$ is the noise autocorrelation between time 0 and t. The detector sensitivity is defined as

$$\tilde{h}(t) \equiv \sqrt{S_n(t)} \tag{2.26}$$

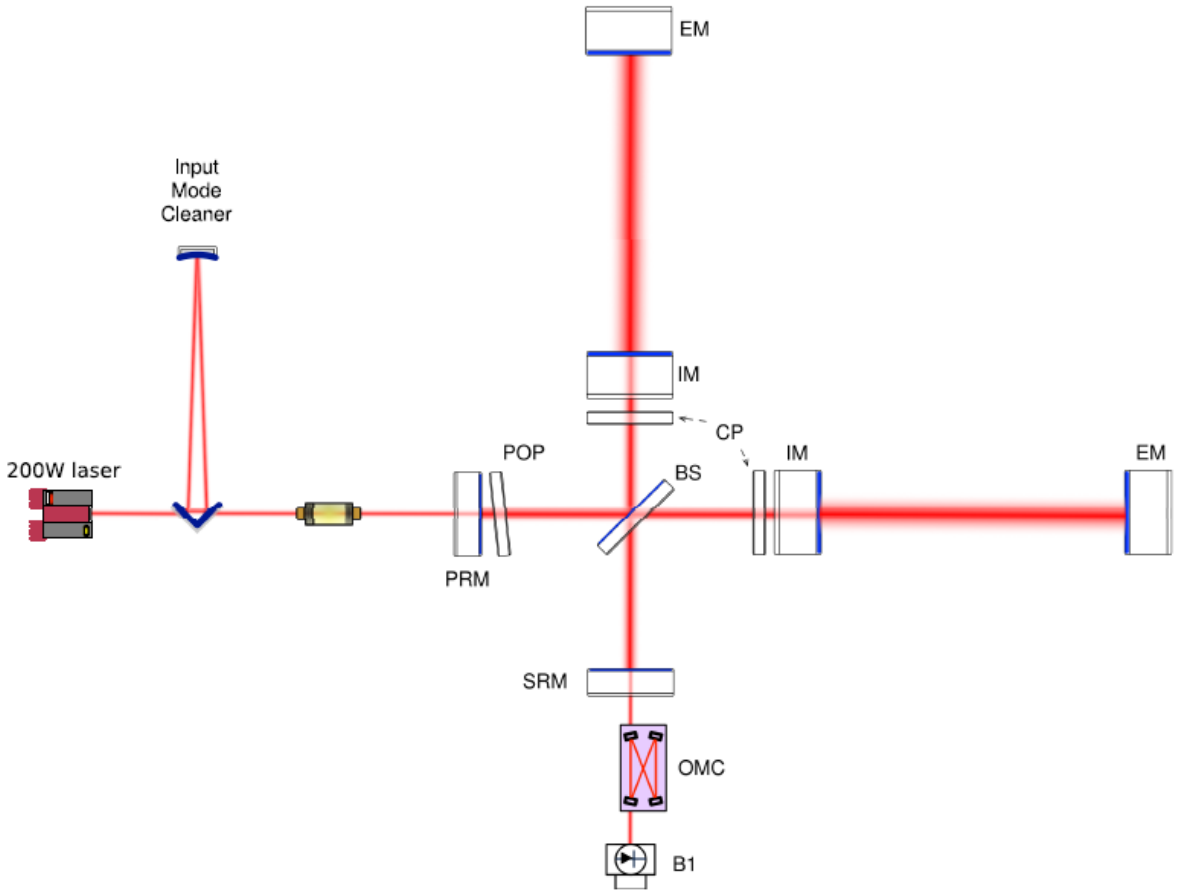

Figure 2.7: Simplified optical layout of Advanced VIRGO

It is measured in $1/\sqrt{Hz}$.

Great part of the sensitivity band is limited by the fundamental noise: it arises from the quantum fluctuations of the laser power which translate into noise at the read-out photodiode on the one hand and in mirror displacement for radiation pressure noise on the other hand. In addition to that, environmental and technical noise sources must be taken into account.

2.3 Noise sources in ground based interferometric Detectors

The main sources of noise, that limit the detection of the gravitational signal, are [69]:

- **seismic, Newtonian noise (at low frequencies)**
- **thermal noise (at medium frequencies)**
- **shot noise (at high frequencies)**

2.3.1 *Seismic Noise*

The dominant noise at low frequencies below $3\,Hz$ is represented by seismic noise originating from vibrations of the ground which are transferred to the test masses via their suspensions. Seismic noise has both natural and human origins and can vary by few orders of magnitude from site to site.

The typical linear spectral density of seismic displacement can be modeled as

$$\tilde{x}_{seism}(f) \simeq \frac{\alpha}{f^2} \tag{2.27}$$

the coefficient α depends on the site and is about $10^{-7} mHz^{\frac{3}{2}}$ in Cascina.

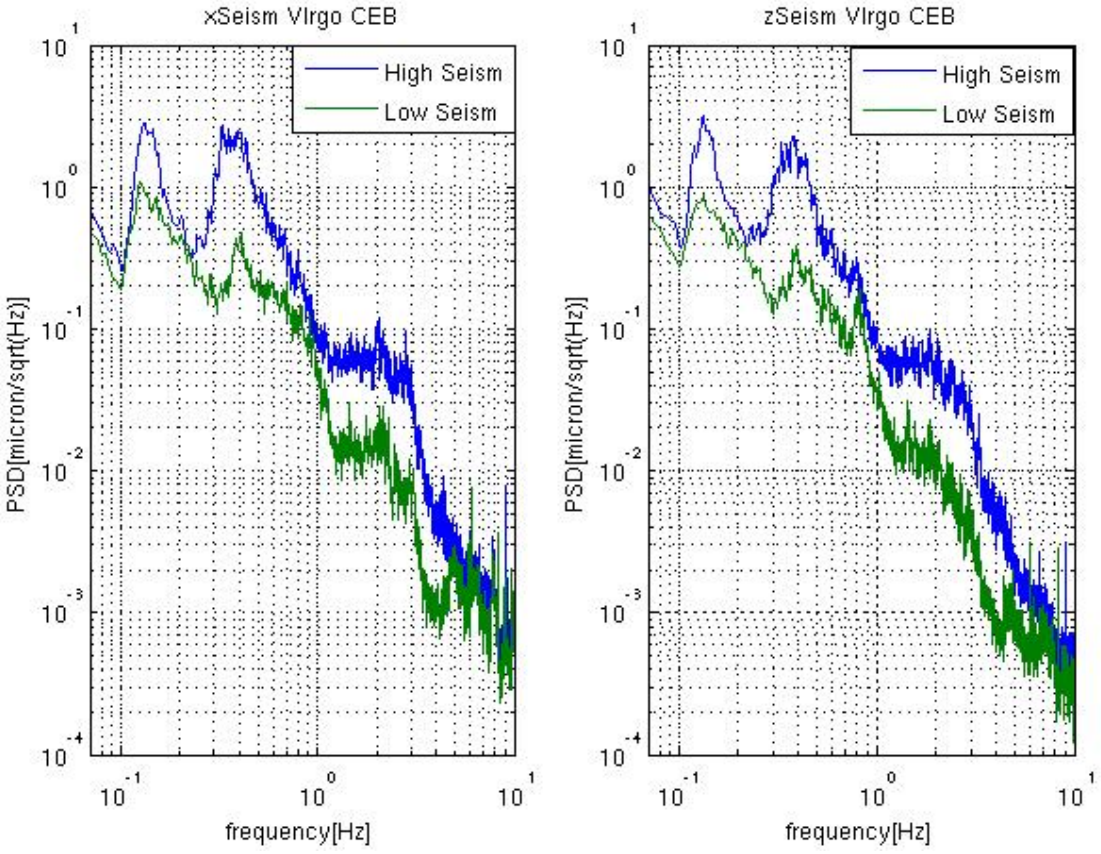

Figure 2.8: Power Spectral Density (PSD) of microseism acquired by the environmental sensors disseminated on EGO site. This figure shows two different seismic conditions along to the longitudinal axis to the North direction (right figure) and West direction (left figure). In particular, blue and green curves show the typical PSDs of the microseism that occurs in winter and summer seasons respectively.

The intensity of these phenomena changes according to the seasons and it becomes particu-

larly high in winter. In Figure 2.8 two different seismic phenomena are shown.

If we compare $\tilde{x}_{seism}(f)$ with the $10^{-18} m/\sqrt{Hz}$ displacement induced by a GW , we see that we need an isolation system capable to attenuate the seismic noise by 11 orders of magnitude at 1 Hz.

In the Part II of this thesis we will discuss in great detail about the Seismic Isolation System adopted in Virgo and the seismic noise on EGO site.

2.3.2 Newtonian Noise

Seismic Newtonian noise (or *Gravity gradient noise*) is generate by the local gravitational fluctuations due to the seismic waves in the ground. These fluctuations changes the mass density distribution around the mirrors.

Essentially, we have many sources of local gravitational fluctuations:

-the motion of macroscopic objects around the test masses;

-the seismic motion of ground;

-the random motion of particles of then atmospheric particulate matter (*atmospheric Newtonian noise*).

An estimation of the gravity gradient power spectra has been obtained by P. Saulson in [69]and it assume the following form

$$\tilde{h}_{gg} \simeq \frac{1 \cdot 10^{-11}}{f^2} \tilde{x}_{seism} \tag{2.28}$$

More refined estimates [68] of the gravity gradient noise give results that are agree with the Eq. (2.28) but, its behavior at low frequencies has been correct

$$\tilde{h}_{gg} \simeq \begin{cases} \frac{\beta \cdot 6 \cdot 10^{-23}}{0.6\sqrt{Hz}} \left(\frac{10}{f}\right)^2 & 3Hz < f < 10Hz \\ \\ \frac{\beta \cdot 6 \cdot 10^{-23}}{0.6\sqrt{Hz}} \left(\frac{10}{f}\right)^4 & 10Hz < f < 30Hz \end{cases} \tag{2.29}$$

with $0.15 < \beta < 1.4$ depending on the site seismic activity.

This noise dominates in the frequency band below 5 Hz and acts directly on the mirrors bypassing their isolation system, so a ground-based detector can not have a frequency detection band below this frequency.

Future GW detectors, the so-called 3rd generation interferometers, are expected to extend their detection band to lower frequencies (f < 10 Hz). This range is dominated by seismic motion as well as from the gravity gradient noise: for this reason one solution to reduce these noise sources, is to build future interferometers in deep underground sites (see Sec. 4.4).

2.3.3 Thermal Noise

Thermal noise is another disturbance particularly important for interferometric GW detection in the low frequency range.

The interferometer mirrors are in radiative thermal equilibrium with the vacuum chambers that are at room temperature [37]. The energy exchange generates the Brownian motion of the particles of mirror glass, coating and suspension system and consequently induces a fluctuation in the measured cavity length.

The power spectrum of the fluctuating force F_{therm} induced by the dissipation simply as

$$\tilde{F}^2_{therm} = 4k_B T \Re(Z(f)) \tag{2.30}$$

where k_B is the Boltzmann's constant, T is the temperature and $\Re(Z(f))$ is the real part of the mechanical impedance $Z(f)$. The relationship (2.30)can be written as

$$\tilde{x}^2_{therm} = \frac{k_B T}{\pi^2 f^2} \Re(Y(f)) \tag{2.31}$$

where $\tilde{x}_{therm}$ is the power spectrum of the system fluctuating displacement and $Y(f) = 1/Z(f)$ is the mechanical admittance.

There are several contributions to thermal noise that can be grouped in two categories:

suspension thermal noise

- *Pendulum thermal fluctuations*: are oscillations in the suspensions due to thermal fluctuations. They induce a horizontal displacement of the mirrors;
- *Vertical thermal fluctuations*: are vertical motion of the suspensions. This becomes important even if we are interested in horizontal distance between the mirrors because of the vertical-horizontal coupling due to the fact that, given the Earth curvature, the direction of the vertical, at the end mirrors, is not the same;
- *Violins modes:* noise due to the fluctuations of the normal modes of the wires the mirrors are suspended to.

mirrors thermal noise

- *Brownian motion of the mirrors:* is due to the kinetic energy of the mirrors atoms at temperature T;

- *Thermo-elastic fluctuations*: take place both in the mirror bulk and in the mirror coating. They are due to the thermal expansion of the material.;

- *Thermo-refractive fluctuations:* is the noise due to the variation of the material refractive index with the temperature.

2.3.4 Shot noise and Radiation Pressure Noise

Shot noise and radiation pressure noise are two faces of quantum noise is one of the main noise sources that limit the sensitivity of an interferometric gravitational wave detector. They appear as a power fluctuation of the power at output port of the interferometer: they are originated from the statistical fluctuations in photons number (shot noise) and from the radiation pressure fluctuations acting on the end mirrors. Both these noises are due to the zero-point fluctuations (vacuum noise) of the electromagnetic field entering in the unused port of the interferometer [12].

Shot Noise

The shot noise is a fundamental disturbance associated to the quantum nature of light that poses a limitation on power measurements. This process is caused by the Poissonian distributed counting of the photons hitting the interferometer photodetector.

The average number of photons N of frequency ν, impinging on a photodiode of quantum efficiency η , in a time interval Δt can be written as:

$$N = \frac{\eta P_{ASY} \Delta t}{2\pi\hbar\nu} \tag{2.32}$$

For a Poisson distribution the standard deviation $\sigma = \sqrt{N}$, the corresponding variation in power is

$$\delta P_{shot} = \sqrt{\frac{P_{ASY} 2\pi\hbar\nu}{\eta \Delta t}} \tag{2.33}$$

Therefore the signal to noise ratio can be written as

$$SNR = \frac{|\delta P_{GW}|}{\delta P_{shot}} \tag{2.34}$$

In order to find the best operating point, we have to maximize the expression (2.34) respect to the static phase ϕ.

If we consider the contrast $C \simeq 1$, we get

$$\phi_{OP} = \pm k\pi \tag{2.35}$$

This is the dark fringe condition and it corresponds to $P_{ASY} = 0$.

The minimum detectable signal expressed in terms of GW amplitude linear spectral density is found imposing $SNR = 1$

$$\tilde{h}_{shot} = \frac{1}{L}\sqrt{\frac{\hbar c\lambda}{2\pi\nu P_{IN}}} \tag{2.36}$$

If we consider an interferometer with its arms constituted by two Fabry-Perot cavities, assuming very high reflectivities and very low loss of the mirrors, we can write the Equation (2.36) as

$$\tilde{h}^{FP}_{shot}(f) \simeq \frac{1}{8FL}\sqrt{\frac{\pi\hbar c^2}{\nu P_{IN}}}\sqrt{1+(4\pi f_{GW}\tau_s)^2} \tag{2.37}$$

this determines the frequency dependence of the interferometer sensitivity.

Radiation Pressure

The radiation pressure noise is due to photons that impinge the mirrors and are reflected back from them. Since this pressure fluctuates, it generates a stochastic force on the mirror that can not be compensated.

The photons are Poissonian distributed, we expect a displacement fluctuation of the mirrors $\tilde{h}_{rp} \propto \sqrt{P_{IN}}$.

The radiation pressure noise spectrum is written as

$$\tilde{h}_{rp}(f) = \frac{1}{mLf^2}\sqrt{\frac{\hbar P_{IN}}{2\hbar^3 c\lambda}} \tag{2.38}$$

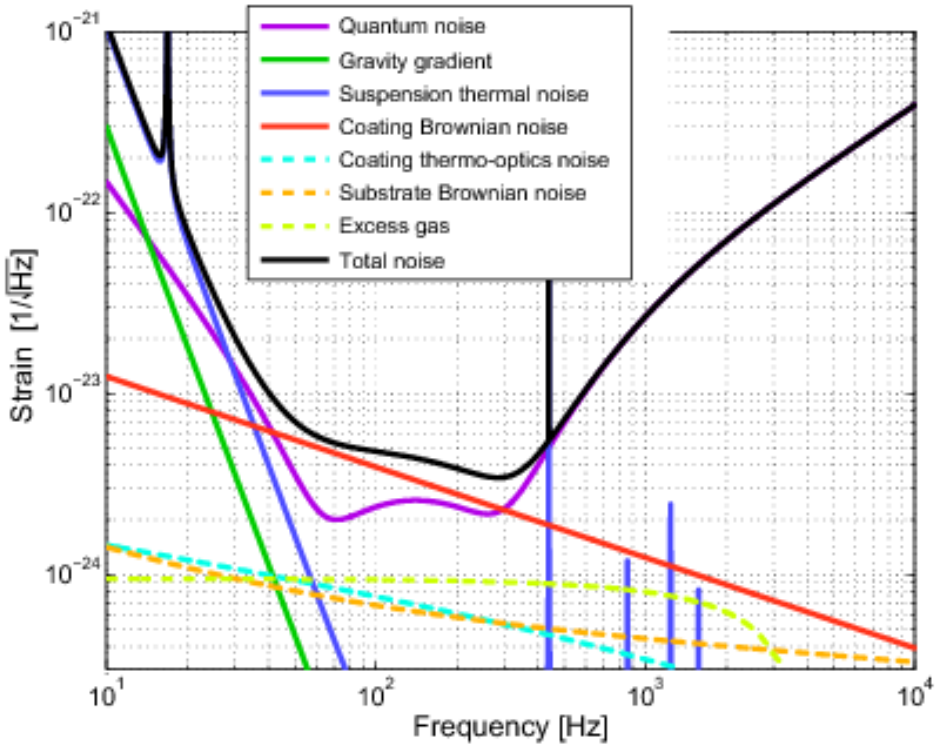

Figure 2.9: Reference Advanced Virgo sensitivity and expected noise contributions.

Chapter 3

Direct detection of GW by using ground based interferometers

The existence of gravitational waves was demonstrated by the discovery of the binary system PSR1913+16, performed by Hulse and Taylor [41], and by the observation of its energy loss by Taylor and Weisberg [80]. In 1974, Hulse and Taylor observed a pulsar with an anomalous behavior of its period. They understood that this variation in period was due to the Doppler shift caused by the presence of a companion object: the pulsar form, in fact, a close binary system with a neutron star. The measured orbital period is $P = 7\,h\,75\,m$ and its decrease over time is in agreement with the energy loss due to the gravitational radiation emission. After the discovery of the binary system, the shift of its orbital period has been observed for more than 30 years; figure 3.1 shows the result of these measurements compared with the General Relativity prediction. The perfect agreement conrfims the existence of gravitational waves.

The direct observation of gravitational waves has been possible thanks to the development and construction of the modern ground based interferometers.

3.1 The first direct gravitational wave detection: GW150914

On February 11, 2016 the Virgo and the LIGO collaborations simultaneously announced the first gravitational wave detection.

This is the abstract of the detection paper [32]:

On September 14, 2015 at 09:50:45 UTC the two detectors of the Laser Interferometer Gravitational-Wave Observatory simultaneously observed a transient gravitational-wave signal. The signal sweeps upwards in frequency from 35 to 250 Hz with a peak gravitational-wave strain of 1.0×10^{-21}. *It matches the waveform predicted by general relativity for the inspiral*

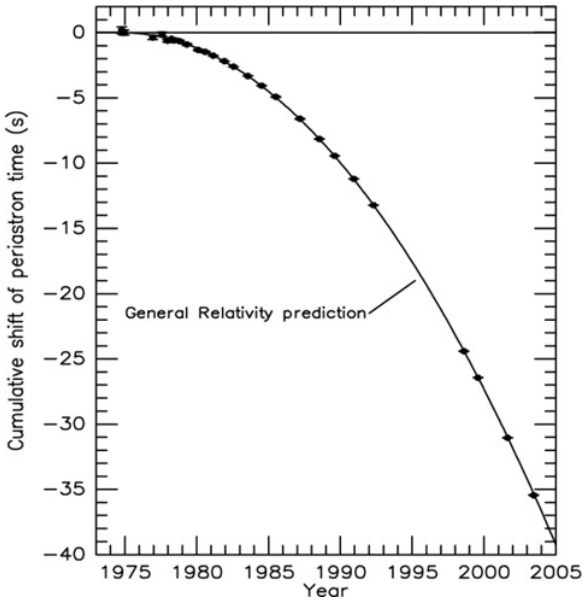

Figure 3.1: Orbital phase residuals for the binary system PSR1913+16. If the orbital period had remained constant, the points would be expected to lie on a straight line. The curvature of the parabola drawn through the points corresponds to the general relativistic prediction for loss of energy to gravitational radiation. This caption quotes the caption of FIG. 6. in the original paper of Taylor and Weisberg, that takes into account the measurement performed in 7 years [80].

and merger of a pair of black holes and the ringdown of the resulting single black hole. The signal was observed with a matched-filter signal-to-noise ratio of 24 and a false alarm rate estimated to be less than 1 event per 203 000 years, equivalent to a signicance greater than $5.1\,\sigma$ *. The source lies at a luminosity distance of* 410^{+160}_{-180} *Mpc corresponding to a redshift* $z = 0:09^{+0.03}_{-0.04}$*. In the source frame, the initial black hole masses are* $36^{+5}_{-4}\,M_{\odot}$ *and* $29^{+4}_{-4}\,M_{\odot}$ *, and the final black hole mass is* $62^{+4}_{-4}\,M_{\odot}$ *, with* $3:0^{+0.5}_{-0.5}\,M_{\odot}c^2$ *radiated in gravitational waves. All uncertainties define 90% credible intervals.* ***These observations demonstrate the existence of binary stellar-mass black hole systems. This is the first direct detection of gravitational waves and the first observation of a binary black hole merger.***

In figure 3.2 the SNR time series, Time-frequency representation of the strain data and the Time-domain detector data (in color) respectively are shown for the GW event GW150914.

3.2 The first direct gravitational wave detection for AdV: GW170814

The era of gravitational wave (GW) astronomy began with the detection of binary black hole (BBH) mergers, by the Advanced Laser Interferometer Gravitational Wave Observatory (LIGO) detectors. The Advanced Virgo detector joined the second observation run on August 1, 2017.

On September 27, 2017 the the Virgo and the LIGO collaborations simultaneously announced the first gravitational wave detection observed with a three-detector network.

This is the abstract of the detection paper [31]:

On August 14, 2017 at 10:30:43 UTC, the Advanced Virgo detector and the two Advanced LIGO detectors coherently observed a transient gravitational-wave signal produced by the coalescence of two stellar mass black holes, with a false-alarm-rate of < 1 in 27000 years. The signal was observed with a three-detector network matched-filter signal-to-noise ratio of 18. The inferred masses of the initial black holes are $30.5^{+5.7}_{-3.0} M_{\odot}$ *and* $25.3^{+2.8}_{-4.2} M_{\odot}$ *(at the 90% credible level). The luminosity distance of the source is* 540^{+130}_{-10} *Mpc, corresponding to a redshift of* $z = 0.11^{+0.03}_{-0.04}$. *A network of three detectors improves the sky localization of the source, reducing the area of the 90% credible region from 1160 deg*^{2} *using only the two LIGO detectors to 60 deg*^{2} *using all three detectors. For the first time, we can test the nature of gravitational wave polarizations from the antenna response of the LIGO-Virgo network, thus enabling a new class of phenomenological tests of gravity.*

In figure 3.3 the SNR time series, Time-frequency representation of the strain data and the Time-domain detector data of the Advanced LIGO – Advanced Virgo network(in color) respectively are shown for the GW event GW170814.

3.3 First observation of Gravitational Waves from a Binary Neutron Star Inspiral: GW170817

During the second observing run (O2) the three-detector network LIGO-Virgo observed a gravitational-wave signal from the inspiral of two low-mass compact objects.

On October 16, 2017 the the Virgo and the LIGO collaborations simultaneously announced at the world the first gravitational wave detection generated from a Binary Neutron Star Inspiral: GW170817 .

This is the abstract of the detection paper [30]:

On August 17, 2017 at 12:41:04 UTC the Advanced LIGO and Advanced Virgo gravitational-wave detectors made their first observation of a binary neutron star inspiral. The signal,

GW170817, was detected with a combined signal-to-noise ratio of 32.4 and a false-alarm-rate estimate of less than one per 8 . 0 × 10 4 years. We infer the component masses of the binary to be between 0.86 and 2.26 $M_\odot$ *,in agreement with masses of known neutron stars. Restricting the component spins to the range inferred in binary neutron stars, we find the component masses to be in the range* 1.17–1.60 $M_\odot$ *, with the total mass of the system* $2.74^{+0.04}_{-0.01}$ $M_\odot$ *. The source was localized within a sky region of 28 deg*^{2} *(90% probability) and had a luminosity distance of* 40^{+8}_{-14} *Mpc, the closest and most precisely localized gravitational-wave signal yet. The association with the* γ*-ray burst GRB 170817A, detected by Fermi-GBM 1.7 s after the coalescence, corroborates the hypothesis of a neutron star merger and provides the first direct evidence of a link between these mergers and short* γ*-ray bursts. Subsequent identification of transient counterparts across the electromagnetic spectrum in the same location further supports the interpretation of this event as a neutron star merger. This unprecedented joint gravitational and electromagnetic observation provides insight into astrophysics, dense matter, gravitation, and cosmology.*

This detection marks the birth of a new astrophysics: **the multimessanger astrophysics.**

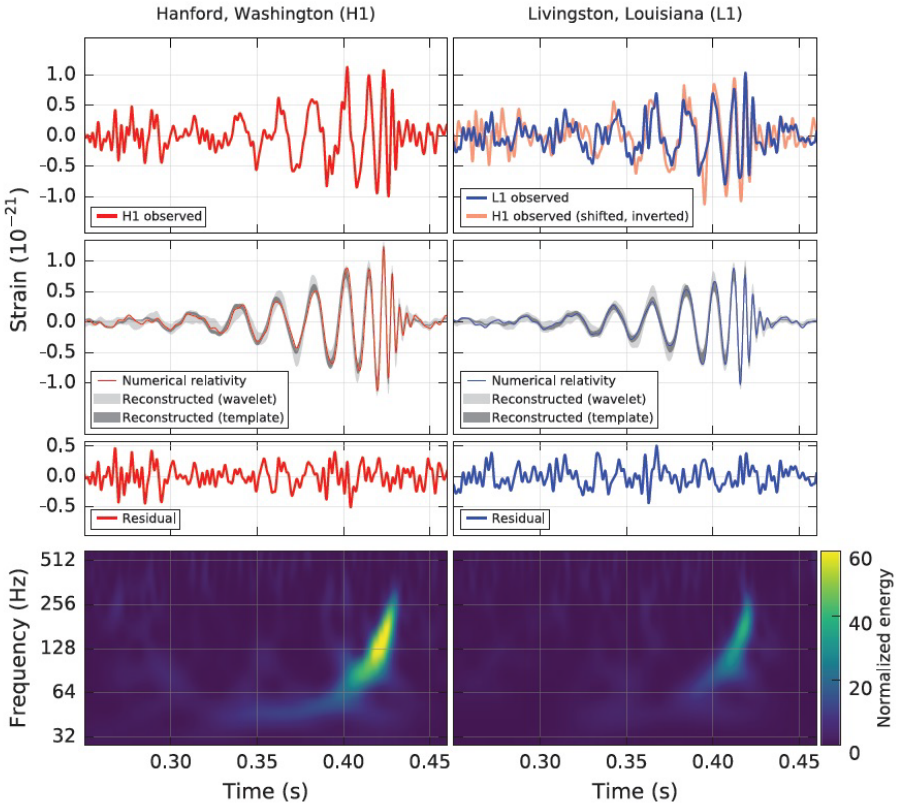

Figure 3.2: The gravitational-wave event GW150914 observed by the LIGO Hanford (H1, left column panels) and Livingston (L1, right column panels) detectors. Times are shown relative to September 14, 2015 at 09:50:45 UTC. Top row, left : H1 strain. Top row, right: L1 strain. GW150914 arrived rst at L1 and $6.9^{+0.5}_{-0.4}$ ms later at H1; for a visual comparison, the H1 data are also shown, shifted in time by this amount and inverted (to account for the detectors' relative orientations). Second row: Gravitational-wave strain projected onto each detector in the 35-350 Hz band. Solid lines show a numerical relativity waveform for a system with parameters consistent with those recovered from GW150914 [48, 50]conrfimed to 99:9% by an independent calculation. Third row: Residuals after subtracting the ltered numerical relativity waveform from the filtered detector time series. Bottom row: A time-frequency representation [16] of the strain data, showing the signal frequency increasing over time [32].

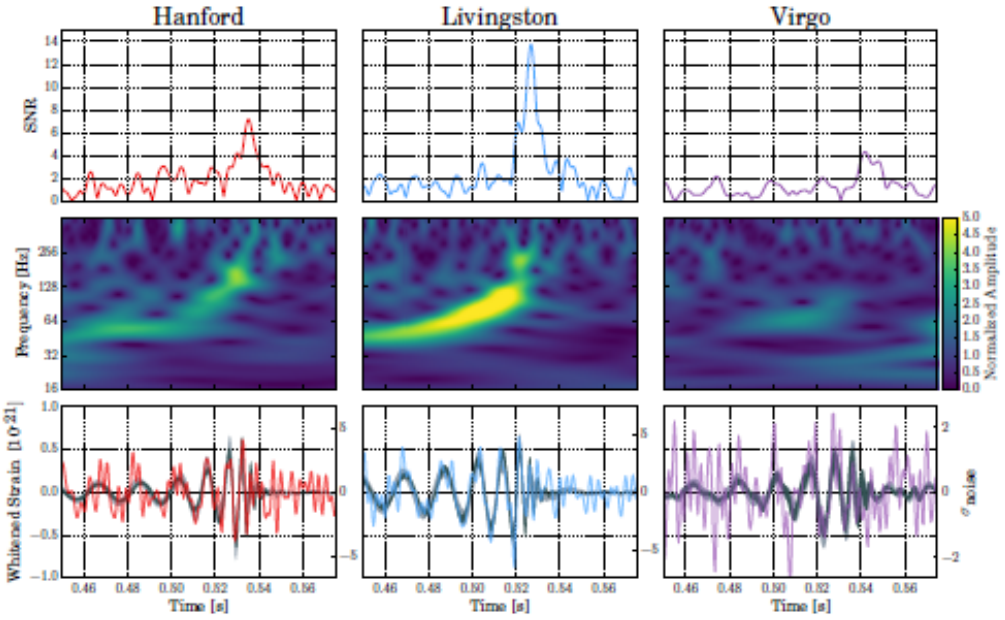

Figure 3.3: The GW event GW170814 observed by LIGO Hanford, LIGO Livingston and Virgo. Times are shown from August 14, 2017, 10:30:43 UTC. Top row: SNR time series produced in low latency and used by the low-latency localization pipeline on August 14, 2017. The time series were produced by time-shifting the best-match template from the online analysis and computing the integrated SNR at each point in time. The single-detector SNRs in Hanford, Livingston and Virgo are 7.3, 13.7 and 4.4, respectively. Second row: Time-frequency representation of the strain data around the time of GW170814. Bottom row: Time-domain detector data (in color) [31].

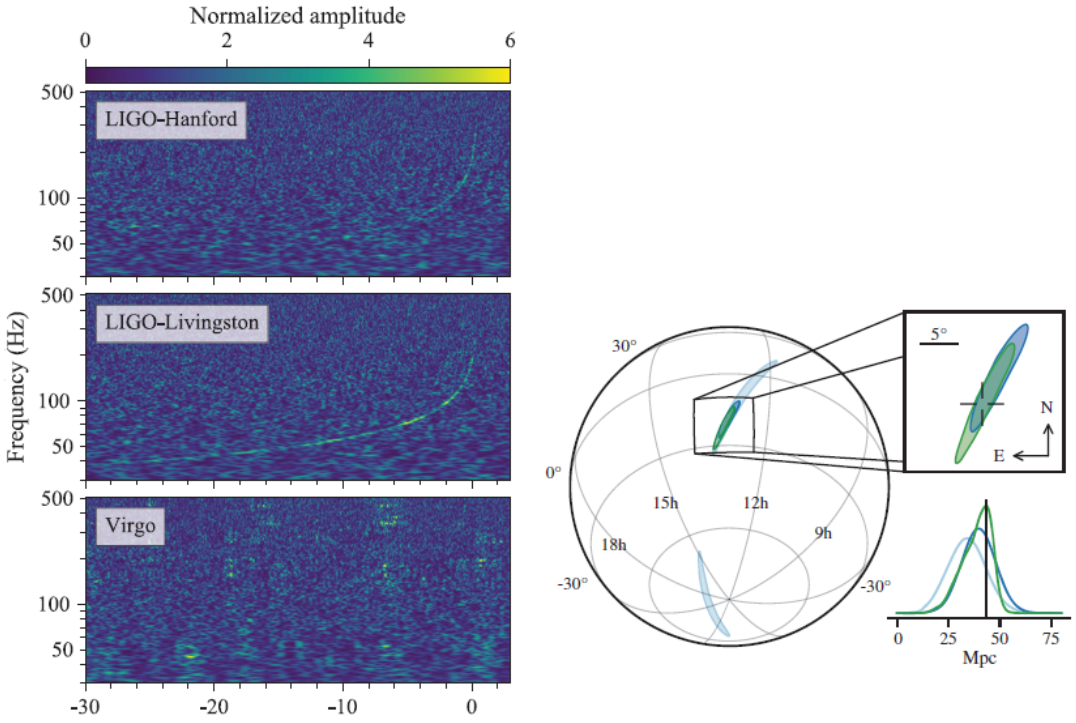

Figure 3.4: Left figure: Time-frequency representations of data containing the gravitational-wave event GW170817, observed by the LIGO- Hanford (top), LIGO-Livingston (middle), and Virgo (bottom) detectors. Times are shown relative to August 17, 2017 12:41:04 UTC. The amplitude scale in each detector is normalized to that detector ' s noise amplitude spectral density [30]. Right figure :Sky location reconstructed for GW170817 by a rapid localization algorithm from a Hanford-Livingston (190 deg^2 , light blue contours) and Hanford-Livingston-Virgo (31 deg^2 , dark blue contours) analysis [30].

Part II

Seismic attenuation systems

Chapter 4

Seismic Noise

Seismic noise is a generic name to identify a relatively persistent and variable (in frequency and amplitude) ground vibration, that is not interpretable as component of signal detected by seismometers. Since high precision measurements and high sensitivity experiment performed with ground based instruments are influenced by this noise source, a deep study on the origin of any possible disturbance is a fundamental passage in identifying a possible impact of seismic noise on them. This is also very useful for a deeper knowledge of the geological structure of the Earth.

The critical frequency region of the modern ground based interferometric detectors for GW, is in the range $0.1 \div 10\,Hz$ because it influences the detector sensitivity as well as the possibility to operate them with high duty cycle in observational mode.

4.1 Seismic waves

Seismic signals are waves of energy that travel through the layers of the Earth as result of earthquakes, volcanic eruptions, magma movement, large landslides and large explosions [76, 77]. Many other natural and anthropogenic sources create low amplitude waves commonly referred to as ambient vibrations. The propagation velocity of the waves depends on density and elasticity of the medium through which they travel. Their velocity increases with the depth ranging from 2 km/s up to 8 km/s in the surface crust of the Earth and reaching the velocity of 13 km/s in the deep mantle.

Earthquakes create distinct types of seismic waves traveling through the Earth medium with different velocities.

According to our approach two main categories can be distinguished as follows:

- **Body waves**

- **Surface waves**

In the first group we include all the waves travelling through the Earth core influenced by the density and stiffness of the material which turns out to be influenced by temperature, chemical composition and material phase. They are Primary waves (P-Waves) that are compressional waves traveling in longitudinal direction and Secondary waves (S-waves) that are shear waves traveling in transverse direction.

S-waves in an earthquake event displace the ground perpendicular to the direction of propagation (see first panel second row in Fig. 4.1). The S-waves can travel only through solids materials, because the fluids (liquids and gases) do not support shear stresses. S-waves are slower than P-waves, and their typical speed is about 60% of that of P-waves in any material.

Within the second category we group all the waves travelling on the surface of the Earth. They can be classified as a form of mechanical waves and their amplitude decrease as a function of the distance from the source. They move through the Earth surface slowly then the body waves (P and S) with an amplitude of several centimeters.

Are included in this second category **Rayleigh waves** also called ground roll representing surface waves that travel as ripples with motions that are similar to those of waves on the water surface, as well as **Love waves** the horizontally polarized shear waves (SH waves) having a large amplitude (with the respect to the Rayleigh waves).

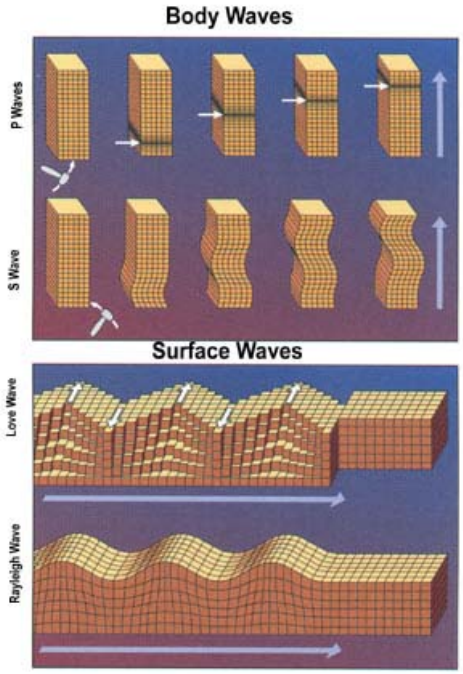

Figure 4.1: Body waves and surface waves

4.2 Wind waves

Wind waves are mechanical surface waves propagating along the interface between water and air. As restoring force of this waves is provided by gravity, they are often referred to as surface gravity waves [38, 45]. Every time the wind blows, pressure and friction perturb the equilibrium of the water surface and it transfers energy from air to water. The natural formation of wind waves can be considered a random process. For this reason the height, the duration, and the shape can be predicted in very limited ways: they are considered as a stochastic process governed by the standard stochastic physic.

Such waves are typical **Rayleigh waves** formed on the seabed increasing seismic noise. In the sketch of Fig. 4.2 a few important parameters influencing the behavior of these waves are reported: their speed is controlled by gravity, wavelength and water depth. Wavelength determines the size of the orbits of water molecules within a wave and water depth determines the shape of the orbits. The path of water molecules in a wind wave are circular only when the wave is traveling in deep water. Considering the waves in a deep water level, their speed can be approximated by:

$$v_{ww} = \sqrt{gL/2\pi} \tag{4.1}$$

where g is the gravitational acceleration, and L is wavelength.

While, the speed of shallow-water waves is described by the following equation:

$$v_{sw} = \sqrt{gd} \tag{4.2}$$

where d is the depth of the water.

Seismic noise due to wind waves represents main source of local disturbances in operating any high precision instruments. In particular the effect of this noise source deteriorates the duty-cycle of a laser interferometric detector for gravitational waves continuous observations. For this reason is fundamental to have detail monitor on the sea condition close to the interferometer site.

Thanks to a measurement campaign performed in the time period 1989-2005 by using a wave buoy located close to the Tyrrhenian sea coast, a local detailed characterization of the surface waves formation has been done. The used sensor recorded the height of the wave and its period, for the waves of the Tyrrhenian sea close to the cost located not far away from the EGO laboratory site (about 15 Km).The histogram in Fig.4.3 shows the statistical trend of the average period of the sea waves in relation to their average height as measured by the boa [74].

It can be observed that, the seismic noise due to the wind waves is in the frequency range $0.150 \div 0.450 Hz$, while the wave height range between 0.5m and 3.5m.

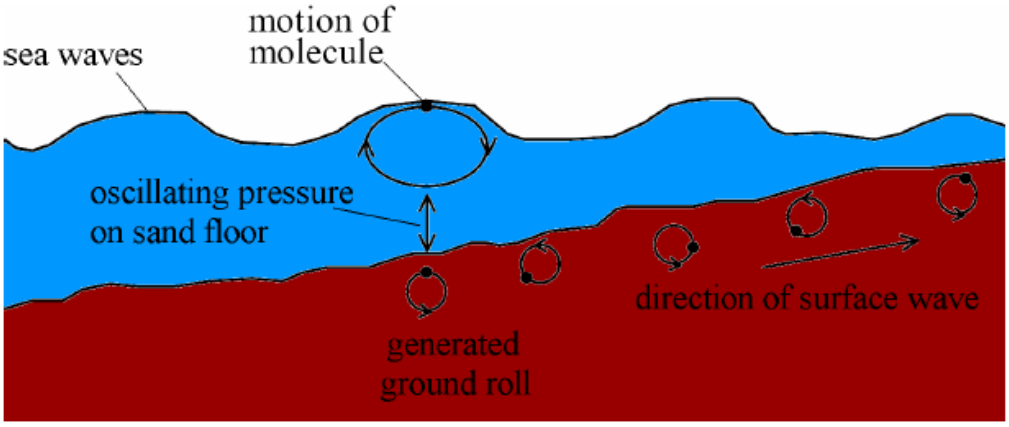

Figure 4.2: The pressure variation on the seabed due to gravity waves generates earth-roll seismic waves.

This represents the contribution to micro-seismic noise on the EGO site due to the Tyrrhenya Sea motion.

4.3 Microseism

Microseism is defined as a faint earth tremor caused by natural phenomena: it is a well detected and measured signal everywhere on Earth by using a broad-band seismograph.

With the aim to monitor the seismic noise, in 1993 J. Peterson collected and analyzed data from 75 seismic stations around the world developing two seismic noise models: the New Low Noise Model (NLNM) and the New High Noise Model (NHNM) that are now commonly used as a reference [61]. The models are hypothetical background spectra obtained from the combination of the lowest spectra in each sites (NLNM) and from the average of the noisiest sites (NHNM) in the seismometer network.

In Figure 4.4, the results of this analysis are shown. The dominant microseism signals from the ocean/sea are linked to the characteristic ocean swell periods, and they occur with a frequency ranging between 0.250 Hz to 0.03 Hz .

Microseismic noise usually shows two predominant peaks, in the region 0.1-0.5 Hz range, called microseismic peaks. The first one (around 0.1 Hz) is for the larger periods, typically close to $16\,s$ can be explained by the effect of surface gravity waves in shallow water. These peaks have the same period as the water waves that generate them, and are usually called '*primary microseisms*' [1].

[1] It is generated by a particular case of a wave-wave interaction process in which one wave is fixed.

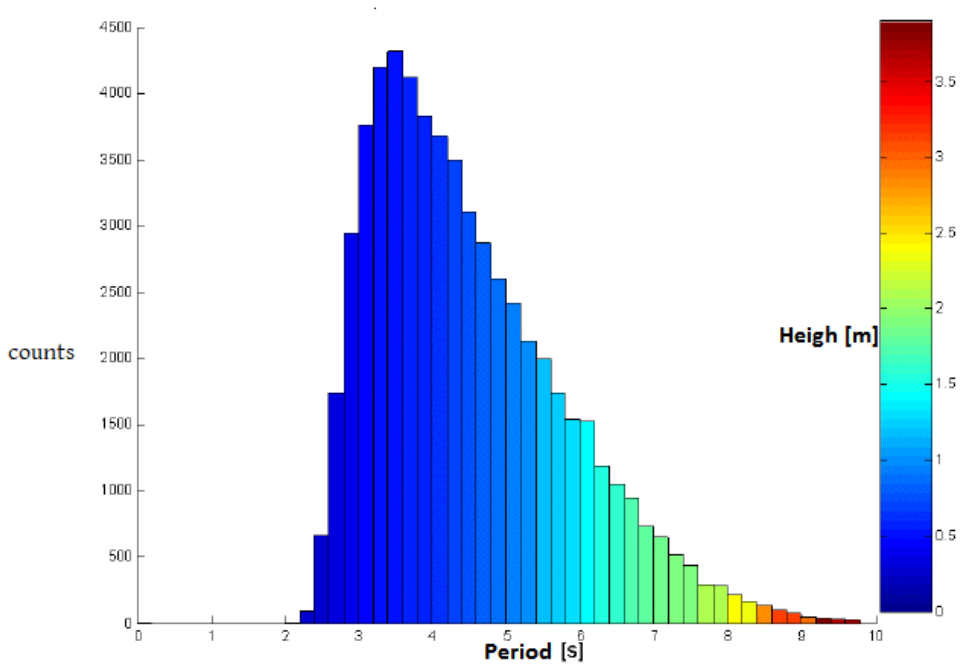

Figure 4.3: Distribution of the average period and relative mean height of the waves in the sea region close to La Spezia (43 ° 55.7 N, 09 ° 49.6 E) as measured in the time period from 1989 to 2005.

4.3.1 Seismic noise on EGO site

The VIRGO and AdV interferometers have been designed with the precise intent to develop an experimental apparatus for gravitational waves signals having a detection bandwidth extended in the low frequency region. For these reasons it is important to have a good isolation from any kind of vibrations which can influence the detection of this weak signal. Seismic noise give the most important contribution in this range where gravitational waves emitted by catastrophic events are expected.

Whit this intent the monitoring of the local seismic spectra has a key role to disentangle a real signal from fake one and to this purpose, over the area covered by the EGO laboratory, a large number of vibration sensors are disseminated.

In the figure 4.5 the location of these sensors are shown:

- Triaxial Guralp 40T sensors placed in the Central, End and Mode Cleaner buildings (CEB, NEB, WEB, MCB).
- 8 seismometers Lennard 3D placed outdoor the EGO site.

They are broad-band seismometers used for a continuous monitoring of the local vibrations.

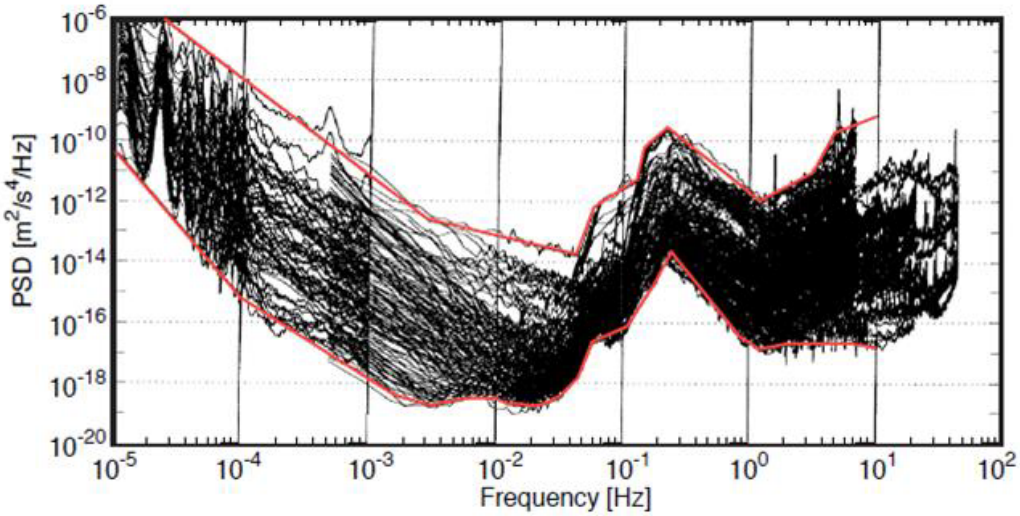

Figure 4.4: Power spectral density of the seismic motion as a function of frequency, measured in 75 sites around the world

The signals of this sensors are included on the data acquisition chain of the experiment to be used in the real time analysis.

With the intent to provide a set of reference spectra for seismic noise on the experimental area, a measurement campaign has been performed on EGO site in 2011 the results of which are reported in fig. 4.6. These data have been collected with the sensors listed above over different time periods lasting from 1 week to 1 year. In agreement with the location displayed in the figure 4.5 different data sets have been recorded at various location and for each data sample statistical percentile curve has been calculated [33]. The results of this analysis for the data set collected in 2011 are showed in Fig. 4.6.

Looking at few details, the curves reported in the Fig. 4.6 present the typical structures characterizing micro-seismic noise in the frequency range $0.1 \div 1 Hz$ Hz at the EGO site; they are generated from the crashing sea wave water of coast about $15 km$ away from the experimental site.

The high peak appearing in the frequency region $0.2 \div 0.4 Hz$ is associated with the Tyrrhenian sea motion and and it changes its shape according with the season and weather conditions.

The pressure generated by the wind on the ground (Seismic noise due the wind) and the structures attached to it (buildings, etc.) causes low-frequency soil vibrations concentrated in the band between 0.01 Hz and 1 Hz.

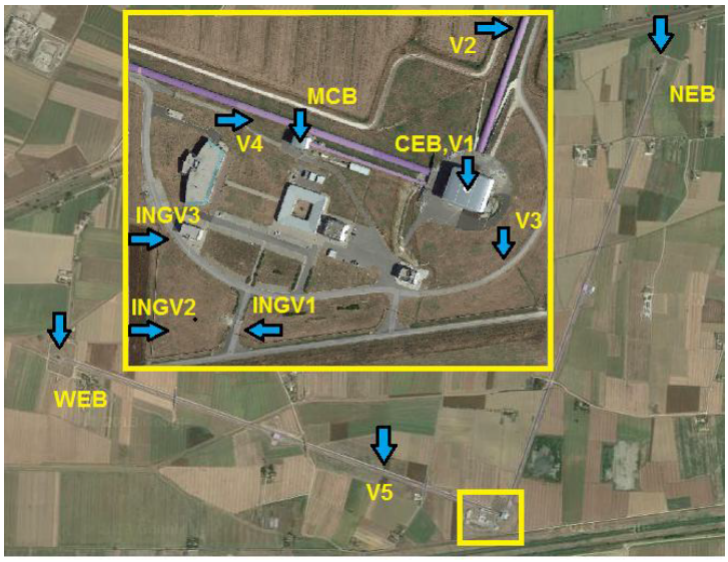

Figure 4.5: Site map location of the vibration sensors disseminated on the EGO laboratory area.

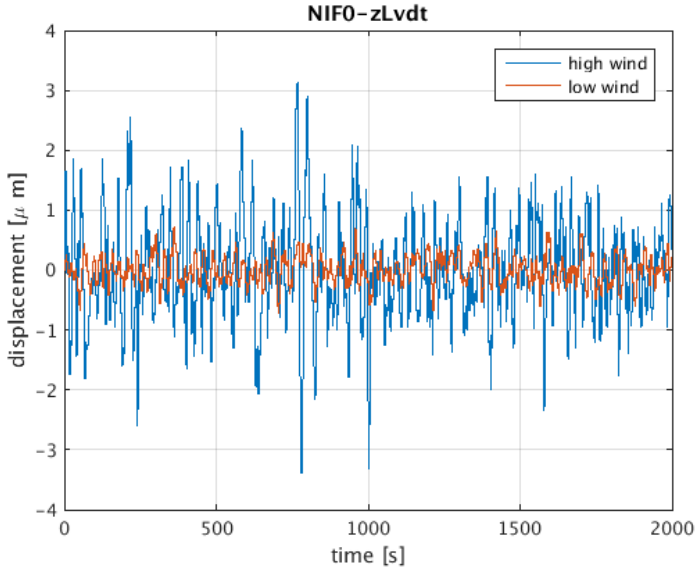

Figure 4.7: The time evolution of the suspension point horizontal displacement as measured by a LVDT sensor mounted on the top stage of a Suspension. The blue curve represents the typical suspension point status with high wind noise and the red one with the low wind noise.

However, unlike other sources of seismic noise, such as that one due to the sea, it seems that wind activity does not give a rise to the real seismic waves bat it induces only a slight oscillation of the soil surface on which it interacts.

As it can be seen in the Fig. 4.8, on the EGO site a strong wind is recorded more frequently with a direction East-West [74]. This induces a big oscillation on the VIRGO Suspensions in

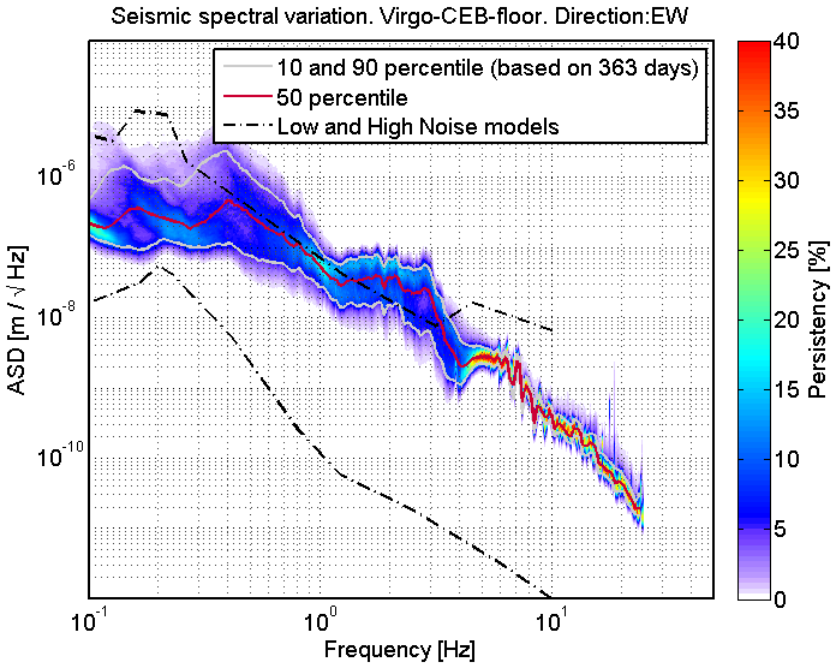

Figure 4.6: Seismic spectral density on Virgo's site based on 1 year statistic (2011). This plot shows us that, considering a period of 100 days , 90 of these are characterized by the microseismic condition out of range from Peterson' high noise model, and for 10 days the microseismic condition is below of the Peterson' high noise model.

the frequency region $0.01 \div 0.1$ Hz and it is detected by the positioning sensors accommodated on the top stage of the system (see fig. 4.7).

Local traffic noise - Another important contribution to the seismic noise spectrum of the EGO site comes from the local traffic. The frequency of these vibrations is limited in the band $1 \div 4$ Hz with an important peak around 2.5 Hz. Even in this case, it has been verified that most of the ground vibrations come from the bridge of the **FI-PI-LI** freeway approximately 3 km far away from the experimental site. Also for these vibrations the propagation speed was measured to be between 300 m/s and 600 m/s on the ground of the experimental area.

Environmental noise - Within this noise category we include all the disturbances due to the standard human activity. Among these the presence of a Wind Turbines Park at about 11 km from the Advanced VIRGO interferometer represents a potential noise source to be taken in consideration for a detailed mapping of noise sources. Their characteristic rotation frequency has been identified around 1.7 Hz. Some additional information can be inferred also comparing the curves of the Peterson's seismic noise models (see fig. 4.4) with a power spectral density of the local micro-seismic noise measured on EGO site in different days of the year.

The figure 4.9 shows the typical behavior of seismic spectrum measured on EGO site

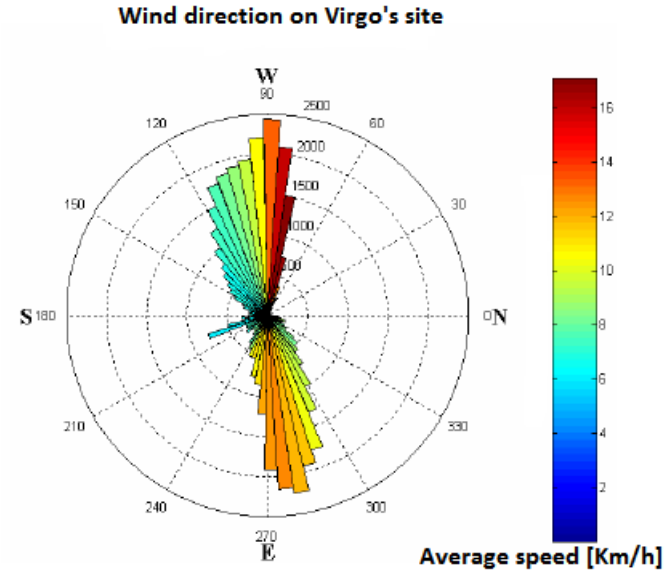

Figure 4.8: Polar wind direction directions measured at the VIRGO site, with their mean speeds. Data was sampled at 15-minute intervals over a 2-year period (2003-2005). In plot

(displacement spectral density) compared with the Peterson's noise models as reported in Fig. 4.4 too. In the frequency band $0.2 \div 1$ Hz, where the effect of microseism of the site is visible, the spectra are out of the limits fixed by the Peterson's study. This result can be interpreted only considering the fact that Italian seismic stations were not present in the measurement campaign.

4.4 Seismic noise in the underground sites

The selection of an experimental site has a key role to limit the impact of seismic noise on interferometric detectors for Gravitational Waves observations. In underground locations the perturbations caused by the atmospheric fluctuation due to the weather conditions are minimal, the environmental conditions are more stable and, as a consequence, the measurable noise on the surface level is attenuated. For all these reasons underground sites seem to be a natural choice for the installation of a high precision instrument.

The dependence of seismic noise of a typical underground site is characterized by an exponential law:

$$\frac{\tilde{x}_{seism}(f,d)}{\tilde{x}_{seism}(f,d=0)} \propto e^{-4\frac{d}{\lambda}} \tag{4.3}$$

where d is the depth of the site and λ is the wavelength of the seismic wave.

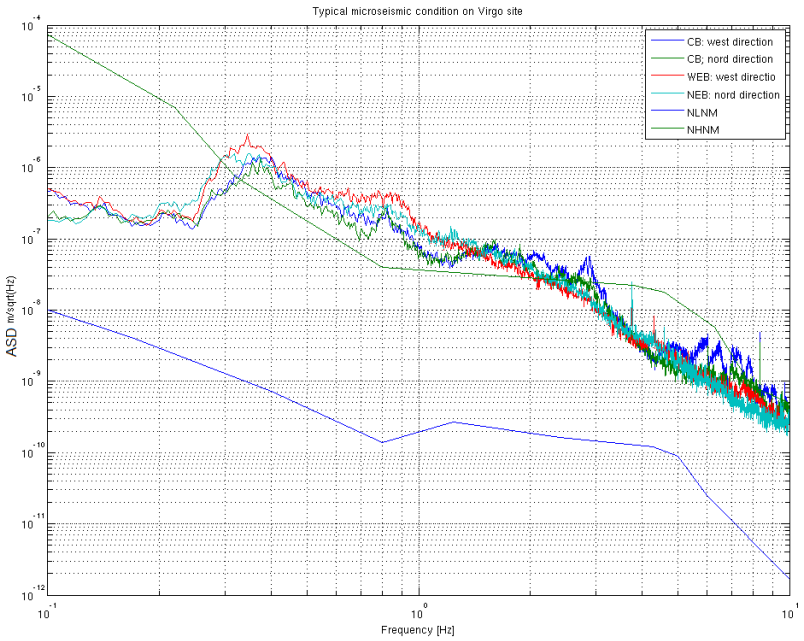

Figure 4.9: Peterson's New Low Noise (NLNM) and New High Noise Models (NHNM) limits are compared with the seismic noise spectral density displacement on EGO site (June 2017).

Seismic noise, in underground sites, is about 100 time smaller than those ones on surface and its spectrum can be approximated by the following relationship:

$$\tilde{x}_{us} \simeq 10^{-9}\left(\frac{m}{Hz^2}\right)\left(\frac{1\,Hz}{f}\right)^2 \tag{4.4}$$

Exactly as for surface sites, the differences among underground locations are set by the proximity to the coast, by the proximity to the urban centers as well as by their geological history. This situation is well represented by the Kamioka mine (Japan) selected as experimental site of the KAGRA interferometer with two orthogonal arms 3 km long each one [24]. In Fig. 4.10 seismic noise measurements, in different locations of the experimental area are plotted and compared with the typical seismic spectrum on surface (blue curve).

For completeness in Fig. 4.11 a comparison between the typical seismic noise spectrum on EGO site, measured in June 2017, and that one of the Kamioka mine (underground) measured in 20 10 is showed.

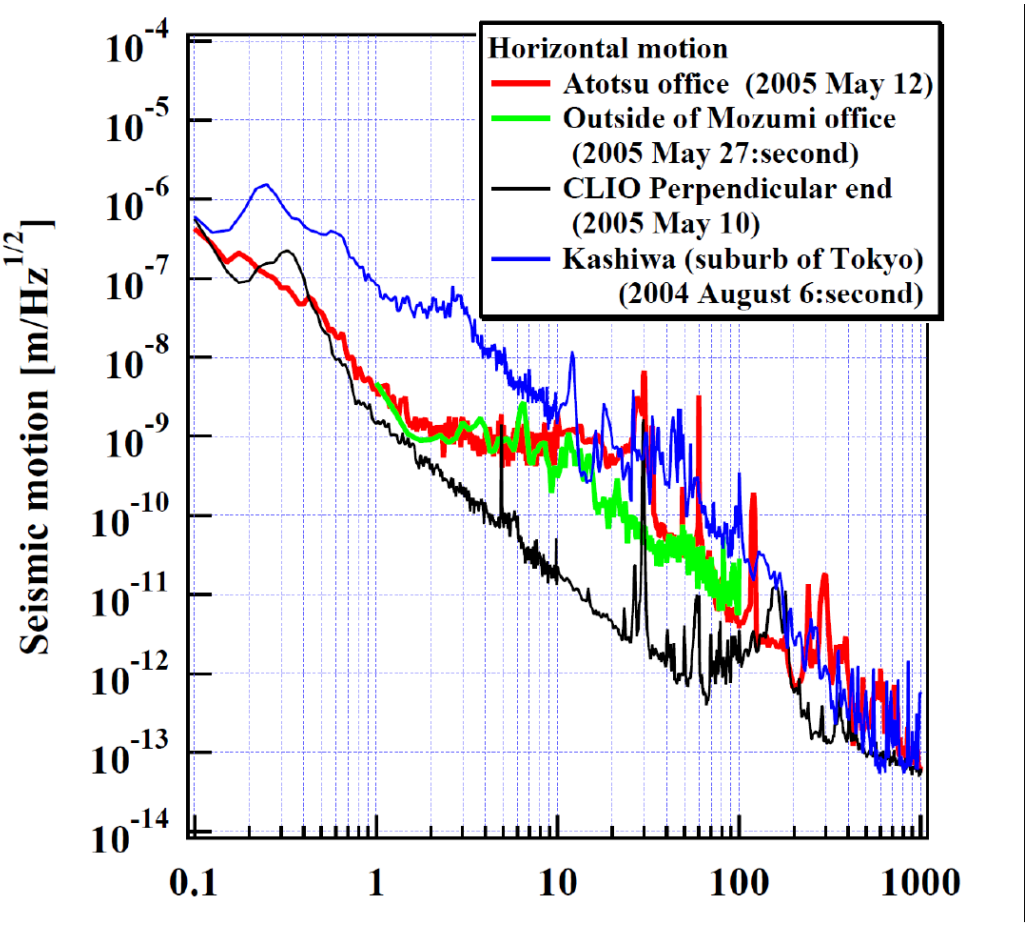

Figure 4.10: Comparison between seismic noise spectrum on surface in the Tokyo area and the measurements performed at differents levels inside the Kamioka mine (Japan).

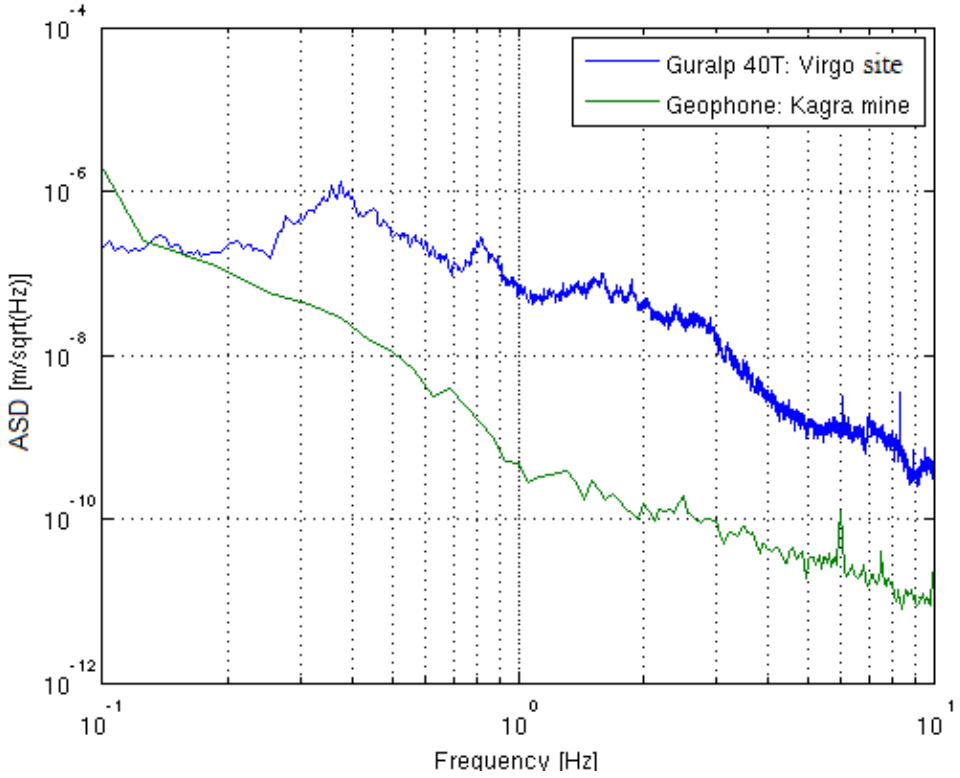

Figure 4.11: Typical seismic noise spectrum on EGO site in Italy (blue curve) measured in 2017 and that one (green curve) measured in 2010 within the Kamioka mine (Japan).

Chapter 5

Advanced VIRGO: Seismic noise attenuation

Suspending optical components represents a crucial task in the construction of interferometers for gravitational waves detection. In fact the gravitational waves observation depends on the capability to include into the experimental apparatus a free falling mass (test mass), well isolated from all the noise sources which are relevant in the observational frequency band.

Seismic noise gives the most important contribution in the low frequency, where gravitational waves emitted by black holes, pulsar and coalescing binaries are expected. For these reasons the ground based and broad-band interferometers have been equipped with an appropriate suspension system of the test masses including complex mechanical structures studied to inhibit noise transmission. To this purpose the INFN Pisa Group of the Virgo Collaboration has developed and built a very sophisticated system to isolate from seismic noise and local disturbances the free falling masses of the interferometer. With this solution it has been possible to extend the detection bandwidth in the low frequency region starting from a few Hertz.

5.1 Mechanical attenuators of seismic vibrations

As described in the previous chapter the natural motion of the Earth represents the main limitation to the sensitivity of any ground based detector of gravitational waves. In particular in the low frequency region.

A good approximation of a free falling mass is represented by a simple pendulum composed by a thin wire, as elastic element, connected to a body of mass m . Thanks to this simple solution it is possible to filter seismic noise in a real experiment to the optical level by using a harmonic oscillator.

Let us consider a body of mass m supported by an elastic spring with stiffness k . Applying a force F the equation of motion of the linear system is:

$$m\ddot{x} = -k(x - x_0) \tag{5.1}$$

In the frequency domain the same equation becomes:

$$-m\omega^2\tilde{x} = -k(\tilde{x} - \tilde{x}_0) \tag{5.2}$$

Introducing the concept of mechanical *Transfer Function* as the ratio between output and input signals of a linear system :

$$TF_{in\to out} = \frac{\tilde{x}_{out}(\omega)}{\tilde{x}_{in}(\omega)} \tag{5.3}$$

the transmission of any perturbation to the output of the linear system can be studied.

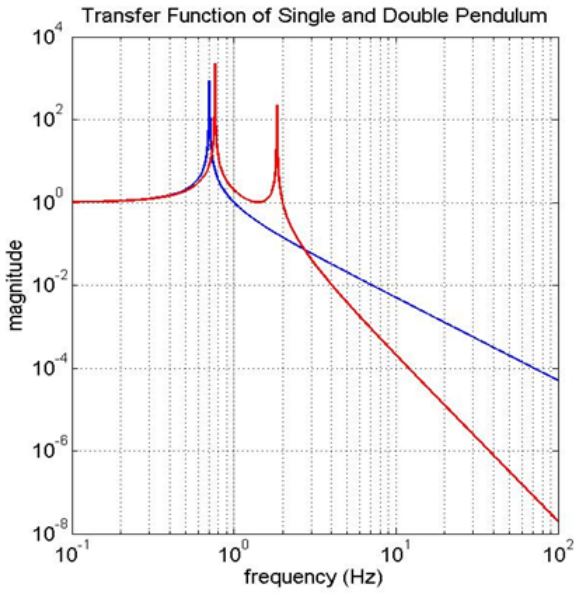

Figure 5.1: Mechanical transfer functions of a single (blue curve) and double pendulum (red curve) having the same total length.

With reference to figure 5.1 and considering a harmonic oscillator having resonance mode ω_0 we observe that:

- at low frequencies ($\omega \ll \omega_0$), due to the stiffness of the system, the transfer function is equal to 1 and the perturbation is completely transmitted from input to output;

- for a frequency $\omega = \omega_0$ (the normal mode of the harmonic oscillator) the applied force to the input determines a continuous transfer of energy from input to output amplifying the motion of the system itself with an amplification factor equal to Q (the mechanical quality factor) [1];

- at high frequencies thanks to inertia of the suspended body the transfer function is equal to:

$$| TF |_{in\to out} = \frac{| \widetilde{x}_{out}(\omega) |}{| \widetilde{x}_{in}(\omega) |} \simeq \left(\frac{1}{\omega}\right)^2 \qquad \omega \ggg \omega_0 \tag{5.5}$$

and for frequencies $\omega \ggg \omega_0$ the system behaves as second order low pass mechanical filter.

For all these reasons a harmonic oscillator is a good candidate to inhibit seismic noise transmission in an interferometric detector designed to observe gravitational waves.

In the figure 5.1 the transfer function of a single pendulum as well as that one of a double pendulum having the same total length is reported. It is evident that increasing the number of stages in a mechanical structure represents a good approach to improve the total attenuation factor of seismic noise at the level of the test masses. In such a way cascading N harmonic-oscillators (N stages) the transfer function can be written as:

$$\frac{| \widetilde{x}_{out}(\omega) |}{| \widetilde{x}_{in}(\omega) |} = \prod_{i=1}^{N} \frac{1}{1-(\omega/\omega_i)^2} \simeq \left(\frac{A}{\omega^{2N}}\right) \quad with\ A = \omega_1^2 \cdot \omega_2^2 \cdot \cdots \omega_N^2 \tag{5.6}$$

5.1.1 The Advanced VIRGO (AdV) Suspensions

The solution adopted for the AdV interferometer is based on the idea to replicate a certain number of harmonic oscillators so that to form a filtering chain enhancing the natural capability of a single stage to attenuate the noise transmitted in all degrees of freedom at the next level. The system must provide a good isolation of seismic noise in vertical direction as well as the horizontal one. For this reason any simple pendulum should be equipped with an elastic element taking care of the vertical attenuation too.

[1] In the equation of the harmonic oscillator, the stiffness can be expressed in the form $k(1+i\phi)$, where $\phi = 1/Q$ and it represents the different dissipative effects due to the constraining reaction, which may be due to viscous friction or damping of other nature. The quality factor (Q) is proportional to the ratio between the energy stored by the oscillator and the energy dissipated in a cycle. Re-writing the transefr function in the frequency domain,it assume the form:

$$\frac{| \widetilde{x}_{out}(\omega) |}{| \widetilde{x}_{in}(\omega) |} = \frac{\sqrt{1+\phi^2}}{\sqrt{1-\left(\frac{\omega^2}{\omega_0^2}\right)^2+\phi^2}} \tag{5.4}$$

Since the performance of the suspension adopted to isolate the optical components in VIRGO interferometer has been considered compliant to the requirements of the second generation detector (AdV), minor changes have been included in the new experimental set-up in agreement with the following requirements:

- **isolation from seismic vibrations -** in figure 5.2 the design sensitivity of the AdV is reported (black curve), where the target spectral sensitivity $\tilde{h}(10Hz) \sim 10^{-21}/\sqrt{Hz}$ corresponding to a residual displacement of $\tilde{x}(10Hz) \sim 3 \cdot 10^{-18} m/\sqrt{Hz}$ is shown;

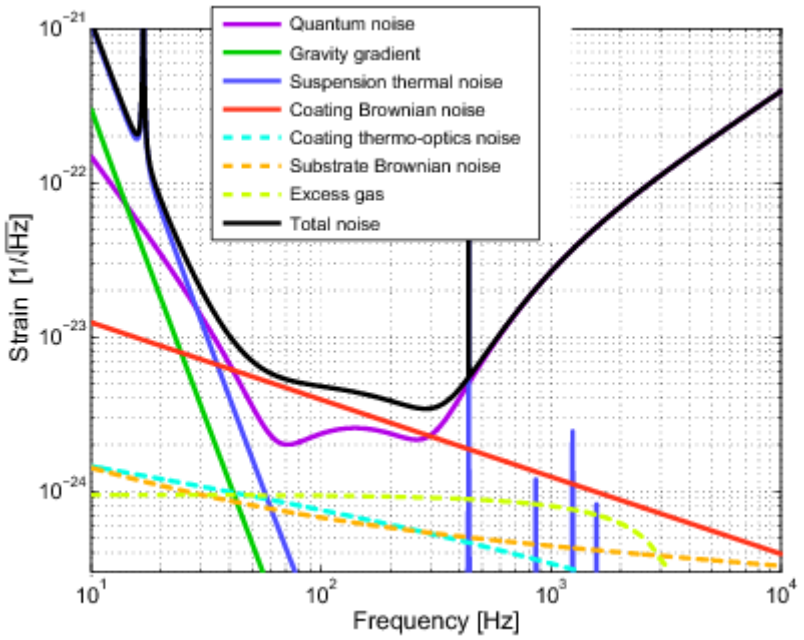

Figure 5.2: AdV design sensitivity curve.

- **capability to control the mirror position -** the locking of the interferometer has a very stringent requirement: $\delta x_{rms} \sim 10^{-12} m$. Mirrors position must be controlled down to DC without re-injecting noise in the detection band;

- **low level of internal disturbances -** around 4Hz and above, Thermal Noise (TN) becomes the dominant noise source. The possibility of lowering this noise source depends on the use of low loss angle ϕ material. For AdV this has been implemented by suspending end and input test masses with fused silica fibers ($\phi_{FS} \simeq 10^{-9}$) to form a monolithic structure with the mirror bulk. Making a coarse [2] evaluation of the Thermal Noise contribution of a simple pendulum to the detector sensitivity in the low frequency region by using the equation:

[2] A general definition of the quantity ϕ_{eff} take into account all dissipative contribution into material : $\phi_{eff} =$

$$S^{pen}(\omega) = \frac{4K_BT}{m\omega} \cdot \frac{\phi_{eff}\omega_p^2}{(\omega^2 - \omega_p^2)^2 + \omega_0^4\phi_{eff}^2}. \tag{5.7}$$

where $\omega_p = \sqrt{\frac{g}{l}}$ is the pendulum mode and K_B is the Boltzmann constant, it is evident that suspending heavier mirrors together with increasing the pendulum length are key parameters to reduce Thermal Noise. In a typical ITF set-up, the pendulum TN of the mirror suspension is dominant from a few Hz to about 100 Hz, while the mirror bulk TN is dominant from 100 Hz to a few kHz.

5.1.2 The Advanced VIRGO Superattenuator

The new optical layout of the Advanced VIRGO interferometer (ITF) is shown in the figure 5.3 where mirrors and benches are schematically represented. Each one of these elements is suspended from a mechanical system, called **Superattenuator (SA)**, adopted to isolate it from seismic noise and local disturbances.

The SA is the final result of a long and detailed research and development program performed by the INFN Pisa Group with the intent to extend the detection bandwidth of the interferometer in the low frequency region (below 50Hz).

To fulfill the detector requirements two types of SA have been built: **short chain** and **long chain**. The first type is used to suspend optical benches and small mirrors while the second ones is used to hang the high quality optics: Power Recycling Mirror (PRM), Beam Splitter Mirror (BS), Fabry-Perot cavity optics (NI,NE and WI,WE) and the Signal Recycling Mirror (SRM) , included in the optical set-up of the second generation ITF.

A few guide lines have been considered during the development of the mechanical system:

- the normal modes of the pendulum mechanical structures are confined in the low frequency region (below 4 Hz);
- the introduction of a pre-isolation stage to be used as mechanical support of the chain suspension point with the possibility to move it applying small forces. In this way, any noise re-introduction at the top stage level, is passively filtered by the mechanical structure of the pendulum.

Keeping in mind these guide lines the SA has been designed as a hybrid system formed by a passive mechanical filters chain connected through ground by a three legs structure based on the working principle of the Inverted Pendulum (IP).

$\sqrt{\frac{EI}{\tau L^2}}(\phi_{struct} + \phi_{therm} + \phi_{surf}) + \phi_{recoli}$, where E is the Young modulus, I is the cross section moment of inertia, τ is the mechanical tension applied to the wire of length L and where structural, thermal, surface and recoil losses have been considered as thermal noise contributions.

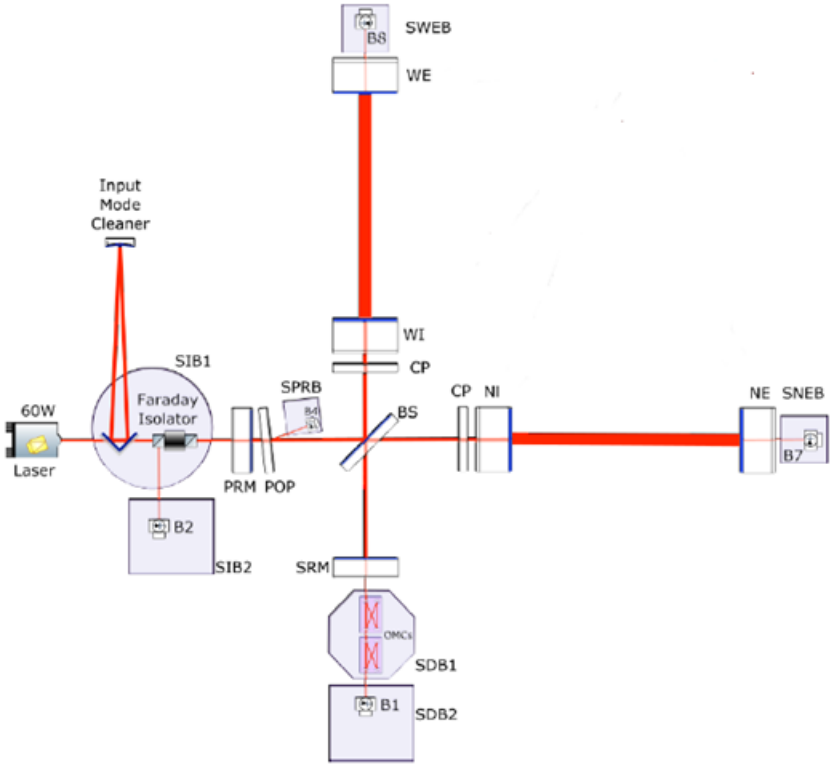

Figure 5.3: Optical layout of AdV ITF.

Looking at the figure 5.4 , where a long suspension technical drawing is reported, we identify three main parts:

- Pre-isolation stage: **the Inverted Pendulum (IP-3 legs structure)** on top of which a mechanical filter **(called Filter 0-F0)** is bolted through a metallic ring.
- The passive multi-stage pendulum chain formed by five mechanical Filters **F1**, **F2**, **F3**, **F4** and **F7** (Steering Filter);
- Last stage or **payload** formed by the **marionette and** the **mirror.**

The main difference between long and short chains is represented by the number of the passive mechanical filters which is equal to six and three respectively. When a single-stage is considered in “stand-alone mode” its natural frequency is about $0.5Hz$ (cut-off frequency along two longitudinal directions), while the all resonance frequencies of the chain are spread out over the range $0.1 \div 3\,Hz$.

From now on we will focus our attention in the description of a long chain for completeness reasons.

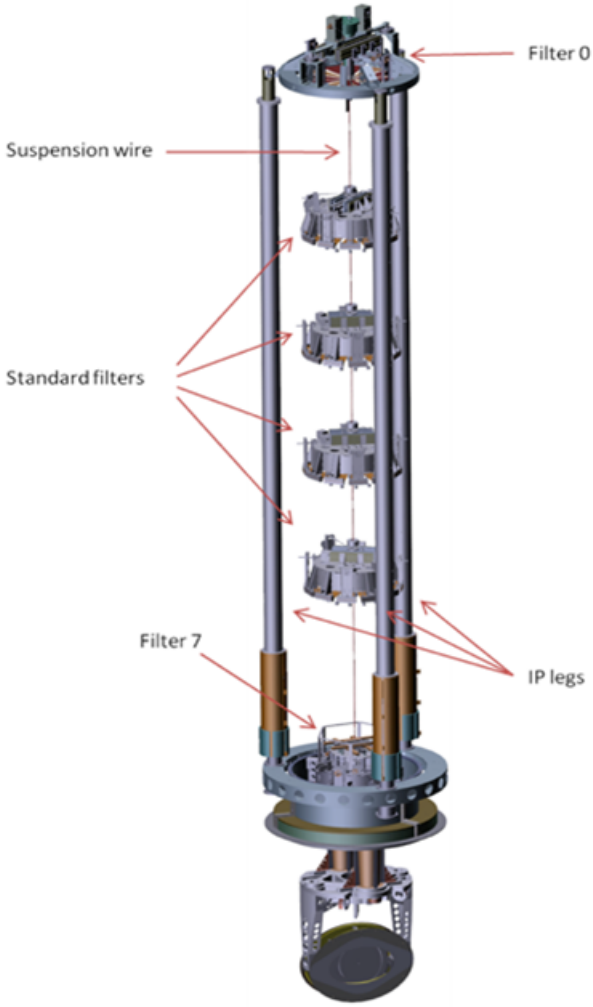

Figure 5.4: A 3D technical drawing of the AdV Suspension system (long chain).

5.1.3 Passive attenuation: standard filter

A *standard filter* is a drum-shaped rigid cylinder made of stainless steel weighting 120 kg with 70 cm diameter and 18.5 cm hight (Figure 5.5). Within the theoretical scheme of a multi-stage harmonic oscillator, it substitutes a single pendulum acting as a second order low pass filter on two longitudinal degrees of freedom.

Each filter is suspended from the top stage by using Maraging steel wires (each section 1.2 m long and with a diameter ranging from 1.85mm and 4.0mm depending on the load to be hung) connected to the body at a distance of 5 mm from the system center of mass. This choice

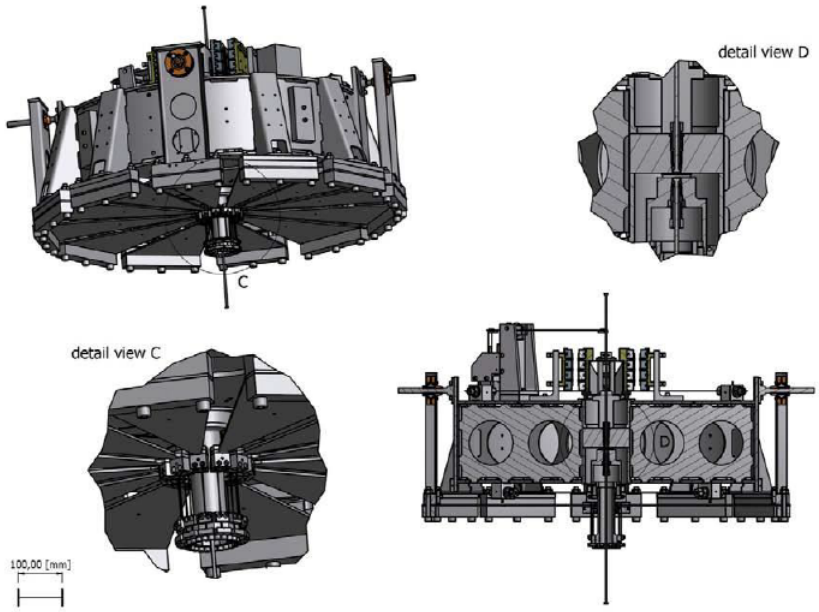

Figure 5.5: Technical drawing of the mechanical filters for the AdV Superattenuator.

has been done to minimize the restoring force and the coupling between tilt and horizontal motions. The bottom part of the filter body is completed with a set of triangular cantilever spring blades clamped on the outer circumference of the structure (see fig. 5.6). Considering the typical seismic noise spectrum at the EGO site, it has been decided, for a good filtering action, to cascade a sequence of six mechanical filters forming a chain with an attenuation factor A bigger than 10^{10} in all degrees of freedom.

5.1.3.1 Triangular blades

The blades are elastic elements included in the design of the mechanical filters to implement the filtering effect on the vertical degree of freedom. This element has been built with a triangular shape machined by using Maraging alloy. The use of this ultra high resistance steel (UHRS) in place of the standard one, has been employed to minimize micro-creep effect due to the high load applied [27, 56].The blades are pre-bent at constant curvature radius so that they became flat and horizontal as soon a load is attached to their tip (see figure 5.7 a) [71]. Thanks to this shape the stress distribution is uniform along the blade, minimizing the maximum internal stress, which is kept at level of the 50-60% of the material elastic limit. The load capability of each spring set is selected by changing the number of blades (ranging from 12 to 4and going from top to the bottom of the chain) and their triangular base width for each mechanical filter

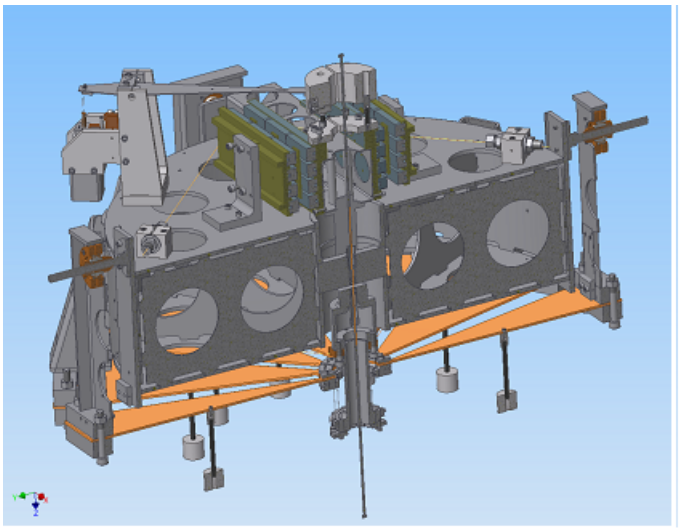

Figure 5.6: Cross section of the filer body showing the mechanical structure together with the triangular blades clamped on the circumference of the body bottom part.

as a function of the total load to be supported.

The tip of each blade is attached to a central column representing the movable part of the filter, constrained by a set of centering wires, to move only in the vertical direction through the central hole of the filter body. Connected to the central column there is a crossbar: a mechanical structure designed to support the magnetic antisprings (see next subparagraph) across the top surface of the filter body. The crossbar and the matrices with permanent magnets complete the movable part of the filter together with the central column supporting the final load of the next filter through a suspension wire [3]. Once properly loaded the main vertical resonance frequency of each filter is about $1.4\,Hz$, depending on the blade geometry, stiffness and attached load.

5.1.3.2 Magnetic anti springs

Since the suspension wire length fixes the pendulum normal mode at about $0.5\,Hz$ for the two horizontal directions (x,z) we need to have a similar cut-off frequency in vertical direction too. Only in this way our experimental apparatus will have an isotropic response in all d.o.f.

To this purpose and with the aim to reduce the main vertical normal mode frequency of each filter at $0.4\,Hz$, a set of magnetic antisprigs , mounted in repulsive configuration have been accommodated on top of the filter body[55].

They consist of four matrices of permanent magnets: the crossbar supports two arrays of magnets, while a second pair of arrays are bolted on the filter body. When they are perfectly

[3] Each section of the suspension wire ($1.2\,m$ long) is machined with nail head at both ends fixing the pendulum resonance frequency of each stage in in two horizontal directions (two d.o.f.) at about $0.5\,Hz$

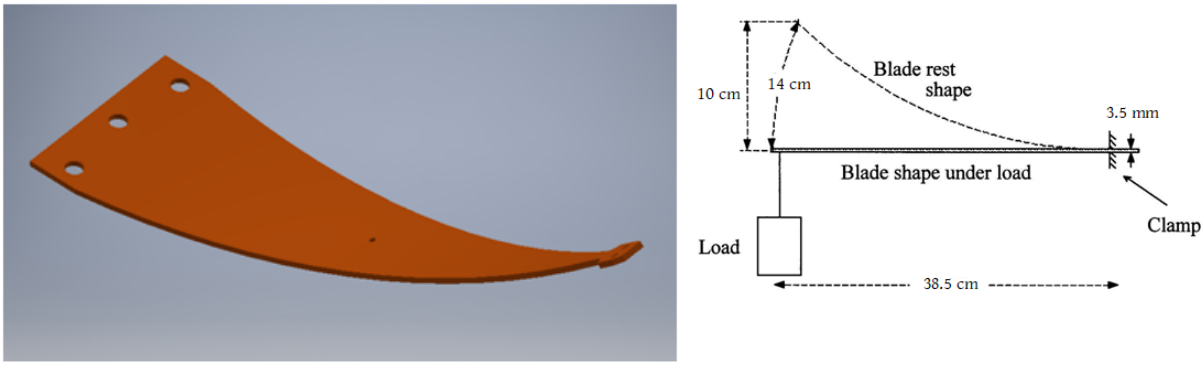

(a)

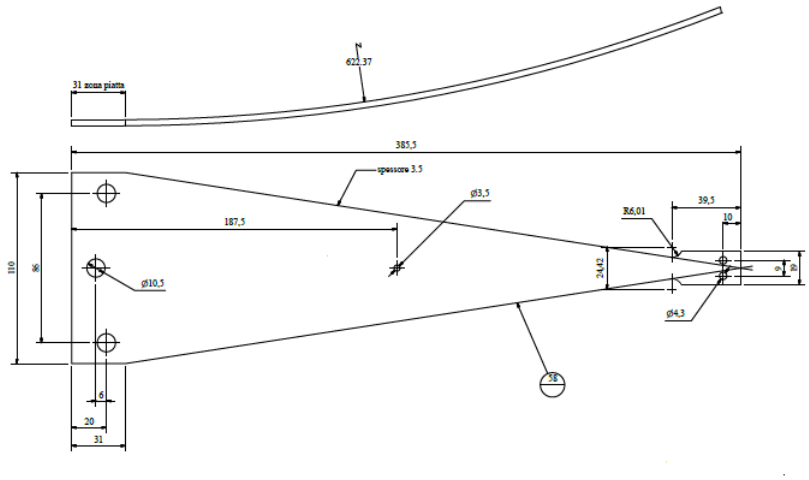

(b)

Figure 5.7: Triangular blade

aligned, the repulsive force does not have any vertical component, but as soon as they oscillate a vertical component appears. The moving magnets, indeed, are vertically displaced by a small amount δy, and a vertical *antispring* force appears*:*

$$F_{as} = F sin(\alpha) \sim F \delta y / d \tag{5.8}$$

where$F$ is the module of the repulsive force and d is the magnet separation in our experimental set-up (see fig.5.8). This device is equivalent to a vertical spring with a negative elastic constant (antispring) whose module is: $k_{as} = F/d$. Its rest position is that one for which the two couples of matrices are perfectly faced.

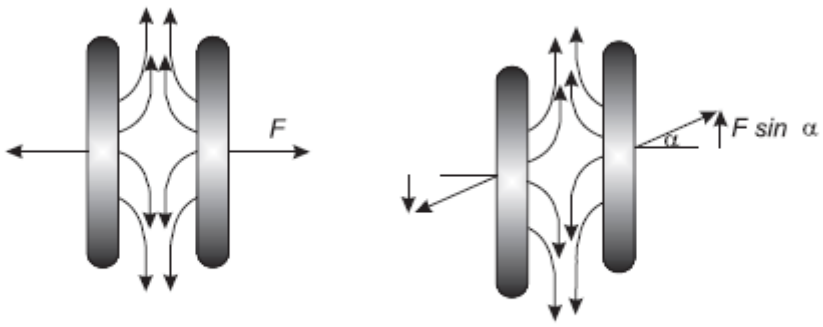

Figure 5.8: The working principle of the magnetic anti-spring system

On a seismic filter the magnetic anti-springs act on the crossbar in parallel with the blade mechanical springs, so that the overall elastic constant is reduced and the vertical mode frequencies of the chain can be confined below the highest frequency of the horizontal modes. To this purpose writing down the equation of the mechanical system with the combined action of the blade springs and the magnetic anti-spring, it turns out:

$$m\ddot{y} = -k_b \delta y + k_{as} \delta y \tag{5.9}$$

where k_b e k_{as} are the stiffness of the blade springs and that one obtained by the fine tuning of the magnets distance mounted on the crossbar and on the filter body respectively. From the equation (5.9) defining:

$$(\omega_0)^2 = (k_b - (F/d))/m \tag{5.10}$$

it is evident that the elastic constant of the system and then the vertical mode frequency (see equation 5.10) can be changed modifying the distance of the permanent magnets pairs bolted on the mechanical filter in accordance with the equation 5.8.

The device working principle requires that in the rest position all the magnetic anti-springs are perfectly aligned, in order to null the vertical component of the magnetic force. To this end a small remotely adjustable cantilever blade (the so called 'fishing rod' visible in fig. 5.9) has been added on top of each filter, to bring the anti-springs to the correct working point. This is also possible thanks to the presence of a vertical displacement sensor (LVDT - Linear Variable Differential Transformer) which is able to monitor the relative position of the crossbar with respect to the filter body.

In addition, the permanent magnetic field of the anti-spring is very sensitive to the temperature variation: the magnitude of the field decreases (increases) as soon as the temperature increases (decreases) causing a variation of the vertical resonance frequency of a single filter in accordance with the following experimental measurement:

$$\frac{\partial f_0}{\partial T} = 15 \pm 2 \frac{mHz}{^\circ C} \tag{5.11}$$

This result is in good agreement with the temperature dependence of the expected anti stiffness which is of the order of 0.4%/°C. [62]

Moreover the thermal variation of the vertical frequency is the sum of two contributions: the magnetic field strength and the blade stiffness. While the contribution of this last one is turned out from the experimental value [11]:

$$\frac{\Delta k}{k \cdot \Delta T} = 2.1 \times 10^{-4} / ^\circ C \tag{5.12}$$

the first one is the most important one and it represents a potential source of filter performance degradation if not properly controlled (the fine actuation by means of a fishing rod is used for this purpose too). For all these reasons the Superattenuator structure in maintained inside a vacuum vessel, called tower, and within a well temperature controlled environment.

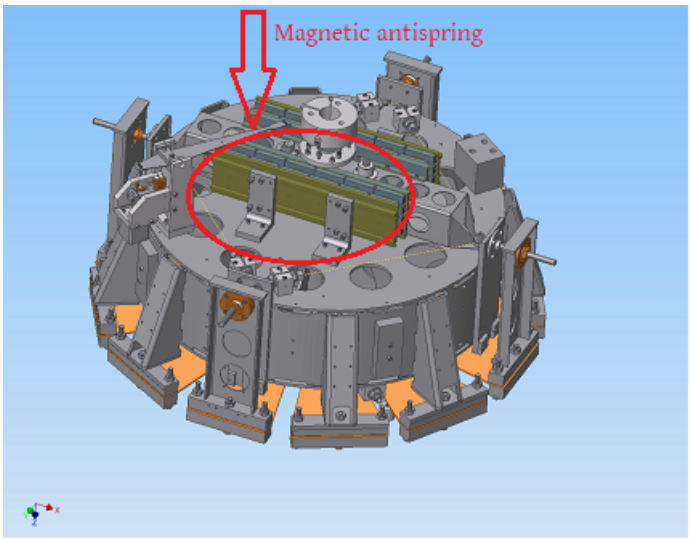

Figure 5.9: A 3D technical drawing of a standard filter where the magnetic anti-springs are visible (within the red circle) together with the fishing rod actuator .

5.1.4 Pre-isolation stage

The pre-isolation stage of the Superattenuator is based on two main mechanical elements: a seven meter high three legs Inverted Pendulum (IP) interconnected on its top by means of a metallic Top Ring and a modified standard filter (the so called Filter0 - F0) bolted on it. All these elements are ground connected through a large bottom ring having a diameter of about 1.5 m supported by three feet housing three piezoelectric actuators (3 PZT) acting in vertical direction along the leg axis..

The introduction of the IP in the SA technical design has been guided by the following requirements:

- to provide the SA with a very soft suspension point positioning system;
- to introduce a horizontal pre-attenuation stage at very low frequency (down to 30mHz) and improving the overall attenuation performance;
- to crate a platform equipped with sensors and actuators to perform an Active Mode Damping and seismic noise depression (reducing the SA resonance modes level).

The F0 is a modified standard filter integrated into the IP structure to complete its attenuation action in vertical direction too. On the crossbar mechanical structure a vertical hoist with a dynamic range of $\pm 35\,mm$ is installed and it is used for the mirror vertical positioning during the alignment phase of the ITF. The F0 and the Top Ring form a platform where positioning sensors (LVDTs), horizontal and vertical accelerometers as well as three magnet-coil pairs mounted in pin-wheel configuration have been placed. All these devices are fundamental tools for the positioning of the chain suspension point and in the Active Mode Damping feedback control strategy.

5.1.5 The IP working principle

An ideal Inverted Pendulum can be conceived as a mass-less vertical bar of length L ground connected by means of an elastic joint with stiffness k and supporting a mass m on its top (see fig. 5.10. The equation of a similar system can be written:

$$I\ddot{\theta} = -k\theta + mgLsin(\theta) \tag{5.13}$$

where I is the cylinder moment of inertia, the first addendum of the equation right side is the elastic torque due to the mechanical joint and the second one is the gravity torque. Considering

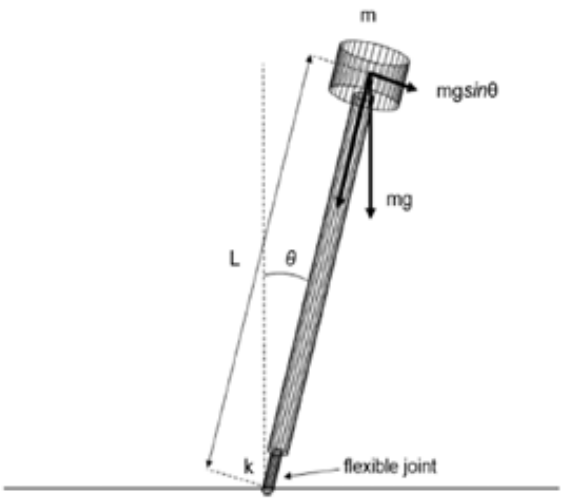

Figure 5.10: IP working principle

the system in the small oscillation regime, the equation 5.13 can be written:

$$\ddot{\theta} + (\frac{k}{mL^2} - \frac{g}{L})\theta = 0 \tag{5.14}$$

where $I = mL^2$ is the generic moment of inertia for a mass-less bar and then the Inverted Pendulum resonant frequency will be:

$$f_{IP} = \sqrt{\frac{k}{mL^2} - \frac{g}{L}} \tag{5.15}$$

From Eq. 5.15 it is evident that, with a fixed bar length the resonance frequency depends from the mass m connected on its top. The frequency value can be lowered by increasing the mass m until the mechanical instability is reached while the gravity acts as an anti-spring; such mechanical structure can operate at very low frequency (in AdV around 30 mHz). Attaching the suspension point of the multistage pendulum chain on the top of an inverted pendulum, it acts as an ultralow frequency pre-isolator stage that suppress a large part of the input horizontal seismic noise.Moreover, due to its very low overall stiffness, the inverted pendulum can be moved applying small forces. For example, considering the typical mass $M \sim 10^3 Kg$ of the AdV Superattenuator and the resonance mode of the pre-isolation stage fixed at 30 mHz, a displacement of $\Delta x \sim 10^{-2} m$, can be obtained by applying a force:

$$\mid F \mid = M \cdot (2\pi f_0)^2 \cdot \Delta x \sim 0.36 N \tag{5.16}$$

With the same approach, since the rotational mode frequency around the vertical axis of a typical inverted pendulum it is about 300mHz, it turns out that the needed force to rotate

the system by 1 mrad is just 3.6 N .In figure 5.11, 5.12 the experimental measurements of the chain normal modes for the long Superattenuators accommodated along the interferometer arms, are shown. They have been obtained by using the natural seismic noise vibration along the horizontal axis (x and z d.o.f.) as input and looking at the horizontal accelerometer signals installed on the IP top stage as output. By integrating two times this last signal, an evaluation of the displacement-displacement transfer function can be performed with the intent to get important information on the attenuation performance of the system.

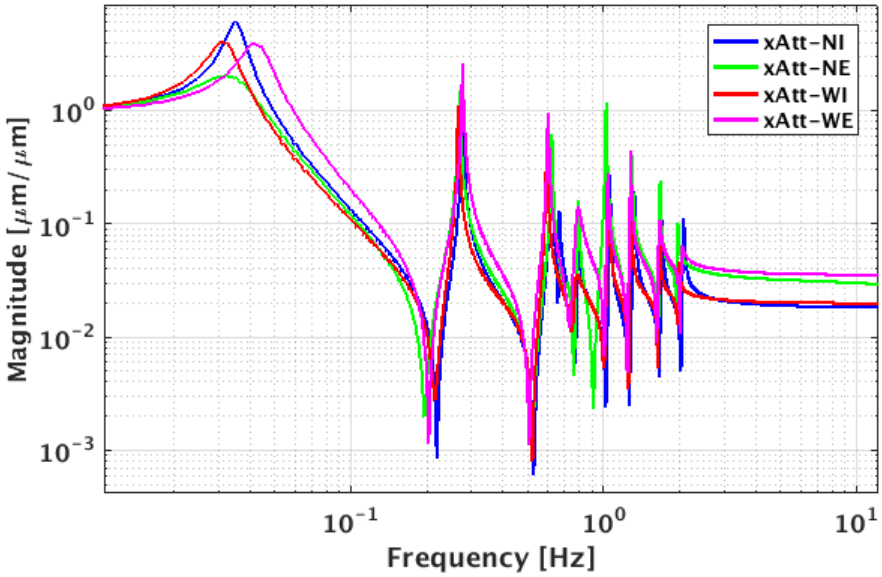

Figure 5.11: Normal modes distribution of different SA chains for the AdV interferometer. The experimental displacements induced by seismic noise along the x d.o.f. are plotted for the suspension chains accommodated along the interferometer arms (NI, NE, WI and WE). The curves put in evidence the resonance modes of each mechanical element of the chain starting from the IP normal mode at about 30 mHz.

5.1.6 The last stage: Filter7

The last mechanical filter of the chain is historically called Filter7 (see figures 5.13 and 5.14). The drum shaped structure of this element is identical to that one of each standard filter with four blades supporting the load of the next stage: the Payload (PAY). An interconnection mechanical element, meant as an interface, is bolt to the filter body bottom part. It has a shape of a cone or a two legs structure depending on the payload attached on it. This interface has an important role because it represents the connection point between the Payload and the passive chain of the SA. In addition, it is the mechanical structure on which the actuators at

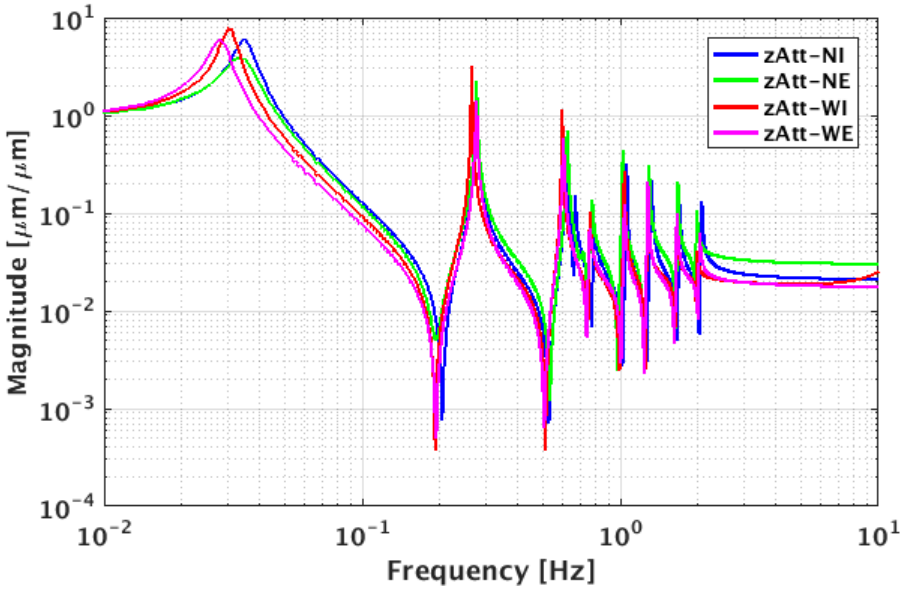

Figure 5.12: Normal modes distribution of different SA chains for the AdV interferometer. The experimental displacements induced by seismic noise along the z d.o.f. are plotted for the suspension chains accommodated along the interferometer arms (NI, NE, WI and WE). The curves put in evidence the resonance modes of each mechanical element of the chain starting from the IP normal mode at about 30 mHz.

the Marionette and Mirror level are bolted (see fig. 5.16 for a schematic view of the Filter7 working principle).

With the new geometry of the AdV Payload the role of Filter7 within the hierarchical feedback control of the Superattenuators has became more important. While in the first generation detector VIRGO, the Filter7 was mainly used with a monitoring purpose of the payload suspension point, in the control strategy adopted for AdV interferometer it plays an active role thanks to the possibility to steer it in three d.o.f. $[\theta_X, \theta_Y, \theta_Z]$.

To this purpose six sensor-actuation devices (three horizontal and three vertical) have been installed on the external circumference of the Filter7 body (see photo of the fig.5.13). They are based on LVDT positioning sensor and on magnet-coil pair integrated in a single device. By using them it is possible to perform an Active Pre-Damping (APD) of the F7 assuring a back-action effect every time an active control is engaged at the payload level.

The Filter7 technical equipment is completed with two stepper motors installed respectively on top of the filter body and on the bottom part of its mechanical structure. Thanks to the presence of two ball bearings, the first motor can be used to rotate around the vertical axis the structure Filter7-PAY with respect to the passive filters chain by a few degrees, while acting on the second one a rotation of the PAY with respect to the Filter7 can be performed with a similar

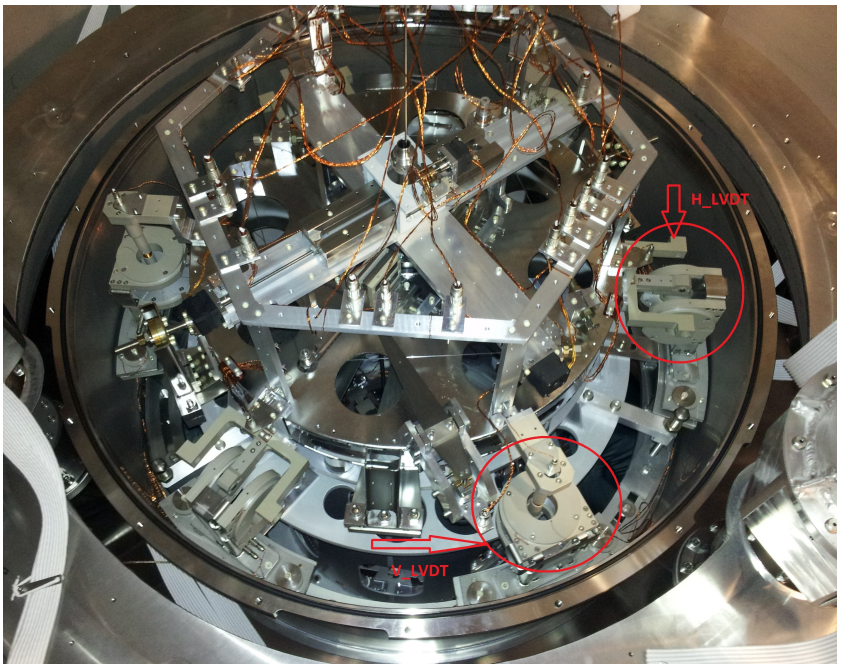

Figure 5.13: Filter 7 photo where the sensor-actuation devices are put in evidence within the red circles (three H_LVDT and three V_LVDT).

dynamic around the same vertical axis. These devices together with two balancing trolleys accommodated on top of the filter body (see fig. 1.13), have an important role in the Filter7 and Payload fine positioning phase.

5.1.7 The AdV Payload: Marionette and mirror (PAY)

The AdV Payload is the last element of the harmonic oscillators chain including the sophisticated optical components .The new design of this stage has been influenced by the heavier mirrors (42 kg each one) made of high quality optical material (low loss material) having the same diameter of the previous version (350 mm as in the VIRGO interferometer) but with a double thickness 200 mm. The second element of the Payload is the Marionette, the metallic structure above the mirror on which four silica fibers (400 micron in diameter) are anchored. At the lower end these fibers (SiO_2) are connected directly to the mirror lateral side by means of a silicate bonding process, minimizing the Thermal Noise. The octagonal shape of the Marionette structure is completed with four wings supporting permanent magnets having horizontal axis along the magnetic field and four wings supporting permanent magnets having vertical axis along the magnetic field. All these wings (eight in total) have been machined by using thermoplastic material (PEEK) Ultra High Vacuum compatible and each one is in front of a coil accommodated on a large flange bolted to the interface element (cone or legs)

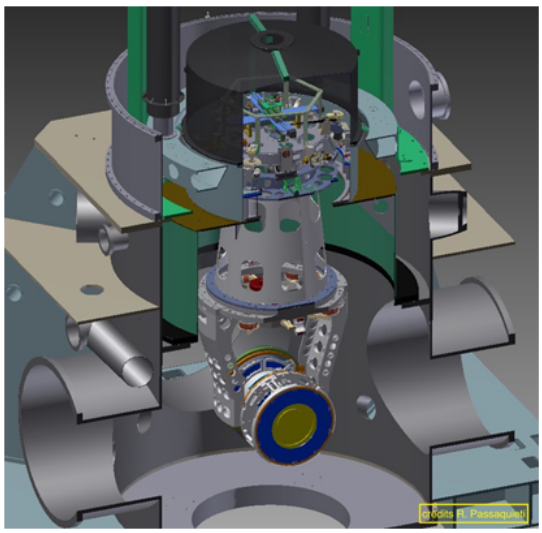

Figure 5.14: 3D technical drawing of the of suspension last stage. The conical interface connecting the Filter7 to the Payload is accommodacated within the tower vacuum vessel delimited by the cupola structure.

attached to the Filter7. The Marionette and the Mirror form a double stage pendulum structure connected to the Filter7 movable apparatus through a thin Maraging steel wire, identical to those ones used to interconnect the passive stages of the chain. On the Mirror back side four small permanent magnets, with magnetic field axis orthogonal to the mirror surface, are glued in front of the coils so that they form a set of actuators linked to the entire structure of the Filter7 used for feedback purpose. In fig. 5.14 a technical 3D drawing of the Superattenuator bottom part is visible; the Filter7, the conical interface and the whole Payload suspended from a multistage pendulum chain are well identified. Some additional details of the AdV payload setting up are also visible in the photos of the fig. 5.15, where, from left to right, a complete payload is visible before its installation within the vacuum tower and immediately after the integration on a Superattenuator (last photo on right side).

5.1.8 Hierarchical control

In the previous paragraphs a detailed description of the Superattenuator working principle has been presented putting in evidence the guide lines used for its development and final design. Moreover, with the help of the experimental measurements reported in fig. 5.11 and in fig. 5.12 where the frequency response of the mechanical structure is visible, the presence of the system normal modes in the region below 3 Hz is confirmed. The higher value of this frequencies group is considered a characteristic lower limit of the SA (the SA cut-off frequency) above which the passive performance of the filters cascade inhibits seismic noise transmission to the

mirror level.

Thanks to the presence of sensors and actuators accommodated all along the mechanical structure, a hierarchical feedback control system has been implemented in three different points: on top of the suspension, on the Filter7-Marionette stage and on the Mirror (see fig. 5.16). The intent of the feedback action is to reduce the swinging of the free falling masses (the mirrors) together with the possibility to maintain the interferometer looked on its best working point.

The Superattenuator Top Ring and Filter0 represent a platform where a set of sensors and actuators are installed for feedback control purpose. In particular three LVDT displacement sensors, three horizontal accelerometers, two vertical accelerometers together with three horizontal coil-magnet actuators, two vertical coil-magnet actuators and three stepping motors are the devices used to perform a very low frequency control of the chain suspension point (up to 200 mHz) as well as an Active Mode Damping (AMD) of the SA resonance modes for seismic noise depression. A preliminary fine positioning of the suspension point is performed by using the three motorized mechanical spring connected to the IP legs and measuring its spatial coordinate (x,z and θ_Y) with the LVDT sensors. Then, the feedback control loops are engaged with the correction signals obtained by the measurements coming out from positioning sensors and accelerometers. With this technique 4 d.o.f. (x,y,z and θ_Y) are controlled on this first actuation point by using the 5 coil-magnets pairs (3 horizontal and 2 vertical).

A second actuation point is located at the level of Filter7-Marionette, downstream to the suspension point and close to the free falling mass. Here a combined action is performed on the Filter7 and on the Marionette mechanical structure. On the first element an Active Pre-Damping (APD) is applied assuring a back-action effect every time an active control is engaged at the Payload level, while on the Marionette four feedback loops are engaged for the θ_X, θ_Y θ_Z and z d.o.f.. They are based on the correction signals sent to the eight coil-magnet pairs bolted to the flange connected to the Filter7 mechanical interface. Marionette and Mirror are monitored by using a system of sensors based on Optical Levers installed on the base tower. Two auxiliary laser beams, passing through optical view-ports and impinging on the suspended elements, are reflected back on a Positioning Sensor Device located outside the vacuum vessel. Even if this is considered a high precision sensor, it is not seismic noise free and the feedback control loops engaged using these signals are considered active Local Controls just in the frequency range 0.2-2 Hz. In this case the re-injected seismic noise is passively filtered at the mirror level by the pendulum structure.

The last actuation point of the AdV hierarchical control is located on the back side of the Mirror: the last suspended element of the Superattenuator. Four small permanent magnets with magnetic field perpendicular to the mirror back-side are glued on it and in front of the coils bolted on the mechanical structure connected to the Filter7. They define an ideal cross on the

mirror back-side forming a set of actuators to be used in the feedback strategy based on Optical Lever sensors. Three d.o.f. (θ_X, θ_Y and z) of the mirror are controllable at frequency higher than 2 Hz. This last actuation point plays a crucial role also in the locking acquisition process of the whole interferometer. Applying a force on the mirror back-side the optical cavity locking can be reached as well as a viscous damping can be engaged to restore the standard working conditions of a Superattenuator after a violent unlock event of the interferometer.

5.2 Towers

Long and short Superattenuators are installed within a vacuum chambers 10 m and 4.5 m high respectively called towers. The SA mechanical structure as described in the previous paragraphs together with the cables serving the electronic devices installed at any stage, are maintained in vacuum at a hydrogen partial pressure of $10^{-7}\,mbar$. This has been done to guaranty the detector performance and minimizing the noise from residual gas presence.

While the vacuum volume structure of the three short towers did not change in the AdV upgrade program, the volume of the longest ones have been re-organized taking into account the new geometry of the payload. A small tower (with a volume of about 14 m^3) is organized in a single compartment where the volume upper part is in direct contact with the lower zone where the optical benches are suspended. The vacuum compartment of a long tower (about 32 m^3 of total volume) is, instead, divided in two sections separated by a cupola structure above which the IP legs, the standard filters and their cables are installed (see fig. 5.17). Below the cupola the Filter7 and the Payload are accommodated to form a compartment where a differential vacuum level is maintained with the possibility to improve it down to $10^{-9}\,mbar$ of hydrogen partial pressure. This has been meant to minimize the noise due to the residual gas presence as well as to reduce the aging effect on the mirror surface influenced by the combined action of the laser beam and the hydrocarbon contaminants.

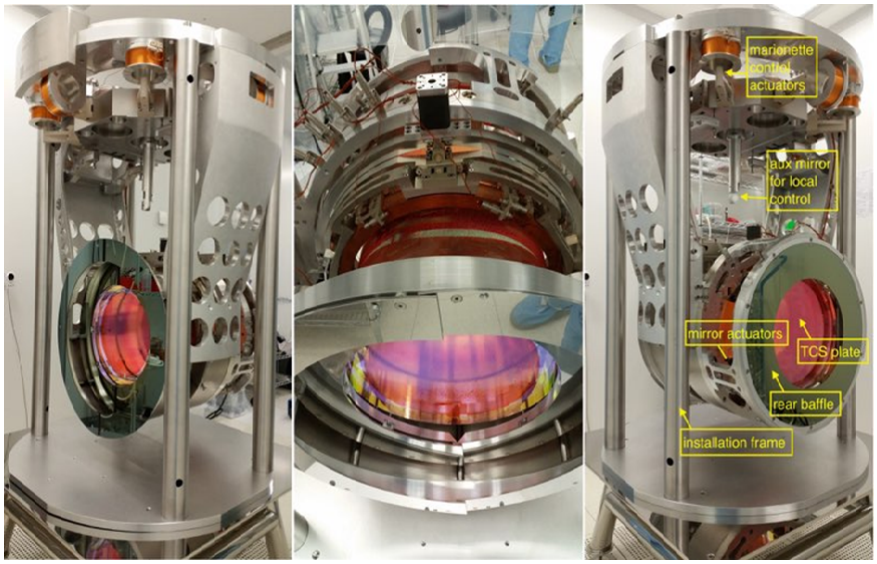

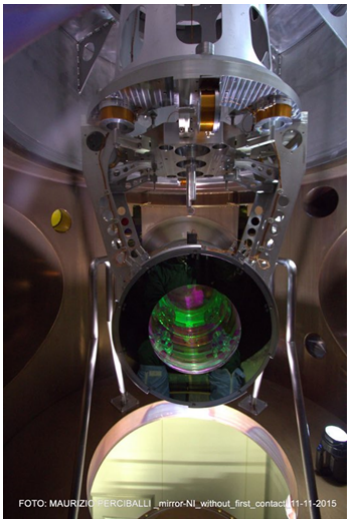

(a)

Figure 5.15: AdV Payload. In the figure upper part a complete Payload before its integration on the Superattenuator is shown. In this image a detailed setup is visible: from left to right the marionette, the position of the coil actuators, mirror, front baffle and the position of the mirror coil actuators are well identified in the right panel. In figure 5.15a the photo of the same Payload is shown after its integrartion within the Superattenuator (tower bottom part).

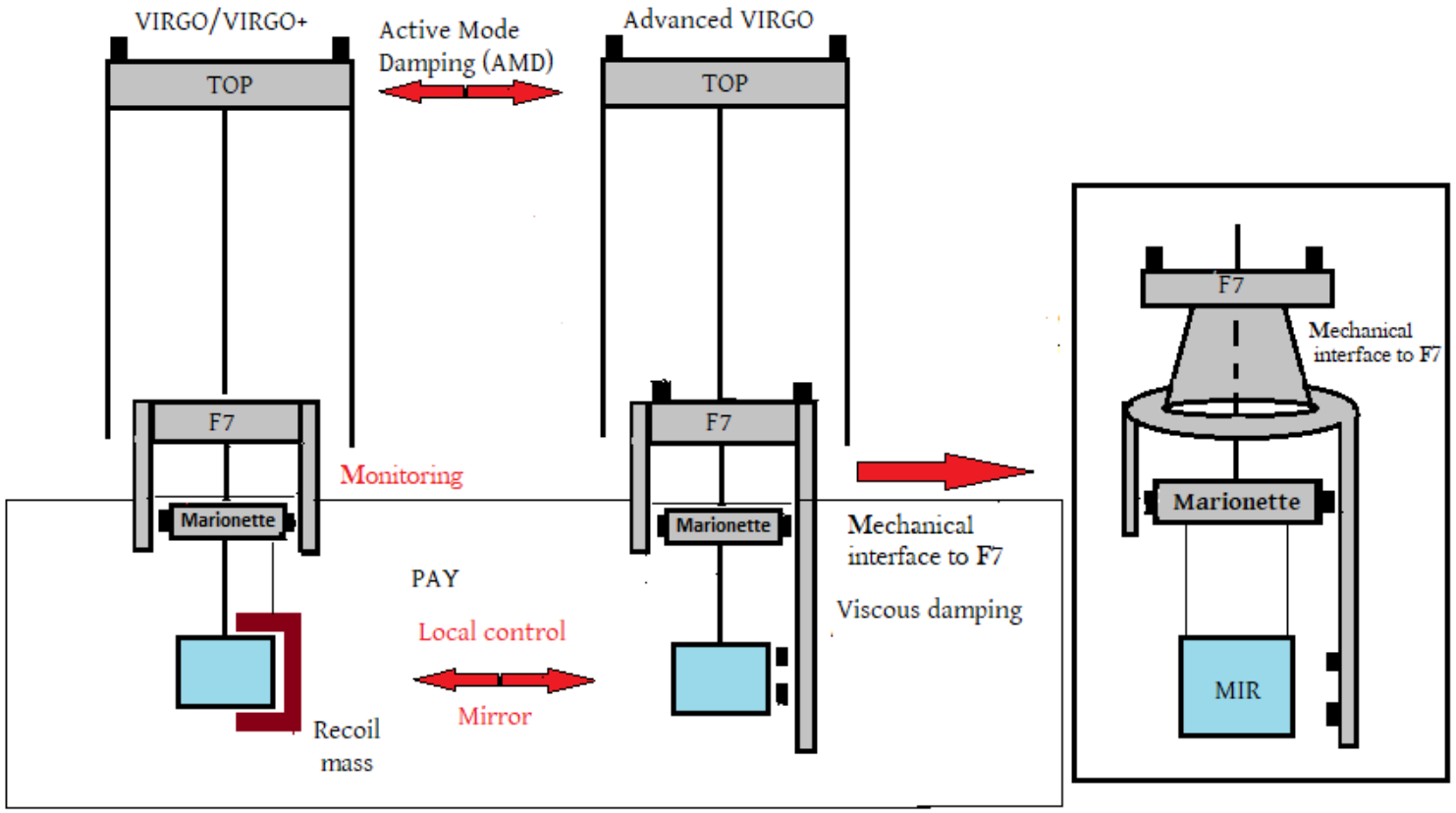

Figure 5.16: Schematic view of a long Superattenuator where the important elements for its hierarchical control are put in evidence. The three actuation points are meant to reduce the mirror swinging as well as to perform an active feedback action to lock the interferometer maintaining it in the best sensitivity conditions. In this scheme is also visible the setting up difference between VIRGO and AdV. With new payload geometry the Recoil Mass surrounding the VIRGO mirror has been replaced by a more complex mechanical structure directly connected to the conical interface of the Filter7 (see the box on right side where a more detailed scheme is showed).

Figure 5.17: 3D technical drawing of the base tower. The lower part of the vacuum compartment delimited by a cupola structure is shown. Below the cupola the Filter7 and the mechanical interface connecting it to the Payload is also visible.

Chapter 6

Modeling the Superattenuator transfer function and its overall behavior

The main goals of the development of a SA model are linked to the need to validate the strategy in suppressing seismic noise in correspondence of the chain normal modes and to have a simulation tool checking the stability and the performance of the feedback controlled system [7]. In this chapter we present a SA modeling devoted to simulate the behavior of a rigid bodies chain representing the attenuation system developed to inhibit seismic noise transmission at the mirror level. By using this simple model it is possible to obtain a realistic description of our mechanical structure in the small oscillations regime. It is based on the assumption that any element along the suspension chain can be represented with a rigid body or with an interconnection elastic element. In this framework the most relevant ones are:

- the body of a standard filter;
- the crossbar;
- the blades and the magnetic anti-springs;
- the Filter7;
- the Marionette and the Mirror;
- the legs and the flex joints of the Inverted Pendulum;
- the centering wires (on top of each filter body) and the Maraging suspension wires.

6.1 A schematic approach

Looking at figure 6.1, a simple mechanical filter is the result of a connection among different bodies (crossbar, a set of blades and magnetic anti-springs) through the centering wires installed on the filter structure. Thanks to these wires the crossbar is forced to move in vertical direction

only, but, from simulation model point of view, they are considered a "weak constraint". Two consecutive standard filters are linked together by means of a Maraging suspension wire (the crossbar of a filter is directly connected to the body of next one). The suspension wires are considered very rigid along the vertical direction but thy are soft in horizontal and angular d.o.f. . For this reason in our modeling they are classified as "strong constraint" along the vertical d.o.f. and "weak constraint" for all other d.o.f. . A similar situation is present on the suspension top stage, where the Filter0 is connected to ground through the IP legs which are considered very rigid in vertical direction but as a "weak constraint" for translational and rotational motions around the vertical axis.

Going down to the Filter7 level, it should be noted that its crossbar is the mechanical element from which the Payload (Marionette and Mirror) is suspended. From modeling point of view, the Marionette is considered a rigid body in vertical direction and the connection through a suspension wire is classified as a "strong constraint". With the same approach the Mirror and the monolithic suspension fibers complete the modeling of our suspension system.

6.2 Superattenuator transfer function

The Superattenuator behavior can be studied introducing a linear operator called *transfer function*. This operator put in relation the vibrations at the input point where the excitation is applied and those ones transmitted . by the mechanical structure to the output.

In the frequency domain this is identified by $\mathbf{T}_{in\rightarrow out}(\omega)$ and using it the relationship between an input vector $\mathbf{x}_{in}(\omega)$ and output vector $\mathbf{x}_{out}(\omega)$ is given by

$$\mathbf{x}_{in}(\omega) = \mathbf{T}_{in\rightarrow out}(\omega) \cdot \mathbf{x}_{out}(\omega) \tag{6.1}$$

Just to make an example, introducing a variation on the input variable $x_{i,in}(\omega)$ an evaluation of the output $x_{j,ou}(\omega)$ can be done knowing the component $t_{ij}(\omega)$ only (where $t_{ij}(\omega)$ is the element of the matrix $\mathbf{T}(\omega)$).

6.2.1 Transfer function: impedance matrix approach

From a theoretical point of view, the problem of vibration transmission in a mechanical system can be decomposed ideally dividing the main mechanical system into different subsystems subsystems connected each other in different way: in parallel, in series and in derivation.

In frequency domain, the study of these subsystems, can be performed using the **impedance matrix approach**[57, 63, 65]. In this case the state of each mechanical system is fully described by the temporal evolution of two vectors: the coordinates vector $\mathbf{x}(\omega)$ and $\mathbf{f}(\omega)$ vector where

the information on the forces and momenta applied are stored. Moreover, all the information necessary to describe the transmission properties of a single element are collected in a matrix $Z(\omega)$ called *impedance matrix*. By using this formalism the equation of motion are

$$\begin{pmatrix} \mathbf{x}_{out}(\omega) \\ \mathbf{f}_{out}(\omega) \end{pmatrix} = \mathbf{Z}(\omega) \cdot \begin{pmatrix} \mathbf{x}_{in}(\omega) \\ \mathbf{f}_{in}(\omega) \end{pmatrix} \quad with \quad \mathbf{Z}(\omega) = \begin{pmatrix} \mathbf{A}(\omega) & \mathbf{B}(\omega) \\ \mathbf{C}(\omega) & \mathbf{D}(\omega) \end{pmatrix} \tag{6.2}$$

where $\mathbf{A}(\omega)$, $\mathbf{B}(\omega)$, $\mathbf{C}(\omega)$, $\mathbf{D}(\omega)$ are square matrices of order equal to the number of input/output d.o.f. .

For a complex systems like our superattenuator these matrices should verify following properties

$$\begin{cases} \mathbf{Z}^{-1}(\omega) = \begin{pmatrix} \mathbf{D}(\omega)^t & -\mathbf{B}(\omega)^t \\ -\mathbf{C}(\omega)^t & \mathbf{A}(\omega)^t \end{pmatrix}; \quad \mathbf{Z} \cdot \mathbf{Z}^{-1} = \mathbf{I} \\ \\ \mathbf{A}^t \cdot \mathbf{D} - \mathbf{B}^t \cdot \mathbf{C} = \mathbf{I}; \quad \mathbf{A}^t \cdot \mathbf{B} = \mathbf{B}^\mathbf{t} \cdot \mathbf{A}; \quad \mathbf{C}^t \cdot \mathbf{D} = \mathbf{D}^\mathbf{t} \cdot \mathbf{C} \end{cases} \tag{6.3}$$

Thanks to the equation (6.2) the relationship between the applied forces and the displacements can be calculated for two different situations:

- setting to zero the output force we have the equation

$$\mathbf{x}_{out}(\omega) = (\mathbf{D}^t(\omega))^{-1} \mathbf{x}_{in}(\omega) \tag{6.4}$$

-setting to zero the output force and fixing $\mathbf{x}_{out}(\omega) = \mathbf{x}_{in}(\omega)$ we have the equation

$$\mathbf{x}_{out}(\omega) = -(\mathbf{C}(\omega)^{-1})^t \, \mathbf{f}_{in}(\omega) \tag{6.5}$$

In this way the the displacement-displacement transfer function of our subsystem can be estimated by using the relationship (6.4)

$$\mathbf{T}_{in \to out}(\omega) = \frac{\mathbf{x}_{out}(\omega)}{\mathbf{x}_{in}(\omega)} = (\mathbf{D}^t(\omega))^{-1} \tag{6.6}$$

Assuming that the actuation point is coincident with the measurement point (where the sensor is installed), from equation 6.5 the force-displacement transfer function is

$$\mathbf{T}_{in \to out}(\omega) = \frac{\mathbf{x}_{out}(\omega)}{\mathbf{f}_{in}(\omega)} = -(\mathbf{C}(\omega)^{-1})^t \tag{6.7}$$

6.2.2 Series, parallel and derivative connection of mechanical systems

With the same general philosophy based on the impedance matrix method, a representation of a whole mechanical system can be done associating an algebraic operator to each real mechanical element. A key role is played by the different connection techniques as well as by their formalism.

Considering two elementary mechanical systems sys_1 and sys_2 with their relative impedance matrices ($\mathbf{Z}_{sys1}(\omega)$ and $\mathbf{Z}_{sys2}(\omega)$), the final impedance matrix representing a new system can be calculated connecting the two starting matrices in accordance with the following rules:

- **System connected in series**: sys_1 and sys_2 are connected in series when the output vector ($\mathbf{f}_{out}(\omega)$ or $\mathbf{x}_{out}(\omega)$) of the first system is coincident with the input vector of the second system ($\mathbf{f}_{in}(\omega)$ or $\mathbf{x}_{in}(\omega)$). In this configuration the total impedance $\mathbf{Z}_{series}(\omega)$ of the system is:

$$\mathbf{Z}_{series}(\omega) = \mathbf{Z}_{sys1}(\omega) \cdot \mathbf{Z}_{sys2}(\omega) \tag{6.8}$$

- **System connected in parallel**: sys_1 and sys_2 are connected in parallel when they have the same output vector ($\mathbf{F}_{out}(\omega)$ or $\mathbf{X}_{out}(\omega)$) or input vector ($\mathbf{F}_{in}(\omega)$ or $\mathbf{X}_{in}(\omega)$) . In this case the total impedance $\mathbf{Z}_{\|}(\omega)$ of the system is:

$$\mathbf{Z}_{\|} = \begin{pmatrix} \mathbf{A}_1 + \mathbf{B}_1 \cdot (\mathbf{B}_2 + \mathbf{B}_1)^{-1} \cdot (\mathbf{A}_2 - \mathbf{A}_1) & \mathbf{B}_1 \cdot (\mathbf{B}_1 + \mathbf{B}_2)^{-1} \cdot \mathbf{B}_2 \\ \mathbf{C}_1 + \mathbf{C}_2 + (\mathbf{D}_1 - \mathbf{D}_2) \cdot (\mathbf{B}_1 + \mathbf{B}_2)^{-1} \cdot (\mathbf{A}_2 - \mathbf{A}_1) & \mathbf{D}_1 + (\mathbf{D}_2 - \mathbf{D}_1) \cdot (\mathbf{B}_1 + \mathbf{B}_2)^{-1} \cdot \mathbf{B}_1 \end{pmatrix} \tag{6.9}$$

When $\mathbf{A}_1 = \mathbf{A}_2 = \mathbf{A}$ and $\mathbf{D}_1 = \mathbf{D}_2 = \mathbf{D}$ the expression (6.9) becomes:

$$\mathbf{Z}_{\|} = \begin{pmatrix} \mathbf{A} & \mathbf{B}_1 \cdot (\mathbf{B}_1 + \mathbf{B}_2)^{-1} \cdot \mathbf{B}_2 \\ \mathbf{C}_1 + \mathbf{C}_2 & \mathbf{D} \end{pmatrix} \tag{6.10}$$

- **System connected in derivation:** sys_2 is connected in derivation to sys_1 when its output ($\mathbf{f}_{out}(\omega)$ or $\mathbf{x}_{out}(\omega)$) is free and its input ($\mathbf{f}_{in}(\omega)$ or $\mathbf{x}_{in}(\omega)$) is coincident with the input or the output vector of sys_1. In this case; the total impedance $\mathbf{Z}_d(\omega)$ of the system is:

$$\mathbf{Z}_{d,in} = \mathbf{Z} \cdot \begin{pmatrix} I & 0 \\ \mathbf{C}_d & I \end{pmatrix}; \ \mathbf{Z}_{d,out} = \begin{pmatrix} I & 0 \\ \mathbf{C}_d & I \end{pmatrix} \cdot \mathbf{Z}; \tag{6.11}$$

A mechanical system mimic our superattenuator can be connected in two different derivative ways:

- input or output of the derivative system is connected to the ground

$$\mathbf{Z}^G_{d,in} = \mathbf{Z} \cdot \begin{pmatrix} I & 0 \\ \mathbf{B}_d^{-1} \cdot \mathbf{A}_d & I \end{pmatrix}; \ \mathbf{Z}^G_{d,out} = \begin{pmatrix} I & 0 \\ \mathbf{B}_d^{-1} \cdot \mathbf{A}_d & I \end{pmatrix} \cdot \mathbf{Z}; \tag{6.12}$$

- input or output of the derivative system is a *floating point*:

$$\mathbf{Z}_{d,in}^{Float} = \mathbf{Z} \cdot \begin{pmatrix} I & 0 \\ \mathbf{D}_d^{-1} \cdot \mathbf{C}_d & I \end{pmatrix}; \quad \mathbf{Z}_{d,out}^{Float} = \begin{pmatrix} I & 0 \\ \mathbf{D}_d^{-1} \cdot \mathbf{C}_d & I \end{pmatrix} \cdot \mathbf{Z}; \tag{6.13}$$

It will be shown that the approach adopting the impedance matrix description is quite effective to describe a complex mechanical systems like the AdV suspension. In the next, we will calculate the Z matrix of the overall suspension system connecting the Z matrices representing each of their subsystem.

6.3 Impedance matrix of suspension subsystems

By using the formalism described above a complex mechanical system can be easily simulated just evaluating the impedance of each real mechanical element. As an example [63], let us evaluate the matrix impedance of an harmonic oscillator formed by a body of mass m attached to a mass-less spring with stiffness k. From the equation (6.2) the impedance matrix Z_m of the body is

$$Z_m = \begin{pmatrix} 1 & 0 \\ m\omega^2 & 1 \end{pmatrix} \tag{6.14}$$

and that one for a spring with stiffness k

$$Z_k = \begin{pmatrix} 1 & -1/k \\ 0 & 1 \end{pmatrix} \tag{6.15}$$

Connecting in series the body and the spring the matrix impedance of an harmonic oscillator (Z_{osc}) can be obtained

$$Z_{osc} = \begin{pmatrix} 1 & -\frac{1}{k} \\ m\omega^2 & 1 - \frac{m\omega^2}{k} \end{pmatrix} \tag{6.16}$$

Using this technique the impedance matrix of all subsystems can be evaluated, as we are going to show here below.

6.3.1 Impedance matrix of a rigid body

Let us calculate the impedance matrix of a rigid body in small oscillation regime considering only two degrees of freedom, x and θ. When the center of mass is coincident with the input

and the output of the system, ($x_{in} = x_{out}$ and $\theta_{in} = \theta_{out}$) the equations of motion become

$$\begin{cases} f_{in}(\omega) - f_{out}(\omega) = -m\omega^2 x_{in}(\omega) \\ \\ m_{in}(\omega) - m_{out}(\omega) = -I\omega^2 \theta_{in}(\omega) \end{cases} \tag{6.17}$$

where m and I are the mass and momentum of inertia of the body. For this system the impedance matrix is[1]

$$Z_{I,m} = \begin{pmatrix} 1 & 0 & 0 & 0 \\ 0 & 0 & 0 & 0 \\ m\omega^2 & 0 & 1 & 0 \\ 0 & I\omega^2 & 0 & 1 \end{pmatrix} \tag{6.18}$$

$Z_{I,m}$ is a 4×4 matrix while considering all d.o.f. we will handle a 12×12 matrix.

More in general, the study of the rigid body dynamic described by 6 d.o.f., can be performed with the help of the linear (δx) and the angular ($\delta\theta$) coordinates of a point P with respect to a reference frame. Let us consider the generalized Lagrangian coordinates $\underline{q_P} = (\delta x, \delta\theta)$ and the generalized vector of the force ($\underline{f_P} = (f, m)$) acting on P. If the dynamic evolution of the system is represented with a point Q, whose distance from P is given by the vector b, the components of the vector $\underline{f_Q}$ can be calculated by applying the matrix Λ_b to the vector $\underline{f_P}$ as follows:

$$\underline{f_Q} = \Lambda_b \underline{f_P} \tag{6.19}$$

$$\underline{f_Q} = (\delta x + b \wedge \delta\theta \, , \delta\theta \, , f, \, m - b \wedge f)^t \tag{6.20}$$

with [2]

$$\Lambda_b = \begin{pmatrix} 1 & b_\wedge & 0 & 0 \\ 0 & 1 & 0 & 0 \\ 0 & 0 & 1 & 0 \\ 0 & 0 & -b_\wedge & 1 \end{pmatrix} \tag{6.21}$$

By considering also the term $-(b \wedge f) \wedge \delta\theta$, the last component of the vector Eq. (6.20) becomes

[1] Considering just two d.o.f. of a real mechanical system, the impedance matrix is 4×4 matrix, because the force and displacement vectors have two components: horizontal translation and rotation around the longitudinal axis ($\mathbf{F} \to \mathbf{F}(x, \theta)$,$\mathbf{X} \to \mathbf{X}(x, \theta)$) .

[2] The symbol $\wedge$ means vector product: $c = a \wedge b \Rightarrow \; c^m = \eta^{mi} \varepsilon_{ijk} a^j b^k$. Where the indices i , j , k correspond to vector components and ε_{ijk} is the Levi-Civita symbol.

$\overrightarrow{m}_Q = \overrightarrow{m} - (b \wedge f) - (b \wedge f) \wedge \delta\theta$, and the new Λ_b matrix that realize this transformation is

$$\Lambda_b = \begin{pmatrix} 1 & b_\wedge & 0 & 0 \\ 0 & 1 & 0 & 0 \\ 0 & 0 & 1 & 0 \\ 0 & -(b \wedge f)_\wedge & -b_\wedge & 1 \end{pmatrix} \tag{6.22}$$

where

$$-(b \wedge f) = \begin{pmatrix} b_y f_y + b_z f_z & -b_x f_y & -b_x f_z \\ -b_y f_x & b_x f_x + b_z f_z & -b_y f_z \\ -b_z f_x & -b_z f_y & b_x f_x + b_y f_y \end{pmatrix}; \quad b_\wedge = \begin{pmatrix} 0 & b_z & -b_y \\ -b_z & 0 & b_x \\ b_y & -b_x & 0 \end{pmatrix}; \tag{6.23}$$

This matrix will be used to evaluate the impedance matrix of any subsystem of the SA any time its input/output is different from the system center of mass.

6.3.2 Impedance matrix of centering wires

This mechanical element can be modeled by considering it to a cylinder of radius d , length L made of material having Young modulus E .

$$k_{c,x} = \frac{\pi E d^2}{L}; \; k_{c,\theta} = k_{c,x} \cdot (s^2 + a^2) \tag{6.24}$$

where a is the vertical distance between the ideal wire center and the crossbar center of mass and s is the geometrical distance between the real filter body plane and that one defined by the centering wire connected to it. Considering this element as elastic constrain, its impedance matrix is given by:

$$Z_{cwire} = \begin{pmatrix} 1 & 0 & -\frac{1}{k_{c,x}} & 0 \\ 0 & 1 & 0 & -\frac{1}{k_{c,\theta}} \\ 0 & 0 & 1 & 0 \\ 0 & 0 & 0 & 1 \end{pmatrix} \tag{6.25}$$

6.3.3 Impedance matrix of suspension wires.

In a similar way, the suspension wires can be modeled by using the parameters: wire length$L$, wire mechanical tension T , wire sectional area S , the material density ρ, the Young module E of the material and the transversal sectional momentum of inertia J [7]. Considering just two

d.o.f. $[z,\ \theta_x]$ the impedance matrix of a suspension wire is:

$$Z_{[z,\theta_x]} = \begin{pmatrix} \frac{\lambda_1^2 c_3+\lambda_3^2 c_1}{d} & \frac{L(\lambda_3 s_3+\lambda_1 s_1)}{d} & \frac{L^3(-\lambda_1 s_3+\lambda_3 s_1)}{d} & \frac{L^2(c_3-c_1)}{EJd} \\ \frac{\gamma^2(-\lambda_1 s_3+\lambda_3 s_1)}{dL} & \frac{\lambda_3^2 c_3+\lambda_1^2 c_1}{d} & \frac{L^2(-c_3+c_1)}{EJd} & -\frac{L(\lambda_3 s_3+\lambda_1 s_1)}{EJd} \\ \frac{EJ\gamma^2(-\lambda_1^3 s_3+\lambda_3^2 s_1)}{dL^3} & \frac{EJ\gamma^4(-c_3+c_1)}{L^2 d} & \frac{\lambda_1^2 c_3+\lambda_3^2 c_1}{d} & \frac{\gamma^2(\lambda_1 s_3-\lambda_3 s_1)}{dL} \\ \frac{EJ\gamma^4(c_3-c_1)}{L^2 d} & \frac{EJ(-\lambda_1^3 s_3+\lambda_3^2 s_1)}{dL} & -\frac{L(\lambda_3 s_3+\lambda_1 s_1)}{d} & \frac{\lambda_3^2 c_3+\lambda_1^2 c_1}{d} \end{pmatrix} \tag{6.26}$$

Below 10 Hz ($f \ll f_c = \frac{T}{2\pi\sqrt{\rho SEJ}}$) typically, the effects due to the mass of the wire are negligible and the matrix can be written as

$$Z_{[z,\theta_x]} = \begin{pmatrix} 1 & \lambda sh & -\frac{\lambda sh-L}{T} & \frac{1-\lambda sh}{T} \\ 0 & ch & \frac{ch-1}{T} & -\frac{sh}{\lambda T} \\ 0 & 0 & 1 & 0 \\ 0 & \lambda T sh & \lambda sh & ch \end{pmatrix} \tag{6.27}$$

with

$$\begin{array}{ccc} c_3 = cos(\lambda_3); & c_1 = cosh(\lambda_1); & s_3 = sin(\lambda_3); \\ \lambda_1 = (\frac{\sqrt{\tau^2+4\gamma^4}+\tau}{2})^{1/2}; & \lambda_3 = (\frac{\sqrt{\tau^2+4\gamma^4}-\tau}{2})^{1/2}; & s_1 = sinh(\lambda_1); \\ \tau = \frac{L^2}{\lambda^2}; & \gamma^4 = \frac{\omega^2 \rho S L^4}{EJ}; & \lambda = \sqrt{\frac{EJ}{T}}; \\ & d = \sqrt{4\gamma^4+\tau^2} & \end{array} \tag{6.28}$$

where $sh = \sinh(\frac{L}{\lambda})$, $ch = \cosh(\frac{L}{\lambda})$ and f_c is the frequency value to which the effect due to the mass of the wire shows-up.

In Eq. (6.27)and (6.26) the hyperbolic functions s_1 , c_1 sh and ch , whose arguments depend on the length and thickness of the superattenuator wires, become highest and then the matrix is numerically unstable. Indeed, considering the typical values of length $L \sim 1\,m$ and bending length $\lambda \sim 0.01\,m$ of suspension wires, the values of these functions are large as $sh \sim ch \sim c_1 \sim s_1 \approx e^{\tau} \approx e^{100}$. In order to delete these divergent terms we can connected, in parallel to them, a virtual wire represented by an impedance matrix similar to that of the centering wire (Eq. (6.25)) [63]. In order not to introduce spurious terms in the transfer function, k_θ must be chosen small enough to fulfill the constraint $\frac{k_\theta}{I} \sim 1\,mHz$, where I represents the momentum of inertia of the load mass. From the expansion in series of the coefficients of the parallel connection between Eq. (6.27) and (6.25), in terms of $\alpha = \frac{\lambda T}{k_\theta}$, it is possible to have

the analytical expression for the impedance at low frequency approximation,[63]

$$Z_{[z,\theta_x]} = \begin{pmatrix} 1 & 2\lambda(1+\frac{\alpha}{2}) & \frac{2\lambda(1+\frac{\alpha}{2})-L}{T} & -\frac{\lambda}{k_\theta} \\ 0 & 1+\alpha & \frac{\lambda}{k_\theta} & -\frac{1}{k_\theta} \\ 0 & 0 & 1 & 0 \\ 0 & 2\lambda T(1+\frac{\alpha}{2}) & -2\lambda(1+\frac{\alpha}{2}) & 1+\alpha \end{pmatrix} \tag{6.29}$$

To study the internal dynamics of the wire its mass must be considered. Also in this case, starting from the coefficients of the parallel connection between the Eq. (6.26) and (6.25) and, by expanding in series, in term of the parameter $\alpha = \frac{\lambda T}{k_\theta}$, it is possible to deduce the analytical expression of the impedance matrix of the wire. This calculation has been performed some years ago [67], and we report the results $Z_{[z,\theta_x]}$

$$Z_{[z,\theta_x]} = \begin{pmatrix} \mathbf{A}_w & \mathbf{B}_w \\ \mathbf{C}_w & \mathbf{D}_w \end{pmatrix} \tag{6.30}$$

where the sub-matrices $\mathbf{A}_w$, B_w, $\mathbf{C}_w$, $\mathbf{D}_w$ are given by

$$\mathbf{A}_w = \begin{pmatrix} \frac{\gamma^2 s_3}{\lambda_1^2} + c_3 + \frac{EJ\gamma^4}{Lk_\theta\lambda_1^3} & \frac{L(d+2\gamma^2 s_3+\tau c_3)}{d\lambda_1} + \frac{EJ}{k_\theta} \\ \frac{\gamma^4 EJ}{\lambda_1^2 L^2 k_\theta} & \frac{EJ\lambda_1}{Lk_\theta} + 1 \end{pmatrix}; \mathbf{B}_w = \begin{pmatrix} \frac{L^3(2c_3-\frac{\tau s_3}{\gamma^2})}{EJdk_\theta} + \frac{L^2}{\lambda_1^2 k_\theta} & \frac{-L}{\lambda_1 k_\theta} \\ \frac{L}{\lambda_1 k_\theta} & -\frac{1}{k_\theta} \end{pmatrix}; \tag{6.31}$$

$$\mathbf{D}_w = \begin{pmatrix} \frac{\gamma^2 s_3}{\lambda_1^2} + c_3 + \frac{EJ\gamma^4}{Lk_\theta\lambda_1^3} & -\frac{EJ\gamma^4}{L^2 k_\theta \lambda_1^2} \\ -\frac{L(d+2\gamma^2 s_3+\tau c_3)}{d\lambda_1} - \frac{EJ}{k_\theta} & \frac{EJ\lambda_1}{Lk_\theta} + 1 \end{pmatrix}; \tag{6.32}$$

$$\mathbf{C}_w = \begin{pmatrix} \frac{EJ\gamma^2 d}{\lambda_1 L^3} s_3 + \frac{(EJ\gamma^4)^2}{L^4\lambda_1^4 k_\theta} & \frac{EJ\gamma^2}{L^2}(s_3 + (1-c_3)\frac{\gamma^2}{\lambda_1^2}) + \frac{(EJ\gamma^2)^2}{L^3\lambda_1 k_\theta} \\ -\frac{EJ\gamma^2}{L^2}(s_3 + (1-c_3)\frac{\gamma^2}{\lambda_1^2}) - \frac{(EJ\gamma^2)^2}{L^3\lambda_1 k_\theta} & \frac{EJ(-2d\lambda_1^2+2\gamma^4 c_3-\gamma^2\tau s_3)}{dL\lambda_1} - \frac{EJ\lambda_1^2}{L^2 k_\theta} \end{pmatrix}; \tag{6.33}$$

6.3.4 Impedance matrix of the inverted pendulum

Within the mechanical structure of the Inverted Pendulum two different elastic elements are present: the flex joints connecting the aluminum pipes to the base ring and the short suspension wires (31 mm long) connecting the top ring to the upper end of the IP legs. These elastic elements are distributed, in a plane geometry, on the vertices of an equilateral triangle (at 120 degrees each to the other). The flex joint can be modeled by a rigid metallic cylinder on top of

which a load is applied and it flexes under the action of the chain load, while the IP leg is a simple aluminum pipe under compression due to the static load of the chain on its top. In these working conditions the impedance matrix of these elements is similar to that one reported in Eq. (6.30), but with an important difference: the mechanical tension appears with a negative sign ($T \rightarrow -T$) because on top of the system a compression load is applied. The full impedance matrix for the joints (Z_{joint}) and the columns/legs (Z_{col}) are:

$$Z_{joint} = \begin{pmatrix} \mathbf{A}_j & \mathbf{B}_j \\ \mathbf{C}_j & \mathbf{D}_j \end{pmatrix}; \; Z_{col} = \begin{pmatrix} \mathbf{A}_c & \mathbf{B}_c \\ \mathbf{C}_c & \mathbf{D}_c \end{pmatrix}; \tag{6.34}$$

Since all these elastic elements are arranged in a pin-wheel configuration, they move under the action of a momentum due to the gravity force:$-(b \wedge f) \wedge \delta\theta$. To this purpose the right transfer function and the impedance matrix evaluation should be performed in the points v_i (the three vertices of the triangle) while the transformation defined in the Eq. (6.22) must be applied to all input/output points of these elements

$$Z'_{joint} = \Lambda^{ou}_{v_i,} Z_{joint} \Lambda^{in}_{v_i,}; \; Z'_{col} = \Lambda^{out}_{v_i,} Z_{col} \Lambda^{in}_{v_i,}; \; Z'_{wire} = \Lambda^{out}_{v_i,} Z_{wire} \Lambda^{in}_{v_i,} \tag{6.35}$$

Finally, an IP leg is the result of a serial connection of two elements working with a compression load applied (column and joint) and another element working under a tension load (the short suspension wire used to hang the top stage):

$$Z_{IP} = Z'_{joint} \cdot Z'_{col} \cdot Z'_{wire} \tag{6.36}$$

6.3.5 Impedance matrix of the triangular blade

Like the others elastic element of the chain, also the triangular blade is characterized, in our modeling, by the Young module of the material E, the mechanical tension T applied to the tip, the flex length L of the cantilever, the base width of the triangular geometry S and its thickness d. However the knowledge of these parameters together with the evaluation of the generic matrix (6.30) are not sufficient to reproduce, in accurate way, the behavior of this element. This problem can be fixed dividing the blades in N elastic elements each one with length l_N, width s_N and thickness d . For each element the impedance matrix can be evaluated through the equation (6.30) described above. Moreover, to reproduce the whole triangular blade, the N elements derived from the previous passage should be connected in series with the intent to get

the overall impedance matrix representing this elastic element within our simulation:

$$\begin{aligned} Z^{Blad}_{wire,1} &= Z^{1}_{wire,l_1,s_1} \cdot Z^{2}_{wire,l_2,s_2} \\ &\vdots \\ Z_{Blad} &= Z^{Blad}_{wire,N-1} \cdot Z^{2}_{wire,l_N,s_N} \end{aligned} \tag{6.37}$$

As last step of the process, the complete set of blades installed on each filter body and reproducing a circular configuration, is modeled by connecting in parallel n matrices like that one (6.37), each one representing a real blade.

6.4 Overall impedance matrix

In these sub-paragraphs we give some details on the process to connect all together the Inverted Pendulum, the mechanical filters and the Payload with the aim to have a detailed tool representing the Superattenuator in our simulation program.

6.4.1 SA inverted pendulum

The Advanced VIRGO Inverted Pendulum is then represented in our model with a impedance matrix Z^{IP}_{AdV} evaluated through the parallel connection of three identical legs as described above (Eq. (6.36)):

$$Z^{IP}_{AdV} = Z^{1}_{IP} \parallel Z^{2}_{IP} \parallel Z^{3}_{IP} \tag{6.38}$$

6.4.2 Standard filter

With reference to Fig. (6.1) a representation of a standard filter can be obtained putting together all the impedance matrices representing the single elements: the blades (Z_{Blad}), the anti-spring (Z_{as} calculated by using the Eq.(6.15)), the rigid body ($Z_{M_{FS}}$calculated by using Eq. (6.17)), the crossbar (Z_{cr} calculated by using the Eq. (6.16)) and the centering wires (Z_{cwire} calculated by using the Eq. (6.25)).Connecting together all these elements, the impedance matrix of a standard filter (Z_{F_S}) is given by:

$$Z_{F_S} = Z_{cr} \cdot Z_{M_{FS}} \cdot (Z_{cwire} \parallel Z_{Blade} \parallel Z_{as}) \tag{6.39}$$

6.4.3 Payload

The Payload is the structure where the Mirror is connected to the Marionette through four special wires made of silica represented by the impedance matrix (Z_{wire}). As we described for the metallic suspension wires, also in this case an evaluation of the impedance matrix Z_{wire} pass through a precise consideration of the input and output points by using the coordinate d describing the distance from the system center of mass as well as the equation (6.22)

$$Z'_{wire} = \Lambda^{ou}_{d,} Z_{wire} \Lambda^{in}_{d,} \tag{6.40}$$

Connecting in parallel four identical elements, each one described by the Eq. (6.40), the impedance matrix of the wires (Z^{pay}_{wire}) is obtained while that one of the payload ($Z_{mi,ma}$) is given by

$$Z_{mi,ma} = M_{mi} \cdot Z^{pay}_{wire} \cdot M_{ma} \tag{6.41}$$

where M_{ma} and $M_{mi}$are the matrices of marionette and mirror masses (see Eq. (6.14)).

The payload, whose impedance matrix is that one reported in Eq. (6.41), is now connected to the Filter7 as last element of the chain. In particular it can be considered as the suspension point of the payload itself and connecting it to the Filter7 crossbar (by means of a suspension wire), the sub-system Filter7-Payload can be studied independently. Connecting the Payload to ground through the crossbar of the Filter7 in derivation (the body of Filter7 is at rest) the impedance matrix to be used is $Z^{G}_{d;wire,F_7} \cdot M_{F_7}$ and then the transfer function Filter7-Payload is given by:

$$P_{ma,F_7} = Z^{Float}_{d;mir} \cdot M_{ma} \cdot Z^{G}_{d;wire,F_7} \cdot M_{F_7} \tag{6.42}$$

where $Z^{Float}_{d;mir}$ represents the impedance of the Mirror calculated by using the Eq. (6.13) and $Z^{G}_{d;wire,F_7}$ is calculated by using the Eq. (6.12).

6.4.4 Overall system

The impedance matrix representing the overall chain of our Superattenuator (Z_{chain}) is obtained connecting the five mechanical filters (each to the next one) through the impedance matrix representing the elastic element of the suspension wire (Z_{wire,F_i}) [3]. Starting from the bottom,

[3] In this notation the subscript F_i refers to the suspension wire connecting the i-th down stage with the upper one.

where the payload ($Z_{mi,ma}$) is accommodated, and going to the top stage the final result is:

$$Z_{chain}: \begin{cases} Z_1 = Z_{mi,ma} \cdot Z'_{wire,F_7} \cdot Z_{F_7} \\ Z_2 = Z_1 \cdot Z'_{wire,F_4} \cdot Z_{F_4} \\ Z_3 = Z_2 \cdot Z'_{wire,F_3} \cdot Z_{F_3} \\ Z_4 = Z_3 \cdot Z'_{wire,F_2} \cdot Z_{F_2} \\ Z_5 = Z_4 \cdot Z'_{wire,F_1} \cdot Z_{F_1} \\ Z_6 = Z_5 \cdot Z'_{wire,F_0} \cdot Z_{F_0} \end{cases} \tag{6.43}$$

Applying a serial connection between the suspension chain (Z_{chain}) and the Inverted Pendulum (Z^{IP}_{AdV}) we get the impedance matrix of the whole Superattenuator Z_{Susp}

$$Z_{Susp} = Z_{chain} \cdot Z^{IP}_{AdV} \tag{6.44}$$

Considering all d.o.f. the Eq. (6.44) is represented by a 12×12 matrix which is the final tool to be used in the simulation of the mechanical transfer function of the system.

6.5 Transfer function of SA: simulations

The method described above and making use of the impedance matrix $Z_{[z,\theta_x]}$ reported in Eq. (6.29), has been applied in the simulation of the Superattenuator behavior including the payload. The results obtained are reported in the document [63]. The tool has been implemented since many years with the goal to study the VIRGO and Advanced VIRGO suspension systems with the possibility to use it in a standalone configuration, for a better evaluation of the behavior a single element of the suspension chain [66]. Giving the complexity and the matrices size, dedicated scripts with the MATLAB package have been implemented and it have been used in this thesis work to evaluate the impact of the vertical active mode damping on the Advanced VIRGO sensitivity (see chapter 10). The result of this computation provides a complex matrix whose elements are transfer functions for selected d.o.f. of the system. Here below in Fig. 6.6 and Fig. 6.5 the simulated transfer functions are reported (vertical and horizontal d.o.f.), while in 6.3 and 6.4 a comparison between the experimental measurements and the simulation results for an horizontal d.o.f. obtained with the transformations(6.6) and (6.7) of the matrix Z_{Susp} are showed.

6.5.1 Payload transfer function: standalone simulation

As last example in the use of our simulation tool kit, here we shortly present the transfer function simulation of the Payload in standalone configuration for three different distance between the Marionette center of mass (CM_{mar} in Fig. 6.2) and the attaching point of the suspension wire (Ap in Fig. 6.2). This is possible thanks to the possibility in fixing the Marionette suspension point in the setting-up phase of the Payload. For this specific application the simulation tool kit is useful to study the Payload response (6.42) as function of the distance p (the free parameter reported in table 6.1) when the excitation is applied to the actuators connected to the Marionette.

0 (m)
-0.008 (m)
-0.0088 (m)

Table 6.1: Used values for p parameter to produce the simulated transfer function reported in Fig.6.7.

The results of this simulation are shown in Fig. 6.7 where the transfer function force-displacement for the Pitch mode of the Mirror (θ_x) is evaluated for the three different values of p. For this mechanical system (Eq. (6.42)) the transfer function force-displacement is equal to $T_{in\rightarrow out} = -A \cdot C^{-1} + (C^{-1})^t$ and the reconstruction of the mirror tilt pass through the application of the transformation (6.6) to the matrix $P_{mi} = M_{mi} \cdot Z^{pay}_{wire}$.

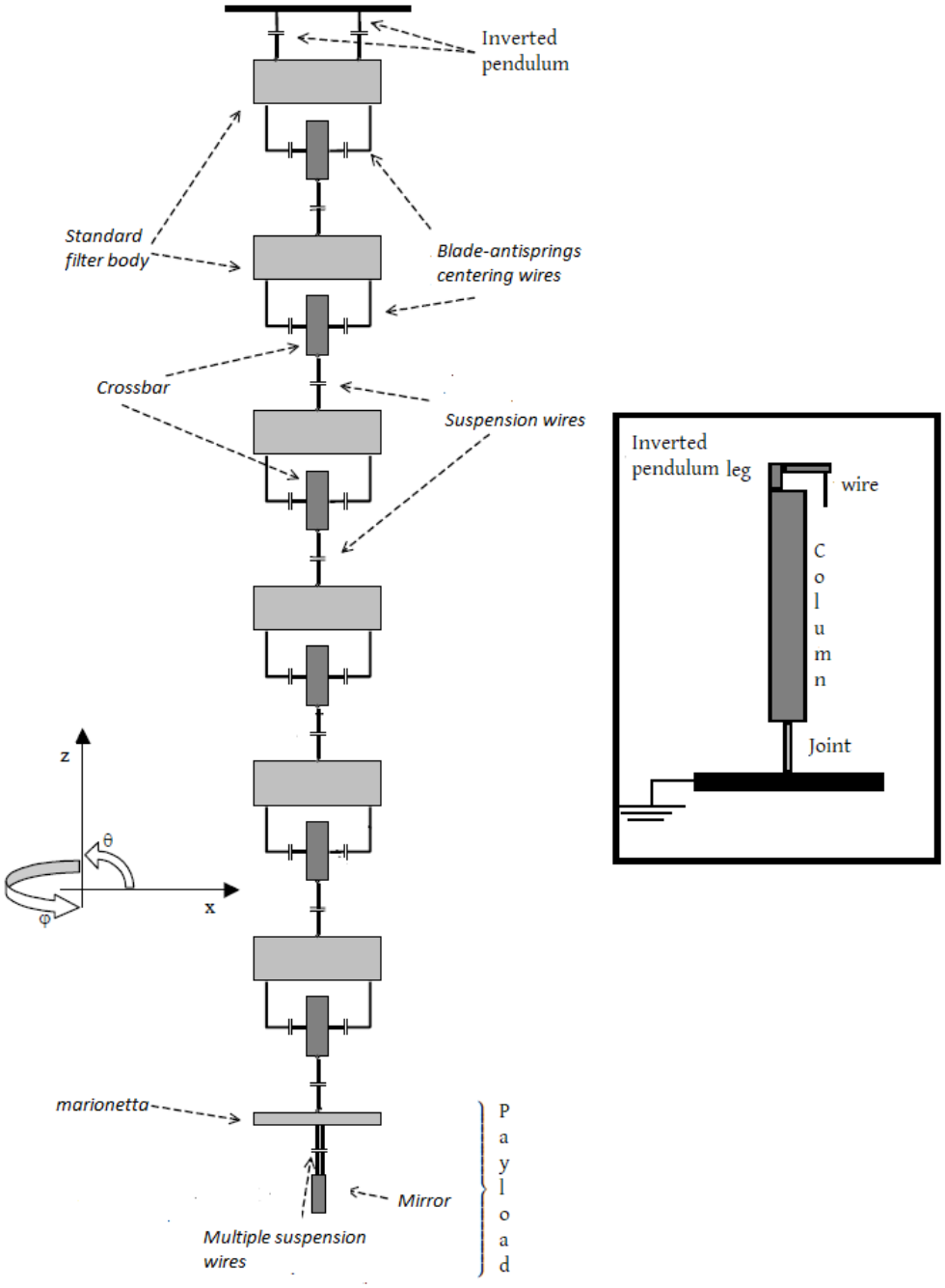

Figure 6.1: Schematic representation of the Superattenuator chain. The scheme includes the Inverted Pendulum used to control the chain suspension point as well as the chain normal modes confined in the low frequency region (below a few Hz). In our reference system the variables x, y, z are the displacement coordinates of the body center of mass along its main inertia axis. We denote with ψ, ϑ, φ the rotation angles of the rigid body around the axes x, y, z.

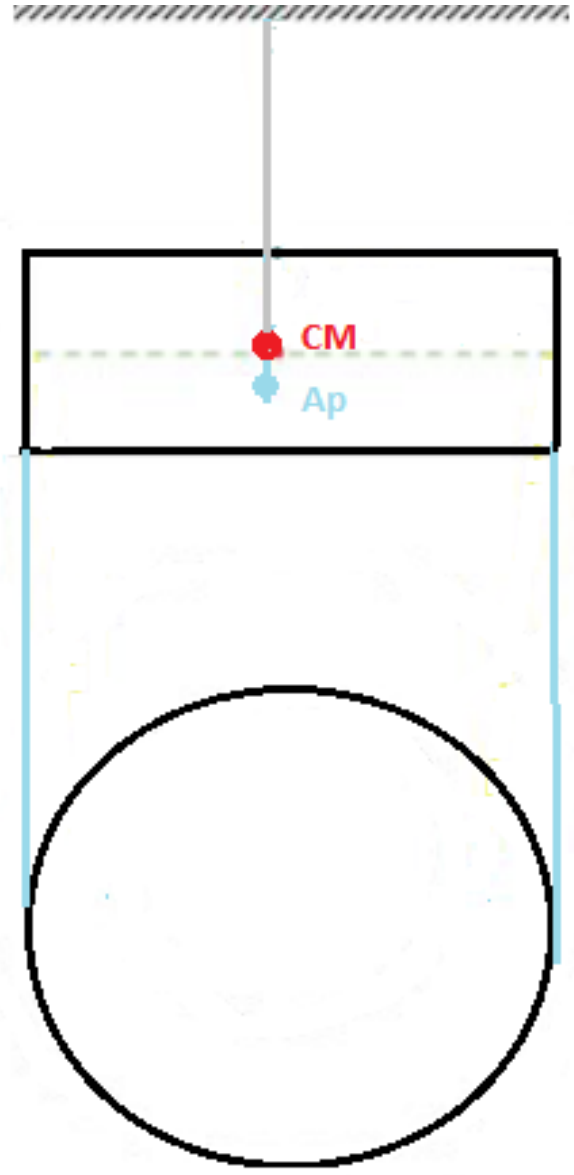

Figure 6.2: Schematic configuration of the Payload: in this figure we can see the positions of the center of mass of the marionette and the attaching point of the suspension wire.

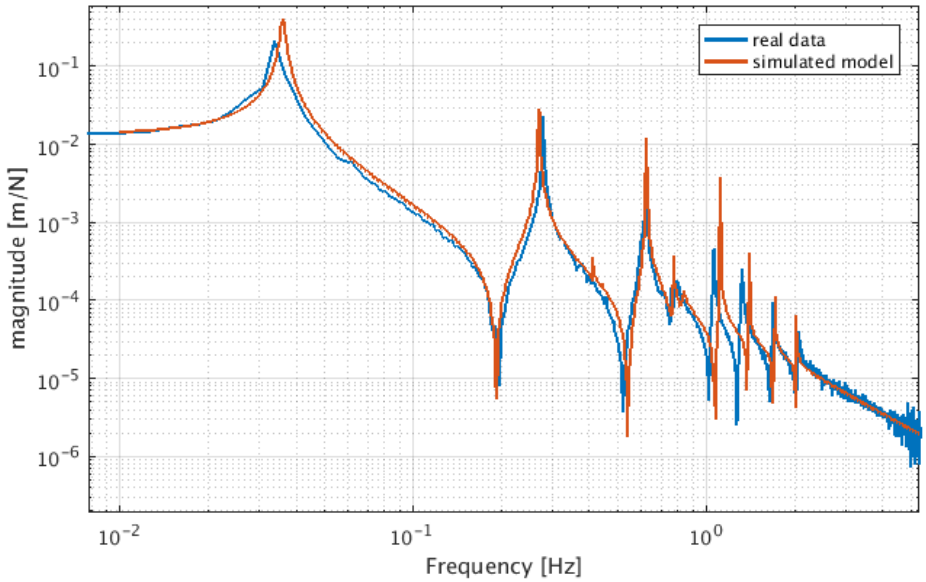

Figure 6.3: Horizontal transfer of AdV superattenuator: comparison between measurement (blue curve) and model (red curve) obtained by using the transformation 6.7 to the matrix Z_{Susp}. In this case the simulation result has been obtained applying at the input point the excitation (in horizontal direction at the level of the Filter0) and the horizontal motion of the IP has been selected as output point of the system (where the response has been sensed).

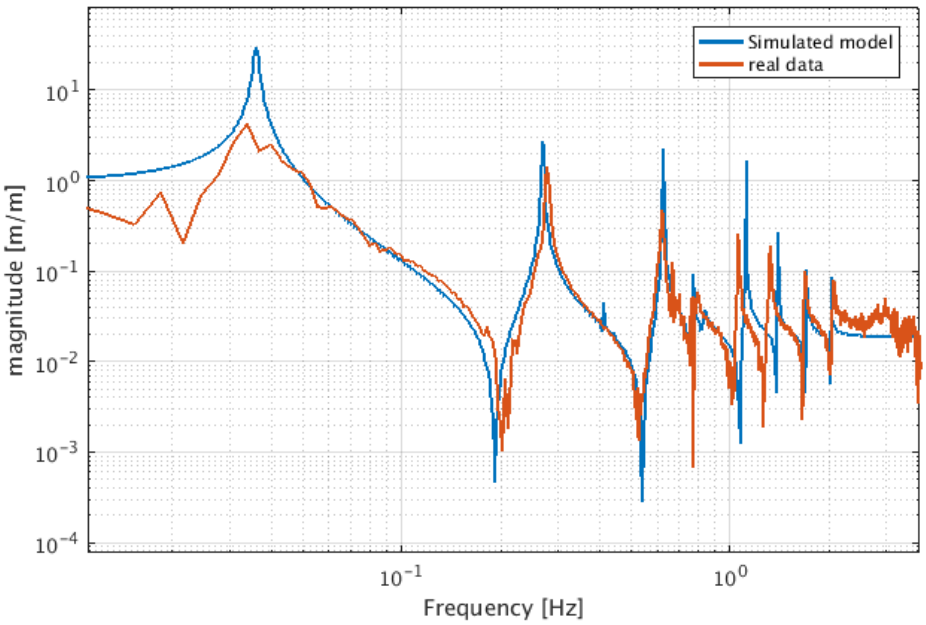

Figure 6.4: Horizontal transfer function of AdV superattenuator: comparison between measurement (blue curve) and model (red curve) obtained by using the transformation 6.6 to the matrix Z_{Susp}. In this case the input point is ground connected and the excitation to the system comes from the natural seismic noise, while the output point is represented by the horizontal motion of the top stage.

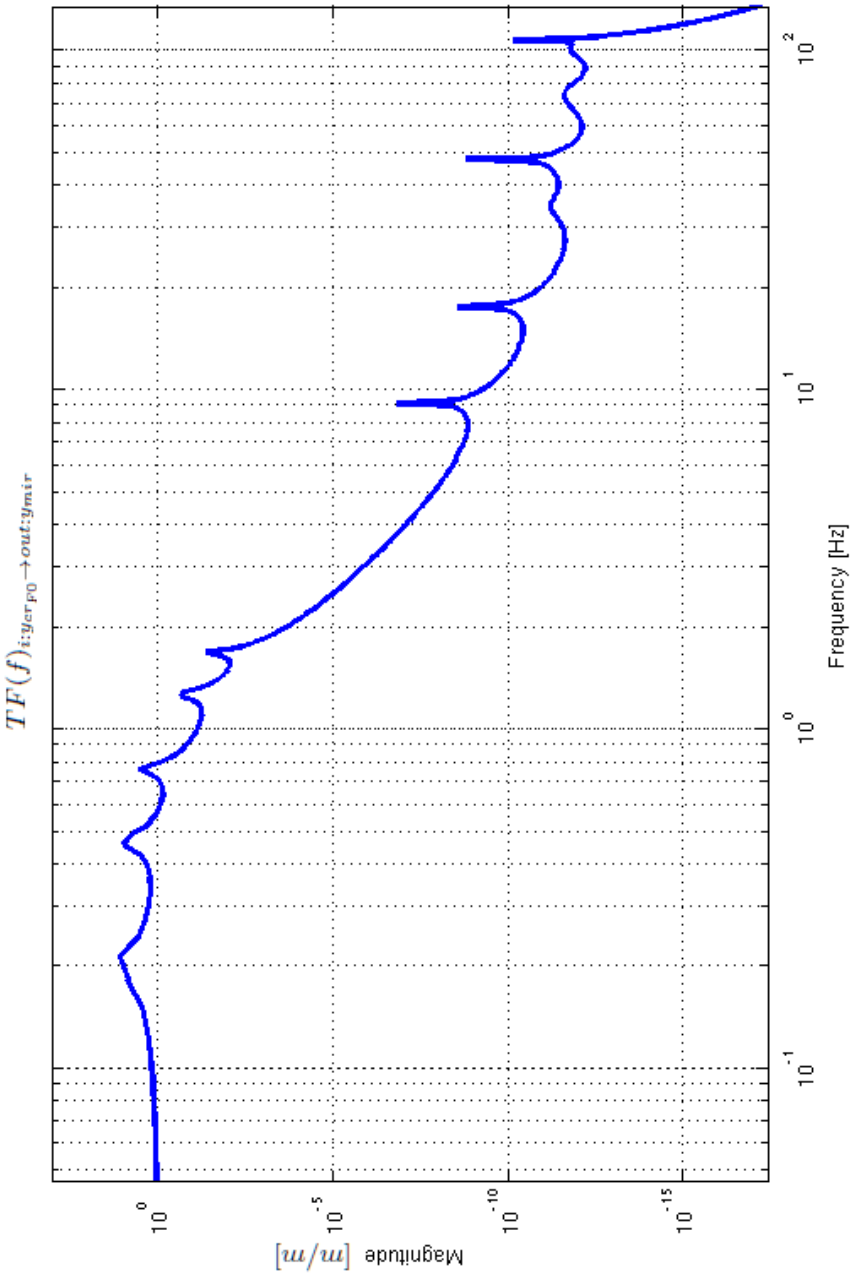

Figure 6.5: Vertical transfer function of the AdV Superattenuator. In this case the simulation result has been obtained applying at the input point the excitation (in vertical direction at the level of the Filter0) and the Mirror has been selected as output point of the system (where the response has been sensed).

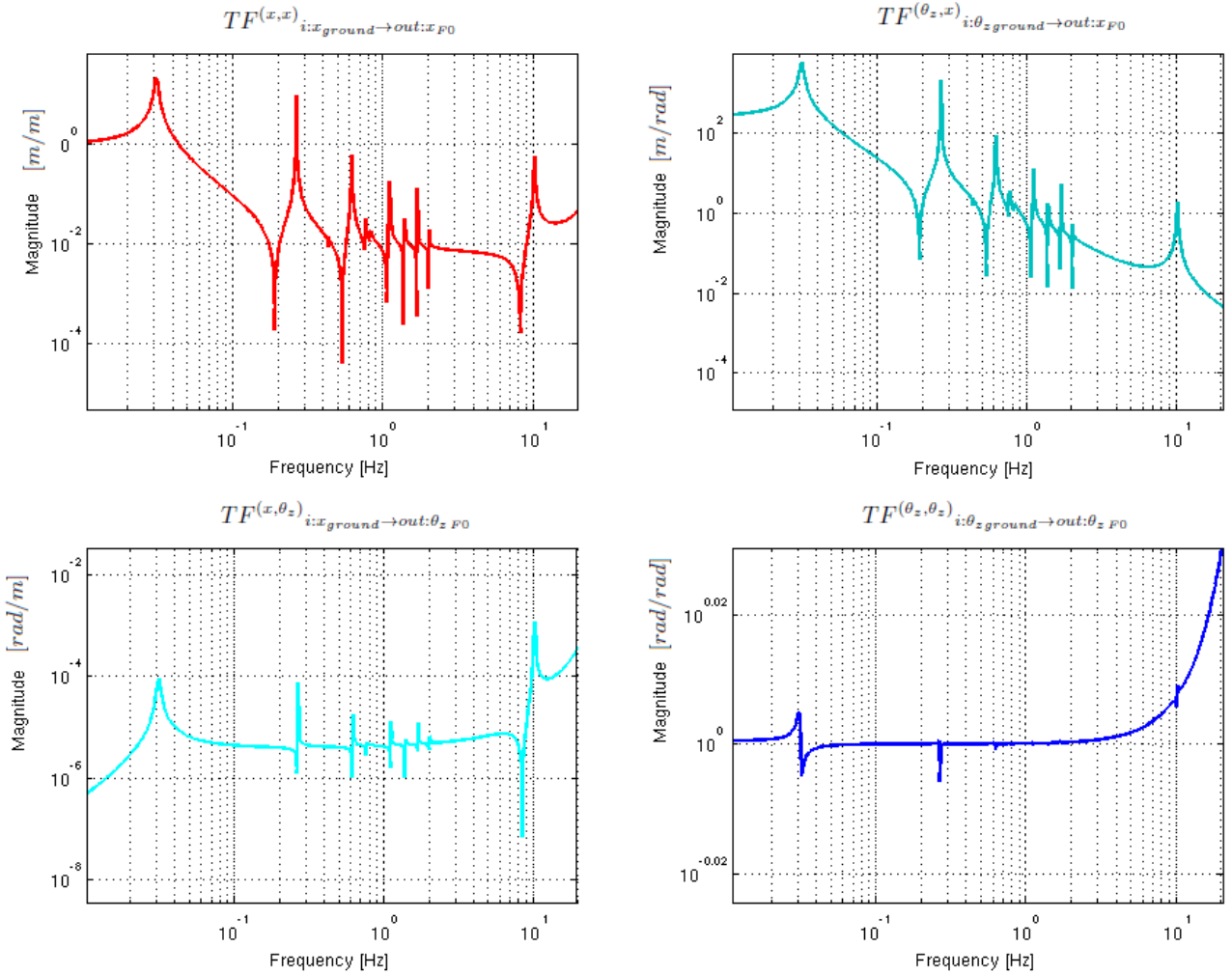

Figure 6.6: Horizontal transfer function of the AdV Superattenuator. In this case the input point is ground connected and the excitation to the system comes from the natural seismic noise, while the output point is represented by the horizontal motion of the top stage. In these plots are visible also the horizontal normal mode of the IP (at about 30 mHz) and the first flexural mode of its leg at about 12 Hz ("banana mode").

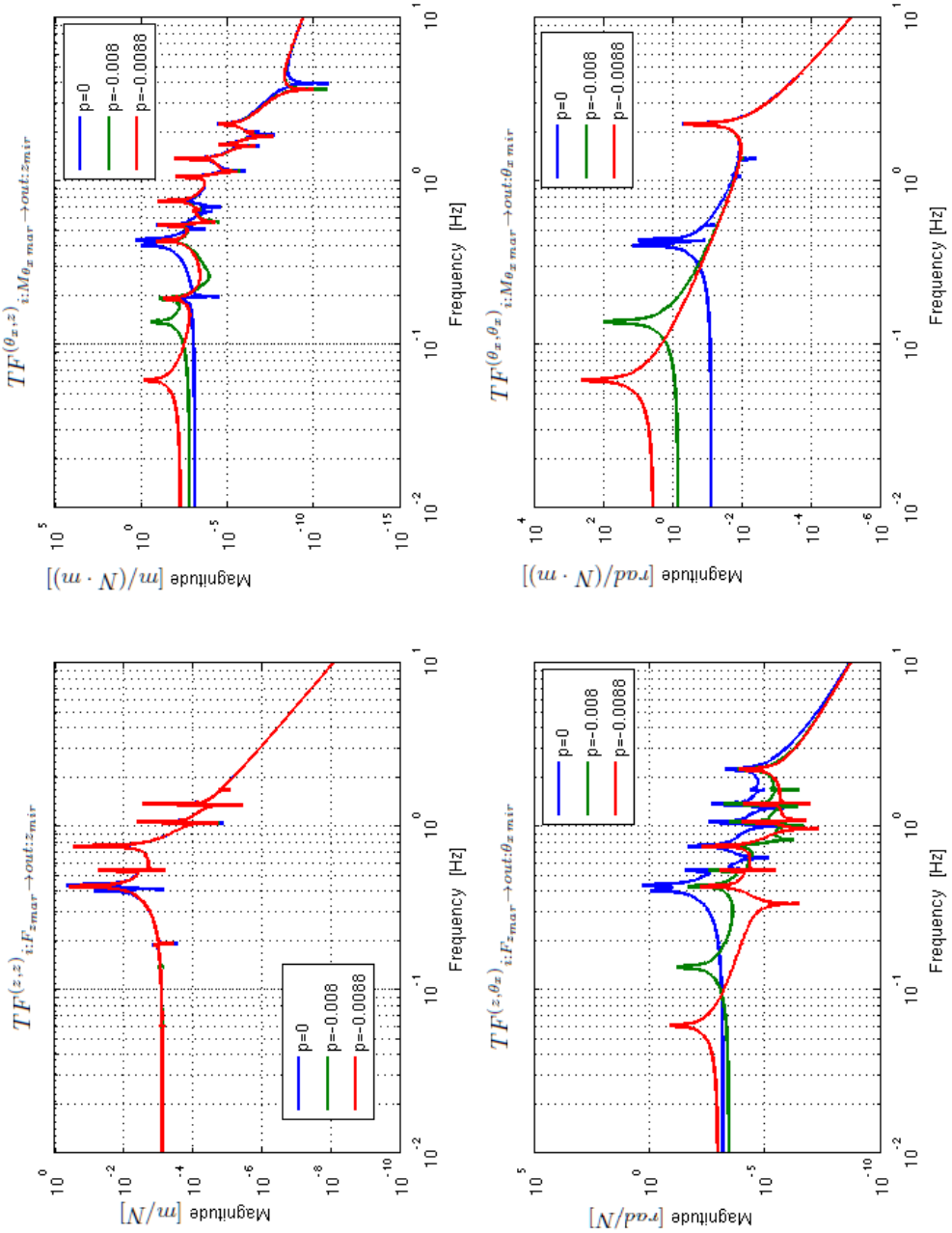

Figure 6.7: Payload transfer function simulation evaluated for three different values of the parameter p. In this configuration the excitation is applied on the marionette (input point) and the results is obtained sensing the mirror (output point). The change of the p value reproduces the behavior evolution of the payload from the VIRGO setting-up (blue curve) to those ones used in the AdV setting-up (input test mass red curve and end test mass green curve).

Part III

Results

Chapter 7

Top stage experimental set-up

We have concluded the Chapter 5 saying that in order to set SA in the correct configuration status, several sensors and actuators capable to monitor and control its displacements have been accommodated all along its structure.With their aid, it is possible implement the so called hierarchical control. At the top stage level an Active Mode Damping (AMD) is implemented and in this chapter we focus our attention on the preliminary operations needed to implement this kind of the control, the so called **Inertial Damping.**

7.1 Top stage: sensors and actuators

The configuration of the sensors and the actuators on the top stage is shown in Fig. 7.1. With reference to the Fig. 7.1 we see that all horizontal sensors are distributed, in a plane geometry, on the vertices of an equilateral triangle (120 degrees between each to other), while the vertical sensors are set on the crossbar of the Filter0. On the top stage we have the following devices: position sensors (LVDT) [1], accelerometers (ACC) and coil-magnet actuators (COIL).

7.1.1 Electronics and software

The signals provided from all these devices installed along the Superattenuator are processed and manipulated through high performant electronic boards and a user friendly software. All electronic components, have been developed at INFN Pisa laboratory to implement the SA active control system. The electronics includes the sensors read-out, the actuators drivers, the ADC-DSP-DAC boards and the software system DSP board (Digital Signal Processor).

[1] In the case of the IP the primary winding is rigidly connected to the top stage, while the secondary winding is clamped on the external safety frame, meant as reference. Thus the LVDT measures the relative displacement of the IP with respect to a reference frame which *is not seismic noise free*.

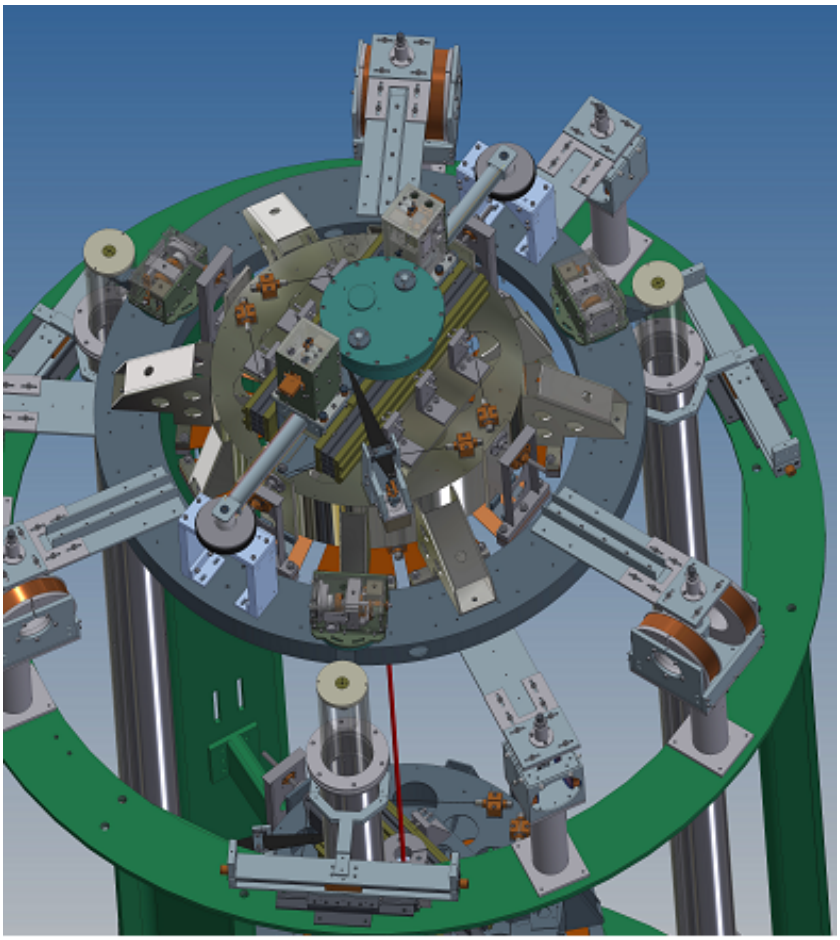

Figure 7.1: Sensors and actuators configuration on the Top stage

The new version of DSP board is UDSPT Board (projected and developed by by INFN Pisa electronic group). The new board which hat mainly includes a powerful DSP, analog-to-digital and digital-to-analog converters have been developed, with a Field Programmable Gate Array (FPGA) that allows these devices to communicate each other and with all the other boards of the experiment. The chosen DSP is a Texas Instruments TMS320C6678, an eight-core fixed and floating point digital signal processor based on KeyStone Architecture, that can run at a core speed up to 1.4 GHz, executing 6 double precision floating point operations per cycle per core, corresponding to a total computing power of 8.4 GFLPOS per core for double precision floating point. For analog-to-digital conversion is used an Analog Devices AD7760. AD7760 is a high performance, 24-bit – ADC that can work up to 4 MSPS. All signals generated by SA sensors are amplitude modulated, with a modulation frequency ranging from 10 kHz up to 50 kHz. The ADC will sample at high rate for then producing a decimated output. The minimum time delay that will be introduced by the ADC is 1.5 μs with an output data rate of 4MHz. The

device used as DAC is Analog Device AD1955. AD1955 is a high performance 2-channel DAC. It includes a multibit − modulator, high performance digital interpolation filters, and continuous-time differential current output DACs.

The DSP is programmed using its assembler language. A user friendly software (**Damping**) has been realized by INFN Pisa electronic group. This software allows to implement the filters by using a client unit, by means of a list of simple instructions containing all information and parameters such as: the ADC channels addresses (for the input signal), the addresses of the DAC channels (for the output signals), the poles and zeroes of the implemented filters and the operation to perform on the variables (linear combinations, mixing, etc.).

Using the Damping software all the logical operations on the signals are very easy and can be implemented using a client unit (computer). As an example, in figures 7.2 and 7.3we show how the software interface is presented to an user.

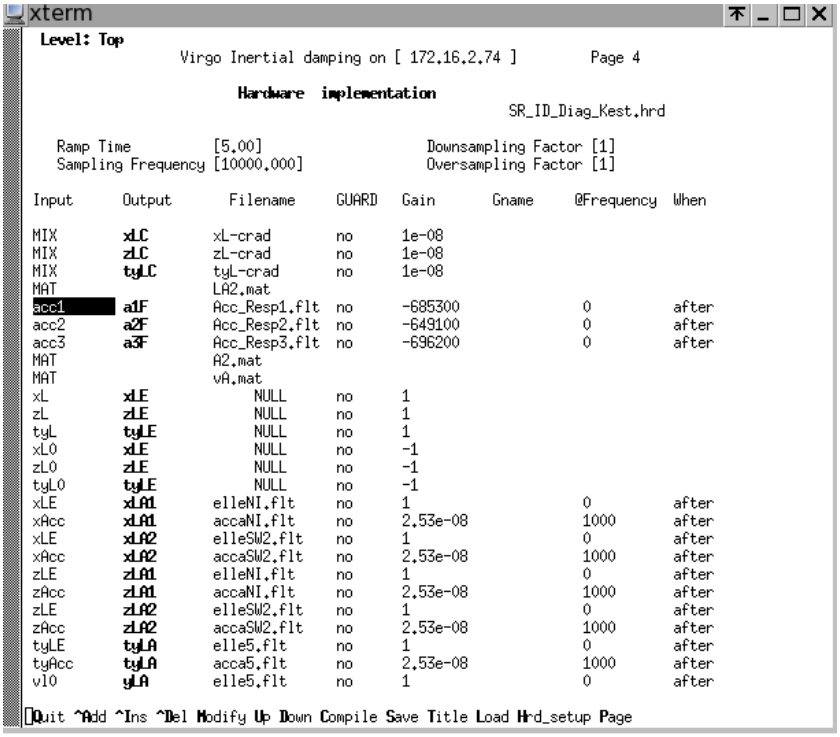

Figure 7.2: User interface of the DSP software: this program is used to implement the active mode dampig control on the AdV suspension top stage. Starting from left to right we have the column of the input signals, the column of the output signals, the digital filters involved in the implementation of this control.

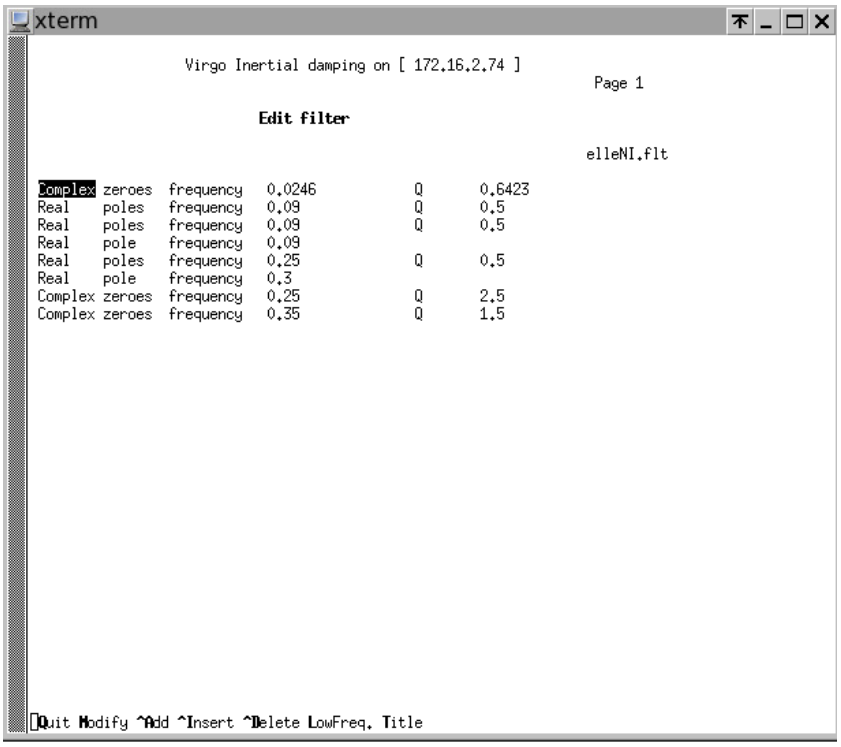

Figure 7.3: Example of implementation of low pass filter.

7.2 Accelerometer

The accelerometer is a devices that measures proper acceleration. Looking inside the box (see Fig. 7.4) it consist of a mass suspended by two Maraging blades in order to form an inverted pendulum [13]. A Linear Variable Differential Transformer (LVDT) displacement sensor measures the position of the mass with respect to the external aluminum structure. Finally, there is a coil-magnet actuator to apply an arbitrary force to the suspended mass. The dynamics of the mass inside the accelerometer is described by a differential equation.

If we call x the position of the pendulum and x_0 the position of the box, with respect to an inertial frame or reference, the equation of motion of the pendulum inside the accelerometer is that of a driven damped harmonic oscillator in one dimension, in Fourier transform is

$$m\omega^2\tilde{x}(\omega) + \gamma\omega(\tilde{x}(\omega) - \tilde{x}_0(\omega)) + \tilde{K}(\tilde{x}(\omega) - \tilde{x}_0(\omega)) = \tilde{F}(\omega) \tag{7.1}$$

where m is the mass of the pendulum, γ is the viscous damping coefficient, k is the elastic constant and F is an external force applied to the mass.

Since the LVDT position sensor in the accelerometer measures the internal position $\tilde{x}(\omega) -$

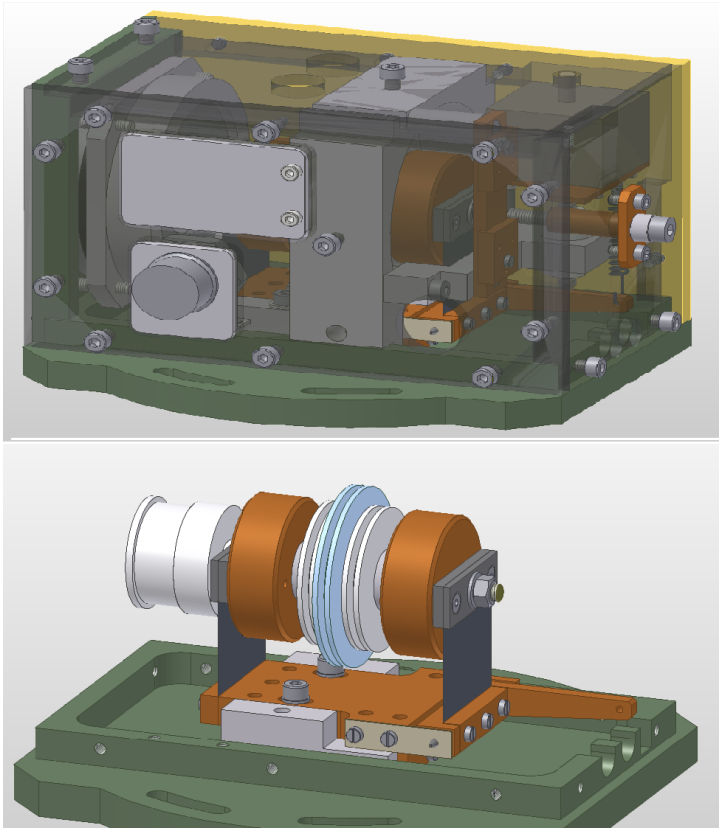

Figure 7.4: AutoCAD project of Virgo horizontal accelerometer. Insight of the most important components of Virgo horizontal accelerometer. At the center is clearly visible inverted pendulum, with the supports for LVDT primary and two secondary coils. The primary coil is attached to the external support, while the secondary coils are fixed to the pendulum. On the left, the coil support for the feedback force. [13]

$\tilde{x}_0(\omega)$, the transfer function between $\tilde{x}_0$ and the position read by the LVDT is

$$TF(\omega): \frac{\tilde{x}(\omega)-\tilde{x}_0(\omega)}{\tilde{x}_0(\omega)} = \frac{\omega^2}{\omega^2+\frac{\omega\omega_0}{Q}+\omega_0^2} \tag{7.2}$$

In figure 9.4, the transfer function expressed by Eq. (7.2) is shown. In this plot we can see that the sensor response $\tilde{x}(\omega)-\tilde{x}_0(\omega)$ is proportional to $\omega^2\tilde{x}_0$, when $\omega \ll \omega_0$. Then only in this frequency domain the signal of the our sensor is an acceleration.

7.3 Accelerometer feedback

The accelerometer has a linear range of at most $0.5\,mm$ around the central position, and to be sure that the pendulum does not leave this region we must add a feedback force.

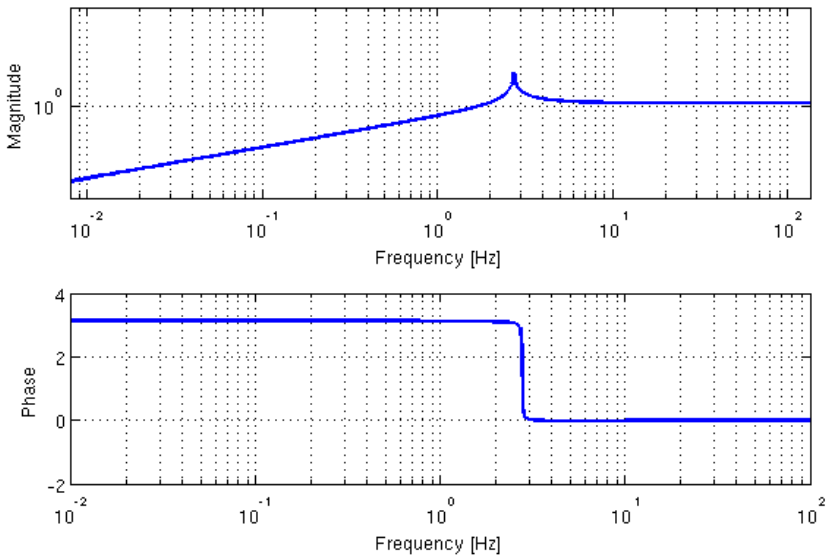

Figure 7.5: Bode diagram of transfer function 7.2, with $\omega_0 = 2\pi \cdot 3Hz$ and $Q = 100$

When the input is a force, in the particular case the force is function of the system output, we get a feedback control. In our case, being the output of the system $\tilde{x}(\omega) - \tilde{x}_0(\omega)$, the external feedback force $\tilde{F}_{feed}(\omega)$ is described by a function

$$\tilde{F}_{feed}(\omega) \approx C(\omega) \cdot [\tilde{x}(\omega) - \tilde{x}_0(\omega)] \tag{7.3}$$

where $C(\omega)$ is the controller.

In Virgo/Virgo+, the sensing element of the accelerometer were controlled by a dedicated PID-based on analogic board. A PID controller [43, 47] (PID stands for Proportional-Integral-Derivative controller) is described by this transfer function

$$C = K_p + \frac{K_i}{\omega} + K_d \omega \tag{7.4}$$

First term (proportional) depends on the present error e , the second K_i (integral) on the accumulation of past errors, and the last one K_d (derivative) is a prediction of future errors. The PID-based controller forced the pendulum to the zero-position, in a certain bandwidth: to do this, it applied a feedback force proportional to its acceleration and could be read as the voltage sent to the actuator coil.

The feedback force $\tilde{F}_{feed}(\omega)$ at frequencies $f < 50Hz$ is proportional to ω^2 and was taken as output of the system. The acceleration signal was deduced from equation (7.3) in this way

$$\tilde{A}(\omega) \approx c \cdot \tilde{F}_{feed}(\omega) \tag{7.5}$$

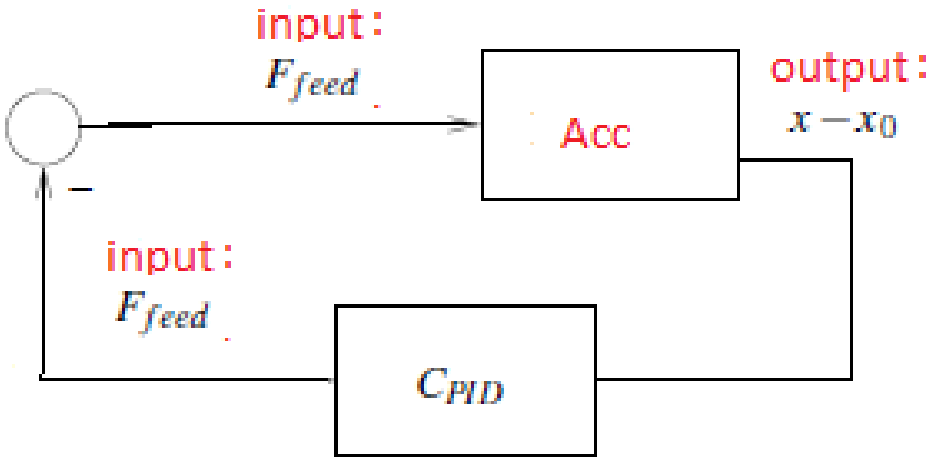

Figure 7.6: Scheme of the accelerometer feedback control used in Virgo/Virgo+. Starting from the Acc block the error signal $x - x_0$ go in to controller box (C_{PID}) that calibrate the feedback force F_{feed} to put the pendulum to the zero-position. This force was at frequencies $f < 50Hz$ is proportional to ω^2 and was taken as output of the system.

where c is a calibration factor to convert the feedback force in acceleration. In figure 7.6 the scheme of the accelerometer feedback control used in Virgo/Virgo+ is reported.

After the big improvement done on the development of the new electronic boards, the INFN Pisa group has also developed and built the electronic board to implement in digital way the feedback control of the accelerometers. For this reason the accelerometer feedback controls are now designed using the optimal control approach.

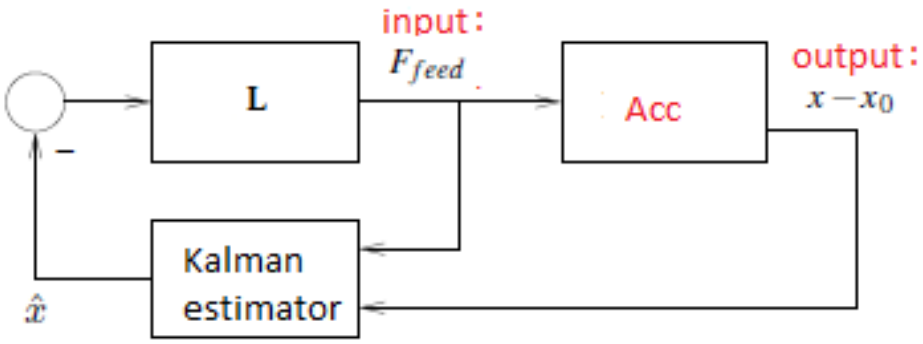

Figure 7.7: Scheme of the accelerometer feedback control used in AdV. Starting from the Acc block the error signal $x - x_0$ go in to estimator box whose output is an estimation of state variable $\hat{x}$. The estimated signal became the input of the LQG controller (box L) that calibrate the feedback force F_{feed} to damp the proper mode of the pendulum and put it to the zero-position. The output signal $x - x_0$ is proportional to acceleration only when $\omega < \omega_0$, that is ~ 3 Hz.

In figure 7.7 a simplified scheme of the this accelerometer feedback control used in AdV

is reported. The Kalman filter and LQG control topic will be discussed in greater detail in Chapter 9. The Design of the accelerometer control with the Kalman filter and LQG optimal control approach, involves that the output signal $\tilde{x}(\omega) - \tilde{x}_0(\omega)$ is proportional to acceleration only when $\omega < \omega_0$, that is ~ 3 Hz (see Fig.7.8). In Fig. 7.8, the open and closed loop for the sensing element of accelerometer box are shown.

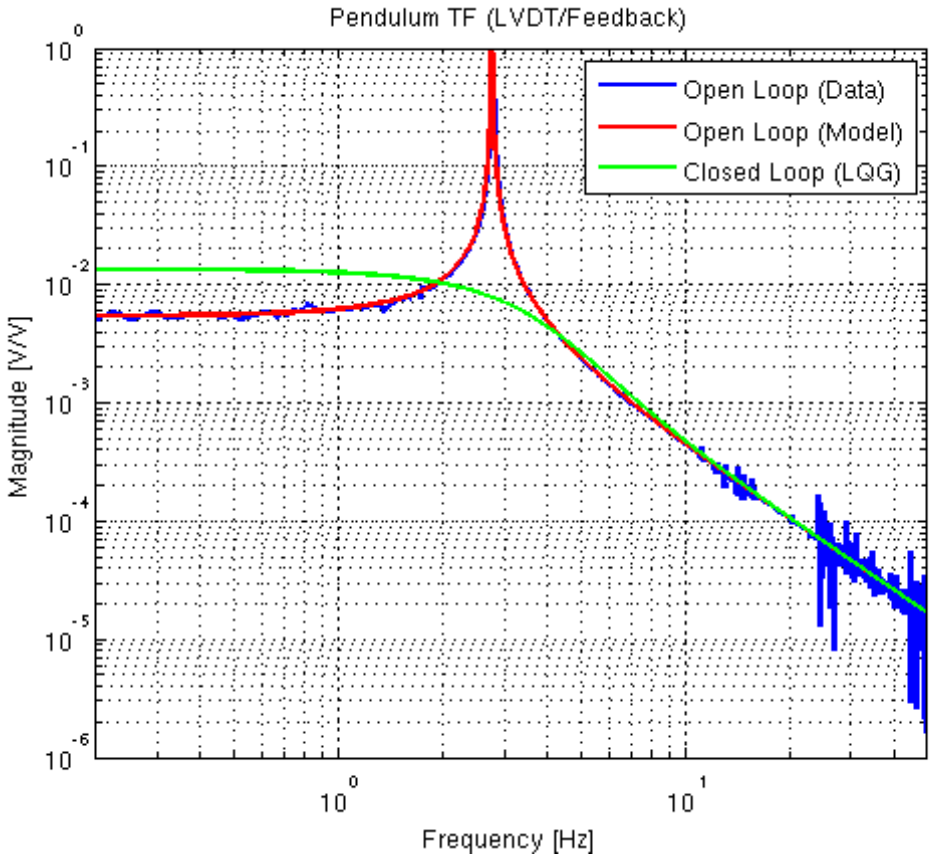

Figure 7.8: Comparison between open loop transfer function response and closed loop transfer function response with LQG controller of the AdV Virgo sensing element of the accelerometer box.

In figure 7.9, the transfer function of the analogic PID controller and LQG controller are shown.

In order to have an acceleration signal until $f \sim 50Hz$ (like that one used in Virgo and Virgo+) , we must calibrate the output response using a proper calibration filter $\tilde{T}_{cal}(\omega)$, one for each accelerometer. The shape of these filters was obtained by fitting the measured transfer function displacement-acceleration between the top stage displacement provided from the LVDT and accelerometers outputs (see Tab. 7.1):

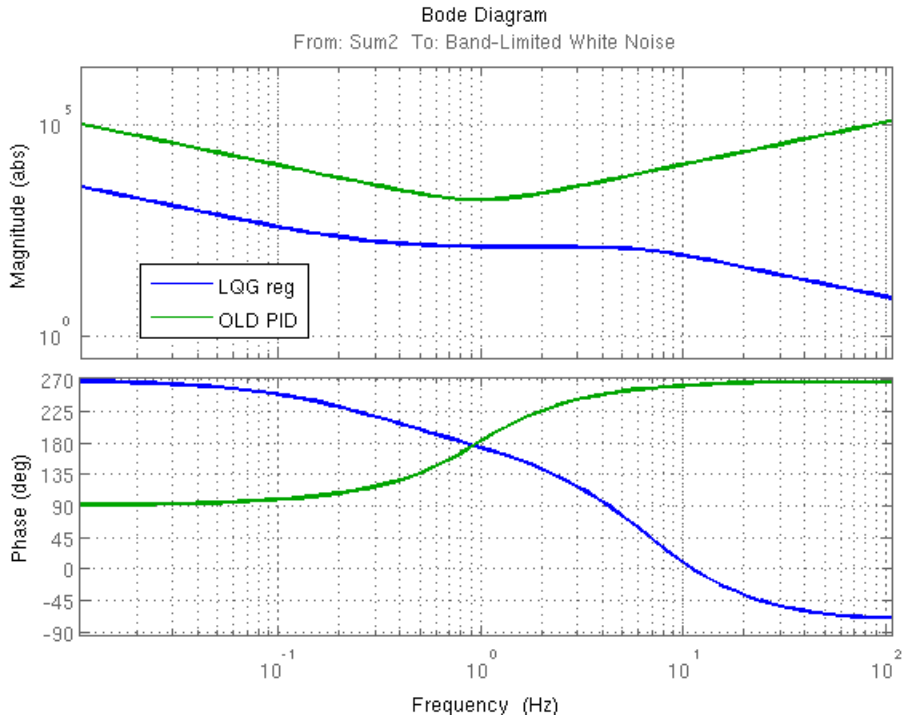

Figure 7.9: Comparison between PID controller (Virgo) and LQG controller (AdV) used to keep in feedback the sensing element of the accelerometer box.

H	V
input: s_{ty}	input: s_y
output: $[A_{H1}, A_{H2}A_{H3}]$	outputs: $[A_{V1}, A_{V2}]$

Table 7.1: Inputs and outputs used to measure the filter $\tilde{T}_{cal}(\omega)$. First column refer to the horizontal devices (H): the input is the signal provided from the diagonalized LVDT s_{ty} and the outputs are the three horizontal accelerometers. Second column refer to the vertical devices (V): the input is the signal provided from the diagonalized LVDT s_y and the outputs are the two vertical accelerometers.

This kind of transfer function can be modeled with a zero-pole model , like that shown in the Tab.7.2.

f	Q	P or Z
2.75	0.75	Z
3.2	0	Z
15	0	P
100	0.5	P

Table 7.2: Example of he calibration filter $\tilde{T}_{cal}(\omega)$ used to restore the acceleration response until $f < 100Hz$.

The implementation of this filter allows us to restore the acceleration response until $f < 100Hz$:

$$\tilde{A}'_j(\omega) \approx \tilde{A}_j(\omega) \cdot \tilde{T}_{cal}(\omega) \;\; j = [H1, H2, H3, V1, V2] \tag{7.6}$$

The first zero (see Tab.7.2), related to the damping of the mechanical resonance of the sensing mass, is different for all accelerometers and then the calibration filter changes according to the system. On all superattenuators, there are fifty accelerometers installed and in the contest of the commissioning of superattenuator the following works where done considering those devices:

-Kalman filters and LQG control design and its implementation in the DSP;

-measure, modeling and implementation in the DSP of the all digital filters like that shown in table Tab.7.2;

-computation of the accelerometer noise budget.

7.3.1 Accelerometer noise budget

To compute the control noise of the accelerometer box we must consider the *sensing noise* $S_N(\omega)$ (of the sensing element) and the *acting noise* $D_N(\omega)$ (of the actuator), respectively

$$\begin{aligned} S_N(\omega) &= s(\omega) \cdot \tfrac{\tilde{F}(\omega)}{\tilde{x}(\omega)} \\ D_N(\omega) &= d(\omega) \cdot TF_{coil}(\omega) \end{aligned} \tag{7.7}$$

Where $\frac{\tilde{F}(\omega)}{\tilde{x}(\omega)}$ is the transfer function between feedback force and displacement (of the sensing element), $TF_{coil}(\omega)$ is the transfer function between the actuator and displacement of the

sensing element (see Fig 7.10) while $s(\omega)$ and $d(\omega)$ have the following form

$$\begin{aligned} s(\omega \ll \omega_0) &= (35 \cdot \sqrt{2}) \times 10^{-9} \frac{m/s^2}{\sqrt{Hz \cdot 2\pi}} \\ d(\omega) &= \sqrt{(1.4 \times 10^{-7})^2 + (21 \times 0^{-6})^2 \cdot \frac{1}{\omega}} \ \frac{nV}{\sqrt{Hz \cdot 2\pi}} \end{aligned} \tag{7.8}$$

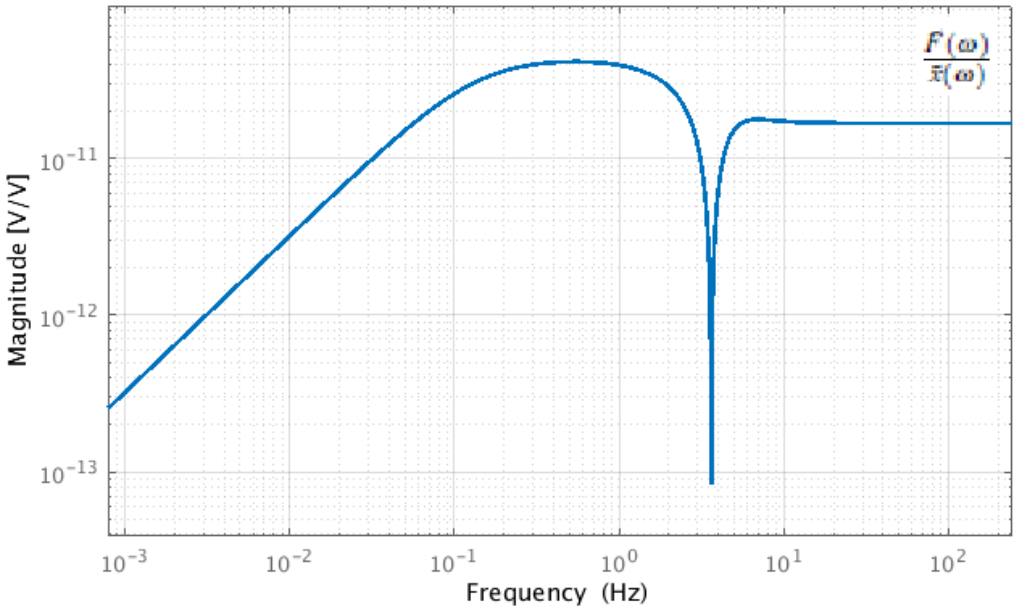

Figure 7.10: Example of the transfer functions $\frac{\tilde{F}(\omega)}{\tilde{x}(\omega)}$ of the horizontal accelerometer.

Using the results expressed in Eq (7.7), the control noise for each accelerometer can be written as

$$\tilde{N}_A(\omega) = \sqrt{S_N(\omega)^2 + D_N(\omega)^2} \tag{7.9}$$

In figure 7.12 the typical sensing (blue curve), acting (red curve) and $\tilde{N}_A(\omega)$ (black curve) contributions are reported.

In order to produce a good estimation of the noise for each accelerometer working on the top stage, also the noise $\tilde{N}_A(\omega)$ is re calibrated through the filter $\tilde{T}_{cal}(\omega)$. After these preliminary operations, the accelerometers can be diagonalized in the Virgo reference frame. In the next section we will see how to diagonalize the sensors and estimate the noise budget of the diagonalized sensors.

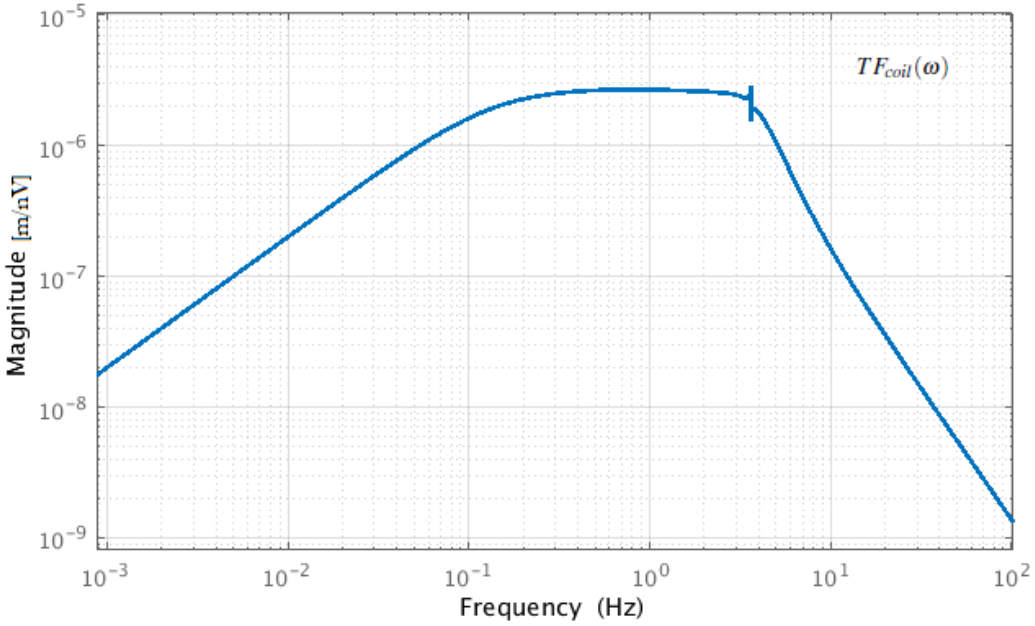

Figure 7.11: Example of the transfer functions $TF_{coil}(\omega)$ of the horizontal accelerometer.

7.3.2 From the sensors reference frame to the VIRGO reference frame

To implement an effective control strategy we must do another important and not trivial choice: the reference frame. Since we are on the Earth, in a limited range of frequency the LVDTs are affected by the seismic noise. Thus if we want to reduce its contamination level on the signals and to do an active damping control we must find a reference frame in which this noise source is well distinguishable. A satisfactory reference frame is the **VIRGO Reference Frame (VRF)**[2]**:**

$$VRF: \begin{cases} \overrightarrow{x}: & EST \\ \overrightarrow{y}: & VERTICAL \\ \overrightarrow{z}: & NORTH \end{cases} \tag{7.10}$$

The choice to work in the VRF has several advantages: the components (x,z,y) of seismic noise are longitudinal along VRF and uncorrelated to each other, the angular seismic contribution is low and the seismic noise contribution of all superattenuator is the same. By applying a suitable transformation matrix **R** on the sensors (sensing matrix) and actuators (driving matrix) we can

[2] In this reference frame the yaw (t_y) is torsion along vertical axis.

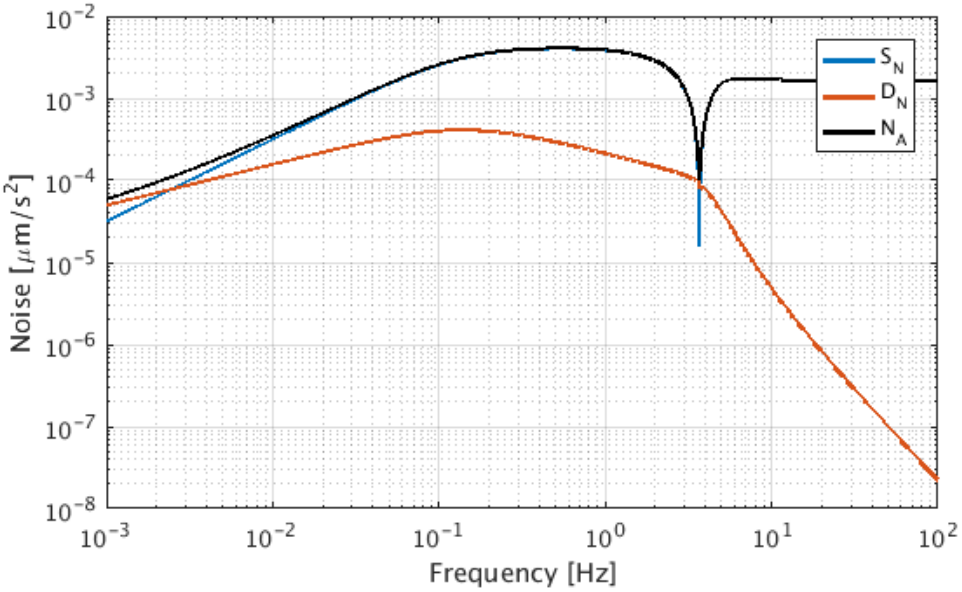

Figure 7.12: Noise budget estimation of the accelerometer feedback control. In this plot the typical sensing (blue curve), acting (red curve) and $\tilde{N}_A(\omega)$ (black curve) contributions of the horizontal accelerometer are shown.

work in the VRF with the new sets of sensors and actuators that are: diagonalized and virtual[3]. By denoting with **S** and **A** the sensing matrices for the LVDTs and accelerometers, and with **D** the driving matrix for the actuators, the horizontal diagonalized sensors and actuators in the VRF are computed as

$$\begin{pmatrix} s_x \\ s_z \\ s_{ty} \end{pmatrix} = \begin{pmatrix} s_{11} & s_{12} & s_{13} \\ s_{21} & s_{22} & s_{23} \\ s_{31} & s_{32} & s_{33} \end{pmatrix} \begin{pmatrix} L_{H_1} \\ L_{H_2} \\ L_{H_3} \end{pmatrix} \tag{7.11}$$

$$\begin{pmatrix} A_x \\ A_z \\ A_{ty} \end{pmatrix} = \begin{pmatrix} a_{11} & a_{12} & a_{13} \\ a_{21} & a_{22} & a_{23} \\ a_{31} & a_{32} & a_{33} \end{pmatrix} \begin{pmatrix} A_{H_1} \\ A_{H_2} \\ A_{H_3} \end{pmatrix} \tag{7.12}$$

[3]To produce the the sensing and driving matrix for accelerometers and actuators we inject a line a 3 Hz. For the driving matrix we inject this line from a single coil and we measure the response of the displacement sensors; in this way we build a matrix with 9 coefficients and its inverse is the driving matrix. The sensing matrix of the accelerometer is build in a similar way: in this case the line is inject from the diagonalized coils and the coefficients of the matrix are measured looking the response of each accelerometer. Also in this case the inverse of this matrix is the accelerometers sensing matrix.

$$\begin{pmatrix} C_x \\ C_z \\ C_{ty} \end{pmatrix} = \begin{pmatrix} d_{11} & d_{12} & d_{13} \\ d_{21} & d_{22} & d_{23} \\ d_{31} & d_{32} & d_{33} \end{pmatrix} \begin{pmatrix} C_{H_1} \\ C_{H_2} \\ C_{H_3} \end{pmatrix} \tag{7.13}$$

Where the components of the vectors $(L_{H_1}, L_{H_2}, L_{H_3})$, $(A_{H_1}, A_{H_2}, A_{H_3})$ and $(C_{H_1}, C_{H_2}, C_{H_3})$ are the LVDTs, the accelerometers and actuators before the diagonalization, while the components of the vectors (s_x, s_z, s_{ty}), (A_x, A_z, A_{ty}) and (C_x, C_z, C_{ty}) are the LVDTs, the accelerometers and actuators after the diagonalization. Therefore, in VRF, the output signals of an LVDT $s_{iL}(t)$ and an accelerometer $a_{iA}(t)$ along the $i-th$ direction can be written as

$$s_{iL}(t) = s_i(t) - s_{iLs}(t) + n_{iLe}(t) \;\; (i, = z, x, t_y) \tag{7.14}$$

$$a_{iA}(t) = a_i(t) - g\theta_j(t) + n_{iAe}(t) \;\; (i, = z, x \;\; , \; j = x, z) \tag{7.15}$$

In the case of the vertical d.o.f. , the diagonalization is simplified because we have one LVDT, two accelerometers and actuators. The sensing and driving matrices of the accelerometers and the actuators are a 2×2 matrix with similar coefficients. In this case the output signals, for the LVDT and the accelerometer, are equal to

$$s_{yL}(t) = s_y(t) - s_{yLs}(t) + n_{yLe}(t) \tag{7.16}$$

$$a_{yA}(t) = a_y(t) + n_{yAe}(t); \;\; a_y(t) = \frac{A'_{V_1}(t) + A'_{V_2}(t)}{2} \tag{7.17}$$

The additional terms $s_{iLs}(t)$,$n_{iLe}(t)$, $g\theta_j(t)$, $n_{iAe}(t)$ that appear in Eq. (7.14),(7.15), (7.13) and (7.17) are the main sources of noise for these kind of devices.

7.4 Noise budget of the diagonalized sensors

The *noise budget* of a sensors, is the estimation of the contamination level due to the noise sources. The equations (7.14),(7.15), (7.13) and (7.17) are written in such way that the main sources of noise for the used devices appear. These sources of noise can classified as: *process noise* (characterized by random phenomena that disturb the behavior of the system) and the *measurement noise* (the intrinsic noise of the sensors). With reference to figure 7.13 we classify as process noise: the seismic contribution $s_{iLs}(t)$ that contaminates the LVDT and the background tilt contribution $g\theta_j(t)$ of the horizontal accelerometer. While, we consider as

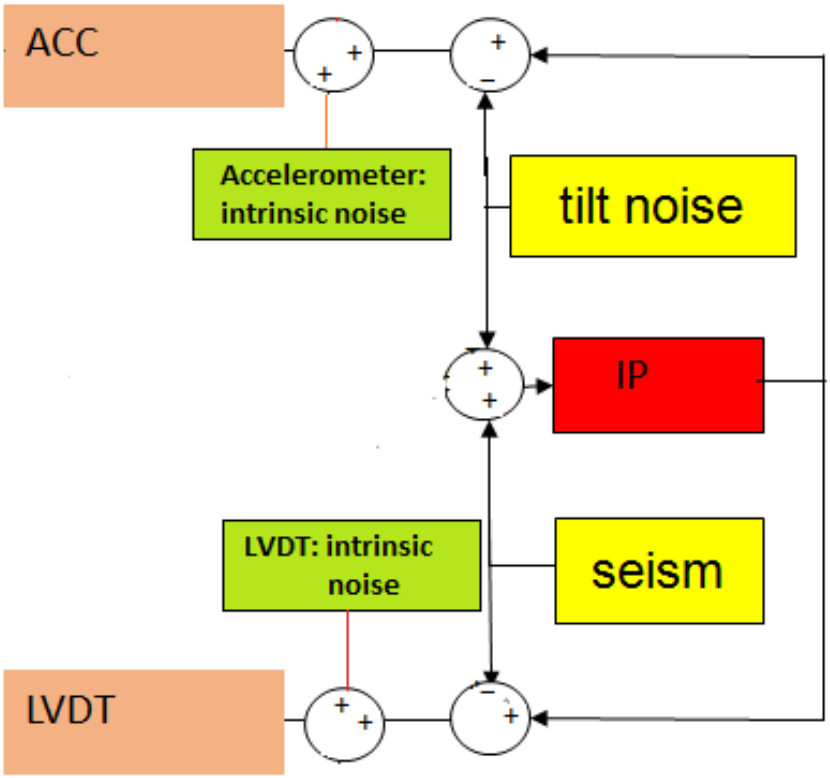

Figure 7.13: Schematic representation of the sources of noise read by the horizontal diagonalized sensors posed on AdV suspension top stage. Starting from the IP (red box), its motion is provided from the LVDT as s_i and by ACC as $\ddot{s}_i$. The ground motion s_{iL_s} (yellow box) gets in the LVDT box: its output can be written as $s_{iL} = s_i - s_{iL_s}$. The 'tilt' $g\theta_j$ (yellow box) gets in the ACC box: its output can be written as $a_i = \ddot{s}_i - g\theta_j$. Considering also the intrinsic noise of the sensors, two outputs become: $s_{iL} = s_i - s_{iL_s} + n_{Le}$, $a_i = \ddot{s}_i - g\theta_j + n_{Ae}$.

measurement noise the intrinsic electronic noise $n_{iLe}(t)$ of the diagonalized LVDT [4] and the intrinsic electronic noise $n_{iAe}(t)$ of the diagonalized accelerometer.

Comparing the signals provided by a sensor and its noise sources we can establish which frequency region of the spectrum is contaminated by these noises and estimate the lower limit of the sensitivity curve of the device. In the Subsection 7.4.1 we report the typical noise budget for one set of diagonalized sensor posed on the top stage. Referring to figure 7.13, the contamination level for all the noise sources considered in this scheme has been estimated by comparing the models (or ASD) with the Amplitude Spectral Density (ASD) [58] of the signals. All analyses have been done when the system was not under control in order to reproduce the configuration plotted in figure 7.13.

[4] Usually this noise is a value given by the manufacturer of the device.

7.4.1 Noise budget: results

We report here four figures showing the experimental results concerning the noise budget. Looking at figures 7.14, 7.15 and 7.16 we observe that: below $100\,mHz$ we are ruled by the sensing noise of the accelerometer while above $100\,mHz$ we are ruled by the sensing noise of the LVDT. Concerning the background disturbance (microseim and tilt) the results are similar. Indeed, the figures 7.18 and 7.17 show us that in the region $0.1 \div 3\,Hz$ the LVDT is contaminated by the seismic noise while in the region $0.01 \div 0.1\,Hz$ the accelerometer is contaminated by the background tilt noise.

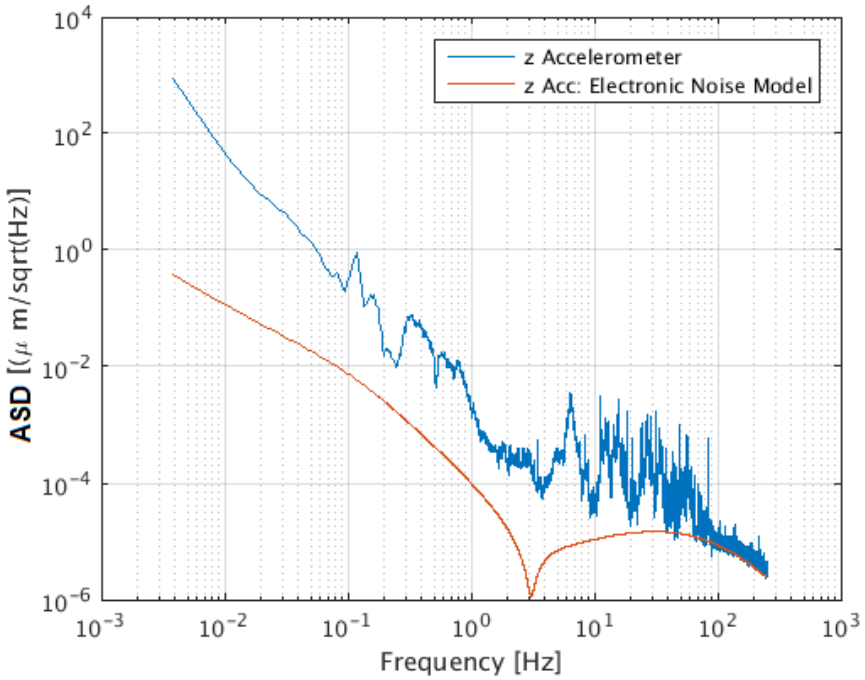

Figure 7.14: Amplitude Spectral Density (ASD) related to the accelerometer signal (blue curve) compared whit its intrinsic noise (red curve).

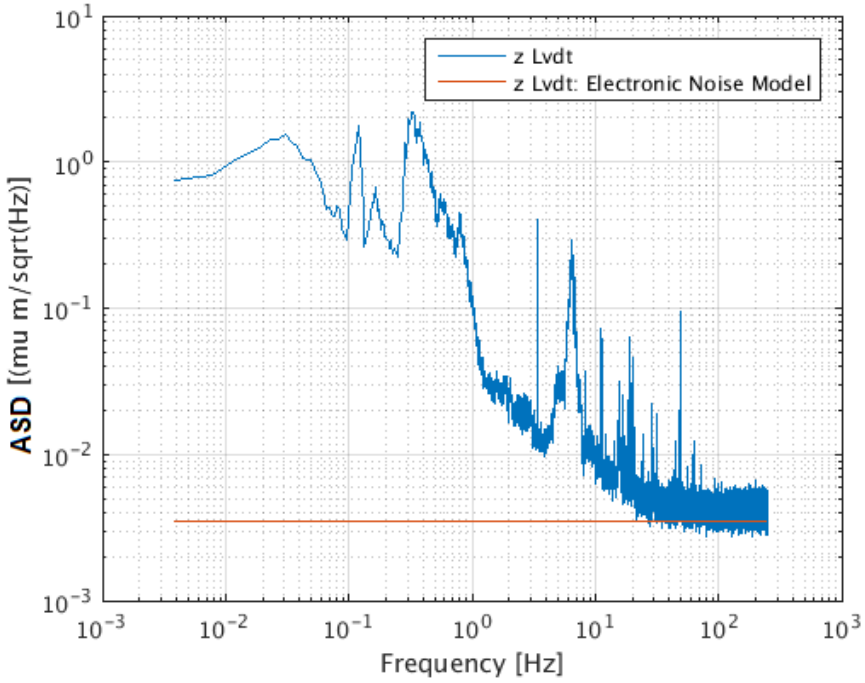

Figure 7.15: Amplitude Spectral Density (ASD) related to the LVDT signal (blue curve) compared whit its intrinsic noise (red line).

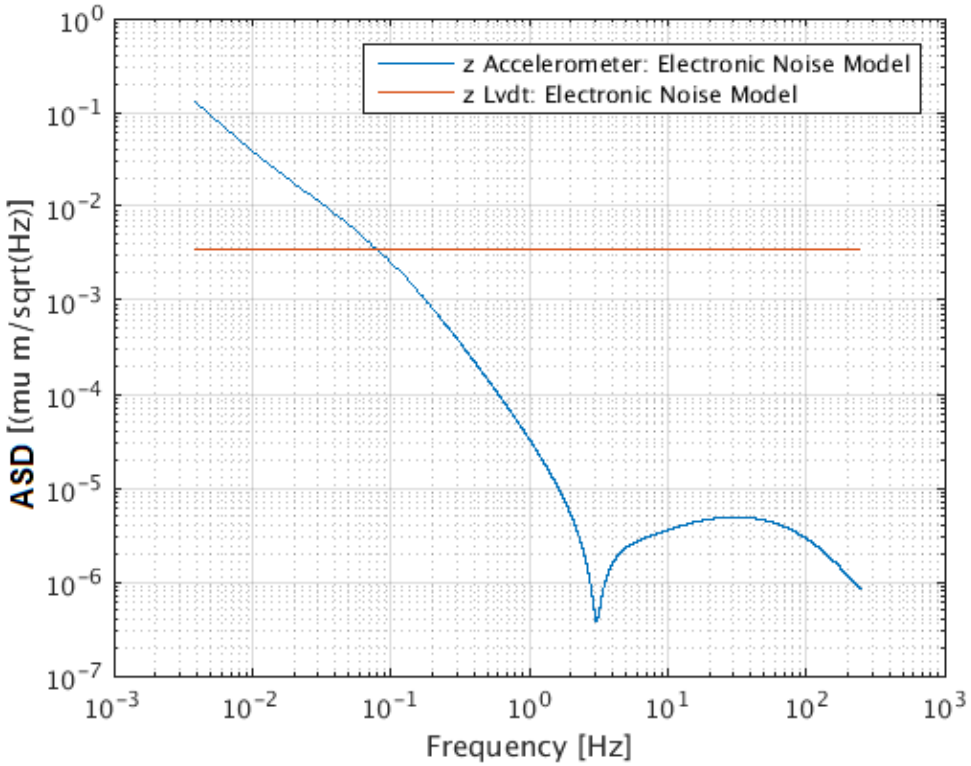

Figure 7.16: Comparison between LVDT (red curve) and accelerometer (blue curve) intrinsic noises.

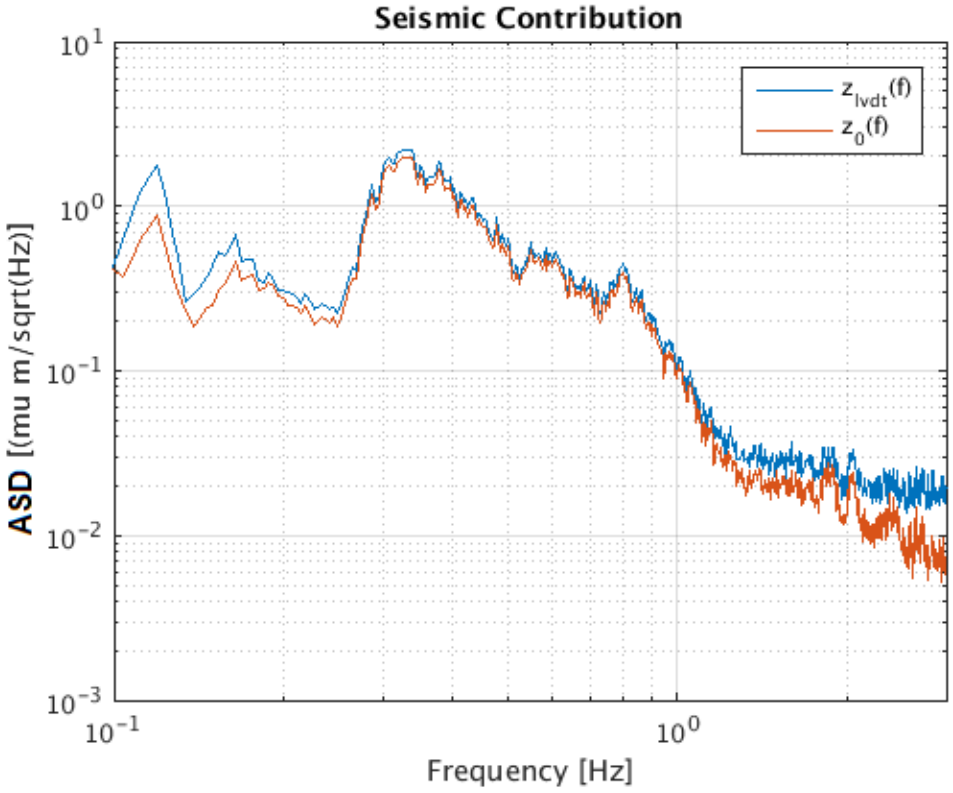

Figure 7.17: Background noise contributions: in figure the comparison between the spectral density of seismic contribution that contaminates the LVDT sensor (clue curve) and that acquired using the external device monitoring the ground vibration (red curve) are reported.

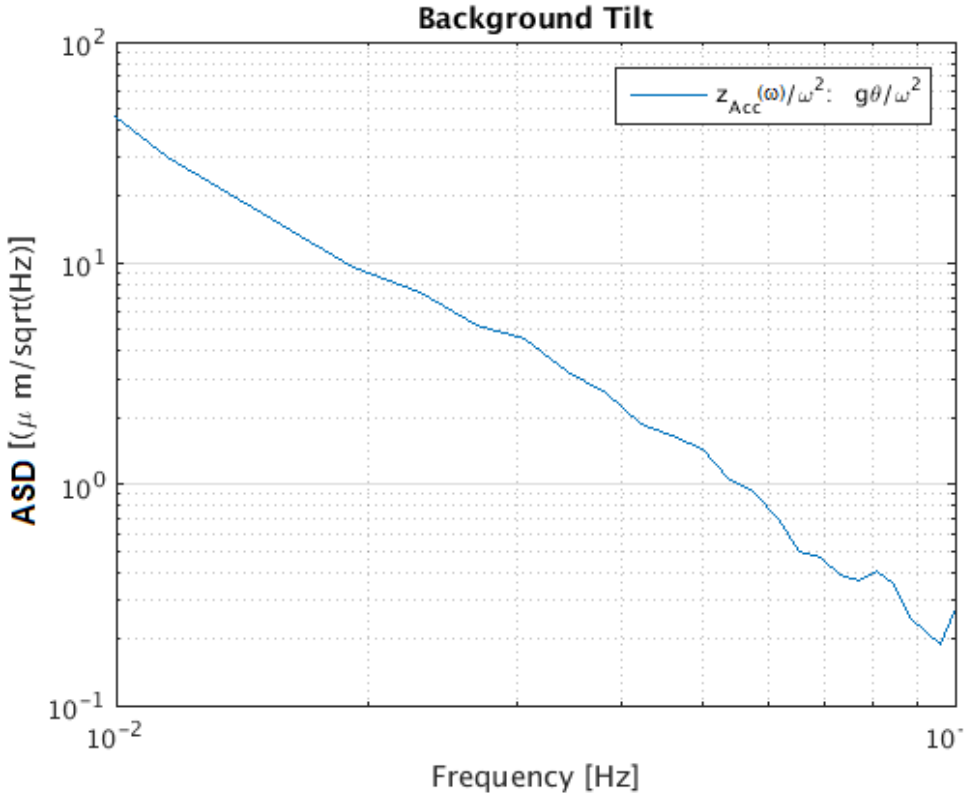

Figure 7.18: Background noise contributions: in figure the comparison between spectral density of he tilt contribution that contaminates the accelerometer signal is reported.

Chapter 8

AdV top stage suspension control

Considering the experimental setup of the sensors and actuators in the VRF, the active mode damping control must be designed to control the position of the top-stage over four d.o.f., and by damping its resonances. Since more than 15 years, Virgo handled this matter by means of blended virtual sensing signals, attained through neutral pre-filtering. The goal of this chapter is to illustrate the performance of the active attenuation reached by using the "**Blending technique**" . It should be specified that the technique is used to control all degrees of freedom on the top stage: horizontals (x, z), torsional (θ_y) and vertical (y). In the next of this chapter the experimental results achieved using this type of control will be illustrated, focusing our discussion on the degree of horizontal d.o.f. [1]

8.1 The Blended Virtual Sensor

In Chapter 7 the noise budget has allowed us to identify which frequency band, for each sensor, does not suffer from its fundamental noises. In particular we have seen that the low frequency signal is clean on the LVDT, while after the $100\,mHz$ the good signal is that of the accelerometer. In order to take the best signal component provided by the two sensors, in VIRGO and also in AdV the sensors are 'blended' through a neutral pre-filtering applying a Low Pass filter (LP) on the LVDT signal and an High Pass filter (HP) on the accelerometer signal.

In this way we obtain a "new sensor" called: *blended virtual sensor* defined as

$$\tilde{S}_{iv}(\omega) = \tilde{LP}(\omega) \cdot \tilde{s}_{iL}(\omega) - \omega^{-2} \cdot \tilde{HP}(\omega) \cdot \tilde{a}_{iA}(\omega) \tag{8.1}$$

where $\tilde{s}_{iL}(\omega)$ and $\tilde{a}_{iA}(\omega)$ are the Fourier transforms [1] of the signals expressed by Eq.(7.14) and (7.14) respectively. The neutral blended pre-filters are calculated starting from n- order

[1] A more detailed description of the basics of linear feed-back systems can be found for example in [43, 47, 60].

polynomial:

$$P_n(\omega) = a_n \cdot \omega^n + a_{n-1} \cdot \omega^{n-1} + \cdots + a_0 \tag{8.2}$$

By Imposing that $HP + LP = 1$, the LP filter must be shaped taking into account the background disturbance and its typical cutoff must be below $100\,mHz$, the deduced couple of low pass and high pass filters is

$$\tilde{LP}(\omega) = \frac{p_{n-2}(\omega)}{P_n(\omega)}; \quad \tilde{HP}(\omega) = \frac{\omega^3 p_{n-3}(\omega)}{P_n(\omega)}; \tag{8.3}$$

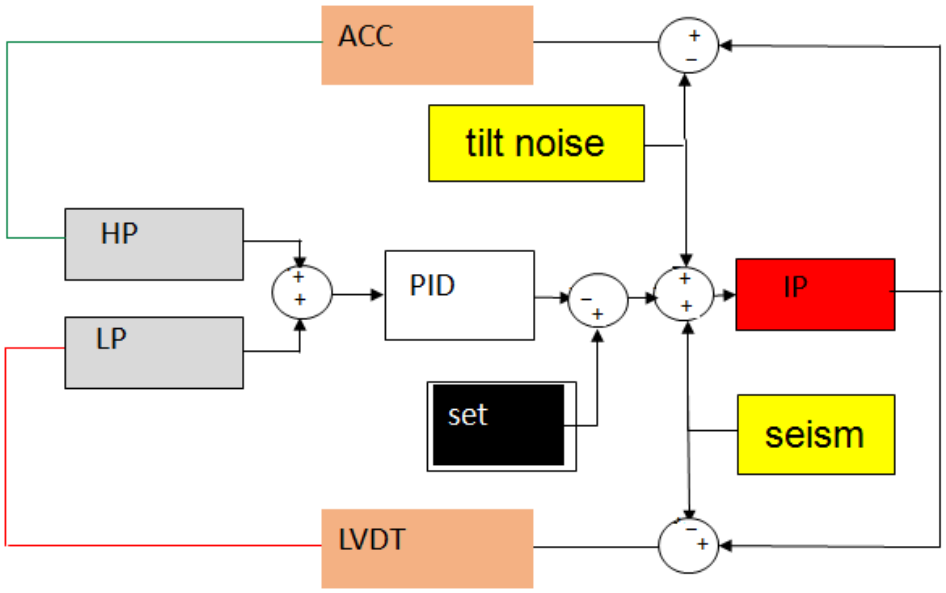

Figure 8.1: Block diagram of the blended virtual sensor in closed loop configuration. Starting from the IP (red box), its motion is provided from the LVDT as displacement s_i and by ACC as $\ddot{s}_i$. The ground motion s_{iL_s} (yellow box) , gets in the LVDT box and its output can be written as $s_{iL} = s_i - s_{iL_s}$. The 'tilt' $g\theta_j$ (yellow box) gets in the ACC box and its output can be written as $a_i = \ddot{s}_i - g\theta_j$. Considering also the intrinsic noise of the sensors, two outputs become: $s_{iL} = s_i - s_{iL_s} + n_{Le}$, $a_i = \ddot{s}_i - g\theta_j + n_{Ae}$. The LVDT is filtered through a low pass filter (LP box) and the ACC signal is filtered through a high pass filter (HP box). After the filtering, the cleaned signals are 'summed' and the result of this operation is given as input at the controller C_i(PID box). The controller apply a viscous force to damp the inner modes of the system and keep it in a set reference value s_{set} (set box) minimizing the error signal $e \sim s_i - s_{set}$.

Referring to figure the 8.1 , after the pre-filtering, the blended the signal $\tilde{S}_{iv}(\omega)$ is given as

input to the controller $\tilde{C}_i(\omega)$: the output closed loop signal is equal to [43, 47, 60]

$$\tilde{S}_{iv}^{CL}(\omega) = \frac{\tilde{S}_{iv}(\omega)}{1 - \tilde{M}_i(\omega) \cdot \tilde{C}_i(\omega)} \tag{8.4}$$

Where $\tilde{M}_i(\omega)$ and $\tilde{C}_i(\omega)$ are the mechanical plant of IP system and the filter control related to the $i-th$ d.o.f. [2]

At present this kind of strategy is implemented on all d.o.f of the stage and in Fig. 8.2 and 8.3 the experimental plants (horizontal and vertical) of the four superattenuators accommodated along Fabry-Perot cavities are shown.

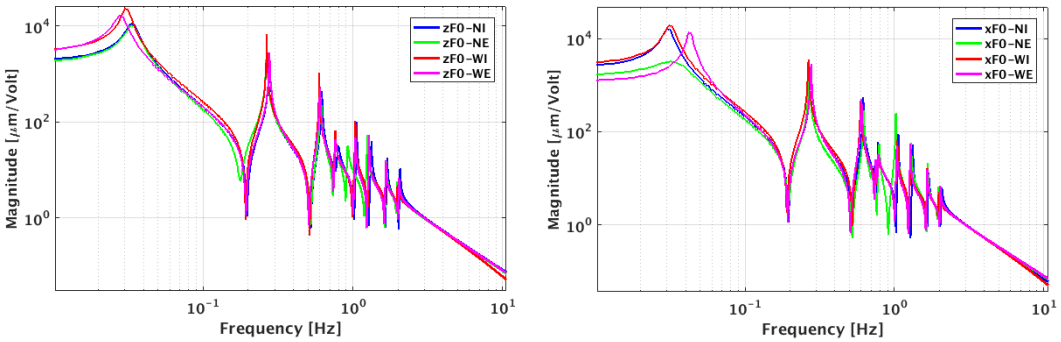

Figure 8.2: Experimental plant related to$z$ d.o.f (on the left) x d.o.f (on the right) of inverted pendulum accommodated along Fabry-Perot cavities are shown. We can see that all resonances are confined below $3\,Hz$ and that the inverted pendulum have a proper resonance about at $30\,mHz$.

8.2 Blending strategy

The starting point of the blending strategy is the calculation of the pre-filters (Low Pass filter (LP) and High Pass filter (HP)) by using the formula (8.3). In figures 8.4 and 8.5, an example of blended strategy implemented on the system and the respective virtual sensor closed loop (when a controller like that reported in the table 8.1 is used) are shown. With reference to Fig. 8.4 we observe that the LP filter is shaped in order to lower the seismic noise in the region$0.25 \div 0.85\,Hz$ (see Fig.8.4) while by looking at Fig. 8.5 we note an excess of seismic noise in $0.1 \div 1\,Hz$ range. This excess of seismic disturbance, in principle, can be reduced shaping the low pass filter (LP) and tuning the controller gain in order to reach the electronic

[2]The used controllers satisfy all stability criterion reported in the standard books of the control theory [43, 47, 60]. In order to have the signal $\tilde{S}_{iv}(\omega)$ in-phase with the motion of the feed-back suppresses, we have put put a minus sign at the summation point of the PID box [43, 47, 60].

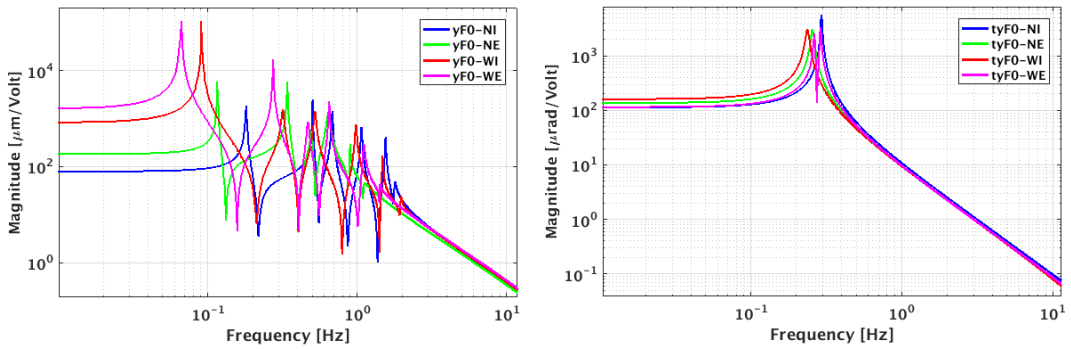

Figure 8.3: Experimental plant related to y (on the left) d.o.f of the chain of pendulum accommodated along Fabry-Perot cavities are shown. We can see that all resonances are confined below $3\,Hz$ and that the first resonance (filter 0 resonances) is localized e about at $100\,mHz$. On the right the experimental plant related to θ_y d.o.f of inverted pendulum accommodated along Fabry-Perot cavities are shown: we can see that the inverted pendulum have a proper resonance about at 300mHz.

noise [3].

Then to best work with the blending strategy it is necessary that a *human mind,* taking into account mutable background conditions (like the wind and the microseism) on the EGO site, shapes the pre-filters by trying to lower the re-injection of the disturbances. In other words we must be able to adapt the control strategy according with the flow of seasons (the changing of background conditions) and mostly to the requirements of the interferometer. This operation is done considering separately two bandwidth regions: above 100 mHz and below 100 mHz. In Sections 8.3 and 8.4 we will show how to achieve this goal.

8.3 Blending strategy: above 100 mHz

In Eq. (8.1) we have been introduce the ***blended virtual sensor*** (**BVS**): it is the used sensor to implement the so called '**Inertial Damping**'. Above the $100\,mHz$, the main source of noise contaminating this sensor, is the seismic noise: therefore to optimize a blending strategy, in the region $0.100 \div 3\,Hz$, we must know how this noise is transmitted to it. For this purpose, the knowledge of the transfer function between the seismic excitation and the BVS is crucial and can be deduced starting from the Eq. (8.1).

With reference to figure 8.6, using a little algebra and the condition $HP + LP = 1$, the BVS

[3]The experience show us that the high frequency peaks that appear , in the region$20 \div 80\,Hz$ (see Fig. 8.5) can be excited when you change the control bandwidth from $3\,Hz$ to $5\,Hz$. In order to stabilize the loop, we add the notches.

f [Hz]	Q	P or Z
0	0	P
0.03	0.5	P
24.605	50	Z
24.605	10	P
26.09	20	P
26.09	200	Z
53.74	10	P
53.74	200	Z
65.52	10	P
65.52	200	Z
77.15	200	Z
77.15	10	P
200	0	P
1000	0	P
G=0.3	f=1 Hz	

Table 8.1: Example of typical filter of control actually implemented along the z direction of NI IP . P means pole, while Z means zero.

output signal can be written as

$$\tilde{S}_{iv}(\omega) = \tilde{s}_i(\omega) - \tilde{LP}(\omega) \cdot \tilde{s}_{iLs}(\omega) \tag{8.5}$$

where $\tilde{s}_i(\omega)$ is the motion of the IP along the $i-th$ d.o.f. and $\tilde{LP}(\omega) \cdot \tilde{s}_{iLs}(\omega)$ is the residual seismic noise affecting the BVS [4].

By considering the Eq. (8.5) we expect that the effective transfer function ($\tilde{T}^{eff}_{s_{iLs} \to S_{iv}}(\omega)$) between the seismic excitation $\tilde{s}_{iLs}(\omega)$ and the displacement of the IP, provided from the BVS, will be

$$\tilde{T}^{eff}_{s_{iLs} \to S_{iv}}(\omega) \approx \tilde{T}_i(\omega) - \tilde{LP}_i(\omega) \tag{8.6}$$

where $\tilde{T}_i(\omega)$ is the mechanical response of the inverted pendulum to the seismic excitation $\tilde{s}_{iLs}(\omega)$ along the $i-th$ direction and $\tilde{LP}(\omega)$ is the applied low pass filter. By using the formula (8.6), we can write the Eq. (8.5) as

$$\tilde{S}_{iv}(\omega) = (\tilde{T}_i(\omega) - \tilde{LP}_i(\omega)) \cdot \tilde{s}_{iLs}(\omega) \tag{8.7}$$

To deduce the effective closed loop transfer function ($\tilde{T}^{eff,CL}_{s_{iLs} \to S_{iv}}(\omega)$) we reproduce the closed

[4] In this equation we not take into account the intrinsic noise of the sensors because, as shown in Fig. 7.14, 7.15 and 7.16 we are not limited from their.

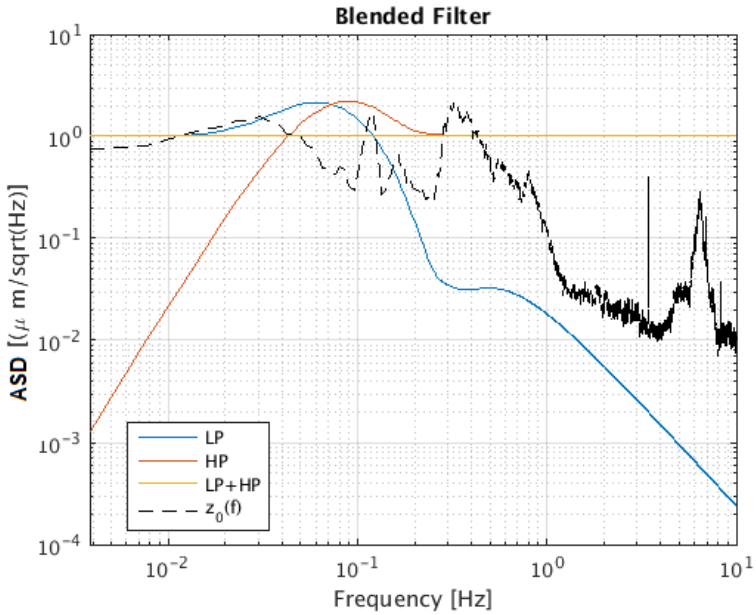

Figure 8.4: Example of neutral prefilter blending with blending frequency at $72\,mHz$. In this plot are reported a couple of low pass filter (blue curve) and high pass filter (red curve) shaped to reduce the typical seismic noise on EGO site (black curve) in the region $0.25 \div 0.85\,Hz$.

loop scheme on the signal expressed by Eq. (8.7) and we compare it with the equation (8.5)

$$\left[\frac{(\tilde{T}_i(\omega) - \tilde{LP}(\omega))}{1 - \tilde{M}_i(\omega)\cdot\tilde{C}_i(\omega)}\right]\cdot\tilde{s}_{iLs}(\omega) = \tilde{s}_i(\omega) - \tilde{LP}(\omega)\cdot\tilde{s}_{iLs}(\omega) \tag{8.8}$$

and by using a little algebra $\tilde{s}_i(\omega)$ can be written as

$$\tilde{s}_i(\omega) = \left[\frac{\tilde{T}_i(\omega)}{1 - \tilde{M}_i(\omega)\cdot\tilde{C}_i(\omega)} - \frac{\tilde{M}_i(\omega)\cdot\tilde{C}_i(\omega)\cdot\tilde{LP}(\omega)}{1 - \tilde{M}_i(\omega)\cdot\tilde{C}_i(\omega)}\right]\cdot\tilde{s}_{iLs}(\omega) \tag{8.9}$$

Looking at Eq.(8.9), we note that $\tilde{T}^{eff,CL}_{s_{iLs}\to S_{iv}}(\omega)$ is composed by a ***mechanical contribution*** $\tilde{A}(\omega)$ and a ***sensing contribution*** $\tilde{B}(\omega)$

$$\begin{gathered}\tilde{A}(\omega) = \frac{\tilde{T}_i(\omega)}{1-\tilde{M}_i(\omega)\cdot\tilde{C}_i(\omega)};\ \ \tilde{B}(\omega) = -\frac{\tilde{M}_i(\omega)\cdot\tilde{C}_i(\omega)\cdot\tilde{LP}(\omega)}{1-\tilde{M}_i(\omega)\cdot\tilde{C}_i(\omega)} \\ \downarrow \\ \tilde{s}_i(\omega) = \left[\tilde{A}(\omega) + \tilde{B}(\omega)\right]\cdot\tilde{s}_{iLs}(\omega)\end{gathered} \tag{8.10}$$

The core of the $\tilde{A}(\omega)$ term are the mechanical response $\tilde{T}_i(\omega)$, the mechanical plant $\tilde{M}_i(\omega)$ and the controller $\tilde{C}_i(\omega)$, while the core of the $\tilde{B}(\omega)$ term is the low pass filter $\tilde{LP}(\omega)$. The results expressed by Eq. (8.10) suggest us that the residual motion ($\tilde{s}_i(\omega)$) of the IP can be reduced by changing the controller gain or the shape of LP. It would seem that we can iterate indefinitely

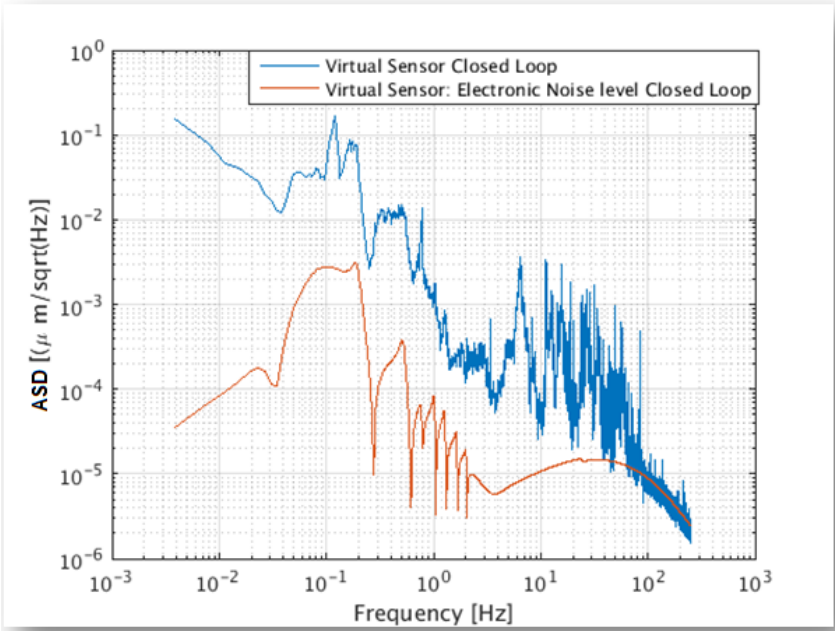

Figure 8.5: Example of the virtual blended closed loop signal compared with its intrinsic electronic noise.

the improvement on the low pass and controller filter, but considering also the intrinsic noises of the used sensors, this is not true: indeed this noise represents the *lower limit* of the device sensitivity.

8.3.1 Above 100 mHz: results

In this subsection, to better understand how reach the intrinsic noise level of the accelerometer we analyze the behavior of the $\tilde{T}^{eff,CL}_{s_{iL_s}\rightarrow S_{iv}}(\omega)$ when different pre-filtering strategy or the gain of the controller are used. The simulations are produced using the MATLAB scripts. In these scripts, changing the shape of the LP or the gain of the controller, is possible to calculate a projection of the power spectral density (PSD) related to the residual motion of the top stage in a specific background noise condition [82]. According to the formula (8.10) and (8.9), to produce these simulations it is necessary to specify: the mechanical plant model $\tilde{M}_i(\omega)$, the mechanical response model $\tilde{T}_i(\omega)$, the controller model $\tilde{C}_i(\omega)$ or its gain G, the low pass filter $\tilde{LP}(\omega)$ as well as the measurement of the seismic contribution $\tilde{s}_{iLs}(\omega)$. The signal $\tilde{s}_{iLs}(\omega)$ can be acquired by using an external device probing the seism at the ground (in our case a Guralp posed in the central or the end building). Preliminary operation, in order to check the goodness of our projection method, is to reproduce the real data (see Fig. 8.7) and comparing it with intrinsic noise of the device (accelerometers). With reference to figure 8.7 we see that:

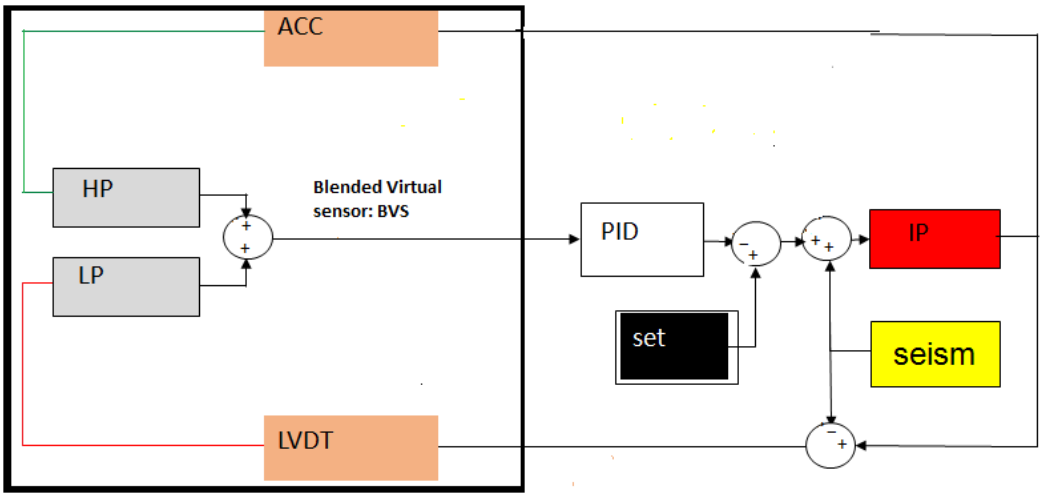

Figure 8.6: Blended virtual sensor in closed loop configuration. Following the block seism (yellow box): this is common to the IP system (red box) and LVDT sensor (pink box). The transfer function between seismic excitation and IP displacement is $\tilde{T}_i(\omega)$. Consequently the Closed Loop transfer function **seism-BVS** for this configuration will be a combination between mechanical attenuation and LP filter: $\tilde{T}^{eff}_{s_{iL_s}\to S_{iv}}(\omega) \approx \tilde{T}_i(\omega) - L\tilde{P}_i(\omega)$.

1. we are able to reproduce the real data;

2. we have still contaminated by the seismic noise;

3. we are far from reaching the intrinsic noise of the sensor (yellow line).

Starting from this point, our goal will be to reach the level of the intrinsic noise (yellow curve). For this purpose, at the first iteration we calculate, without changing the gain (G) of the controller filter, the function $\tilde{T}^{eff,CL}_{s_{iL_s}\to S_{iv}}(\omega)$ when two different couples of blending filters are applied. The selected filters have the blending frequency at $63\,mHz$ (strategy63) and $32\,mHz$ (strategy32) respectively and their shape is reported in Fig. 8.8.

We start by showing the impact of the strategy63 and strategy32 on the function $\tilde{T}^{eff,CL}_{s_{iL_s}\to S_{iv}}(\omega)$ and its components $\tilde{A}(\omega)$ and $\tilde{B}(\omega)$ (see Fig.8.9 and 8.10). We see that changing the pre-filter strategy from strategy63 to strategy32, we have a factor 2 of benefit on PSD on the signal $\tilde{s}_i(\omega)$ express in Eq. (8.10) : this means that we can improve the attenuation of the IP at 300 mHz from1.5×10^{-2} at 8×10^{-3}. To $f = 300$ mHz the value of the intrinsic noise of the accelerometer is about $3\times10^{-3}\frac{\mu m}{\sqrt{Hz}}$ and our goal will be to reach it.

To reach the intrinsic noise level of the accelerometer, as third step, the gain value G has been change from 0.3 to 0.7 (this meas that the bandwidth control change from 3 Hz to 7 Hz). In Fig. 8.11 the impact of the strategy32 and G=0.7 on the $\tilde{T}^{eff,CL}_{s_{iL_s}\to S_{iv}}(\omega)$ (yellow curve) and on

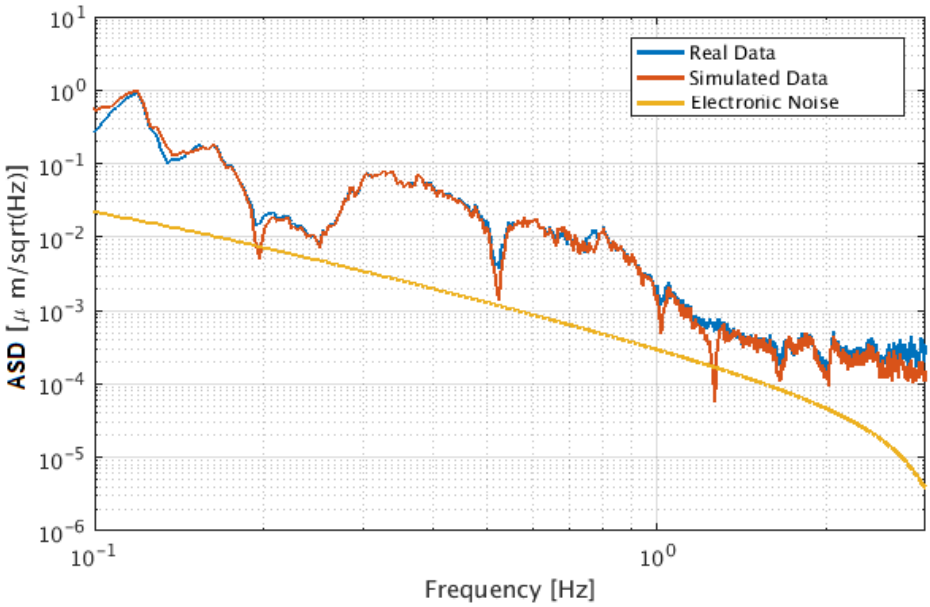

Figure 8.7: Comparison between real and simulated data of residual motion $\tilde{s}_i(\omega)$ along z axis of the top stage accommodated on the input of North arm. In this plot the real ASD (blue curve) and simulated ASD (red curve) are in agreement. These ASDs are also compared with the intrinsic electronic noise of the diagonalized accelerometer in the VRF.

the components $\tilde{A}(\omega)$ (blue curve) and $\tilde{B}(\omega)$ (red curve) are shown. This produce a benefit of a factor 2 on the closed loop attenuation and at $f = 300$ mHz the residual motion is compatible with $5 \times 10^{-3} \frac{\mu m}{\sqrt{Hz}}$ (see Fig. 8.12).

Last step, is to produce the signal $\tilde{s}_i(\omega)$ for each of the three cases illustrated and make the appropriate conclusions (see Fig.8.12). All the PSDs, reported in Fig. 8.12, are produced by using the same background seismic data (blue curve). Starting from the PSD calculated implementing the startegy63 (red curve), we can see how the residual motion $\tilde{s}_i(\omega)$ is reduced by implementing strategy32 (yellow curve), so as to reach the electronic noise by using the combination of strategy32 and G=0.7 (purple curve).

8.4 Blending strategy: below 100 mHz

Above 100 mHz, low values of the frequency blending frequency (f_b like $32\,mHz$) allow us to have a big reduction of IP residual motion. Since in the BVS, the LVDT and accelerometer sensors are interconnected through the filters LP and HP, low values of f_b can cause a re-injection of noise in the region below 100 mHz. Indeed the typical bump that characterize the shape of the HP becomes critical moving the blending frequency (f_b) below 0.1 Hz. This

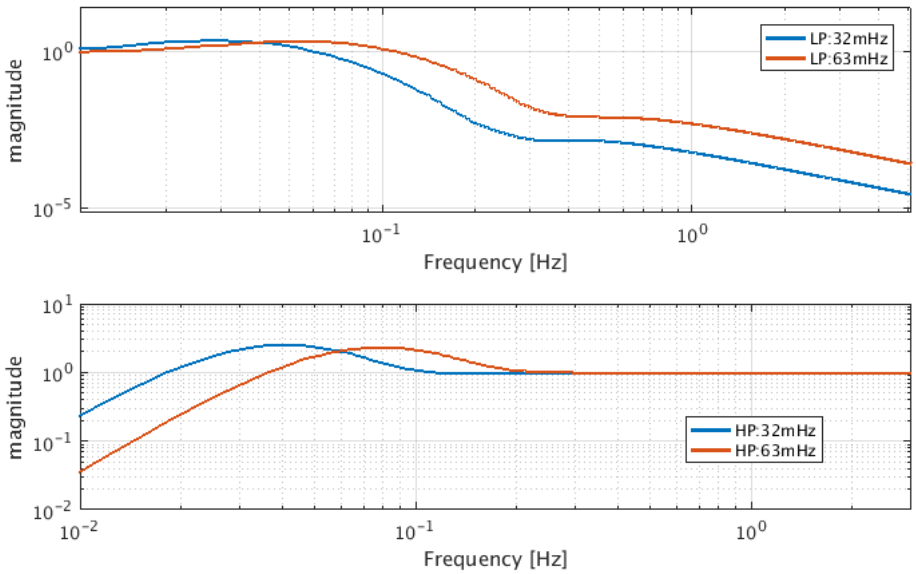

Figure 8.8: Different couples of blending filters used to work with this projection tool. In the first row the comparison between the transfer function of the two LP filters (red curve LP related to strategy63 and blue curve LP related to strategy32) are reported. Switching the strategy from strategy63 to strategy32 we see that the pre-filtering of the seismic disturbance change from 1.5×10^{-2} to 1.5×10^{-3} at 300 mHz. In the second row the comparison between the transfer function of the two HP filters: red curve HP related to strategy63 and blue curve HP related to strategy32 are reported. Switching the strategy from strategy63 to strategy32 we see that the typical bump move from $60 \div 110 mHz$ to $50 \div 20 mHz$.

can induce or amplify some phenomena that are manifested in the strictly frequency range $10 \div 100 mHz$. To stabilize the IP control and then to reduce its residual motion we need to know some particular behavior, like the **cradle effect** and the **tilt**, that are quantifiable by looking the accelerometers response.

8.4.1 Cradle effect

Cradle effect is a direct manifestation of a mechanical coupling between longitudinal translation of the base ring and angular tilt of the top table. The physical causes that produce this effect are: the low stiffness of the cup spring posed under the feet of the IP and a non perfect parallelism of the IP legs.

Concerning the cup springs, this mechanical coupling is generated by the recoil of these: a little displacement, in the $i-th$ direction, of the top stage, induced an inclination of the inverted pendulum. According to this, the cup spring go down or go up depending on which direction the IP tilts. Consequence to this difference of weight supported by the cup springs α_i^{crad} is not

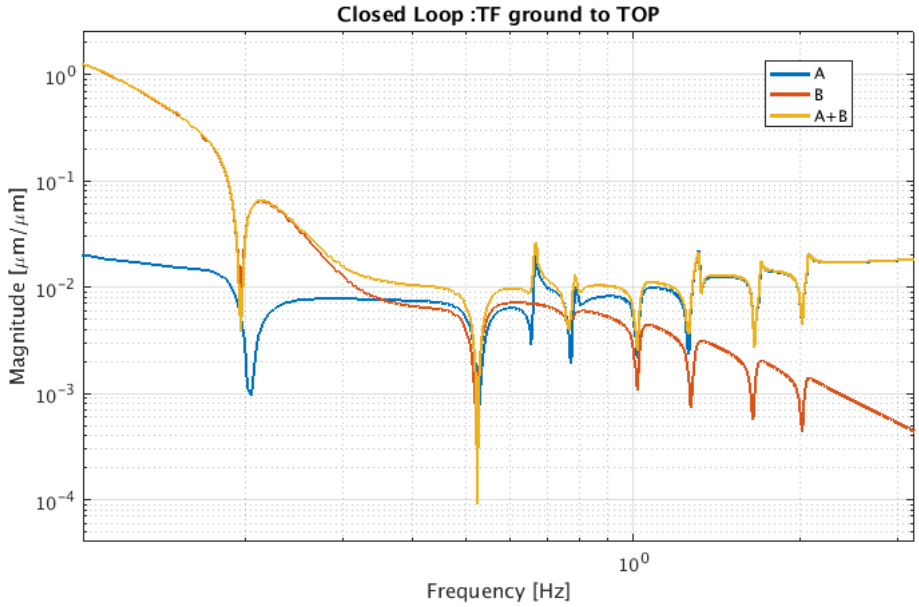

Figure 8.9: Impact of the strategy63 on the $\tilde{T}^{eff,CL}_{s_{iL_s}\rightarrow S_{iv}}(\omega)$ (yellow curve) and on its components $\tilde{A}(\omega)$ (blue curve) and $\tilde{B}(\omega)$ (red curve). This strategy produce an effective attenuation of about 1.5×10^{-2} at 300 mHz.

zero and the value of the transfer function $\frac{\Delta\alpha_i^{crad}}{\Delta s_i}$ is

$$\frac{\Delta\alpha_i^{crad}}{\Delta s_i}\approx\frac{m\cdot g}{K_\theta}\approx\frac{1.2\cdot10^3\,[Kg]\cdot9.8\,[m/s^2]}{10^7\,[Nm]}\approx10^{-3}\,[m^{-1}] \tag{8.11}$$

where m is the total mass of the system, and K_θ is the angular stiffness of the cup spring.

In second case, the mechanical coupling is generated by to the non parallelism of the legs: when the legs are not parallel, the value of transfer function $\frac{\Delta\alpha_i^{crad}}{\Delta s_i}$ is equal to

$$\frac{\Delta\alpha_i^{crad}}{\Delta s_i}\approx\frac{b}{L\cdot R}\approx\frac{10^{-3}\,[m]}{5\,[m]\cdot0.87\,[m]}\approx2.3\cdot10^{-4}\,[m^{-1}] \tag{8.12}$$

where b is the parallelism error, L is length of legs and R is half distance between the legs.

8.4.2 Accelerometer additional contribution: cradle effect

Generally, the accelerometer reads the cradle contribution

$$\tilde{a_i}(\omega)=-\omega^2 s_i(\omega)-g\tilde{\alpha}_i^{crad}\quad(i,=z,x\ ,\ j=x,z) \tag{8.13}$$

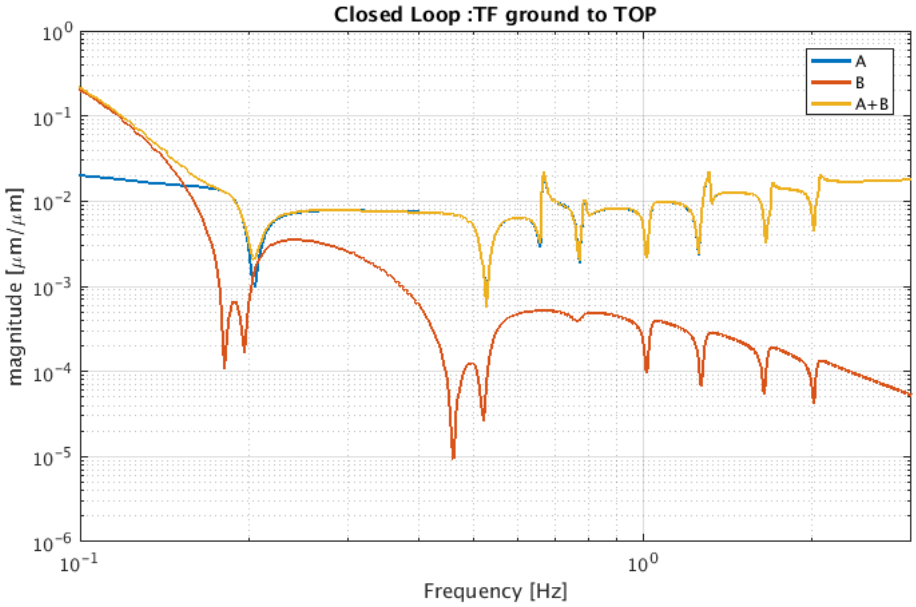

Figure 8.10: Impact of the strategy32 on the $\tilde{T}^{eff,CL}_{s_{iLs}\to S_{iv}}(\omega)$ (yellow curve) and on its components $\tilde{A}(\omega)$ (blue curve) and $\tilde{B}(\omega)$ (red curve). This strategy produce an effective attenuation of about 8×10^{-3} at 300 mHz.

In particular, at frequency $f \ll f_n \simeq 25mHz$ this contribution is more evident and in the accelerometer signal the contribution $-g\tilde{\alpha}_i^{crad}$ is predominant. For this reason, in this frequency range, the related transfer function acceleration- displacement is proportional to $\tilde{\alpha}_i^{crad}$: this angle is the so called *cradle term* and the associated effect is known as *cradle effect*. In Fig.8.13 an example of the transfer function between accelerometer and LVDT is shown.

The presence of this "*cradle term*" $\tilde{\alpha}^{crad}$ modifies the mechanical plant at low frequency in this way

$$\tilde{M}_i(\omega) \to \tilde{M}_i^{'}(\omega) = \tilde{M}_i(\omega)\cdot\left[1-\frac{\tilde{HP}(\omega)}{\omega^2}\cdot\tilde{\alpha}_i^{crad}\right] \tag{8.14}$$

Looking at formula (8.14), it is easy to understand that the impact of this effect on the mechanical plant is related to the pre-filter strategy and becomes very crucial when we apply the blending strategy with low value of f_b. In order to restore the shape of the mechanical plant $\tilde{M}_i(\omega)$, and then to avoid the instability in the control loop we apply the so called "*cradle removal*". In Fig. 8.14, the examples of the IP plant modified by the presence of the cradle term, when a high pass filter with $f_b = 32\,mHz$ is applied (red curve), and the restored IP plant after cradle removal (green curve) are reported.

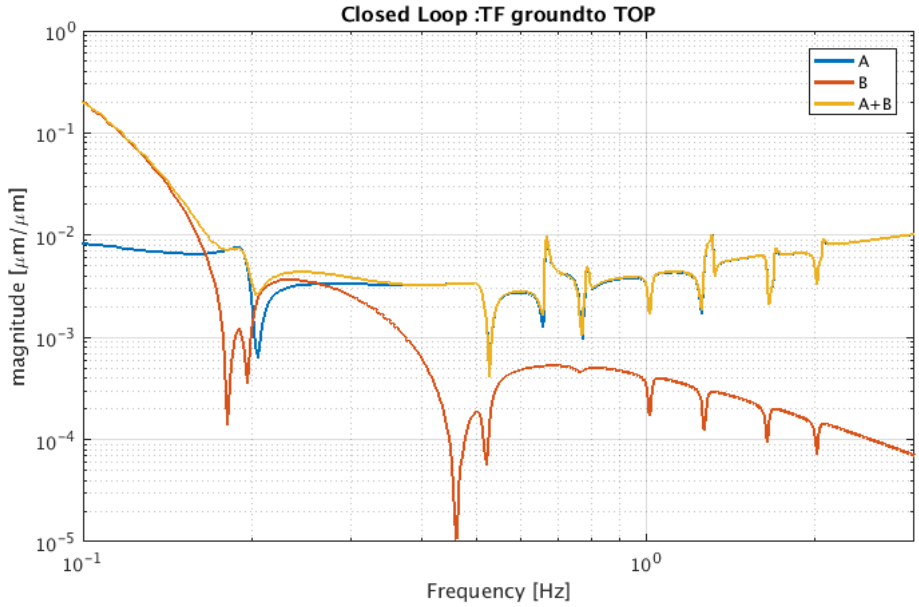

Figure 8.11: Impact of the strategy32 and controller gain $G = 0.7$ on the TF_{eff}^{CL} (yellow curve) and on its components $\tilde{A}(\omega)$ (blue curve) and $\tilde{B}(\omega)$ (red curve). This strategy produce an effective attenuation of about 3×10^{-3} at 300 mHz.

8.4.3 Cradle removal

To apply the cradle removal the estimation of the cradle contribution $\tilde{\alpha}_i^{crad}$ is needed: usually this is done by measuring the low frequency DC level in the transfer function shown in Fig. 8.13. After this estimation, we can write the BVS as [5]

$$\tilde{S}_{iv}(\omega) = \tilde{LP}(\omega) \cdot \tilde{s}_{iL}(\omega) - \omega^{-2} \cdot \tilde{HP}(\omega) \cdot \tilde{a}_{iA}(\omega) - \omega^{-2} \cdot \tilde{HP}(\omega) \cdot \tilde{\alpha}_i^{crad} \cdot \tilde{s}_{iL}(\omega) \tag{8.15}$$

The additional term $\omega^{-2} \cdot \tilde{HP}(\omega) \cdot \tilde{\alpha}_i^{crad} \cdot \tilde{s}_{iL}(\omega)$ is used to restore the right shape of the mechanical plant avoiding instability in the control loop. This operation in some way deteriorates the effectiveness of the low pass, indeed the shape of the LP filter change in this way

$$\tilde{LP}_{eff}(\omega) = \tilde{LP}(\omega) - \omega^{-2} \cdot \tilde{HP}(\omega) \cdot \tilde{\alpha}_i^{crad} \tag{8.16}$$

[5] Concerning the IP of AdV the cradle effect is manifested only for the horizontal d.o.f , the vertical is not affected by it. Looking at the data we see that there are two kind of cradle contributions: direct and transverse. In this dissertation we pose our attention only on the direct cradle effect.

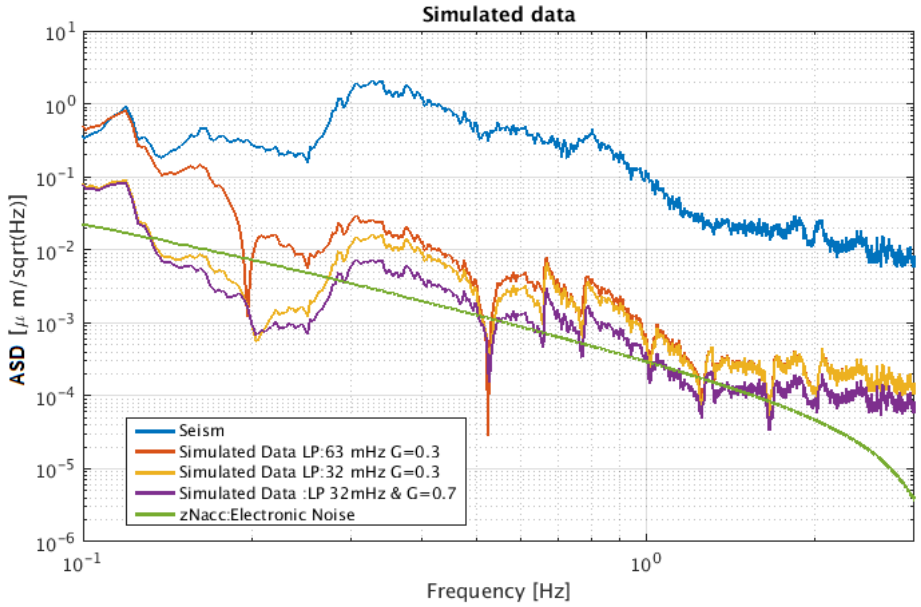

Figure 8.12: In this figure the simulated residual motion $\tilde{s}_i(\omega)$ calculated using Eq.8.10 for the three cases: strategy63 , strategy32, strategy32 and $G = 0.7$ are reported. All these ASDs are compared with the intrinsic noise level of the accelerometer (green curve). These simulations are calculated when background seismic condition (blue curve) was occur. Starting from blue the red curve (strategy63): we can see how $\tilde{s}_i(\omega)$ is reduced by implementing stretegy32 (yellow curve) so as to reach the electronic noise of the sensor using a combination of strategy32 and $G = 0.7$ (purple curve).

In order to reshape the $\tilde{LP}_{eff}(\omega)$ and recover the begin performance of the low pass filter ($\tilde{LP}(\omega)$), we can use a frequency dependent cradle term $\tilde{\alpha}_i^{crad} \cdot \tilde{LP}^{crad}(\omega)$

$$\tilde{LP}'_{eff}(\omega) = \tilde{LP}(\omega) - \omega^{-2} \cdot \tilde{HP}(\omega) \cdot \tilde{\alpha}_i^{crad} \cdot \tilde{LP}^{crad}(\omega) \tag{8.17}$$

In the table 8.2 an example of typical filter $\tilde{LP}^{crad}(\omega)$ used to reshape the low pass filter, is shown.

f [Hz]	Q	P or Z
0.150	0.7	P
0.250	1.5	Z
0.5	0	Z
1.4	0	P

Table 8.2: Example of typical low pass filter LP^{crad} used to reshape the cradle term. P means pole and Z means zero.

In Fig. 8.15 the impact of the cradle term $\tilde{LP}^{crad}(\omega)$ on the shape of LP is shown. In

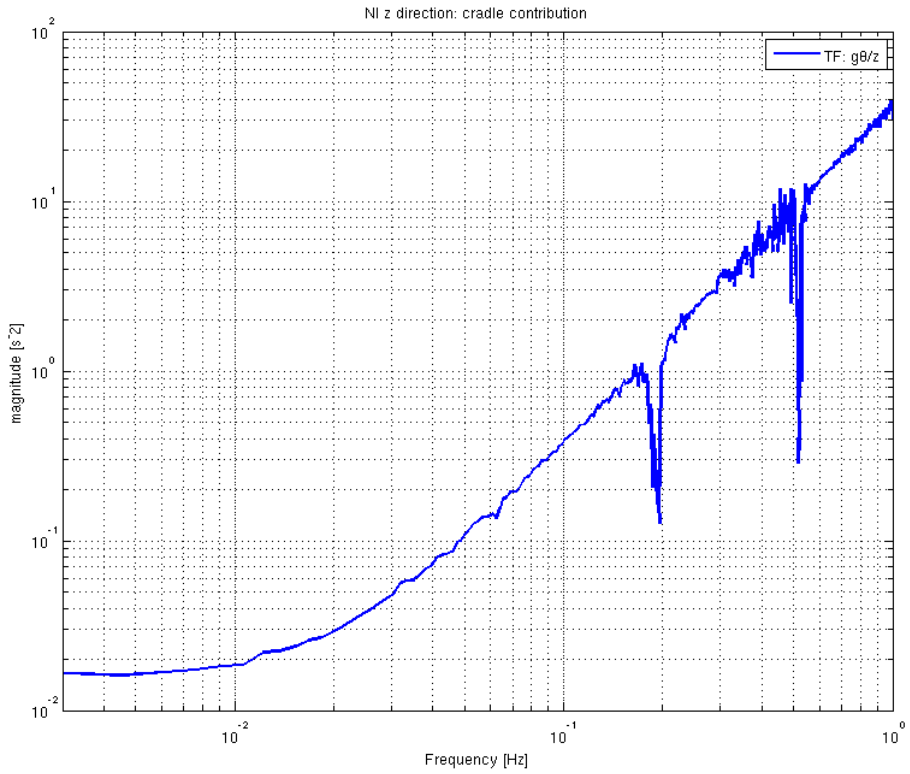

Figure 8.13: Example of the transfer function between accelerometer and LVDT. This tansfer function, above $20\,mHz$, is proportional to f^2 how we expect; while below $20\,mHz$ assume a constant value α^{crad} related to the cradle.

order to produce simulated data compatible with a real situation in the simulation showed in Subsection8.3.1 all results have been calculated taking into account the cradle term and for the two strategies the used low pass is reshaped according to the equation 8.17.

8.4.4 Accelerometer additional contribution: environmental Tilt

At low frequency (f<0.1 Hz) the seismic noise does not affect the locking activity (except in case of strong earthquake). It is possible to convince our-self of this statement controlling the suspensions just through the LVDTs: in this case, the contribution of the low frequency to the locking force rms is negligible. In this frequency region the accelerometers seem to be noisy, because the cavity elongation measured by those sensors is not coherent with the locking force (see Subsection 8.4.5), and it would be definitely too large to be compensated acting on the mirror.

In Figure 8.16 we see the typical PSD of the accelerometers: the expected level of electronic

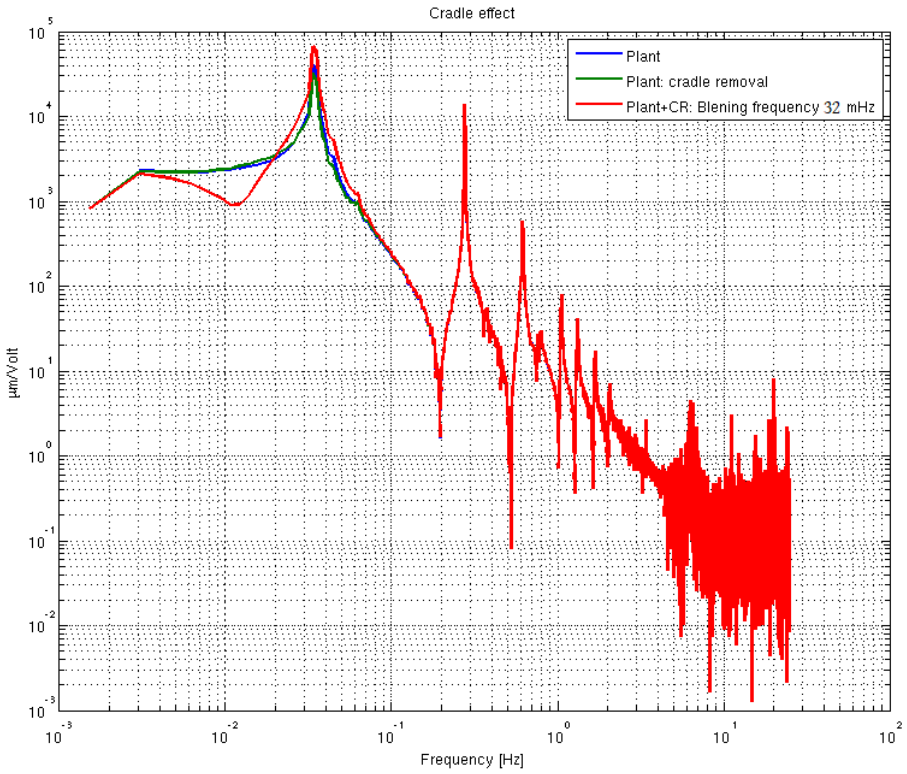

Figure 8.14: Examples of the IP plant modified by the presence of the cradle term, when a high pass filter with $f_b = 32mHz$ is applied (red curve), and the restored IP plant after cradle removal (green curve) are reported.

noise is much lower, but according to the reported experience this cannot be considered the true motion of the IP. Moving to the inertial control, it always happen that the locking force PSD worsen below 0.1 Hz, and the excess noise is perfectly measurable by the LVDTs. This means that low frequency accelerometer noise, even if high-passed, unavoidably spoils the control. The level of noise is not stable: it can change a lot depending on the weather conditions. In particular, it depends on the wind speed on site. These observation leeds us to guess that the accelerometer is measuring the angular motion of the ground, or at least of the building floor.

In general, the virtual sensor in loop can be written

$$\tilde{S}_{iv}(\omega) = \tilde{s}_i(\omega) - \tilde{LP}(\omega) \cdot \tilde{s}_{iLs}(\omega) + \frac{\tilde{HP}(\omega)}{\omega^2} \cdot \left(-g\tilde{\theta}(\omega) + \tilde{n}_{iAe}(\omega)\right) \tag{8.18}$$

As explained above, below 0.1 Hz the ground motion term is negligible and the in-loop signal is dominated by the accelerometer noise. Considering that the loop gain is high ($G > 50$),

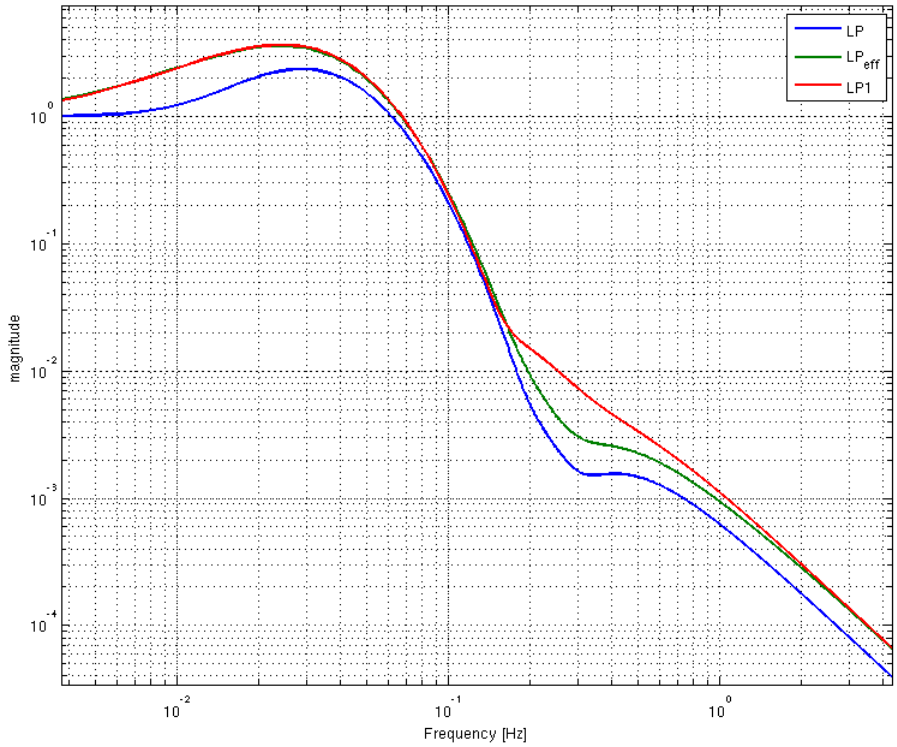

Figure 8.15: Impact of the cradle term on the shape of the LP. In particular we see how change the shape of the LP filter with $32\,mHz$ of blending frequency (blue line) when the a constant cradle removal is applied (red line), thus getting worse its performance in the region $[0.150, 1]\,Hz$. Its shape and in part its performance are recovered when the frequency depended cradle removal is applied (green line).

we can conclude that IP displacement can be written as

$$\tilde{s_i}(\omega) = \frac{\tilde{HP}(\omega)}{\omega^2} \cdot \left(-g\tilde{\theta}(\omega) + \tilde{n}_{iAe}(\omega)\right) \tag{8.19}$$

As shown in the formula (8.19), in this limited band the high pass filter play a crucial role. The residual motion of inverted pendulum is subject to the noise sources of the accelerometer through the high pass filter which, depending of the weather condition, can becomes critical for the lock. In order to understand this phenomenon in Figure 8.17, two LVDT data sets are reported. These data have been acquired when the strategy shown in the Fig. 8.4 was running and when the strong and low wind condition was verified. Looking at this figure (see Fig.8.17), we see that generally the LVDT signal has an amplitude oscillation of about $1.4\,\mu m$ peak to peak in low wind condition while in strong wind condition the amplitude of this oscillation increases reaching the $6.51\,\mu m$ peak to peak.

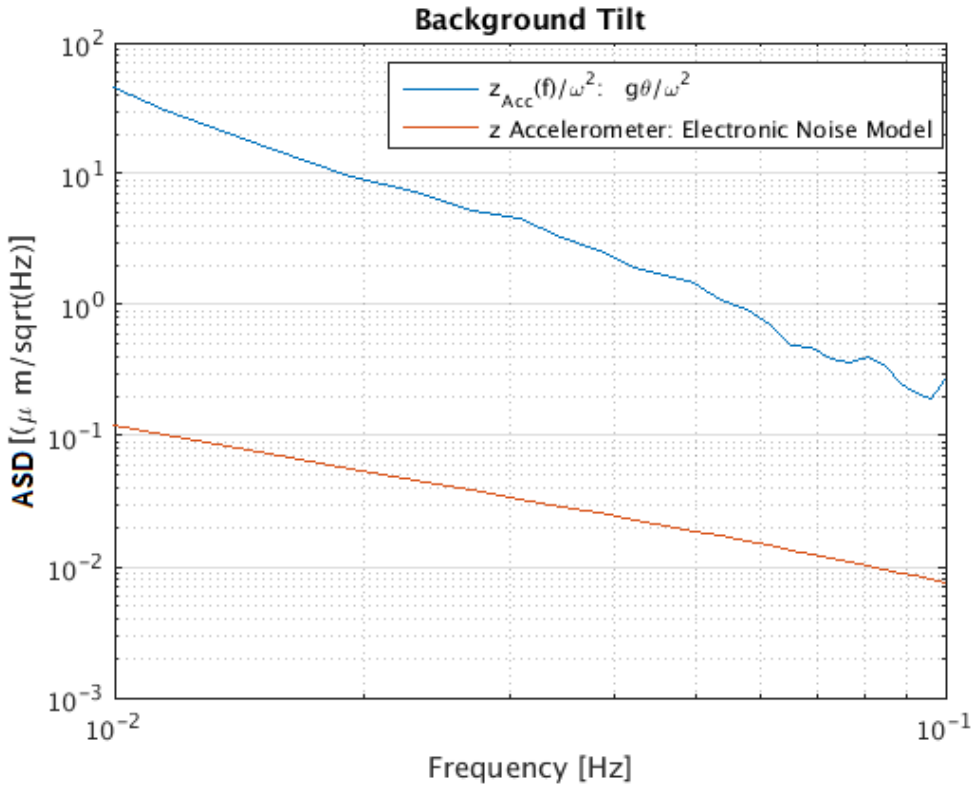

Figure 8.16: Comparison between the intrinsic electronic noise and ASD of a diagonalized accelerometer posed on the Virgo top stage. In this plot the attention is focused in the region below $100\,mHz$

Now we will manipulate these data sets in order to see how the amplitude of the LVDT signal changes when we use a different strategy ($\tilde{HP}(\omega) \rightarrow \tilde{HP}'(\omega)$). The residual motion expressed by the (8.19) becomes

$$\tilde{s}_i'(\omega) = \frac{\tilde{HP}'(\omega)}{\omega^2} \cdot \left(-g\tilde{\theta}(\omega) + \tilde{n}_{iAe}(\omega)\right) \tag{8.20}$$

To quantify the noise injected, changing strategy, we compute the ratio of the high passe filters

$$r(\omega) = \frac{\tilde{HP}'(\omega)}{\tilde{HP}(\omega)} \tag{8.21}$$

By using the ratio $r(\omega)$ we can produce a projection of residual motion of the IP $\tilde{s}_i'(\omega)$ when we use the filter $\tilde{HP}'(\omega)$

$$\tilde{s}_i'(\omega) = r(\omega) \cdot \tilde{s}_i(\omega) \tag{8.22}$$

The Eq. (8.22) is very interesting, because allows us to monitor the low frequency oscillations

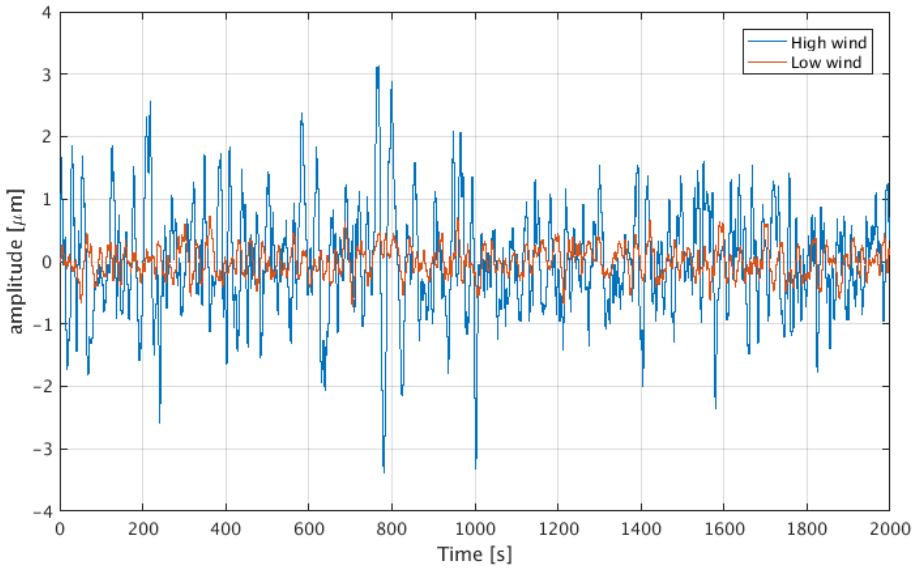

Figure 8.17: In this figure the impact of two different weather conditions on LVDT data are shown. In the low wind condition (red curve), the LVDT the rms of the amplitude oscillation is about 0.24 μm while in strong wind condition the rms increasing reaching the value of 0.82 μm (blue curve).

of the inverted pendulum in a specific background condition, given a chosen pre-filter strategy.

We are interested to understand how different strategies, like strategy32 or strategy63, modify the behavior of our data sets acquired in high wind condition (see blue curve of Fig.8.17). To this purpose we have produce a simulation in which the impact of the mentioned strategies is calculated, by using the indicator *r*. These projections are implemented in MATLAB. In order to give a qualitative estimation in Fig. 8.18 the impact of these strategies on data set, acquired in high wind condition, is shown. Concerning the strategy63 (red curve) the rms of and the amplitude peak-to peak are respectively1.23 μm and 9.7 μm while for the strategy32 (blue curve) the rms and amplitude peak-to peak are respectively 5.4 μm and 34.8 μm.

In extreme condition (like the combination between high wind and strategy32) we can be failing to acquire and stabilize the lock of the interferometer.

8.4.5 Impact of the low frequency oscillations on the locking correction

Now we are interested to quantifier the impact of several strategies on the motion of the suspended masses. This residual motion is given by

$$\tilde{s}_{i,mir}(\omega) = \tilde{D}(\omega) \cdot \tilde{s}_i(\omega) \approx \tilde{s}_i(\omega) \tag{8.23}$$

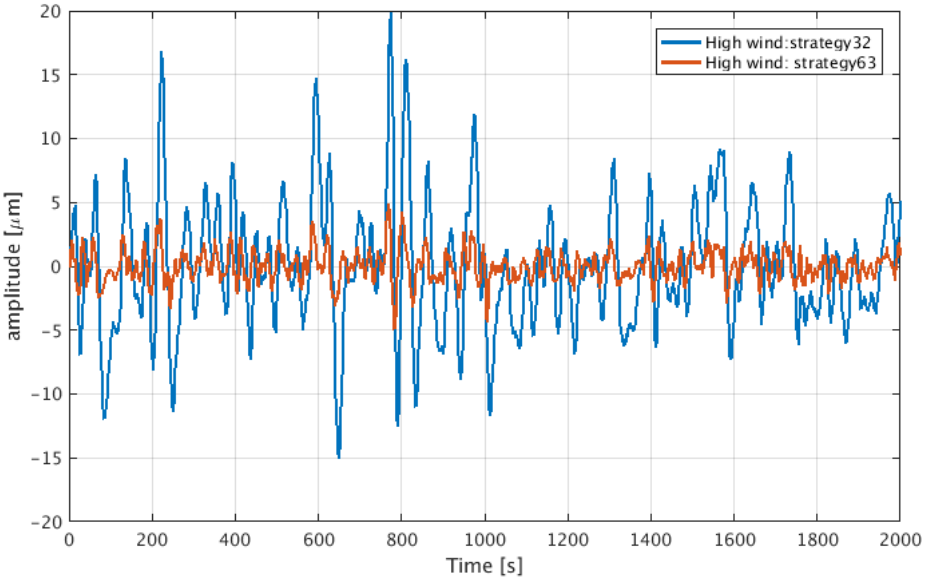

Figure 8.18: In this figure the impact of two strategy on data set in high wind condition is shown. In this condition, the strategy63 (red curve) the rms calculated and amplitude peak-to peak are respectively $1.23\,\mu m$ and $3.5\,\mu m$. In this condition, the strategy32 (blue curve) the rms calculated and amplitude peak-to peak are respectively $5.4\,\mu m$ and $14.2\,\mu m$.

where $\tilde{D}(\omega)$ is the transfer function between the top stage (input) to the mirror (output) and in this frequency range is equal to one. To convince us that Eq. (8.23) is true, we calculate the cavity length ($\tilde{L}_{arm}^{TOP}(\omega)$) using the residual motion $\tilde{s}_z(\omega)$ along the optical axis of the cavity for the end and input IP and we compare it with the cavity length ($\tilde{L}_{arm}(\omega)$) deduced from the locking correction signal ($\tilde{S}_{z,lock}(\omega)$). Let start our demonstration calculating the PSD of the cavity length at level of the top stage $\tilde{L}_{arm}^{TOP}(\omega)$

$$\tilde{L}_{arm}^{TOP}(\omega) = \sqrt{\left(\tilde{s}_z^I(\omega)\right)^2 + \left(\tilde{s}_z^E(\omega)\right)^2} \tag{8.24}$$

where $\tilde{s}_z^I(\omega)$ and $\tilde{s}_z^E(\omega)$ are, respectively, the residual motion of the input IP and end IP accommodated along an arm of the interferometer.

In second case, the cavity length can be calculated as

$$\tilde{L}_{arm}(\omega) = c \cdot \tilde{S}_{z,lock}(\omega) \tag{8.25}$$

$\tilde{S}_{z,lock}(\omega)$ is the "**locking correction signal**" and represents the respective tension expressed in $\frac{V}{\sqrt{Hz}}$ of the necessary force to keep in lock the cavity while c is the calibration factor to convert the signal from V to μm and its value is about $0.75\,\mu m \times V$. In locking condition, in the range $10 \div 150\,mHz$, the arm cavity length calculated with Eq. (8.24) and (8.25) are approximately

equals (see 8.19).

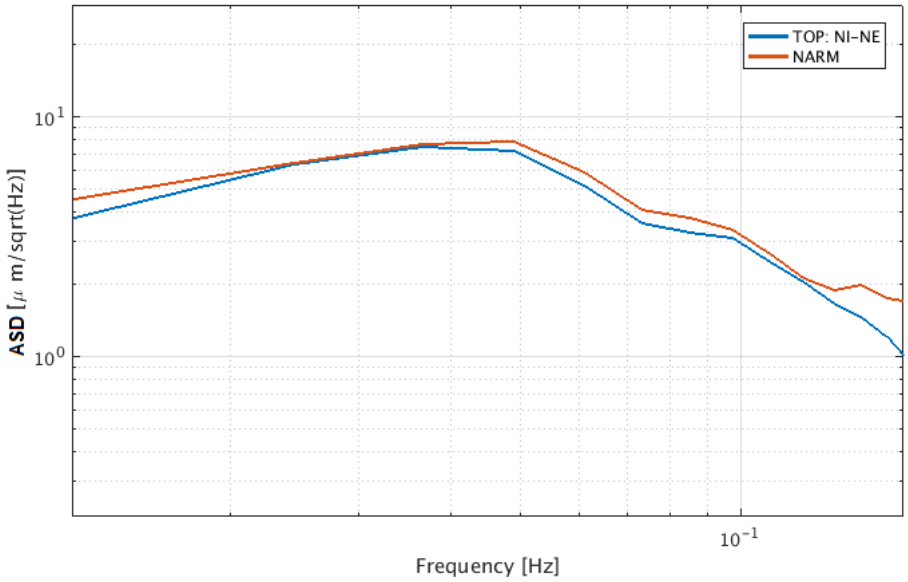

Figure 8.19: In this figure the comparison between the ASD of the North arm (NARM) cavity length estimated using formula (8.24) (blue curve) and formula (8.25)(red curve) is reported. The plot is restricted at frequency range below 100 mHz. We see that two curves are matching.

Since below 100 mHz the residual motion of the IP is transmitted one to one at level of the test mass we can study the impact of several strategies on the locking signal using $r(\omega)$; in particular we can produce a projection of the $\tilde{S}_{z,lock}(\omega)$ in this way

$$\tilde{S}'_{z,lock}(\omega) = r(\omega) \cdot \tilde{S}_{z,lock}(\omega) \tag{8.26}$$

Considering that for the actuator used in AdV, the range of the actuation dynamic is $\pm 10V$, during the commissioning activity we did an analysis to fix a certain tolerable threshold s on the dynamic actuation. The threshold value ($s = 1.8V$) has been fixed analyzing four hours of locking data acquired when the speed of wind ranging to $20 \div 45\, Km/h$ (see Fig.8.20)

With the intent to avoid the saturation of locking correction we have studied the impact of three different strategies on the $\tilde{S}_{z,lock}(\omega)$. In order to understand if the selected blending strategy put in the saturation condition the actuator and to deduce the transformed PSD of the locking correction the Eq. (8.26) has been used. For each transformed PSD also the related spectral root mean square $r_{f,rms}$[6] has been calculated. In figure 8.12 the impact of three strategies on the $\tilde{S}_{z,lock}(\omega)$, when the speed of wind is low ($10 \div 25\, Km/h$), is shown.

[6]Given a vector T wih component (x_i, y_i) where $i = 1 \cdots N$. we define the $T_{rms}$the vector of components

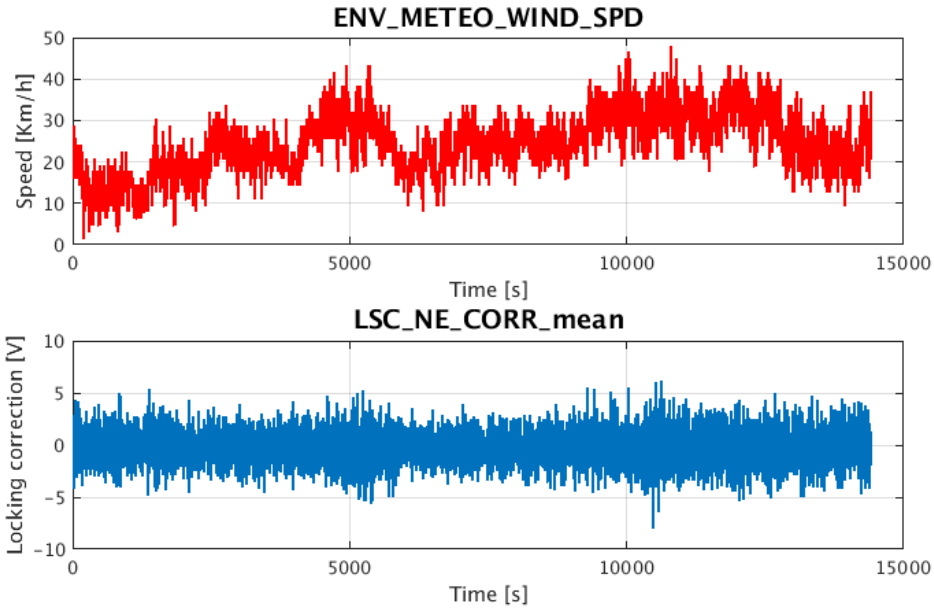

Figure 8.20: In this figure the trend data for the speed wind (red curve) and locking correction (blue curve) are reported. The data have been divided in 8 segment segments of 30 minutes each: for each of these the maximum value (M) of the signal and the related standard deviation σ_M have been calculated. The maximum value of the locking correction is $8.34 \pm 1.80 V$: this means that for speed of wind $v \geq 45 Km/h$ the mirror actuator is very close to the saturation value ($10 V$) and for this reason we have fixed the threshold value s equal to 1.80V.

Looking at the results (see Fig. 8.12) we see that the amplitude of the ASDs of the locking correction and their rms increase by moving the blending frequency below $94 mHz$. In particular, we see that the rms related to the blending frequency equal to $44 mHz$ (black star), in the range $10 \div 30 mHz$, is very close to the threshold value while the rms related to the blending frequency equal to $58 mHz$ (pink star), in the same range, is lower than a factor 2.

8.4.6 Tuning of the blending frequency

At this point the right question is: how to fix the blending frequency, in order to reduce the re-injection of seismic noise and to limit the oscillation of low frequency? Based on the results shown in the Section 8.4.5, we can say:

- In standard microseism conditions and when the speed of wind is low ($v < 20 Km/h$), to

$(x_i, r_{i,rms})$ given by :

$$r_{i,rms} = \sqrt{|\, x_i - x_{i-1} \,| \cdot y_i^2} \tag{8.27}$$

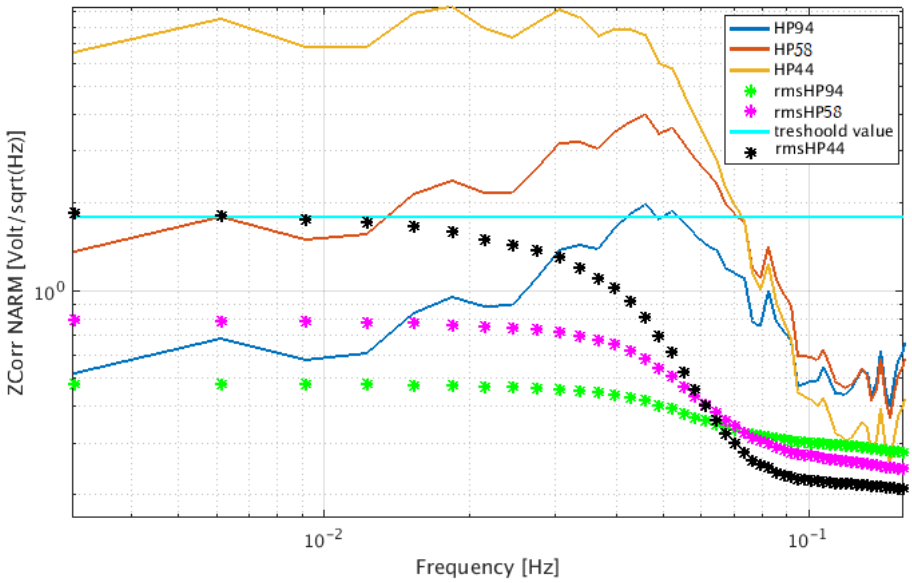

Figure 8.21: Impact on the locking correction and related rms of NARM cavity of three high pass filters. The amplitude of the ASDs of the locking correction and their rms increase by moving the blending frequency below $94\,mHz$. The rms related to the blending frequency equal to $44\,mHz$ (black star), in the range $10 \div 30\,mHz$, is very close to the threshold. The rms related to the blending frequency equal to $58\,mHz$ (pink star) in the same range, is under the threshold of a factor 2.

clean the signal from the seismic noise and to avoid the big low frequency oscillations, we apply a blended strategy with frequency blending $f_b = 44\,mHz$.

- In very bad weather conditions, like very high wind (speed of wind $\geq 50\,Km/h$) , we apply a blending strategy with frequency blending $f_b = 0.94\,mHz$. In this way, reducing the bandwidth of the accelerometer we avoid the big oscillation below $100\,mHz$, but we re-inject a portion of seismic noise.

Considering that the extreme conditions not occur frequently, we prefer not to use the strategy with $f_b = 0.94 mHz$ because the suppression of the seismic noise is not satisfying. The chosen compromise for O2 run is the strategy63 because stay below the threshold value in a large part of the environmental conditions.

8.5 μSeism-Free platform: Global Inverted Pendulum Control (GIPC)

In the Section 8.4.6, we have seen that the tuning of the blending frequency is a "compromise", made to minimize at the same time the re-injection of seismic noise above 100 mHz and the disturbances due to the use of inertial sensors below 100 mHz. For the stand alone suspension control, the 63mHz strategy, is an optimal choice. This strategy is effective above 0.5 Hz, is not too bad for the suppression of the main seismic bump at EGO site (0.3 Hz), but is ineffective for the suppression of microseism at lower frequency (0.1 – 0.2 Hz). In order to reduce considerably the seismic disturbances at low frequency, a blending strategy with crossover below 32 mHz would be needed. This strategy is sustainable if we move to a different control scheme, named Global Inverted Pendulum Control (GIPC). It consists mainly in a base change: the translational coordinates of the different suspensions are mixed in order to build two common coordinates (one for X and one of Z), and many differential coordinates. In other words, we apply a linear operator to the top stage signals

$$\begin{aligned} VRF &\rightarrow VRF^{\mu sF} \\ \mathbf{S}_{i,TOP} &\rightarrow \mathbf{S}'_{\mathbf{i,TOP}} = \mathbf{R}^{\mu sF}\mathbf{S}_{\mathbf{i,TOP}} \end{aligned} \tag{8.28}$$

where $\mathbf{S}_{i,TOP}$is a column vector of top stage signals (LVDTs ($\mathbf{L}_{i,TOP}$) or accelerometers ($A_{i,TOP}$)), $\mathbf{R}^{\mu sF}$ is the transformation matrix to recombine the signals and $\mathbf{S}'_{\mathbf{i,TOP}}$ is the transformed vector.

The matrix $\mathbf{R}^{\mu sF}$ must be satisfy the following properties: the sum of the coefficients appearing in the row of a common signal is equal to one while the sum of the coefficient appearing in the row of a differential signal must be equal to zero.

Concerning the suspensions of the central area, only the common position sensor is affected by the microseism; in the differential position sensors the microseism is subtracted because it is highly coherent in the whole area. For this reason, the new base can be considered a μSeism-Free platform. Using this base, the 32 mHz strategy can be applied to the common coordinates, obtaining the required suppression of 0.1-0.2 Hz microseism. The disturbance due to the use of inertial sensors at low frequency does not affect the ITF performance, because it does not imply an increase of correction required to keep the cavities locked.

The technique cannot be applied to the long cavities, because the coherence of microseism is low. In this case a similar strategy has been developed, in which the differential position sensor is entirely replaced by a signal derived from the locking correction.

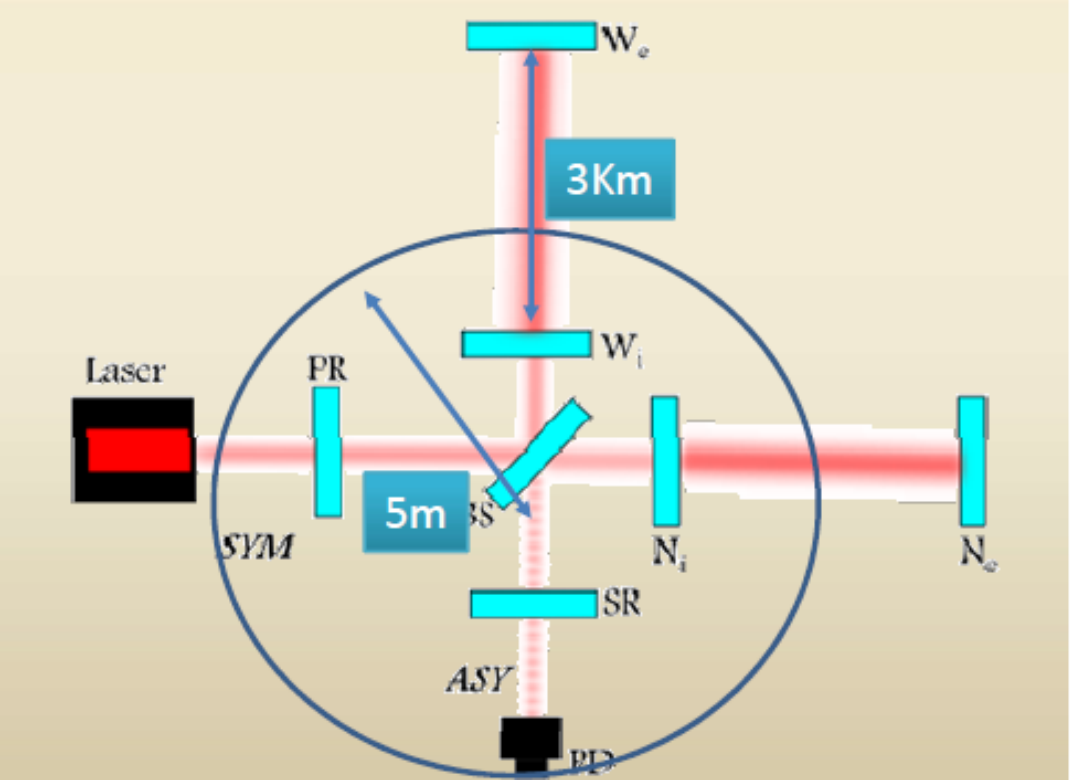

Figure 8.22: In this figure (Not in scale!) the implementation scheme of the GIPC control on the Virgo Interferometer is shown: in the central area the position sensor along the $i-th$ direction, reads coherent seismic contributions and in the GIPC control only common position sensor is affected by the seismic contribution.Being the end and input IP located at 3 Km each to other, seismic contributions contaminating the LVDT (along the $i-th$ direction) are uncorrelated.

8.5.1 GIPC in the central area

In the central area, the diagonalized LVDT sensors read, along the $i-th$ direction, coherent seismic contributions (see figure 8.23).

Adopting the matrix formalism (8.28), a possible choice for $\mathbf{R}^{\mu sF}$, satisfying the above mentioned properties, is given by

$$\mathbf{R}^{\mu sF} = \begin{pmatrix} 0.2 & 0.2 & 0.2 & 0.2 & 0.2 \\ 0.3 & 0.3 & -0.2 & -0.2 & -0.2 \\ -0.2 & 0.3 & 0.3 & -0.2 & -0.2 \\ -0.2 & -0.2 & 0.3 & 0.3 & -0.2 \\ -0.2 & -0.2 & -0.2 & 0.3 & 0.3 \end{pmatrix} \tag{8.29}$$

This transformation, applied to the LVDT produce the expected subtraction of the seismic

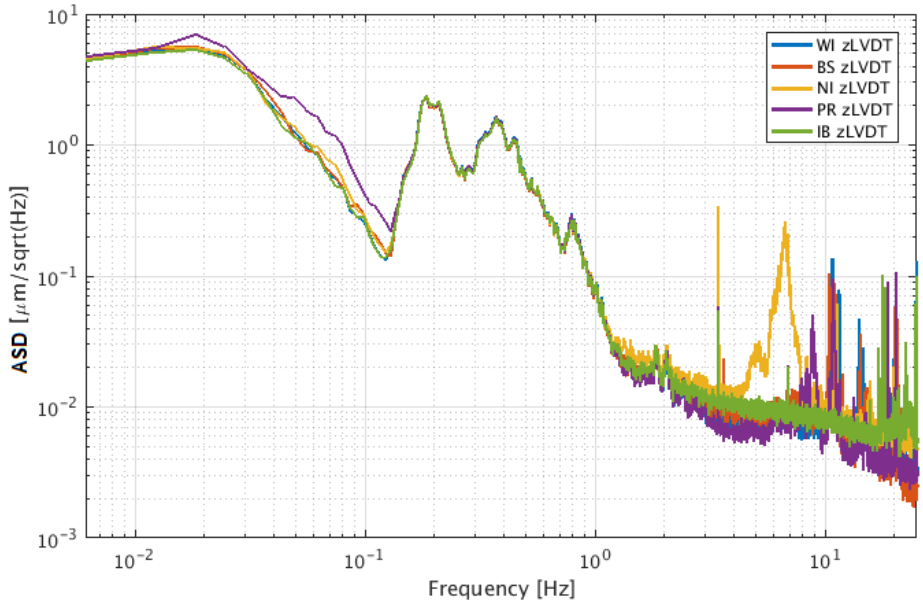

Figure 8.23: In this figure the ASDs of the LVDT signals of the suspensions involved in the implementation of the GIPC control in the central area are reported. We see that when the GIPC control is switched off the ASD of the all LVDT, ranging $0.150 \div 1\,Hz$, are the same. This occurs because in this range the LVDT signal $s_{zL} = s_z - s_{zL_s} \sim s_{zL_s}$.

contribution (see Fig. 8.24).

The same transformation is applied to the accelerometers and the finally blending signals are built:

$$S'_{iv} = LP \cdot \mathbf{L}'_{i,TOP} + HP \cdot \mathbf{A}'_{i,TOP} \tag{8.30}$$

With reference to figure 8.24, to clean the common signal from the seismic component we can use a blending strategy with f_b at $32\,mHz$ (without damaging the locking signal of the interferometer) while we can apply a strategy with f_b at $63\,mHz$ on the differential signals because these not introduce seismic contribution.

After the pre-filtering we come back in the VRF using the inverse matrix $(\mathbf{R}^{\mu sF})^{-1}$

$$(\mathbf{R}^{\mu sF})^{-1} = \begin{pmatrix} 1 & 0 & -2 & 0 & -2 \\ 1 & 2 & 2 & 0 & 2 \\ 1 & -2 & 0 & 0 & -2 \\ 1 & 2 & 0 & 2 & 2 \\ 1 & -2 & 0 & -2 & 0 \end{pmatrix} \tag{8.31}$$

The application of the inverse transformation is necessary in order to not change the mechanical

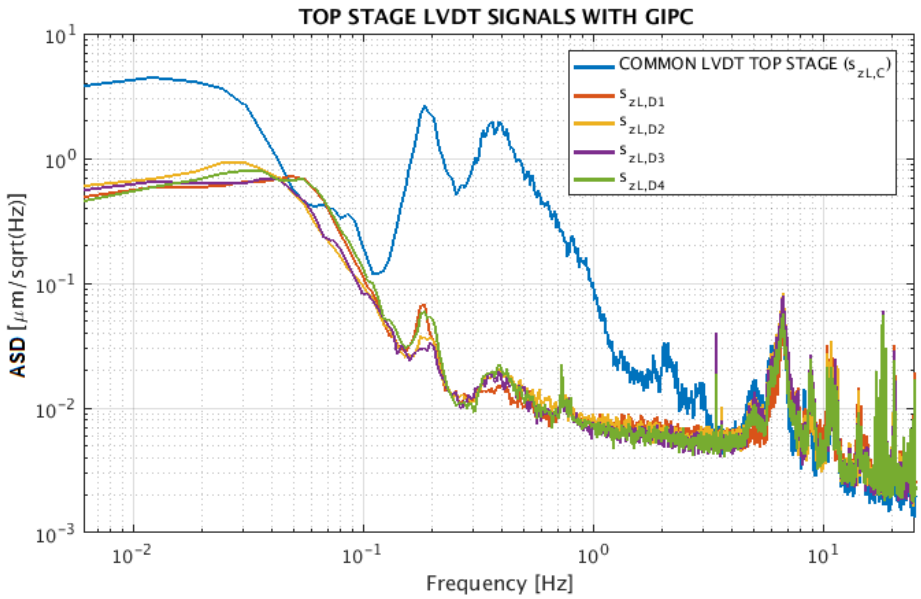

Figure 8.24: In this figure the PSDs of the GIPC LVDT signals in the central area are reported. We see that when the GIPC control is switched on the PSD of the all differential LVDTs signals , ranging $0.150 \div 1\,Hz$, are cleaned and the residual motion of the IP is about $s_z \sim 10^{-2}\frac{\mu m}{\sqrt{Hz}}$. The only one l affected by the seismic noise re-injection s_{zL_s} is the common (blue curve) LVDT. Below 100 mHz we see an other important difference, the low frequency spectrum for the common signal is highest than the spectrum of the differential signals. This occurs because we have applied the strategy63 on differential signal while on strategy32 on the common signal.

plant M_i of the system and have a stable loop.

8.5.2 GIPC on the arms

The seismic contributions contaminating the LVDT of end and input suspensions are uncorrelated and, consequently, the recombination adopting for the central area is non effective. In this case, to correctly implement the GIPC we need of an additional differential signal $D_{z,L}$ that can be deduced from the locking correction of the arm $S_{z,lock}$

$$D_{z,L} = S_{z,lock} \cdot [TF_{z_{corr}\to z_{mir}}] \cdot [TF_{z_{TOP}\to z_{mir}}]^{-1}_{end} \tag{8.32}$$

where $TF_{z_{corr}\to z_{mir}}$ is the mirror mechanical plant along the longitudinal d.o.f of the cavity arm (calibrated in $\frac{\mu m}{V}$) and $TF_{z_{TOP}\to z_{mir}}$is the mechanical attenuation of the end suspension.

At the end of this operation we have the **differential signals** $D_{z,L}$ and its respective differential acceleration that must be filtered using the blending technique. In figure 8.27 the logical scheme of the operations implemented to obtain the differential GIPC blended virtual sensor is

shown.

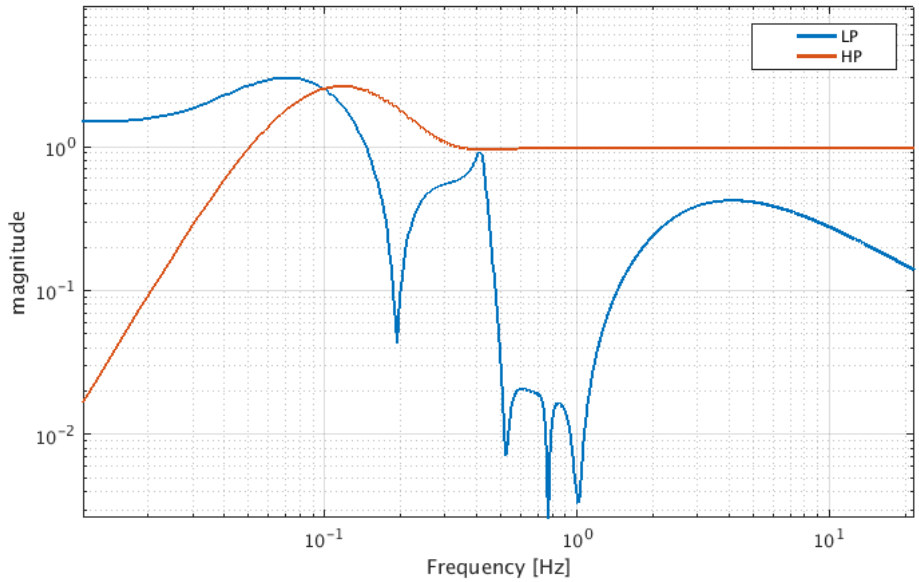

Figure 8.25: Typical transfer function of a low pass and high pass filters used to implement the GIPC control on the arm ($f_b = 120\,mHz$).

In table8.3 the typical zeros and poles of a low pass filter used to implement the GIPC control on the end IP are reported. The blended signal is used to close the loop on the end IP: being controlled with the differential GIPC signals, the end top stage see and consequently follows all displacement of related input IP (see Figure 8.26 upper row on the left), but at the same time the length of the cavity (differential signal) remains unchanged and the locking correction is reduced (see Figure 8.26 bottom row red curve). In this way we can use, at the same time, different strategy controls (for example f_b at $32\,mHz$ and f_b at $63\,mHz$): the length of the cavity remains unchanged and the request of force to keep in the locking condition the interferometer is reduced.

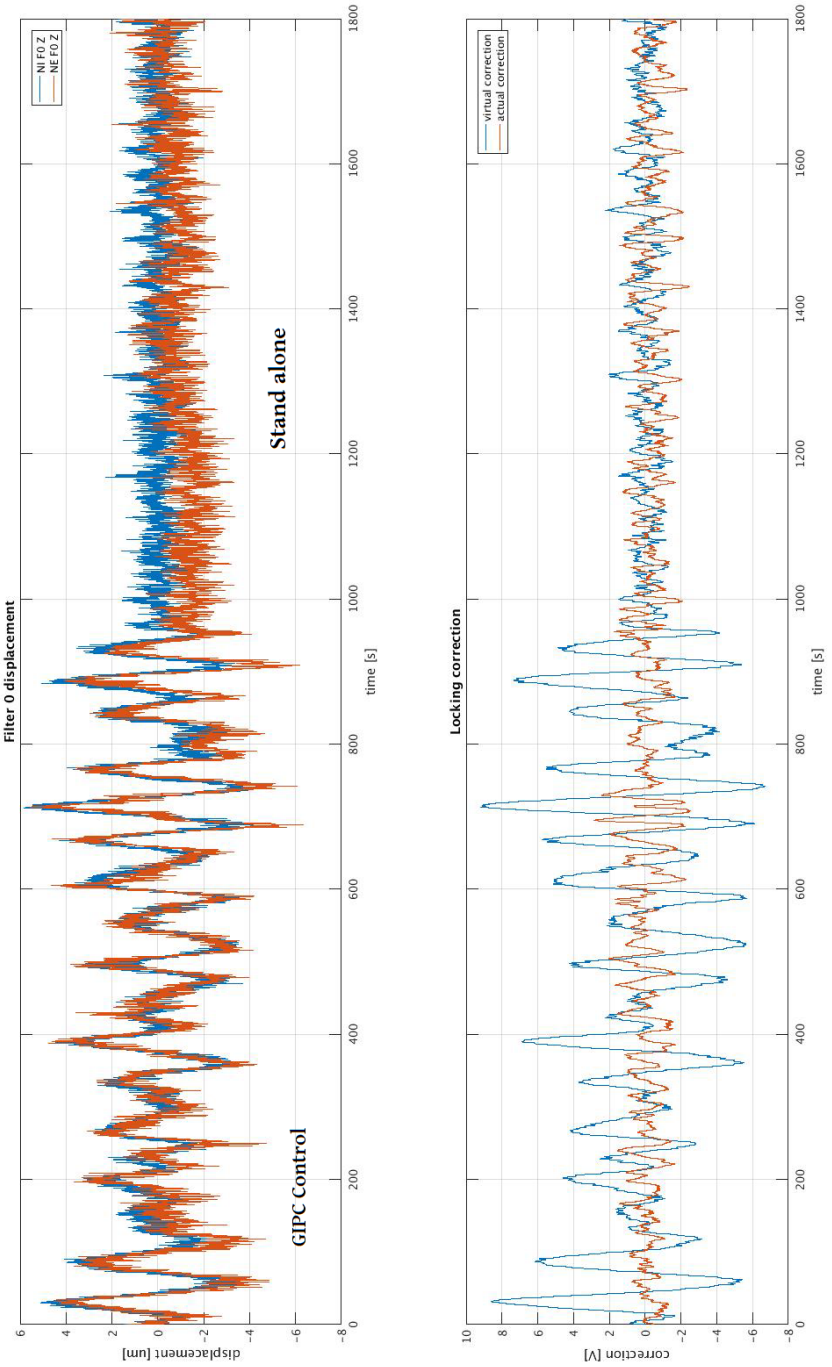

Figure 8.26: GIPC control impact on arm: on the left the GIPC control was on while on the right the GIPC control was off (stand alone condition). In the upper row the top stage motion of an End (red curve) and its related Input (blue curve) is reported: we see that when the GIPC control is switched on the motion of the end top stage follows the displacement of related input. In the bottom row the impact of the GIPC control on the locking correction is reported: we see that the actual locking correction (red curve) thanks to the GIPC control is comparable with the locking correction that we would have if the top stages were controlled with a strategy63 and in stand alone condition (blue curve on the right).

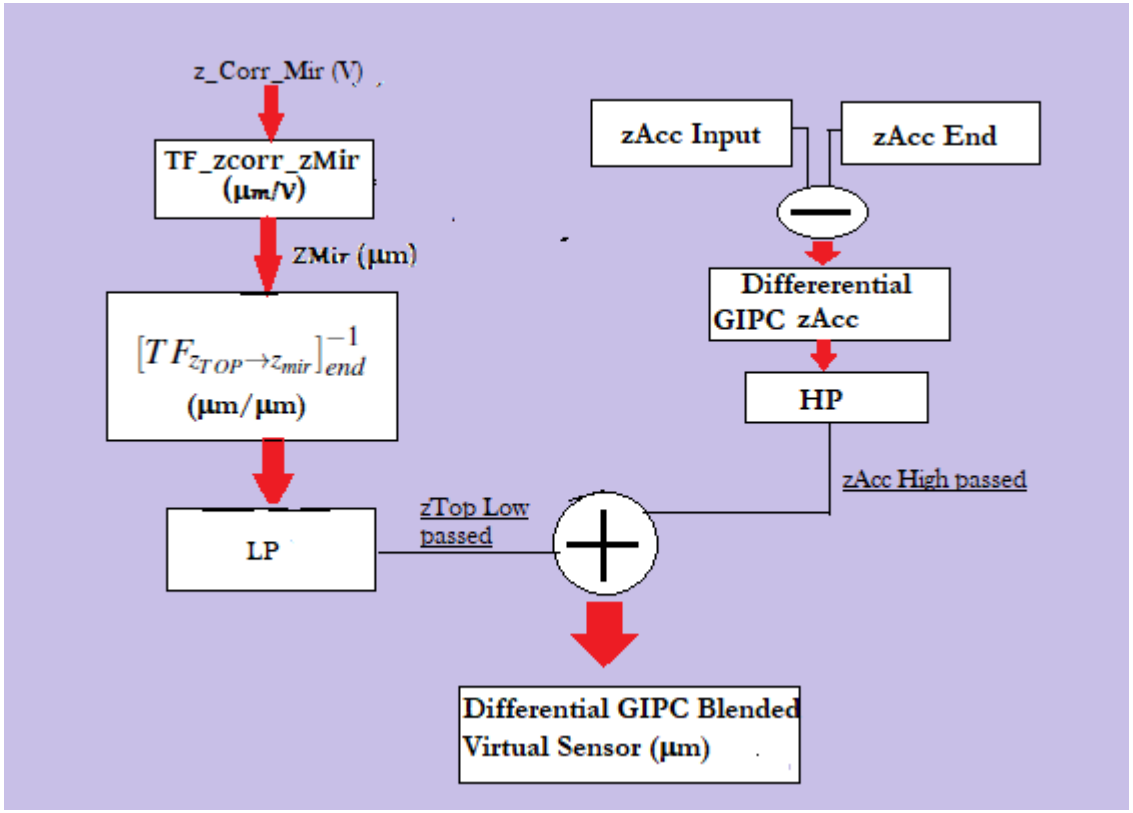

Figure 8.27: Logical scheme of the operation implemented to obtain the differential GIPC blended virtual sensor. Starting from the locking correction applied on the end test mass, applying the transformation 8.32, we produce an equivalent differential LVDT sensor**.** To produce the differential GIPC blended virtual sensor we apply the high pass HP (figure 8.25(red curve)) at the differential GIPC accelerometer and we combine it with the signal zTop low passed.

f (Hz)	Q	P or Z
0.120	0.5	P
0.120	0.5	P
0.120	0.5	P
2.5	0.5	P
2.5	0	P
0.0301	0.65	Z
0.192	30	Z
0.519	30	Z
0.766	100	Z
0.97	30	Z
0.97	23	P
1.01	23	Z
0.418	2.7	P
0.653	2.7	Z
0.763	11	P
gain=1.5	f=0	

Table 8.3: Zeros and poles of Low Pass filter used to implement the GIPC control on the arm. First six values represent the low pass filter with blending frequency at $100mHz$ .Others four zeros, ranging$0.192 \div 0.97 Hz$ are some structures of the transfer function $[TF_{z_{TOP} \to z_{mir}}]^{-1}_{end}$ and last three values are the zeros and the poles of the mechanical plant $[TF_{z_{corr} \to z_{mir}}]$.

Chapter 9

Kalman estimators and LQG control of AdV suspensions

The aim of optimal control is to solve the problem of finding a control law for a given system achieving a certain optimality criterion.

Basically optimal control consists of a set of differential equations describing the paths of the control variables minimizing a predefined cost function. A special case of this general problem is the Linear Quadratic Gaussian (LQG) optimal control. It is applied to uncertain linear systems disturbed by additive white Gaussian noise, having incomplete state information and undergoing control subject to quadratic costs. Since the system is described by a set of differential equations, with fixed initial conditions, its solution is unique. The resulting linear dynamic feedback control law is constituted by the combination of the Kalman filter optimal response and an optimal vector gain. The superattenuator is included in the broad category of systems where optimal control can be applied. Indeed we have a linear mechanical system (SA) and several noise sources (seism and electronic noise of the sensors). Therefore in principle we can design in an automatic way both a Kalman estimator and its associated LQG controller.

In this chapter we will illustrate the first implementation of this control strategy on AdV superattenuator. We will illustrate the used approach to design and implement this control technique on the vertical d.o.f of the SR suspension and we will show the experimental results and the performance of associated LQG controller we have obtained. This test was performed during the AdV commissioning for future developments. We will also discuss the LQG control of the F0 accelerometers that is currently used on every AdV suspensions.

9.1 Kalman filter

Kalman filter [59], also known as Linear Quadratic Estimator (LQE), is a recursive linear filter based on a predictor-corrector estimator. Basically the Kalman filter algorithms are based on **linear dynamical system continuous or discretized models** in the time domain perturbed by Gaussian noise. This algorithm uses:

1) multiple sequential measurements (such as from sensors);

2) statistical noise model and other inaccuracies provided from the measuring devices or from the external disturbances ;

3) system's dynamics model.

Combining all these available information Kalman filter produces an estimate of the state variables that tends to be more accurate over time.

For discrete linear system perturbed by two disturbance sources (assumed to be Gaussian), the state of the system and its measurement data can be represented as vectors written in the recursive form as

$$\mathbf{x}_{k+1} = \Phi_{k+1,k}\mathbf{x}_k + w_k + B_k\mathbf{u}_k \tag{9.1}$$

$$\mathbf{z}_k = \mathbf{H}_k\mathbf{x}_k + D_k\mathbf{u}_k + v_k \tag{9.2}$$

where $\mathbf{x}_k$ is the state vector of the system at time t_k, $\Phi_{k+1,k} \equiv \Phi(t_k, t_{k+1})$ is the state transition matrix between times t_k and t_{k+1}, $\mathbf{H}_k$ is the measurement sensitivity matrix, $\mathbf{w}_k$ is the **process noise** and $\mathbf{v}_k$ is the **measurement noise**. While the latter noise is constituted by the sensor noises, the process noise represents the uncertainties we have in the model of our system. The initial conditions of the system are

$$E < x_0 >= \mathbf{x}_0 \tag{9.3}$$

$$cov < x_0 >= \mathbf{P}_0 \tag{9.4}$$

where $\mathbf{x}_0$ and $\mathbf{P}_0$ are respectively the estimate and the estimation error of x_0. The noise sequences $\mathbf{w}_k$ and $\mathbf{v}_k$ are considered white and Gaussian distributed with zero mean.

In other words, they are uncorrelated and orthogonal

$$E < \mathbf{w}_k, \mathbf{w}_j^T >= \mathbf{Q}_k\delta_{kj} \tag{9.5}$$

$$E < \mathbf{v}_k, \mathbf{v}_j^T >= \mathbf{R}_k\delta_{kj} \tag{9.6}$$

$$E < \mathbf{v}_k, \mathbf{w}_j^T >= 0 \tag{9.7}$$

where $\mathbf{R}_k$ and $\mathbf{Q}_k$ are the covariance matrices of the measurement and process noise sequences at time t_k.

The Kalman filter estimates a process by using a form of feedback control in two steps:

- prediction step: the Kalman filter produces estimates of the current state variables, with their uncertainties;
- correction step: once the outcome of the next measurement is acquired, these estimates are updated using a weighted average.

As such, the equations for the Kalman filter can be divided into two groups: time update equations and measurement update equations. The time update equations are responsible for projecting forward the current state and error covariance estimates in order to obtain a priori estimates for the next time steps

$$\hat{\mathbf{x}}_{k|k-1} = \Phi_{k,k-1}\hat{\mathbf{x}}_{k-1|k-1} \tag{9.8}$$

$$\mathbf{P}_{k|k-1} = \Phi_{k,k-1}\mathbf{P}_{k-1|k-1}\Phi_{k,k-1}^T + \mathbf{Q}_{k-1} \tag{9.9}$$

where the $\hat{\mathbf{x}}_{k|k-1}$, indicates the predicted $\mathbf{x}$ at timet_k computed using $[z_0; \cdots z_{k-1}]$ measurement samples and $\mathbf{P}_{k|k-1}$ is the associated algebraic Riccati equation solution.

In order to obtain a posteriori estimates, the measurement update incorporates a new measurement into the *a priori estimates* :

$$\mathbf{K}_{k|k} = \mathbf{P}_{k|k-1}\,\mathbf{H}_k^T\,(\mathbf{H}_k\,\mathbf{P}_{k,k-1}\,\mathbf{H}_k^T + \mathbf{R}_k)^{-1} \tag{9.10}$$

$$\hat{\mathbf{x}}_{k|k} = \Phi_{k,k-1}\hat{\mathbf{x}}_{k-1|k-1} + \mathbf{K}_k(\mathbf{z}_k -) \tag{9.11}$$

$$\mathbf{P}_{k|k} = \mathbf{P}_{k|k-1} - \mathbf{K}_k\,\mathbf{H}_k\,\mathbf{P}_{k|k-1} \tag{9.12}$$

where $\Phi_{k-1} = \Phi_{k,k-1}$, $\hat{\mathbf{x}}_k(+) = \hat{\mathbf{x}}_{k|k}$ and $\hat{\mathbf{x}}_{k,k-1} = \hat{\mathbf{x}}_k(-)$.[1]

The algorithm is recursive using only the present input measurements, the previously calculated state and its uncertainty matrix. The recursive nature of the algorithm makes it easily implementable in a digital processing system. In the next figure a block diagram of the estimation process is shown.

[1] In the notation the symbol $(-)$ and $(+)$ are used to indicate respectively an extrapolation and an update.

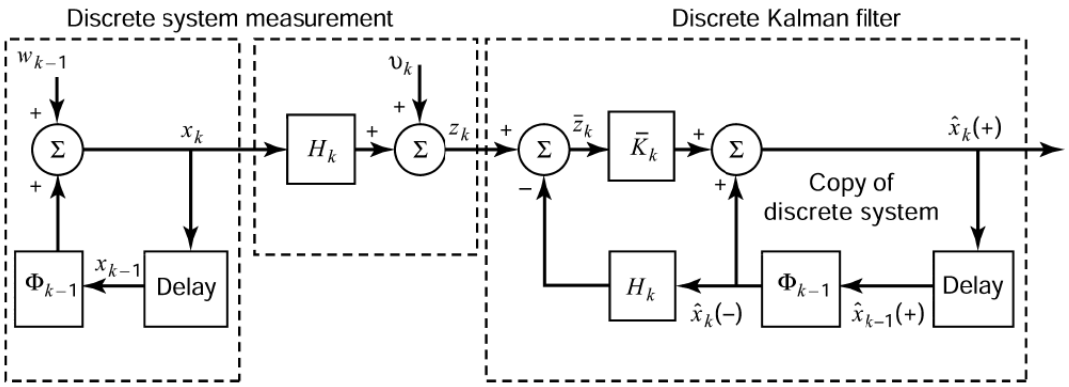

Figure 9.1: Block diagram of a system, its measurement model, and its associated discrete-time Kalman filter [59].

Kalman filters are commonly used for the development of optimal dynamic regulators through the LQG design.

9.2 SIMO and MIMO system identification for AdV suspension

In AdV top stage suspension system we have:

-three horizontal real or virtual actuators;

-three horizontal real or virtual accelerometers;

-three horizontal real or virtual LVDTs;

-two vertical real and one virtual actuators;

- two vertical real and one virtual accelerometer, one real LVDT [2].

By choosing appropriately the reference frame, inputs and outputs, the system can be considered SISO or MIMO.

Since in the sensor reference frame, the system is MIMO system for all d.o.f in the VRF we can choose to treat the system with four SISO models (choice adopted to control the system with the blending strategy) or as a MIMO model. Considering its complexity, in both reference frames, the modeling of the superattenuator as a MIMO system is very hard.

Since in the VRF the main source of disturbance are longitudinal along VRF and uncorrelated to each other, we preferred to generate a mechanical state-space model maintaining the sensor diagonalization. This choice simplifies the modeling of the seismic noise which is one of the fundamental requirement to design an effective Kalman estimator.

[2] With real sensor (or real actuator) we refer to the device placed on the top stage ,while with Virtual sensors (or virtual actuators) we refer to the devices obtained through the diagonalization procedure illustrated in Chapter 7.

Since in our case, the angular-longitudinal mechanical couplings for the vertical and longitudinal d.o.f of the superattenuator are very low, we can assume that all d.o.f of the superattenuator are independent. Therefore in first approximation, and in the frequency range of interest $0.01 \div 10 Hz$, we can generate a MIMO model connecting in series or in parallel n SISO models.

9.2.1 Modeling of the mechanical response of SA

We are going to estimate a *Mechanical Plant* model for the AdV superattenuattor using the pole-zero representation and convert it to state-space format [10, 14]. In frequency domain a zero-pole model transfer function is given by [60][17]

$$TF(\omega) = \rho \frac{\prod_i^n (\omega - z_i) \cdot \prod_i^n (\omega^2 + \frac{1}{Q_{i,}} \omega_i \omega + \omega_i^2)}{\prod_j^m (\omega - p_j) \cdot \prod_j^m (\omega^2 + \frac{1}{Q_{j,}} \omega_j \omega + \omega_j^2)} \tag{9.13}$$

Where ω_i and ω_j are the proper frequencies of the zeros and poles, $Q_{i,}$ and $Q_{j,}$ are the quality factors associated to zeros and poles, and ρ is the gain of the function at a certain frequency (f_ρ).

In order to have an identification of the system, we must find: ρ gain and f_ρ gain frequency, the zeros: $Z_0 = [z_1, \cdots, z_n]$, $Z_{q_0} = [q_{z_1}, \cdots, q_{z_n}]$, the poles: $P_0 = [p_1, \cdots, p_m]$, $P_{q_0} = [q_{p_1}, \cdots, q_{p_m}]$. To estimate the best fit parameters (zeros, poles and q) using this kind of modeling for the superattenuator transfer function, we have developed a MATLAB script, based on the *fminsearch* command, which outputs a list containing the optimized parameters [51]. In this script setting the frequency range to fit the experimental transfer functions for the model and inserting the list of initial parameters we are able to fit the experimental transfer functions $fit(\omega)$ with a 10^{-3} error[3]. To generate a SISO model in state space (*ss*) format first we have to convert the AdV *zpq* model into *ss* format. This conversion is made using MATLAB.

To produce a more complex multiple-input and multiple-output system we can connect in series or in parallel the identified SISO models using Simulink. Using this approach is possible to generate SIMO or MIMO models in order to reproduce the overall mechanical response of the system, neglecting the d.o.f cross coupling.

For example an accurate SIMO model with one input and 3 outputs, for the vertical d.o.f of the superattenuator, is obtainable putting in parallel the vertical LVDT and accelerometers transfer functions. In the Fig. 9.2, the vertical SIMO model for SR superattenuator, using this method, is shown and compared with the experimental transfer functions.

In the same way a MIMO model with 2 inputs and 4 outputs, for the horizontal d.o.f of the

[3] We have defined the estimation error $err(\omega)$ as: $err(\omega) = \frac{|TF(\omega) - fit(\omega)|}{|fit(\omega)|}$

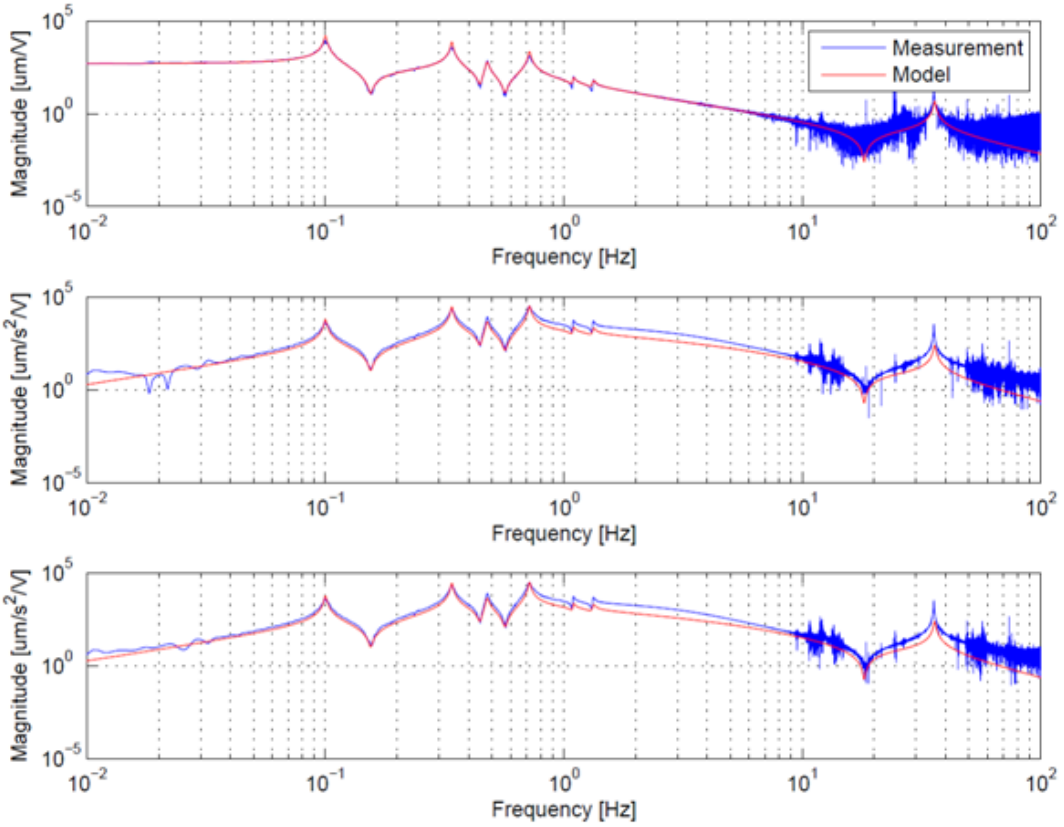

Figure 9.2: In this figure a vertical SIMO model for Adv SR superattenuator, and its comparison with the experimental transfer functions is reported.

superattenuator, is obtainable connecting in parallel the diagonalized LVDTs and accelerometers along x and z axis in the VRF.

9.3 Process and measurement noises

To design a Kalman estimator process and measurement noise models are required. As starting point we made the assumption of having only the process noise as "colored noise" while measurement noise is assumed to be white. In order to generate a complete system that includes also the process and measurement noise models, it is enough adding and linking the individual SISO models (see Fig. 9.3).

In figure 9.3 the Simulink diagram of the SISO model of the Filter0 accelerometers including all the process noises (sys_seism block, sys_alpha block) is reported. This is a simple case to test and implement this kind of strategy; the dimension of the overall system is 3x1: one deterministic input (force applied) , two stochastic inputs (the process noises) and one output (the sensing element displacement). The related number of states is four: one represents the

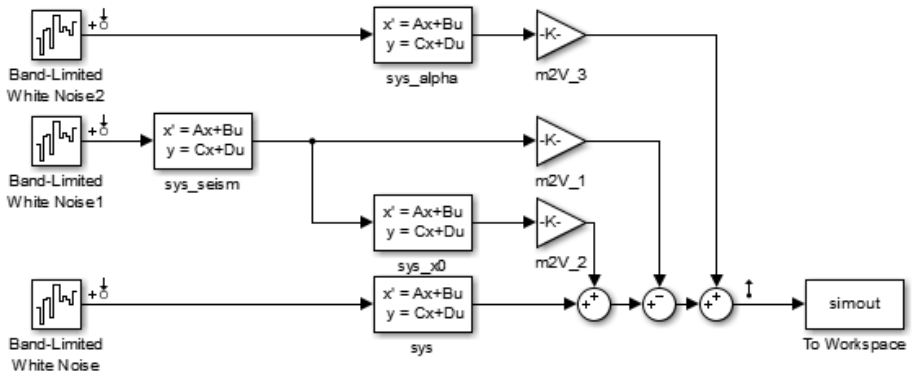

Figure 9.3: In this Simulink diagram a simple SISO model of the accelerometers including all the process noises (sys_seism block, sys_alpha block) is reported.

resonance mode of the sensing element, while other three are the associated states with the process noises. In Fig. 9.4 the bode diagram of the Simulink model shown in Fig. 9.3 is reported.

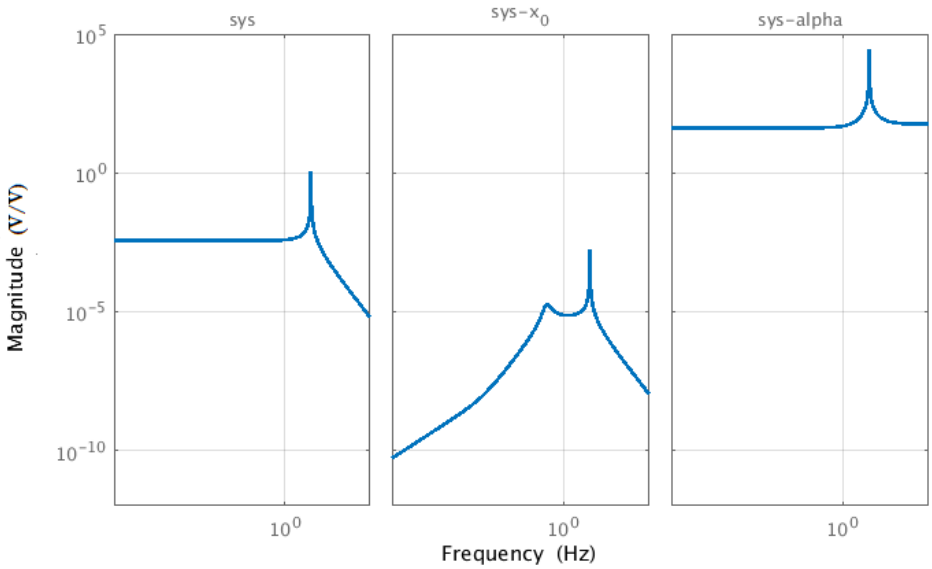

Figure 9.4: The accelerometer model shown in Fig. 9.3: from left to right the mechanical transfer functions, the seismic and tilt process noises are shown.

Using this approach we can build more complex systems. A similar procedure has been used to model the SIMO system, including its associated process noises, of the vertical d.o.f of the Signal Recycling (SR) suspension.

The used model of seismic disturbance are reported in Fig. 9.6. These models are based on

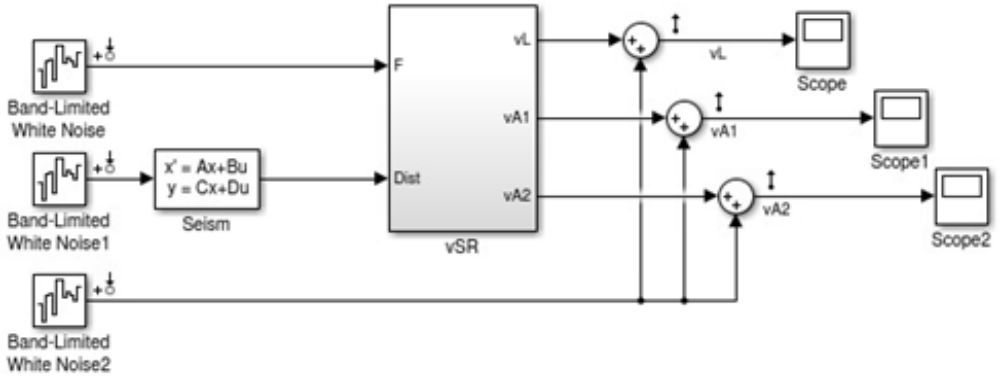

Figure 9.5: In this Simulink diagram of the SIMO model for the AdV vertical d.o.f. (vSR) including also the process noise (seism block) is reported.

the typical spectra of the data measured by the Guralp sensors installed in several locations at EGO site.

Using this procedure we can also add a non-white model of the measurement noise. This has been done for the vertical d.o.f. of the SR suspension and in Fig.9.7, the bode diagram of this complex SIMO model is reported vertical.

9.4 Model reduction: balanced truncation

Since the order of the estimated models is very high (for example the complete model shown in Fig.9.7, has 112 states), in order to implement the associated Kalman filters in the AdV DSP architecture a reduction is needed. A common approach for obtaining a reduced order system is known as *Balanced truncation* [75]. In this approach, a new state-space description is obtained so that the controllability and observability gramian matrices are diagonalized. This defines a new set of invariant parameters known as Hankel singular values.

In order to apply the balanced truncation and to determine if all the state vector components of our estimated model can be sensed and controlled, we have to calculate the system gramian matrices of observability and controllability

$$\mathbf{O} = \int_0^\infty dt\, e^{\mathbf{A}^T t}\mathbf{C}\mathbf{C}^T e^{\mathbf{A}^T t} \qquad \mathbf{C} = \int_0^\infty dt\, e^{\mathbf{A}^T t}\mathbf{B}\mathbf{B}^T e^{\mathbf{A}^T t} \tag{9.14}$$

where $\mathbf{O}$ and $\mathbf{C}$ are symmetric and since the realization is minimal they are also positive definite. The eigenvalues of the product of the controllability and observability gramians play

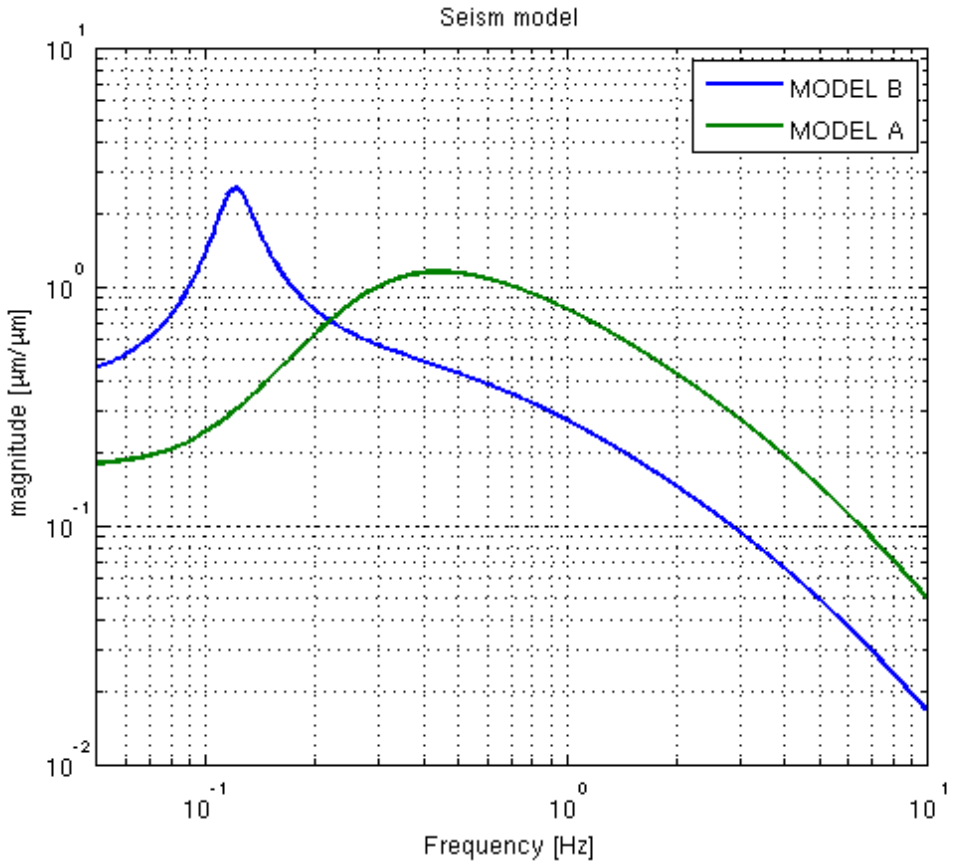

Figure 9.6: We show here two seismic noise models based on typical variation measured by the Guralp velocimeters installed on EGO site. Model A is shaped with a typical bump around $300\,mHz$, while Model B shows a pronunced peck around $100\,mHz$, related to the Atlantic ocean , that is more evident in the winter season on the vertical seismic channel.

an important role in control theory, since we have that

$$\sigma_i = \sqrt{\lambda_i(\mathbf{CO})} \tag{9.15}$$

This set of eigenvalues is called the *Hankel singular values* and gives us an estimate of the energy content of each state vector component.

Let's consider a balanced base in which the exist a matrix Σ including the Hankel singular values written as

$$\Sigma = \begin{pmatrix} \Sigma_1 & 0 \\ 0 & \Sigma_2 \end{pmatrix} \tag{9.16}$$

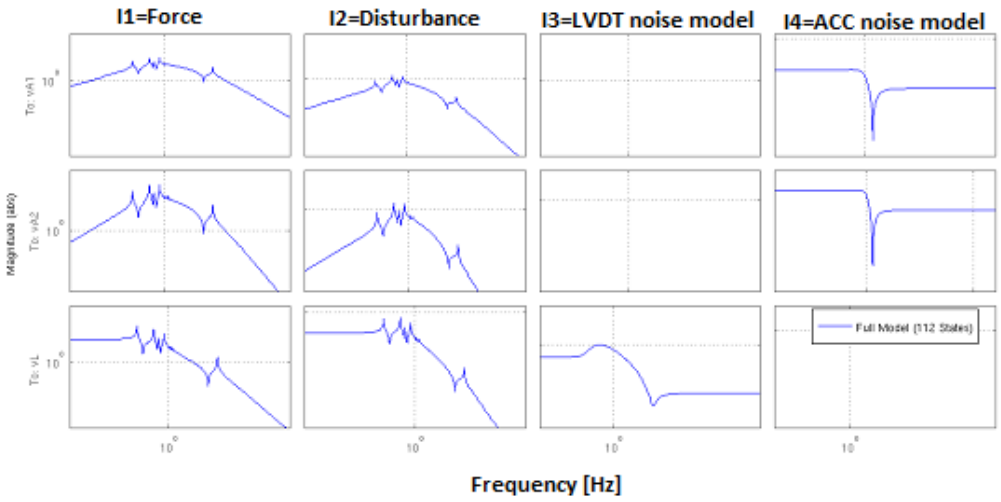

Figure 9.7: Example of full SIMO model for vertical d.o.f of AdV SR superattenuator

The related representation of the system in this base can be written as

$$\hat{A} = \begin{pmatrix} A_{11} & A_{12} \\ A_{21} & A_{22} \end{pmatrix} \quad \hat{B} = \begin{pmatrix} B_1 \\ B_2 \end{pmatrix} \quad \hat{C} = \begin{pmatrix} C_1 & C_2 \end{pmatrix} \tag{9.17}$$

In this base Σ_2 is a submatrix containing only the small Hankel singular values. Using this representation, we can reduce the order of the system with a simple **truncation**

$$\Sigma = \begin{pmatrix} A_{11} & B_1 \\ C_1 & \end{pmatrix} \tag{9.18}$$

This truncation leads to a balanced reduced-order system. The truncated system contains only the largest singular values λ_i of the system transfer function.

Once we have identified the low energy components of the system by plotting its Hankel singular values, we can truncate them using the procedure just described.

Now we would like to obtain coordinate transformation, T , that results in a realization for which the controllability and observability gramians are equal and diagonal. Thus, the diagonal entries of the transformed controllability and observability gramians will be the Hankel singular values $\mathbf{Q} = \mathbf{O} = diag(\sigma_1, \cdots \sigma_n)$. With the coordinate transformation T the new **balanced reduced** system is given by

$$sys_{red,bal} = \begin{pmatrix} T^1 A_{11} T^{-1} & TB_1 \\ C_1 T^{-1} & \end{pmatrix} = \begin{pmatrix} \hat{A}_1 & \hat{B}_1 \\ \hat{C}_1 & \hat{D}_1 \end{pmatrix} \tag{9.19}$$

In this way we have reduced the system. By using the transformation T_c the system can be putted in modal representation: that is a canonical form in which the real eigenvalues of the $\hat{A}_{mod}$ matrix appear on its diagonal, and the complete conjugate eigenvalues appear in 2x 2 blocks on its diagonal

$$\hat{A}_{mod} = \begin{pmatrix} \lambda_1 & & & & & & 0 \\ & \sigma_1 & \omega_1 & & & & \\ & -\omega_1 & \sigma_1 & & & & \\ & & & \ddots & & & \\ & & & & \lambda_k & & \\ & & & & & \sigma_s & \omega_s \\ 0 & & & & & -\omega_s & \sigma_s \end{pmatrix} \tag{9.20}$$

After these transformations our system will be: **reduced and in modal form**. This computation has been implemented in a MATLAB script and applied to the system shown in figure 9.7. In this way we have reduced the number of states from 112 to 29 not altering the frequency response of the system. In figure 9.8 an histogram of the Hankel singular values related to the system full model and the relative comparison between the number of states before and after the balanced reduction (Fig. 9.9) are shown.

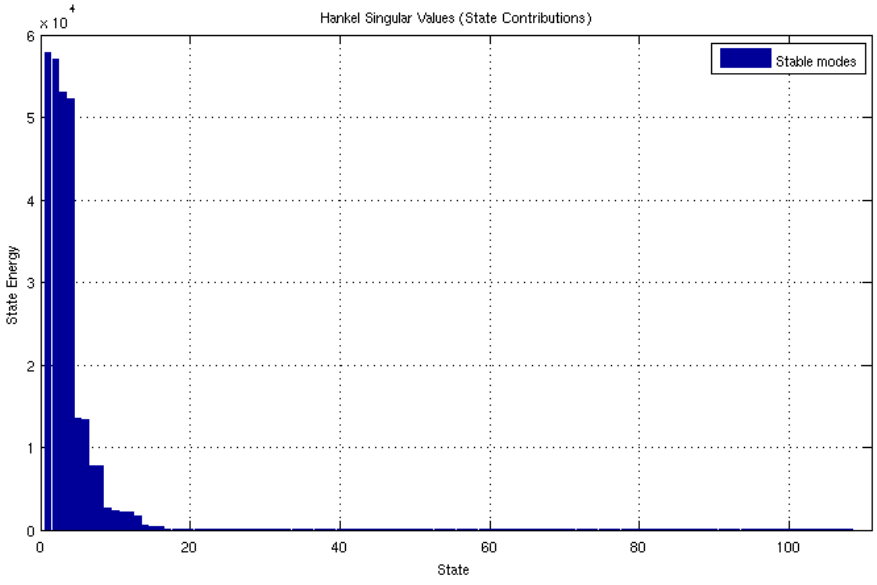

Figure 9.8: Histogram of the Hankel singular values of the full system of figure 9.7

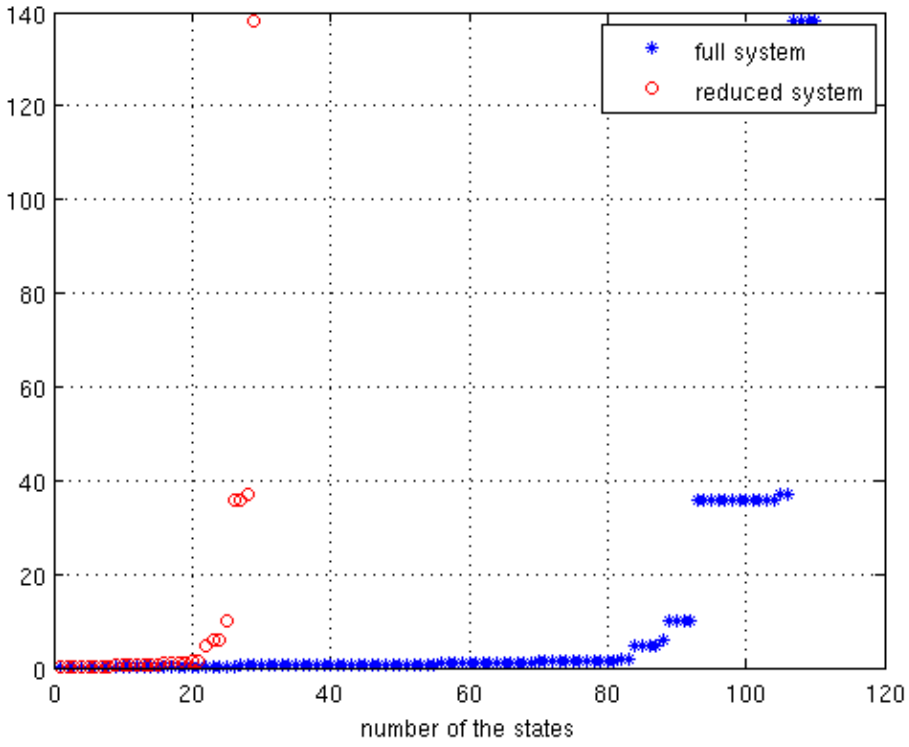

Figure 9.9: Plot showing the energy contribution of each state of the system shown in figure 9.7 before (blue stars) and after the balanced truncation (red circles). We see that the truncation algorithm, in agreement with the Hankel singular values, deletes the redundant states with low and high energy content and preserves only the observable and controllable states.

9.5 Linear-quadratic-Gaussian control

In control theory, LQG control problem is one of the most fundamental optimal control problems [49]. An LQG controller is a combination of a Kalman filter with a linear-quadratic regulator (LQR). The so-called separation principle [60] guarantees that both systems can be designed and computed independently: this property is a consequence of the fact that the eigenvalues of the closed loop system are given by the eigenvalues of the state estimator together with those of the regulator.

Let's be consider the equations (9.1) and (9.2) . The quadratic cost function $\mathbf{J}$ to be minimized is

$$\mathbf{J} = \sum_{k=0}^{\infty} (\mathbf{x}_k^t \mathbf{Q}_k^c \mathbf{x}_k + \mathbf{u}_k^t \mathbf{R}^{\mathbf{c}}{}_k \mathbf{u}_k) \tag{9.21}$$

where $\mathbf{Q^c}$ is the cost matrix for the states of the system and $\mathbf{R}^c$is the control effort. The matrix

$\mathbf{Q^c}$ gives us an estimate of the weight of the final state of the system while $\mathbf{R}^c$matrix can be used to tune the feedback intensity force.

The equations describing a discrete LQG regulator are

$$\hat{\mathbf{x}}_{k+1} = \mathbf{A}_{k,k}\hat{\mathbf{x}}_k + B_k\mathbf{u}_k + \mathbf{K}_{k+1}\left[\mathbf{z}_{k+1} - \mathbf{C}_k\left(\mathbf{A}_{k,k}\hat{\mathbf{x}}_k + B_k\mathbf{u}_k\right)\right] \tag{9.22}$$

$$\mathbf{u}_k = -\mathbf{L}_k\hat{\mathbf{x}}_k \tag{9.23}$$

where $\mathbf{K}$ is the Kalman gain matrix defined in the Eq. (9.2) and $\hat{\mathbf{x}}_k$ is the Kalman state estimate.

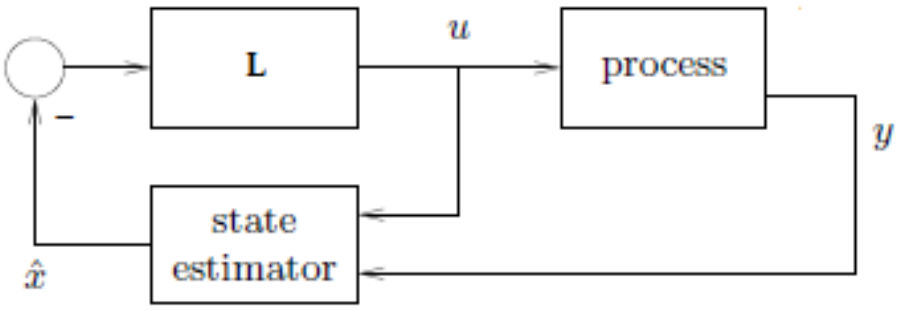

Figure 9.10: Block diagram of a system controlled with an LQG regulator. The process input and output signals u and y are the inputs of an estimator (Kalman filter). The estimated states $\hat{\mathbf{x}}$ are used to close the feedback through the optimal vector gain L.

This problem is a classical variational problem in which the dynamics of the physical system is determined by a variation of a functional, in this case the cost function $\mathbf{J}$. The condition $\delta J = 0$ impose that the system equations (9.22), (9.23) admit the following solution

$$\mathbf{L}_k = (B_k^T S_{k+1} B_k + R_k^c)^{-1} B_k^T S_{k+1} A_k \tag{9.24}$$

$$\mathbf{S}_k = A_k^T (S_{k+1} - S_{k+1}(B_k^T S_{k+1} B_k + R_k^c)^{-1} B_k^T S_{k+1}) A_k + \mathbf{Q}_k^c \tag{9.25}$$

where $\mathbf{L}_k$ is the optimal feedback gain matrix and $\mathbf{S}_k$ is the associated algebraic Riccati equation solution [79].

This kind of approach can be used to control systems with arbitrary dimensions both SISO or MIMO.

9.6 Design of the LQG

The reduced model generated using balanced truncation has been used to design the relative Kalman filter and LQG controller. This operation can be done using a MATLAB script . Using the MATLAB command *@kalmd* we can design a discrete-time Kalman estimator.To use this command, the required arguments are:

1) reduced system in state space format;

2) the covariance matrix relative to process noise Q;

3) the covariance matrix relative to measurement noise R;

The generated Kalman filter will have $n+1$ inputs and $n+N_s$ outputs, where n is the number of sensors. [4]

To generate the LQR control command MATLAB *@lqr* is used. To design a Linear-Quadratic Regulator (LQR) with this command ,we need:

1) full system in state space format;

2) the cost matrices Q_c and R_c;

The output generated is the optimal gain matrix L, and using it we can finally close the feedback . In Fig. 9.11 the Simulink diagram of the complete control system for vertical d.o.f. of SR suspension is shown. The reference trajectory in the sensor reference frame (LVDT,vA1,vA2) is the input of a set of integrators with optimal gain L_i, that constitutes the tracking part of the LQG controller. For our control system the Eq. (9.23) becomes

$$\mathbf{u}_k = -\mathbf{L}_k \hat{\mathbf{x}}_k - L_i x_i \tag{9.26}$$

The outputs of the integrators are summed to the states estimated by the Kalman filter multiplied by the LQR gain vector $\mathbf{L}_k$. The resulting signal is the feedback force sent to the plant.

9.7 SR LQG control: tuning

The main assumption of the Kalman filter is that the process and measurement noises are Gaussian (white noise). In order to respect this assumption we have to include all disturbance models in the overall mechanical model. In particular, we have to adapt this procedure in the VRF, because in this reference frame we are able to distinguish all disturbances and coupling relevant terms of the AdV suspension [51, 83].

In sec. 9.2 we have seen that starting from mechanical and noise models:

[4] The inputs are n+1 because to estimate the system states the Kalman filter takes as input also the feedback force.

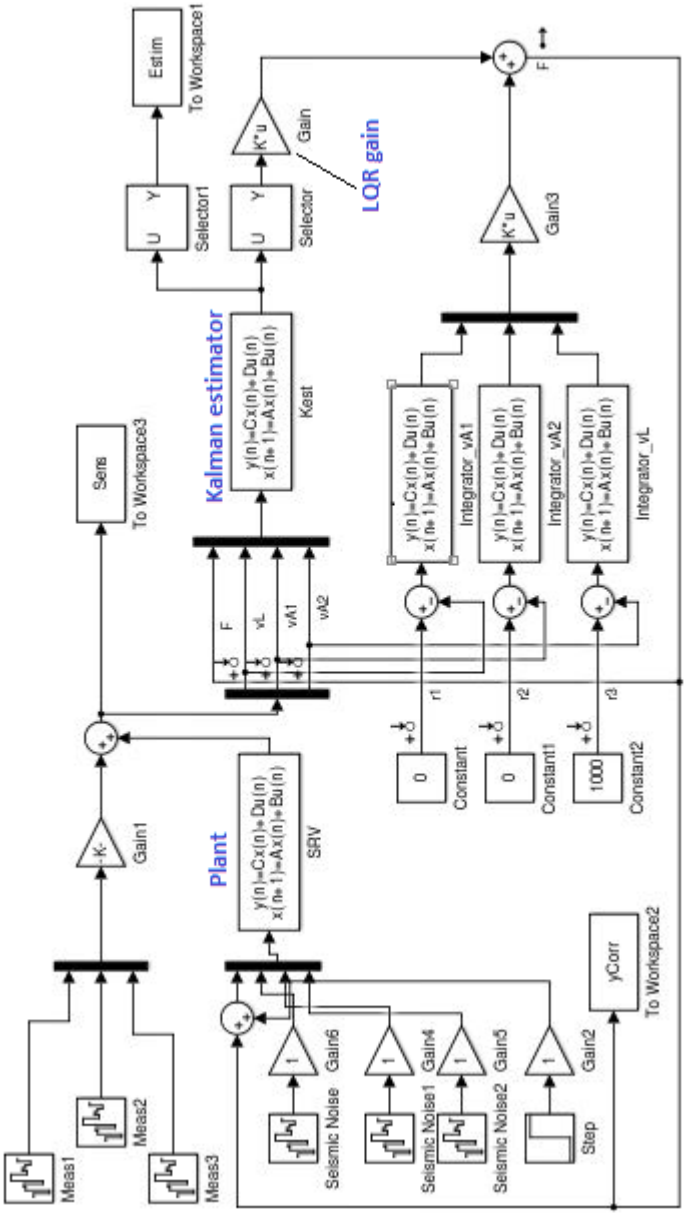

Figure 9.11: Simulink diagram of the LQG SR vertical control system.

1) we can generate an overall MIMO system containing all the mechanical information and noise sources that contaminate the sensors and the system;

2) we can reduce the number of system states using balanced truncation;

3) we can design automatically a stable Kalman filter and an optimal LQG regulator.

Kalman filter could be an automatic way to clean the signal provided by all sensors if we adapt its shape and performance to a change in the noise sources (frequency response, intensity).

If for example, the change is related to the frequency response of seismic noise, in the overall model shown in figure 9.7 we just need to replace the block 'seis' with a new seismic model. After this we generate a new reduced MIMO model and on this design and tune the strategy. If instead the change is related to the intensity of seismic noise, we can express this variation changing the set value of the covariance matrix relative to the process noise Q. In figure 9.6 two examples of seismic noise models are shown.

With each variation of these noise parameters we change the impact of the noise on the system and and as a result we expect to change the frequency response of the Kalman filter and the related LQG regulator.

In any case the output of this variation will be a state space model Kalman filter with $n+1$ inputs and n_f+N, where N is the number of the states overall system (mechanical+disturbances) and n_f is the number of the input sensors cleaned from the noise sources.

In the next subsection we will show how the Kalman filter react on various background conditions, setting different values of Q and R , and on it we will tune the related LQG controller .

To understand and evaluate whether this complete block (Kalman filter +LQG controller) is robust and efficient we will analyze:

- how the designed Kalman filter clean the signal from the noise sources and consequently chooses on which sensor to take the best estimate of a given state. This information can be obtained from the transfer function between input sensor dirtied by the noise and output sensor cleaned. This measurement is important because gives us an idea which sensor uses to make its estimate of physical states;

- how the designed Kalman filter separates and monitors all resonance modes of the system. To select the proper mode of the system within its m outputs, we must compare the A matrices of the full system and of controllable gramian system. The identification is done using a MATLAB script that generates the indices of the physical states of the system. Using this information we look only at the physical states estimated by the Kalman filter;

- We will then design an LQG controller weighting with the appropriate cost matrices, Q_c

and R_c the estimated states of Kalman, and we will evaluate its stability and performance on the system.

9.7.1 Simulation

We show here the simulated results of a vertical SR suspension SIMO model in which we have included only the process noise model while the measurement noises are considered Gaussian (see Fig.9.5). The used SIMO model has 1 force input , 1 disturbance and 3 outputs (1 LVDT and 2 accelerometers posed on the suspension top stage).

To produce a simulation and analyze the behavior and performance of this strategy, we need:

1) a reduced order system with 23 output states;

2) the associated gramian matrices of the mechanical system;

3) the set values Q and R to tune an design the Kalman filter;

4) the cost matrices, Q_c and R_c to tune the LQG controller.

We implement the simulation using MATLAB. The outputs of this simulation are a Kalman filter and the related LQG controller (see Fig.9.11).

According with these three key points mentioned above we plot:

1) the transfer function between input noisy sensors and cleaned output sensors;

2) the transfer function between inputs of the Kalman filter and outputs of the physical estimated states;

3) the closed loop transfer function of the system.

For this model we have produced three different simulations changing only the the set values Q and keeping other values constant.

9.7.1.1 Simulation results

We show here 3 sets of the weighting matrices for the Kalman filter (noise covariance and R) and the related LQG controller for different environmental conditions.

First simulation To reproduce a simulation compatible with a very low seismic noise condition we have set these parameters:

$$\begin{cases} Q = 0.1 \\ R = \begin{pmatrix} 10^{-2} & 0 & 0 \\ 0 & 10^{-4} & 0 \\ 0 & 0 & 10^{-4} \end{pmatrix} \\ Q_c = [s \cdot I^{23\times 23}, diag(1,1,1)] \quad s = 100 \quad R_c = 1 \end{cases} \tag{9.27}$$

In Figures 9.12,9.13 and 9.14 the obtained transfer functions for the set parameters (9.27) are shown.

Looking at these figures we can see that, given the low intensity of the seismic noise, the Kalman filter below $100\,mHz$, and in the range $300 \div 450\,mHz$ uses the signal generated from the LVDT, while in the range $180 \div 300\,mHz$, and above $500\,mHz$ uses the accelerometer signals. In this way the filter is able to better estimate the physical states of the system, that as we can see in the figure 9.13 they are little contaminated by the seismic noise. For this reason the associated regulator uses a low gain to damp the resonances. In the figure 9.14, the closed loop response is shown.

Second simulation In the second simulation, in order to reproduce a condition with a medium intensity of the seismic noise, we have set these parameters:

$$\begin{cases} Q = 1 \\ R = \begin{pmatrix} 10^{-2} & 0 & 0 \\ 0 & 10^{-4} & 0 \\ 0 & 0 & 10^{-4} \end{pmatrix} \\ Q_c = [s \cdot I^{23\times 23}, diag(1,1,1)] \quad s = 100 \quad R_c = 1 \end{cases} \tag{9.28}$$

In figure 9.15,9.16 and 9.17 the obtained transfer functions for the set parameters (9.28) are shown.

Switching the parameter values from (9.27) to (9.28), we can see that this Kalman filter uses the LVDT signal until $700\,mHz$ and uses only the accelerometer signals at higher frequencies (Fig.9.15). In the estimated physical states there is a residual contamination of the seismic

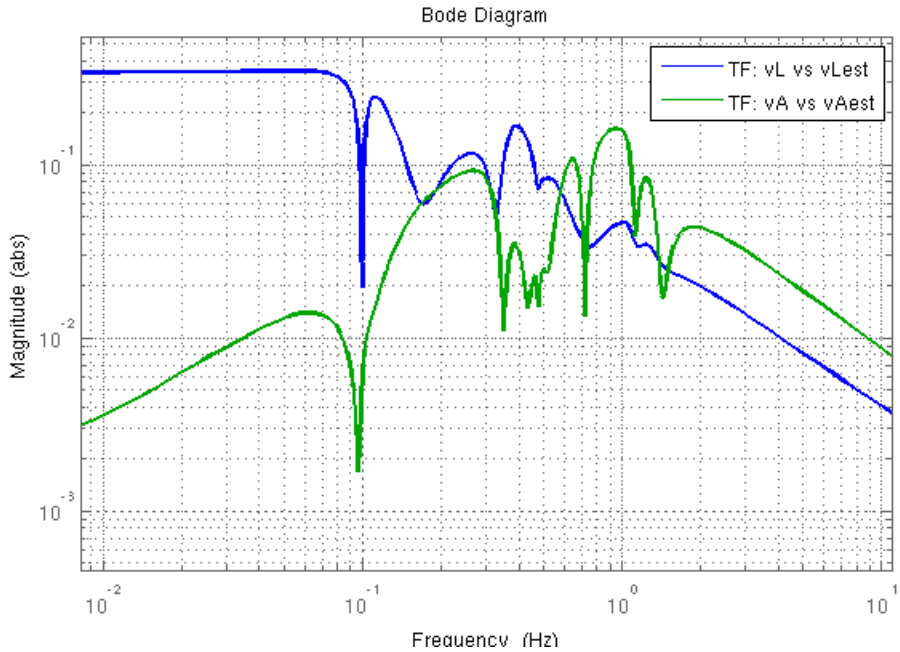

Figure 9.12: Transfer function between the noisy input sensors and output sensors cleaned for the set parameter (9.27)

noise (Fig.9.16) and to reduce this contamination the regulator applies more force: it increases individual gain values related to the most contaminated modes (Fig. 9.17).

Third simulation For the third simulation in order to reproduce a condition with a very intense seismic noise, we have set these parameters:

$$\begin{cases} Q = 20 \\ R = \begin{pmatrix} 10^{-2} & 0 & 0 \\ 0 & 10^{-4} & 0 \\ 0 & 0 & 10^{-4} \end{pmatrix} \\ Q_c = [s \cdot I^{23\times 23}, diag(1,1,1)] \quad s = 100 \quad R_c = 1 \end{cases} \tag{9.29}$$

In the figure 9.18,9.19 and 9.20 the obtained transfer functions for the set parameters (9.29) are shown.

Switching the parameter value from (9.28) to (9.29), we can see that this Kalman filter uses the LVDT signal until $1\,Hz$ and for higher frequencies uses only the accelerometer signals

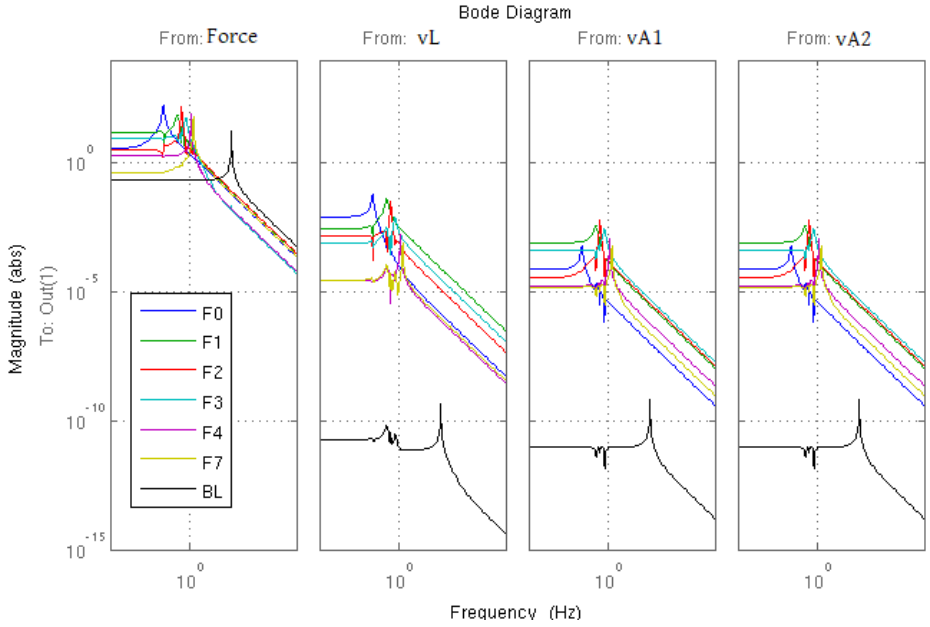

Figure 9.13: Kalman filter: outputs of the physical estimated states for the set parameters (9.27). In abscissa is reported the frequency range [0.01-100] Hz and in ordinate is reported the magnitude $[10^{-15} - 10^{5}]$.

(Fig.9.18). The estimated physical states are contaminated by the seismic noise (Fig.9.19) and to reduce this contamination the regulator applies more force (Fig. 9.20).

9.7.1.2 Full model: simulation results

We show here the last simulation related to the model reported in Fig.9.7.

In this case the Kalman filter will has 4 inputs and 32 outputs where the first 3 outputs are the cleaned sensors and the remaining 29 are the estimates of the states.

To produce a stable Kalman filter and LQG controller we have set these parameters:

$$\begin{cases} Q = 1 \\ R = \begin{pmatrix} 10^{-8} & 0 & 0 \\ 0 & 10^{-8} & 0 \\ 0 & 0 & 10^{-8} \end{pmatrix} \\ Q_c = [s \cdot I^{29\times 29}, diag(1,1,10)] \quad s = 100 \quad R_c = 1 \end{cases} \tag{9.30}$$

In order to check the goodness of the designed Kalman estimator we have injected into it real

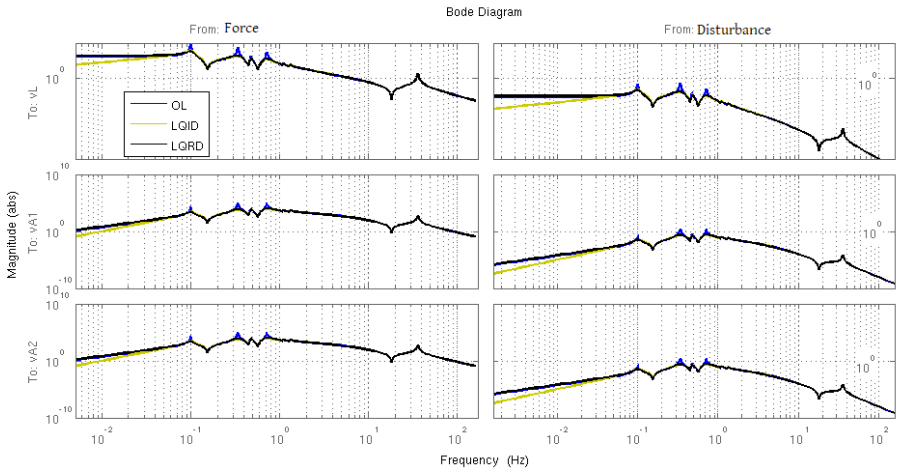

Figure 9.14: Simulated transfer function of the system put in feedback with the LQG controller for the set parameters (9.27). In abscissa is reported the frequency range [0.01-100]Hz and in ordinate is reported the magnitude $[10^{-10} - 10^{10}]$ $\frac{\mu m}{V}$.

the real data acquired through the real sensors of the system and in in Fig. 9.21 the results of this operation is reported [51].

For completeness, also in this case we show the related closed loop transfer function (see Fig.9.22).

9.8 SR LQG control: implementation and experimental results

Last step of the tuning procedure of a control strategy is to test it on a real system[83].

The MATLAB script we developed, generates automatically the estimator state-space and the optimal gain matrix in the Damping software formats. In this way the DSP implementation is straightforward. The chosen sampling frequency of the controller is 10 kHz. In Fig. 9.23, the DSP implementation equivalent to the Simulink diagram 9.11 is reported. We see that the code is extremely simple.

In this section we will show the experimental results of the performance of the Kalman filter and LQG controller designed using the set parameters (9.28).

This test was done in the contest of the AdV commissioning on the vertical d.o.f of the SR top stage. In the next figures the results of this test are shown. In Fig. 9.24 we compare the closed loop transfer function, measured injecting white noise on the SR vertical actuator, with the theoretical one.

While currently on SR, the designed Kalman estimator (Fig.9.25) is running in parallel with

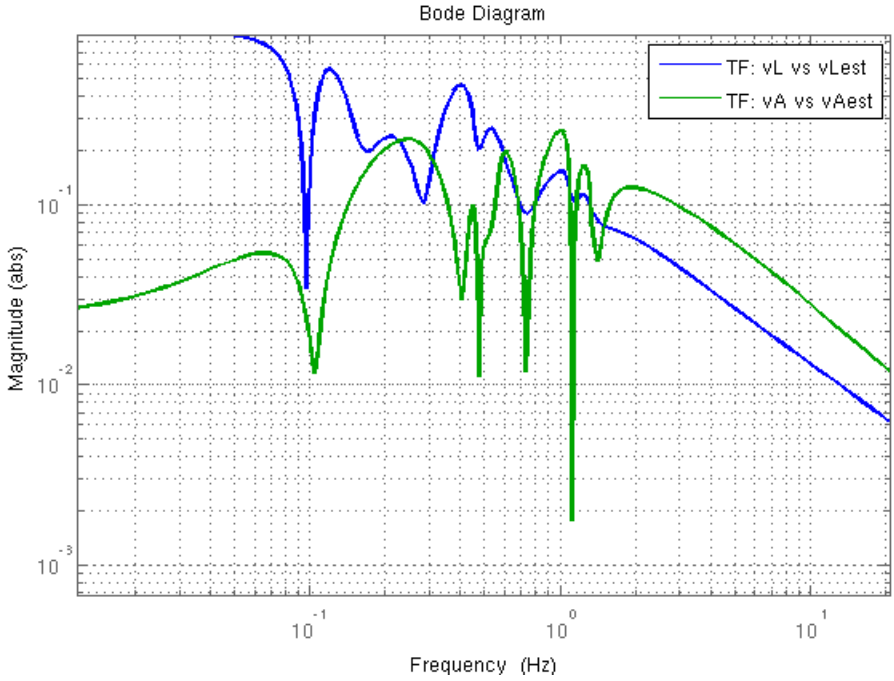

Figure 9.15: Transfer function between the noisy input sensors and output sensors cleaned for the set parameter (9.28)

the traditional controller for monitoring purposes, after the test the standard blended control strategy has been used.

The figure 9.26 shows the comparison between the open loop and closed loop spectra acquired on the three vertical sensors at the level of the top stage: we see that a good damping of the suspension vertical modes is obtained.

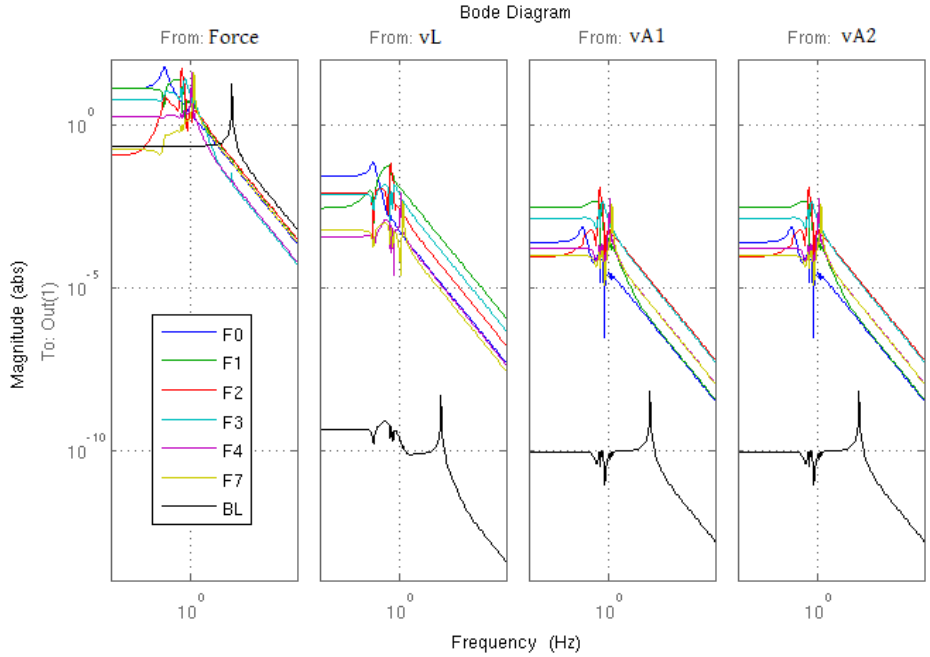

Figure 9.16: Kalman filter: outputs of the physical estimated states for the set parameters (9.28)

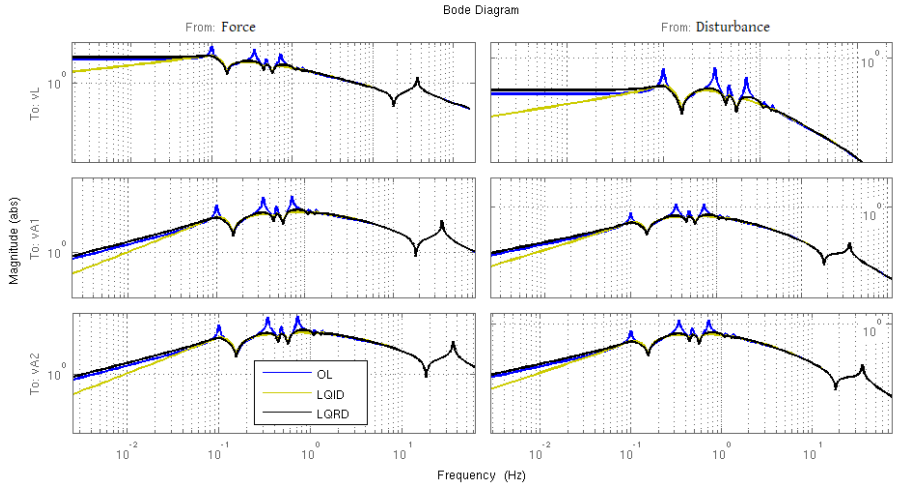

Figure 9.17: Simulated transfer function of the system put in feedback with the LQG controller for the set parameter (9.28). In abscissa is reported the frequency range [0.01-100]Hz and in ordinate is reported the magnitude: $[10^{-2} - 10^{2}]\ \frac{\mu m}{V}$ (colomn on the left) and $[10^{-2} - 10^{1}]\ \frac{\mu m}{V}$ (colomn on the right) .

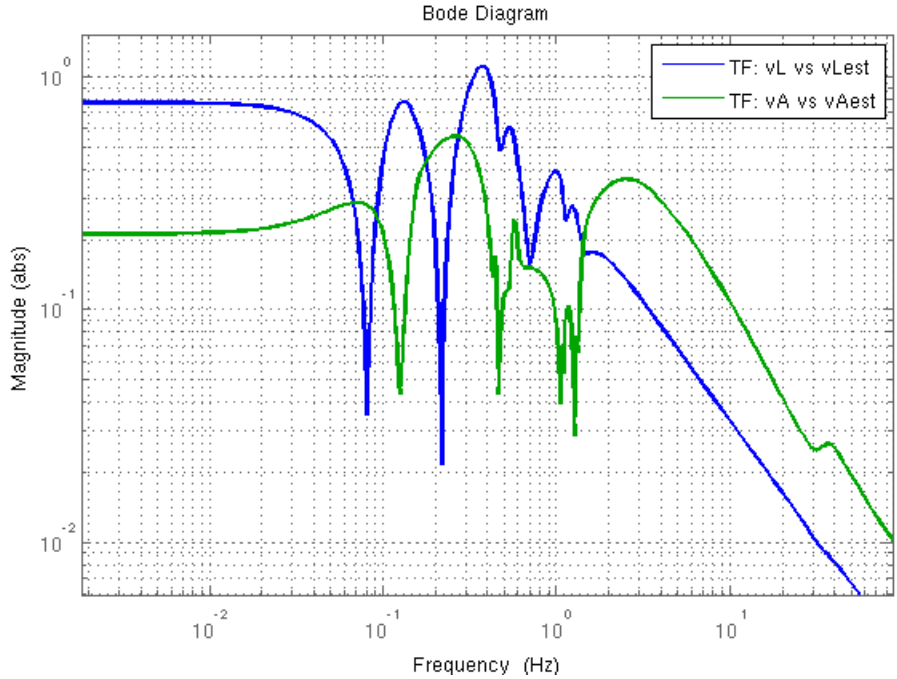

Figure 9.18: Transfer function between the noisy input sensors and output sensors cleaned for the set parameter (9.29)

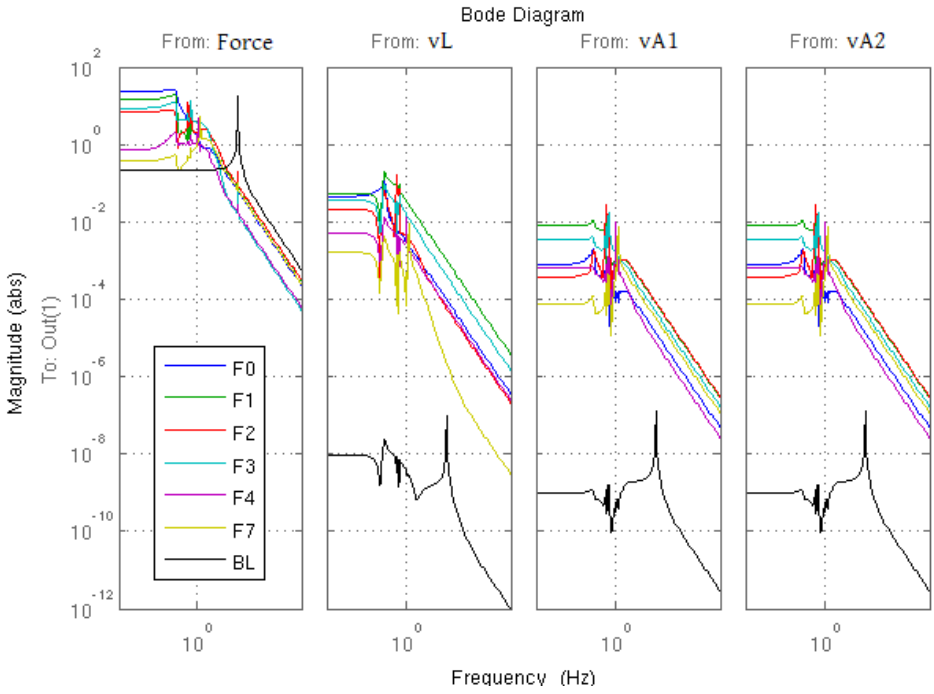

Figure 9.19: Kalman filter: outputs of the physical estimated states for the set parameters (9.29)

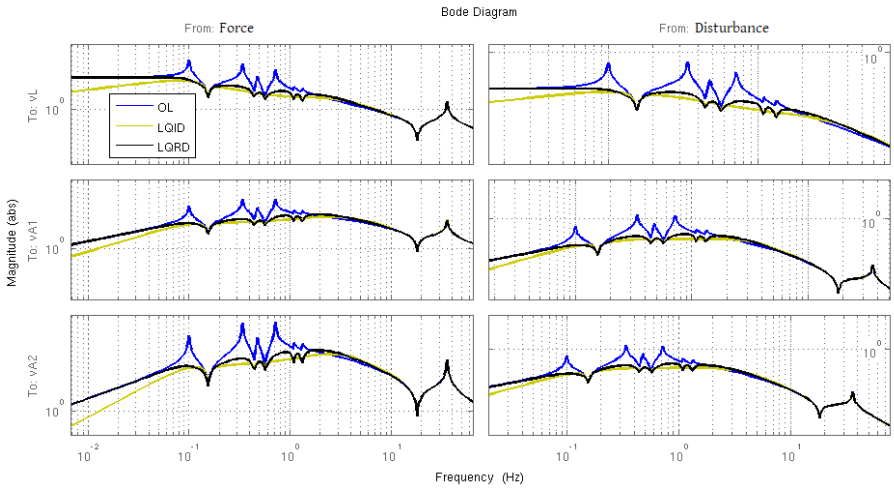

Figure 9.20: Simulated transfer function of the system put in feedback with the LQG controller for the set parameters (9.29). In abscissa is reported the frequency range [0.01-100]Hz and in ordinate is reported the magnitude: $[10^{-2} - 10^{2}]\ \frac{\mu m}{V}$ (colomn on the left) , $[10^{-2} - 10^{1}]\ \frac{\mu m}{V}$ (colomn on the right, second and third rows), $[10^{-3} - 10^{1}]\ \frac{\mu m}{V}$ (colomn on the right, first row).

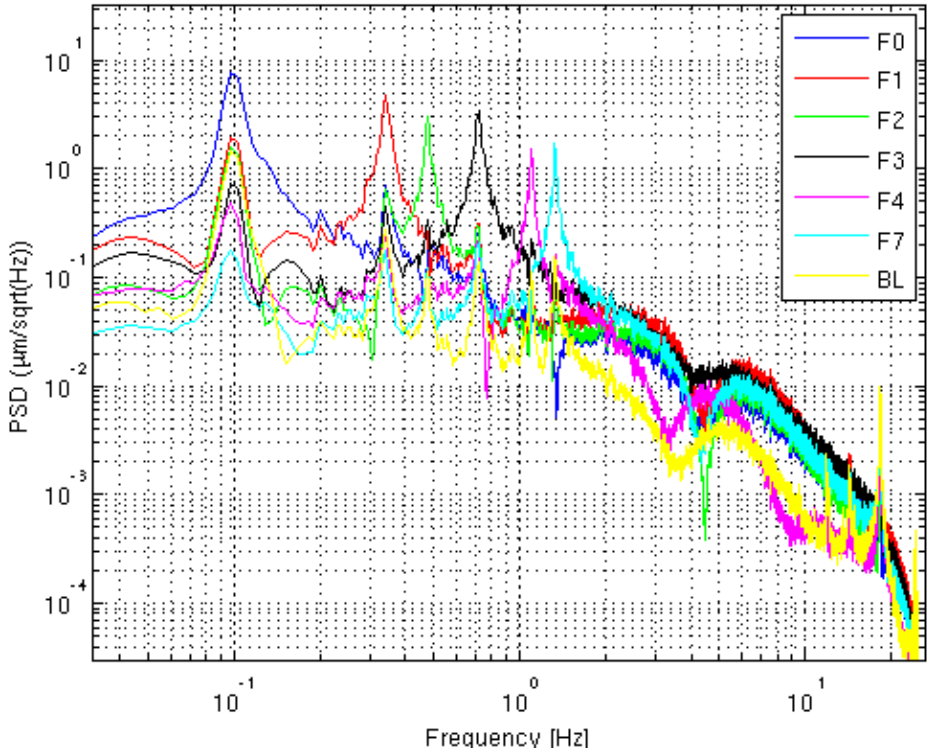

Figure 9.21: Kalman filter state estimation. The data acquired through the real sensors of the system has been injected into it using a MATLAB script. In this figure the PSDs of the estimated states are reported. We see that this filter is able to distinguish all modes with a good level of accuracy [51].

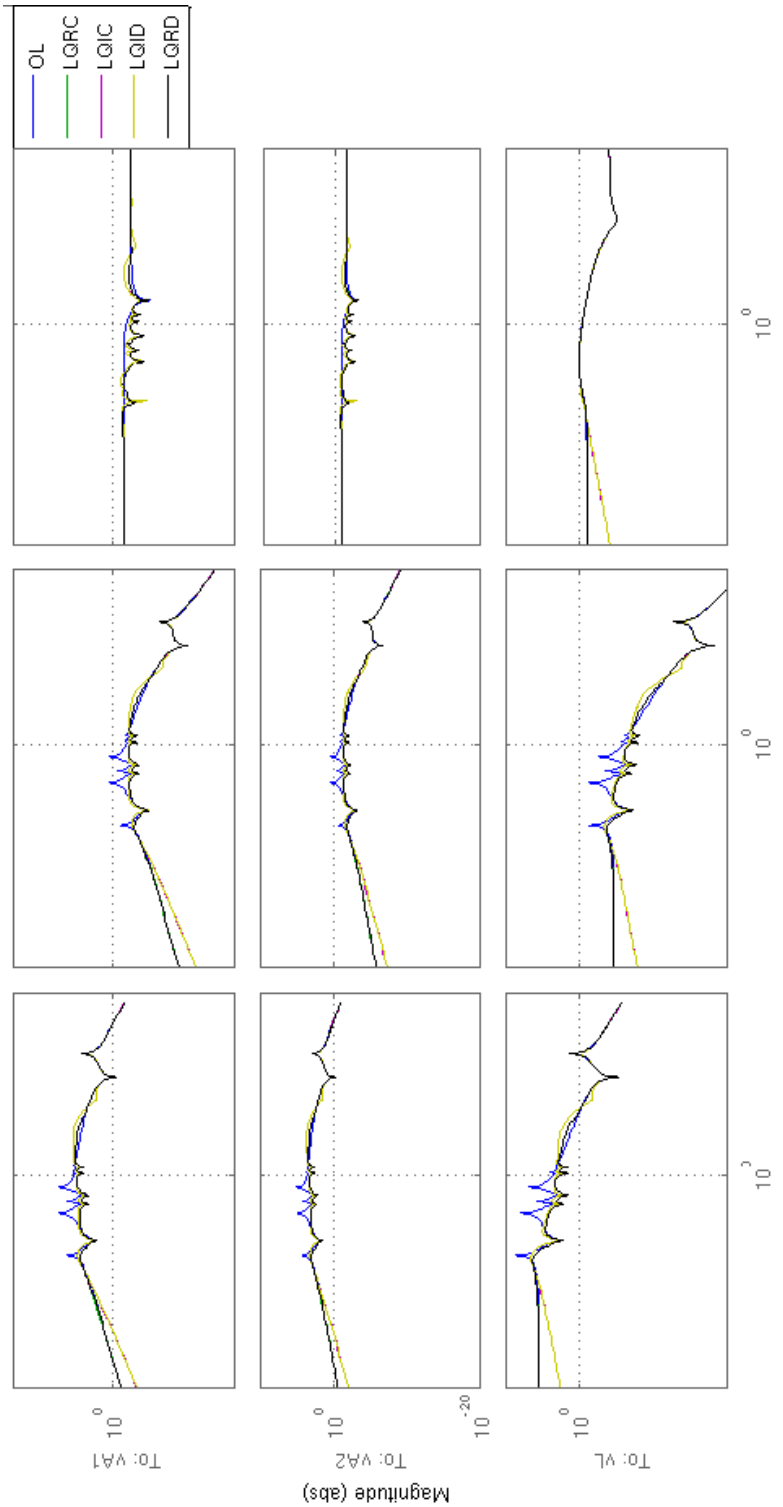

Figure 9.22: Expected performance of an LQG controller for vertical d.o.f AdV superattenuator including also the measurement noise [51]. In abscissa is reported the frequency range [0.01-100]Hz and in ordinate is reported the magnitude: $[10^{-20} - 10^{10}]\ \frac{\mu m}{V}$.

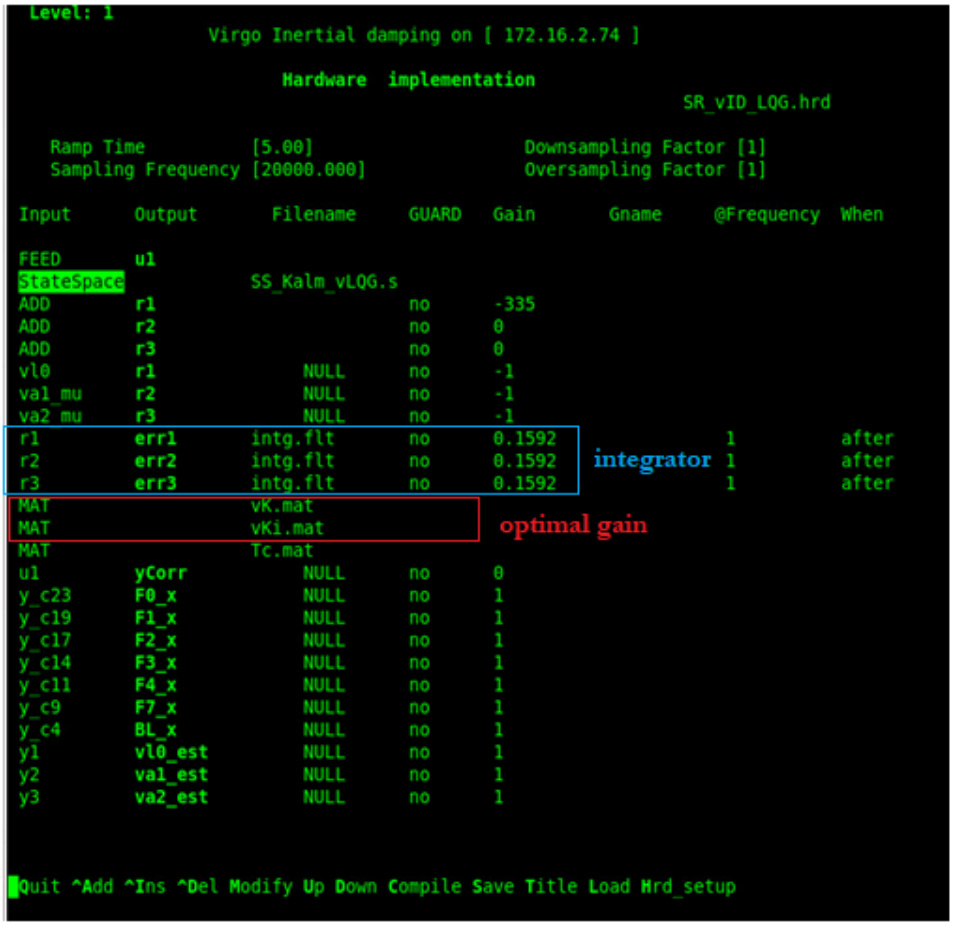

Figure 9.23: Screenshots of the DSP implementation equivalent to the Simulink diagram 9.11 is shown.

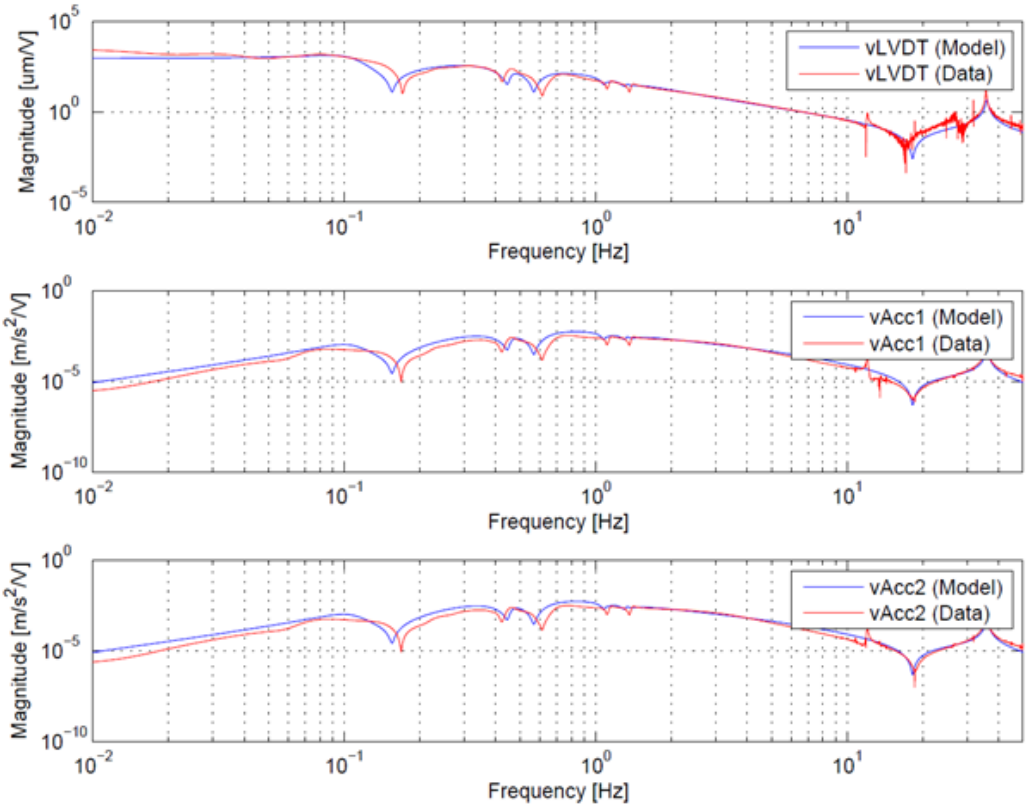

Figure 9.24: Comparison between the theoretical (blue) and the measured closed-loop trasfer function (red).

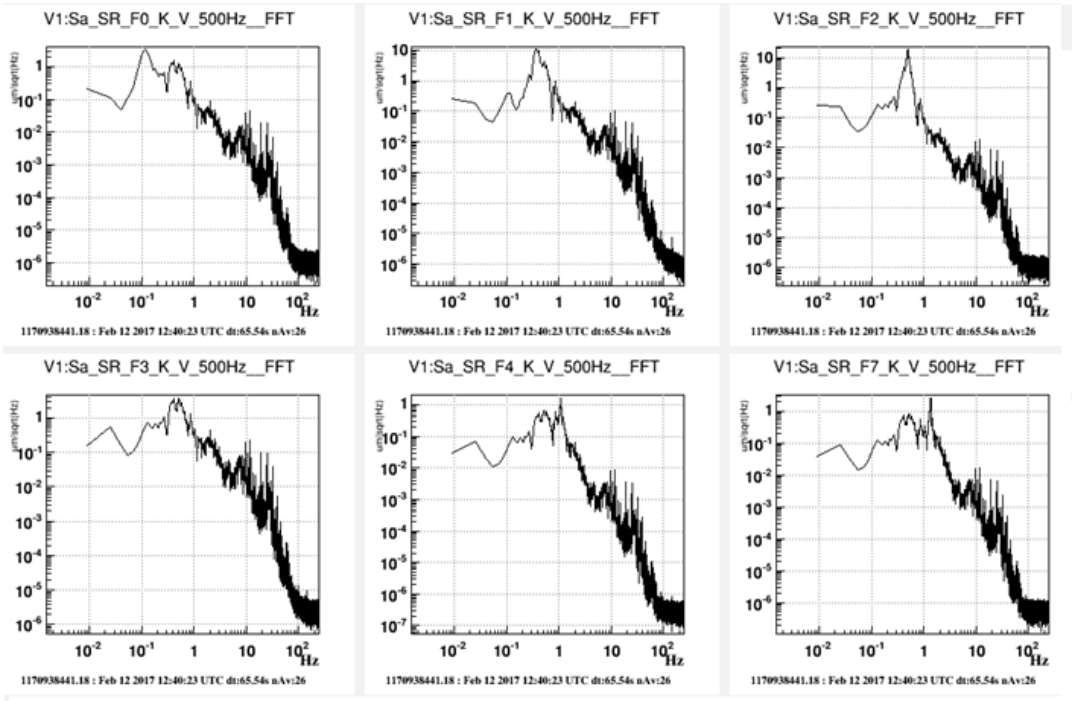

Figure 9.25: Kalman filter states output spectra

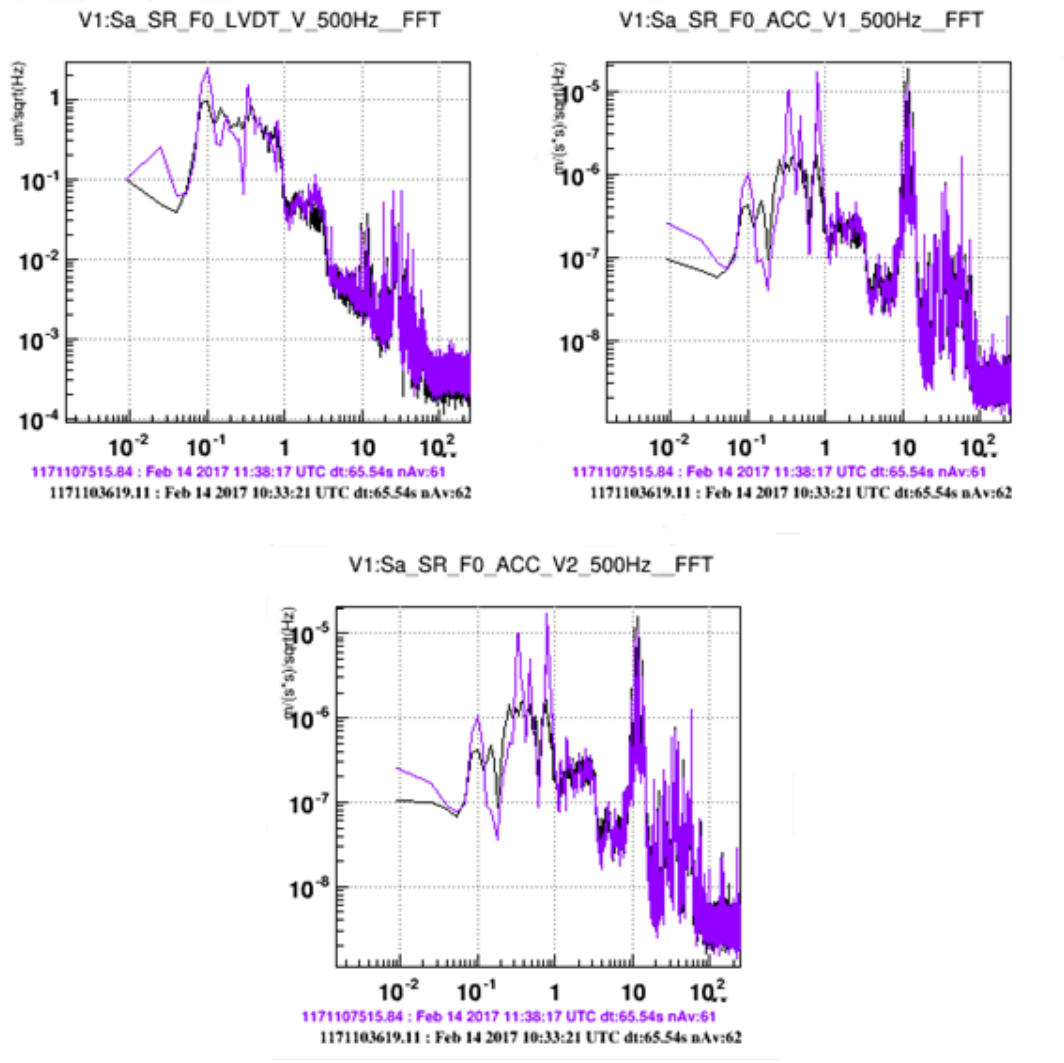

Figure 9.26: Comparison between the open loop (purple curve) and the closed-loop (black curve) spectra acquired on the three vertical sensors at the level of the top stage.

Chapter 10

Suspension control noise

Given the small amplitude of space-time deformation to be measured, gravitational wave detectors have been designed so that all noises sources suitably attenuated or intrinsically low. These noises are generated by many different physical phenomena, and their overall impact defines effectively the detector's sensitivity curve. For this reason the monitoring of the sensitivity curve and the identification of all possible noise sources are required. The dominant noise source is the seismic noise and a sophisticated attenuation system is adopted in Virgo, based on the superattenuator. Expectedly, the seismic noise affects even the performance of the overall system meant to attenuate it, through imperfections present in both the mechanics and the sensing devices used to control it. Thus, specific control strategies accounting the actual characteristics of the system have to be consequently designed in order to attain the highest performance of the overall system.

In Virgo interferometer the signal monitoring the real sensitivity of the interferometer is available starting from about 10 Hz [35, 64]. Below 10 Hz big fluctuations of the angular and longitudinal residual motion of the test masses are large and it is hard to define a sensitivity to gravitational waves. These fluctuations can be caused from seismic noise or a re-injection of it via sensors (LVDT, optical levers, etc..). The estimation of the contamination level due to these fluctuations and the impact of the control loops engaged along the suspension system on the interferometer sensitivity is achievable through a so called noise budget. The aim of the noise budget estimation is to quantify the impact of overall suspension control system on the detector sensitivity curve focusing our attention on the residual motion of the test mass due to the active mode damping control as well as to that due to the angular controls applied on the marionette. In this chapter a procedure to calculate the suspension control noise in the micro-seismic range is presented.

10.1 Virgo detector: sensitivity curve

The effect of the passage of gravitational wave is the variation of the length. For a ground based interferometer this length variation ΔL is defined as

$$\Delta L = D_{arm} \sim X_L^{arm} - Z_L^{arm} \tag{10.1}$$

Looking at the optical layout of the AdV shown in Fig.10.1, the d.o.f. D_{arm} is equal to

$$D_{arm}(t) \sim W_L^{arm}(t) - N_L^{arm}(t) = [(WI(t) - WE(t)) - (NE(t) - NI(t))] \tag{10.2}$$

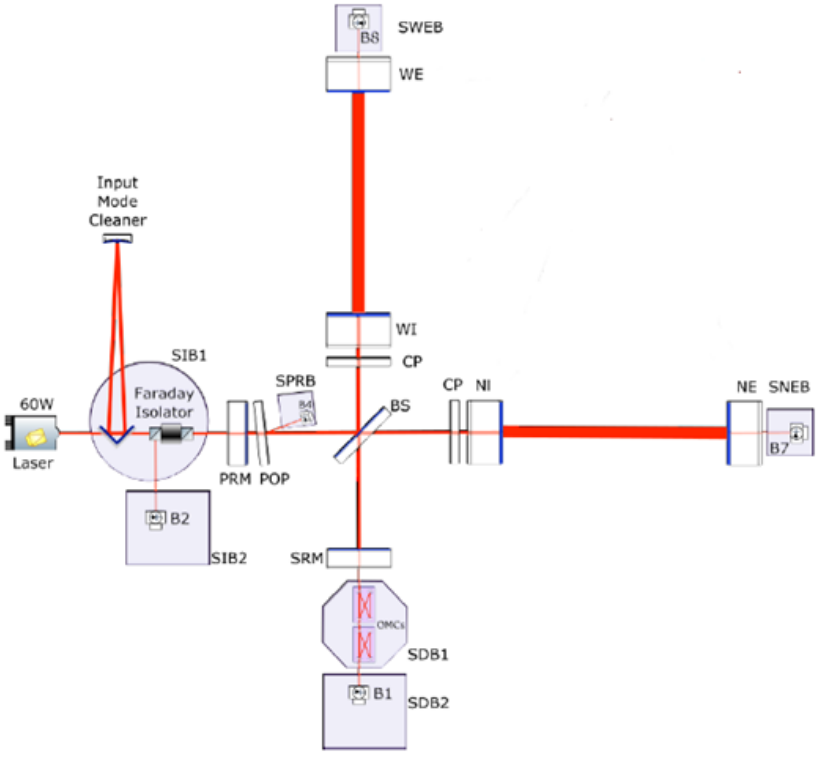

Figure 10.1: AdV optical layout

The signal $D_{arm}(t)$ is related to the strain sensed by the detector $h(t)$ as

$$h(t) = \frac{D_{arm}(t)}{L} \tag{10.3}$$

where L is the Fabry-Perot cavity length and for the Virgo detector is equal to 3 Km. The signal $s(t)$ output of the detector is given by the sum of a gravitational wave signal $h(t)$ and a noise $n(t)$. Assuming that the noise is Gaussian and stationary, we can write the one-sided noise spectral density $S_n(f)$ as

$$\frac{1}{2}S_n(f) = \int e^{2\pi i f} C_n(t)dt \tag{10.4}$$

where $C_n(t)$ is the auto-correlation noise between between time 0 and t.

The strain detector sensitivity $h(t)$ is defined in terms of the spectral density of the noise (10.4)

$$\tilde{h}(f) \equiv \sum_n \sqrt{S_n(f)} \tag{10.5}$$

One way to quantify the effects of the residual noise is through the use of a noise budget, that is a listing of the various sources of noise at a receiver and their associated ranking by importance. In the frequency region $0.1 \div 10 Hz$, the term S_n is connected to the isolation capability from the ground vibrations of the superattenuator and the control filters used to damp its inner modes. Unfortunately, in the region $0.1 \div 10 Hz$ we do not have the signal monitoring the real sensitivity of the interferometer because it is available starting from 9.5 Hz, but we can estimate it using the locking feedback force signal $\tilde{S}_{z,lock}(\omega)$.

The signal $\tilde{D}_{arm}(\omega)$ (see Fig.10.2, (magenta line)) can be deduced from the signal $\tilde{S}_{z,lock}(\omega)$ filtered with the transfer function $\tilde{M}_i(\omega)$ (actuation-displacement along the optical axis of the mirror) .

Indeed, when a loop is engaged and its gain is high, the closed loop signal is given by

$$\tilde{S}_{i,CL}(\omega) = \frac{OL_i(\omega)}{\tilde{M}_i(\omega)\cdot\tilde{C}_i(\omega)} \sim \frac{\tilde{S}_{i,corr}(\omega)}{\tilde{C}_i(\omega)} \tag{10.6}$$

and with a little algebra we can calculate the signal $OL_i(\omega)$

$$OL_i(\omega) \sim \tilde{S}_{i,corr}(\omega)\cdot\tilde{M}_i(\omega) \tag{10.7}$$

In our case there are two $OL_i(\omega)$ signals (because we have two cavity): indeed the signals $\tilde{S}_{z,corr}(\omega)$ is send to the North and the West test masses (NE and WE). For this reason, the $OL(\omega)$ signal , that give us an estimation of the residual fluctuations of $\tilde{D}_{arm}(\omega)$, can be written as:

$$OL(\omega) = \sqrt{(OL_{North}(\omega))^2 + (OL_{West}(\omega))^2} \tag{10.8}$$

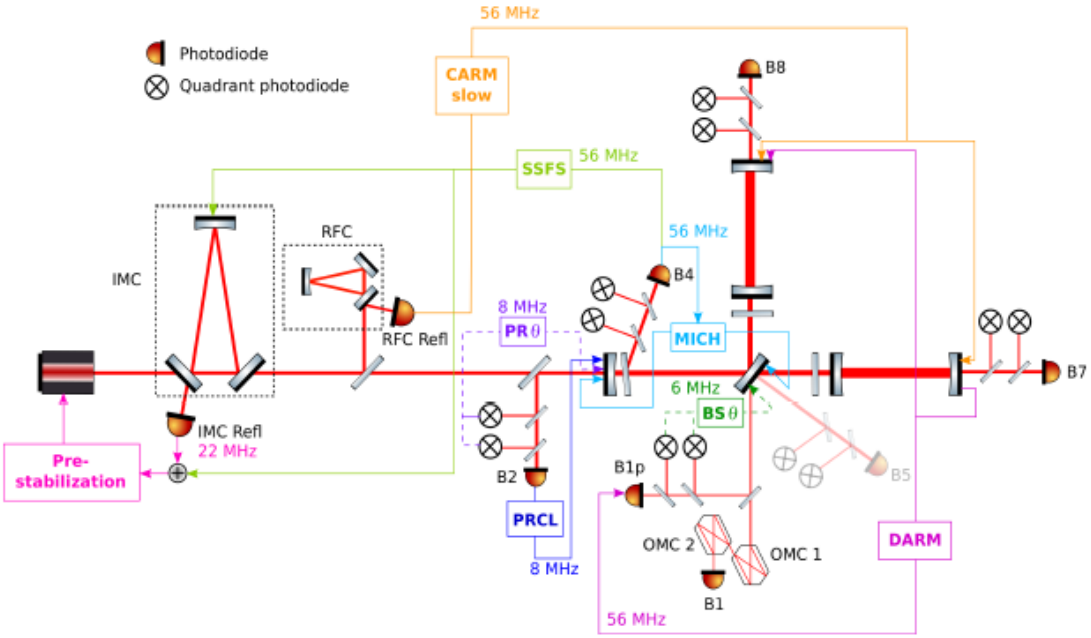

Figure 10.2: Scheme of the longitudinal and angular loops engaged in DF. [18]

By using the Eq. (10.8) we can define a low frequency strain signal as

$$\tilde{h}^{lf}(\omega) = \frac{OL(\omega)}{L} \tag{10.9}$$

Thus, to calculate the signal $OL(\omega)$ we need: the two feedback force signals $\tilde{S}_{z,lock}(\omega)$ (NE and WE) and the transfer function $\tilde{M}_i(\omega)$ (calibrated in $\frac{m}{V}$ for both cavity (see Fig. 10.3)).

10.2 Active mode damping control: residual motion of the test mass

In Chapter 8 we have seen that the residual motion of the IP, subject to the active mode damping control, above $100\,mHz$ is

$$\tilde{s}_i(\omega) = \left[\tilde{A}(\omega) + \tilde{B}(\omega)\right] \cdot \tilde{s}_{iLs}(\omega) \tag{10.10}$$

Now we are interest to quantify the impact of this residual motion on the mirror. To do this estimation, it is necessary to know the effective transfer function of the overall mechanics from ground to the mirror $\tilde{T}^{eff,CL}_{ground \to mir}(\omega)$. Starting from the Eq. (10.10), the effective transfer

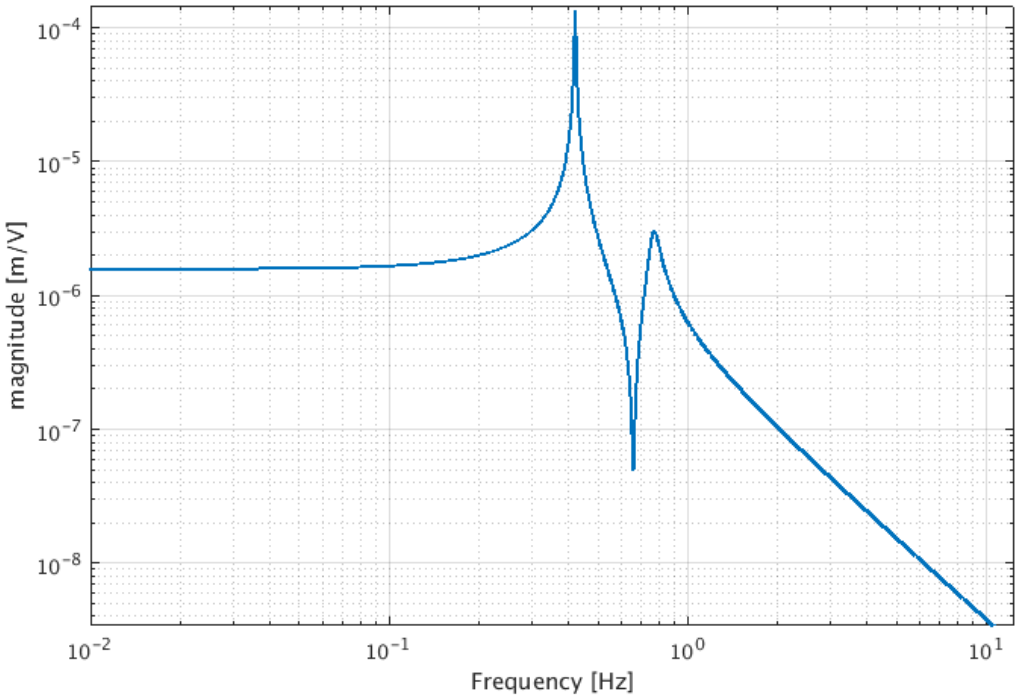

Figure 10.3: Mechanical transfer function $\tilde{M}_i(\omega)$ measured injecting noise with the actuator accommodated on the back side of the mirror and looking at its displacement along the z d.o.f.

function of the overall mechanics can be written as (see Fig.10.5)

$$\tilde{T}^{eff,CL}_{ground\rightarrow mir}(\omega) = \left[\tilde{A}(\omega) + \tilde{B}(\omega)\right] \cdot \tilde{D}(\omega) \tag{10.11}$$

where $\tilde{D}(\omega)$ is the superattenuator transfer function between top stage (input) to mirror (output) (see Fig. 10.4).

By using the formula (10.11), the mirror residual motion $\tilde{s}_{i,mir}(\omega)$ can be written as

$$\tilde{s}_{i,mir}(\omega) = \tilde{D}(\omega) \cdot \tilde{s}_i(\omega) \tag{10.12}$$

where $\tilde{s}_i(\omega)$ is the signal provided from the horizontal diagonalized accelerometers.

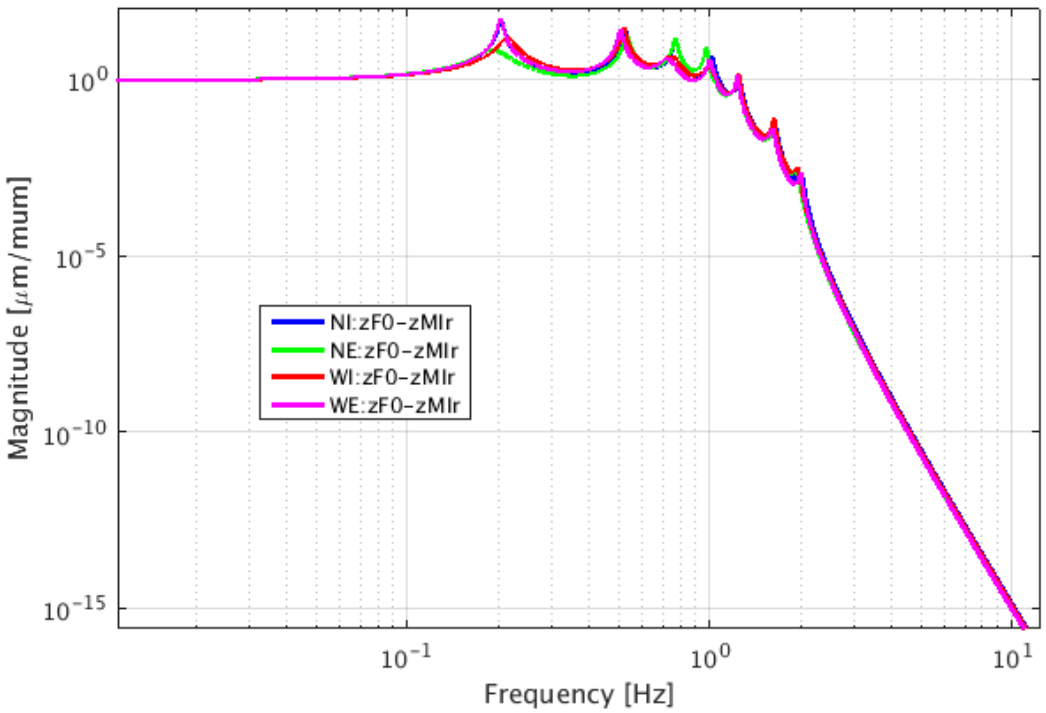

Figure 10.4: Superattenuators attenuation of the AdV interferometer. Experimental displacement transfer function between top stage and test mass (along z d.o.f) for the SA accommodated along the Fabry-Perot cavities (NI,NE,WE, WE).

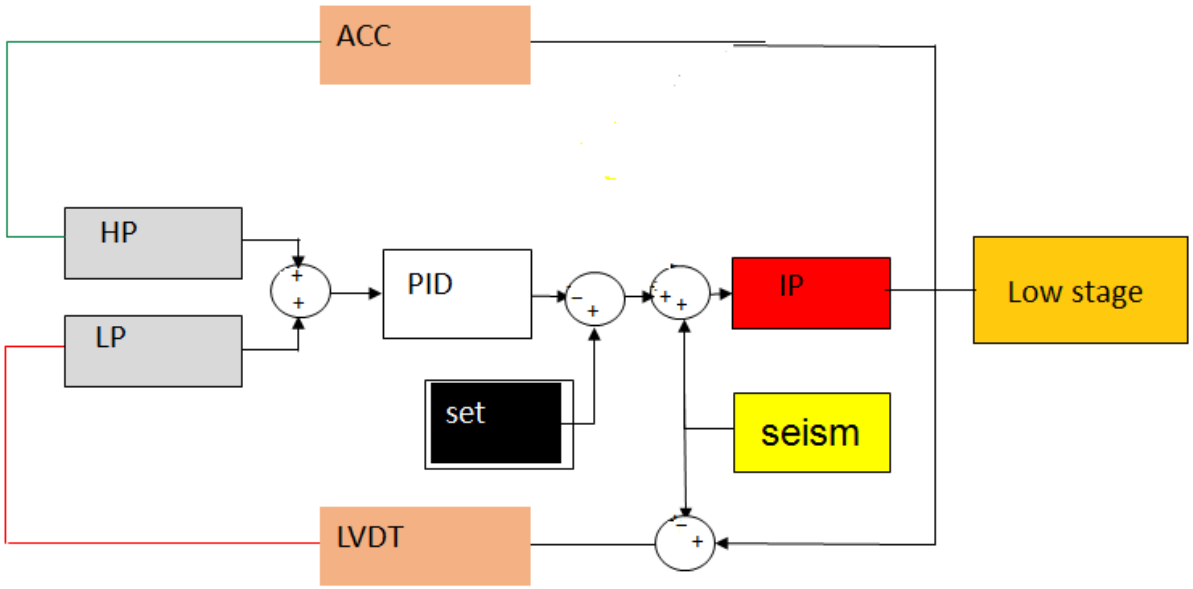

Figure 10.5: Block diagram representing the link between top stage controlled with Inertial damping and low stage (mirror).

In order to have a working detector, all mirrors are interconnected to produce $D_{arm}(t)$. In first approximation and in this frequency range the d.o.f $D_{arm}(t)$ is given by Eq.(10.2): it is controlled and monitored to have a stable sensitivity. In the following we estimate the impact on the sensitivity of the longitudinal and vertical inertial damping acting at level of the top stage for all suspensions involved in the Eq. (10.2).

10.2.1 Impact of the horizontal active mode damping on the sensitivity

The signal $D_{arm}(t)$ is defined as the differential of two length arms. Using the signal expressed by the formula (10.12), the cavity length variation, in this frequency range and for unrelated signals, is given by

$$\tilde{L}_{arm}(\omega) = \sqrt{\left(\tilde{s}^{input}_{z,mir}(\omega)\right)^2 + \left(\tilde{s}^{end}_{z,mir}(\omega)\right)^2} \tag{10.13}$$

and at same way $D_{arm}(t)$ can be computed as

$$\tilde{D}^{A_h}_{arm}(\omega) = \sqrt{\left(\tilde{s}^{NI}_{z,mir}(\omega)\right)^2 + \left(\tilde{s}^{NE}_{z,mir}(\omega)\right)^2 + \left(\tilde{s}^{WI}_{x,mir}(\omega)\right)^2 + \left(\tilde{s}^{WE}_{x,mir}(\omega)\right)^2} \tag{10.14}$$

By using the strain signal definition expressed in equation (10.9) , we can compute the strain $\tilde{h}^{lf}_1(\omega)$ related to the horizontal residual motion as

$$\tilde{h}^{lf}_1(\omega) = \frac{\tilde{D}^{A_h}_{arm}(\omega)}{L} \tag{10.15}$$

When the interferometer works in dark fringe condition (DF), in first approximation, the cavity lengths are fixed through the locking of the four test masses accommodated along the Fabry-Perot cavities (NI, NE, WI, WE). In this frequency range, we expect that the longitudinal motion of $\tilde{D}_{arm}(\omega)$ calculated with Eq. (10.7) and Eq. (10.14) are equal.

10.2.2 Impact of the vertical active mode damping on the sensitivity

In the Chapter 8 we have discuss about of the blending technique focusing our attention on the horizontal active mode damping of the top stage. The same procedure is applied also to control the vertical d.o.f of the top stage. Following the same reasoning and using the Eq. (10.12), the projection of the vertical residual motion $\tilde{s}_{y,TOP}(\omega)$ (measured by using the vertical accelerometers) on the test mass is

$$\tilde{s}_{y,mir}(\omega) = \tilde{D}_y(\omega) \cdot \tilde{s}_{y,TOP}(\omega) \tag{10.16}$$

where $\tilde{D}_y(\omega)$ is the vertical transfer function $TF(\omega)_{i:y_{cr_{F0}} \to out:y_{mir}}$ computed by using the tool adopting the impedance matrix approach discussed in Chapter 6 (see Fig.6.5).

Due to Earth curvature (see Fig.10.6), a coupling between the horizontal and vertical directions is expected and for this reason we are interested in estimating the impact of the vertical residual motion of the mirrors of the Fabry-Perot on the Virgo sensitivity curve.

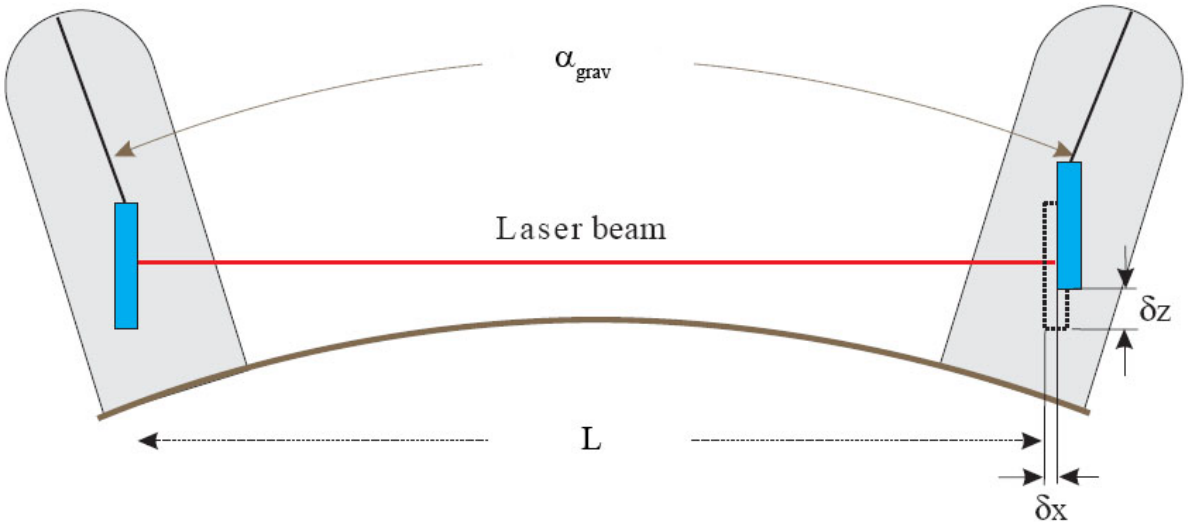

Figure 10.6: Effect of the Earth curvature on mirrors of a ground based detector (Not in scale.).

The input and output mirrors of the Fabry-Perot cavities form an angle $\alpha_{grav} = L/r_{Earth} \sim 4.3 \times 10^{-4} rad$ (where $L = 3km$ is the cavity length and r_{Earth} is the Earth radius) with the global vertical direction. Therefore a vertical displacement δ_z has effect along the beam direction, producing a variation $\alpha_{grav}\delta_z$ of the optical path. Then to calculate the impact of the vertical residual motion on DARM the estimation of the parameter α_{grav} (for the Fabry-Perot suspensions) is needed. The α_{grav} estimation has been done injecting noise on the vertical d.o.f of the Filter7 and looking the behavior of the AdV sensitivity curve. The result of this injection is the transfer function $TF(f)_{F_{7,cr} \to AdVSen}$.

Re-scaling the gain of measured transfer function using the calibration factor k [1] we obtain the calibrated transfer function in $\frac{m}{N}$. To extrapolate the value of α_{grav} we must compare the measurement with the theoretical transfer function (TF^{theo} calibrated in $\frac{m}{N}$). Also in this case the theoretical model can be produced using the Impedance matrix approach described in the Chapter 6[2]:

[1] For these actuators is about $1000 V/N$.

[2] In this case the transfer function has been calculated connecting in series the matrix impedance of F7 crossbar, the matrix impedance of the wire connecting the marionette to F7, the wires connecting the test mass and test mass matrix. To compute this transfer function we assumed that the F7 is connected to the ground.

Since above 10 Hz the test mass can be considered free falling we can re-scale the model obtained TF^{theo} on the measured transfer function so to deduce the value of α_{grav}

$$TF_{F_{F_7} \rightarrow AdV\,sens} = \alpha_{grav} \cdot TF^{theo} \tag{10.17}$$

In Fig. 10.7 the comparison between measured and theoretical transfer function after the re-scaling calculated with the Eq. (10.17) are reported.

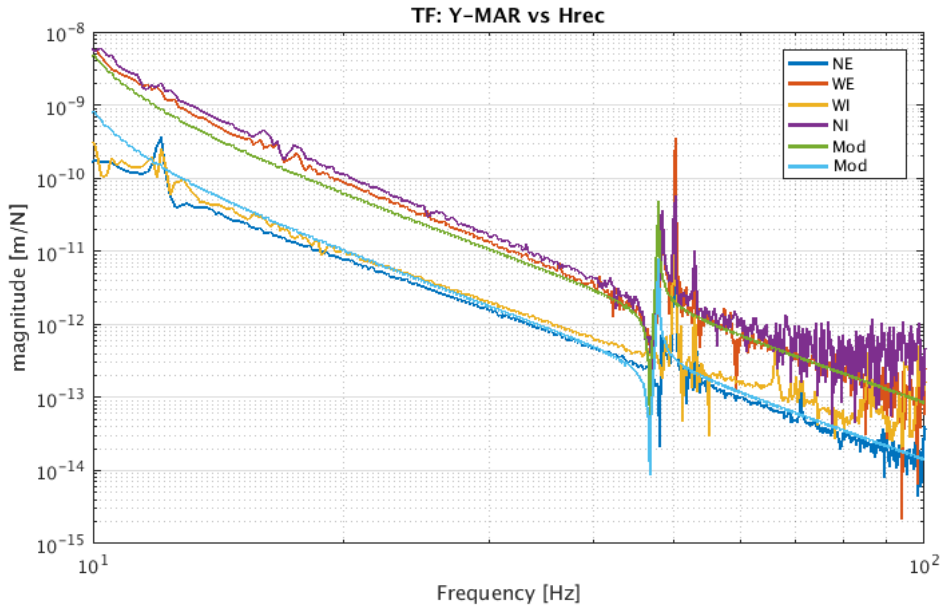

Figure 10.7: Measured transfer function between the vertical motion of the marionette and the AdV sensitivity. In this plot the comparison between measured transfer function (after the rescaling) computed with the Eq.10.17 and model produced using the Impedance matrix approach are reported. We can see that for all test masses the structures appearing at $47 \div 50\,Hz$ are associated with the blade resonances of the F7. These structures are located in the same frequency region expected from the model (green and blue lines).

In the table 10.1 the extrapolated values for α_{grav} of the four mirrors of Fabry-Perot cavities are reported.

	$\alpha_{grav}\ (rad)$
NI	1.5×10^{-3}
NE	9.2×10^{-5}
WI	9.2×10^{-5}
WE	1.5×10^{-3}

Table 10.1: Extrapolated values for α_{grav} of all four mirror of the arms

The coupling between the vertical and the horizontal residual motion (for each mirror) is given by

$$\tilde{s}^{1}_{z,mir}(\omega) = \alpha_{grav} \cdot \tilde{D}_{y}(\omega) \cdot \tilde{s}^{CL}_{y,TOP}(\omega) \tag{10.18}$$

Consequently the projection of residual vertical motion, computed with the Eq. (10.18)(for each test mass), on $\tilde{D}_{arm}(\omega)$ is equal to:

$$\tilde{D}^{A_v}_{arm}(\omega) = \sqrt{\left(\tilde{s}^{1,NI}_{z,mir}(\omega)\right)^2 + \left(\tilde{s}^{1,NE}_{z,mir}(\omega)\right)^2 + \left(\tilde{s}^{1,WI}_{x,mir}(\omega)\right)^2 + \left(\tilde{s}^{1,WE}_{x,mir}(\omega)\right)^2} \tag{10.19}$$

and the respective strain signal is

$$\tilde{h}^{lf}_{2}(\omega) = \frac{\tilde{D}^{A_v}_{arm}(\omega)}{L} \tag{10.20}$$

Now we are able to estimate the impact of the vertical active mode damping on the sensitivity.

10.2.3 Impact of the horizontal and vertical active mode damping on the sensitivity: results

All operations discussed in the Subsections 10.2.1 and 10.2.2 are implemented in a MATLAB script that produces the ASD of the signal expressed by Eq.(10.14), Eq.(10.7) and Eq.(10.19) at given time. The output of this script are a plot showing the ASDs before mentioned. In the following we show an example of this computation.

In Fig. 10.8 the impact of the horizontal and vertical active mode damping on the AdV sensitivity is reported. In this plot the signals computed with Eq.(10.15) (purple curve), Eq.(10.9)(red curve), (10.20)(blue curve), and real sensitivity (orange curve) measured at time of the event GW170814 are reported. Looking at this plot we observe that ranging from $0.1 \div 2 Hz$ we are not ruled by the vertical motion and that purple and red curves are in agreement in this range ($0.1 \div 2 Hz$). Above 2 Hz the effect of the passive mechanical attenuation, how expected, assure us good seismic isolation: $\tilde{h}^{lf}_{1}(\omega)$ (purple curve) at about 3 Hz, where the thermal noise effects are dominant, cross with the theoretical curves (black and green) and about $6 Hz$ is agree with the signal $\tilde{h}^{lf}_{2}(\omega)$ (blue curve) due to the vertical attenuation. At about $9 Hz$, the signal $\tilde{h}^{lf}_{1}(\omega)$ agree with the real sensitivity (orange curve) and at 25 Hz the real sensitivity is close to the theoretical sensitivity (black curve).

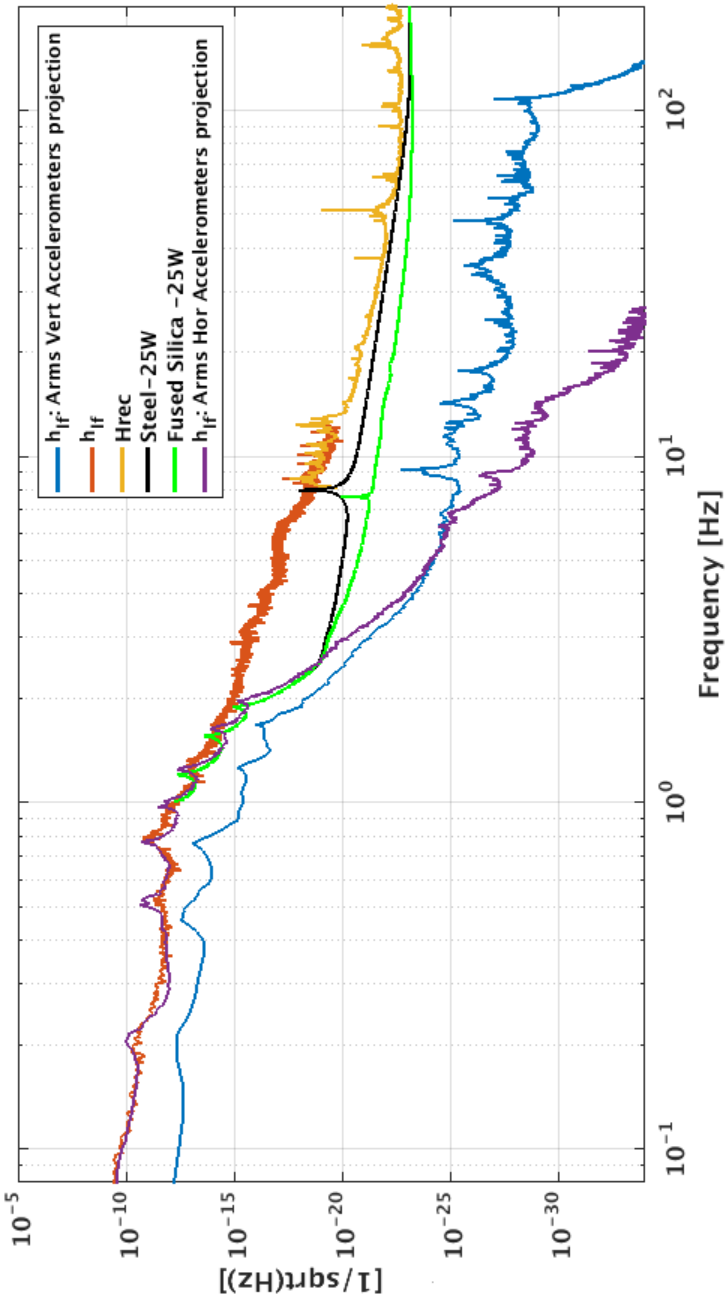

Figure 10.8: Impact of the horizontal and vertical active mode damping on the detector sensitivity. In this plot the signals computed with Eq.10.14 (purple curve), Eq.10.7(red curve), 10.19(blue curve), and real sensitivity (orange curve) measured at time of the event GW170814 are reported.

10.3 Impact of the mirror angular controls on the sensitivity

In the previous section we have seen that ranging from $0.1 \div 2\,Hz$ we are ruled by the residual motion of the top stage, while above 2 Hz the effect of the passive mechanical attenuation, how expected, assure us good seismic isolation. Above 2 Hz, the feedback force send through the coils located on the marionette (see Fig. 10.9) can be re-injected as **angular control noise**: in this section we estimate this contamination level on the low frequency strain signal estimated in Eq. (10.9).

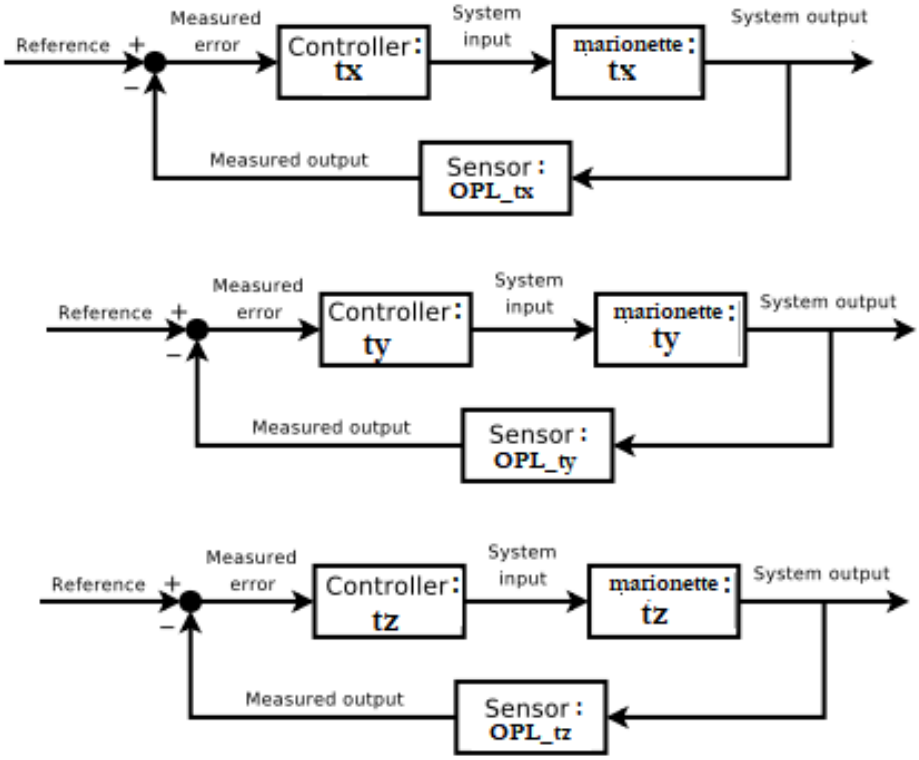

Figure 10.9: Control scheme used to keep in feedback the angular d.o.f of the marionette for all AdV suspensions.

The residual angular motion of the mirror, due to the angular control that acts on the marionette is given by

$$\tilde{s}_{\theta_i,mir}(\omega) \sim \tilde{S}_{\theta_i,Mar_{corr}}(\omega) \cdot TF_{\theta_i Mar_{corr} \to \theta_i,mir}(\omega) \tag{10.21}$$

where $\tilde{S}_{\theta_i,Mar_{corr}}(\omega)$ is the feedback force signal used to control the angular d.o.f θ_i and $TF_{\theta_i Mar_{corr} \to \theta_i,mir}(\omega)$ is the mechanical transfer function between the marionette and the mirror along the θ_i d.o.f. (see Fig.10.12a). To project the signal $\tilde{s}_{\theta_i,mir}(\omega)$ on $\tilde{h}^{lf}(\omega)$ we need to the

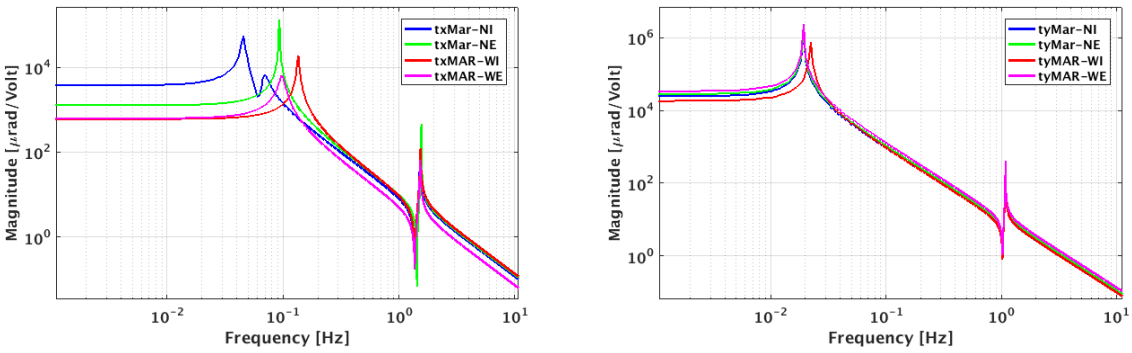

(a)

Figure 10.10: Left figure: Experimental mechanical plant along Pitch d.o.f (θ_x) of the marionette for the test mass payloads (NI,NE,WE, WE). Right figure: Experimental mechanical plant along Yaw d.o.f (θ_y) of the marionette for the test mass payloads (NI,NE,WE, WE)

transfer function

$$\tilde{TF}_{strain\,\theta_i}(\omega) \sim \frac{c_{\theta_i} \cdot TF_{\theta_i Mar_{corr} \rightarrow \theta_i, mir}(\omega)}{L} \tag{10.22}$$

where c_{θ_i} is the parameter that quantifies the decentring of the beam respect to the center of the mirror. By using the transfer function (10.22) we obtain the projection $\tilde{h}_{lf,\theta_i}(\omega)$

$$\tilde{h}_{lf,\theta_i}(\omega) \sim \tilde{S}_{\theta_i, Mar_{corr}}(\omega) \cdot \tilde{TF}_{strain\,\theta_i}(\omega) \tag{10.23}$$

Basically, far from the resonances of the chain marionette-mirror (above 10 Hz) the test mass can be considered free falling and, since in this configuration we have only two stages of attenuation we expect that the behavior of transfer function $\tilde{TF}_{strain\,\theta_i}(\omega)$ is

$$\tilde{TF}_{strain\,\theta_i}(\omega) \sim \frac{c_{\theta_i} \cdot \omega_{0,\theta_i}^4}{\omega^4} \tag{10.24}$$

To verify that the assumption make in Eq. (10.24) is correct, we have excited each angular d.o.f. of the marionettes accommodated along the Fabry-Perot cavities and fitted the ratio [3] of the PSDs of the two channels Hrec (the channel of the detector showing in real time the sensitivity of the interferometer) and angular noise correction injected. In the table 10.2 the extrapolated model for Yaw and Pitch d.o.f. are reported and how expected these models are in agreement with the theoretical assumption (Eq. (10.24)).

A way to estimate the decentring is to measure the transfer function r (calibrated in is $\frac{m}{V}$)

[3] We use the ratio between the spectra because in this condition we expect low coherence and the transfer function is not correct.

	TF model Pitch vs Hrec (strain/Volt)		TF model Yaw vs Hrec (stain/V)
NI	$TF_{NI_{tx},Hrec}(f) \sim \frac{5.9\times10^{-12}}{f^{4.2}}$		$TF_{NI_{ty},Hrec}(f) \sim \frac{1.81\times10^{-12}}{f^{4}}$
NE	$TF_{NE_{tx},Hrec}(f) \sim \frac{1.3\times10^{-11}}{f^{4.2}}$		$TF_{NE_{ty},Hrec}(\omega) \sim \frac{1.81\times10^{-12}}{f^{4}}$
WI	$TF_{WI_{tx},Hrec}(f) \sim \frac{5.9\times10^{-12}}{Lf^{4.2}}$		$TF_{WI_{ty},Hrec}(\omega) \sim \frac{1.79\times10^{-12}}{Lf^{4.1}}$
WE	$TF_{WE_{tx},Hrec}(f) \sim \frac{1.19\times10^{-11}}{f^{4.2}}$		$TF_{WE_{ty},Hrec}(\omega) \sim \frac{1.79\times10^{-12}}{f^{4.1}}$

Table 10.2: Extrapolated model of angular transfer function between angular marionette feedback force and detector sensitivity. We can see that the behavior of model is in agreement with the Eq.10.24.

between $\tilde{S}_{\theta_i,Mar_{corr}}(\omega)$ and $D_{arm}(t)$ at frequency f_l

$$r \sim \frac{\tilde{D}_{arm}(2\pi f_l)}{\tilde{S}_{\theta_i,Mar_{corr}}(2\pi f_l)} \tag{10.25}$$

To extrapolate the value of c_{θ_i} we must divide the measurement r by the value of theoretical transfer function (TF^{theo} calibrated in $\frac{1}{V}$) computed at the same f_l. Also in this case the theoretical model is obtained by using the Impedance matrix approach described in the Chapter 6.

To reduce the misalignment of the beam with respect to the optical axis and to keep the beam centering on test masses the local control set point is driven by "drift control" servo-loop that use sinusoidal dithering angular lines (f_l) and demodulation of dark fringe signal [18]. When the optical axis is not perfectly aligned, the tilt of the mirror induces a length change, that can be seen on the longitudinal error signal.

Looking at Fig. 10.11 we can observe that in case of miscentering, an angular motion in Pitch induces a displacement along the y direction, while an angular motion in Yaw induce a displacement along the x direction. The goal of the drift control is to center the beam on the geometric center of the mirror, in order to minimize the c_{θ_i} values. The presence of a line at f_l on the spectrum of the transmitted power will be minimized when the beam is perfectly superimposed to the optical axis of the cavity. In the table 10.3 the frequency lines used to implement the drift control are reported. For convenience we have chosen to use these lines to

	f_{θ_x} (Hz)	f_{θ_y}(Hz)
NI	11.5	12.5
NE	8.2	9.29
WI	9.5	10.5
WE	8.7	9.9

Table 10.3: Frequency lines used to implement the drift control on the mirrors of arms

estimate the parameters c_{θ_i} .

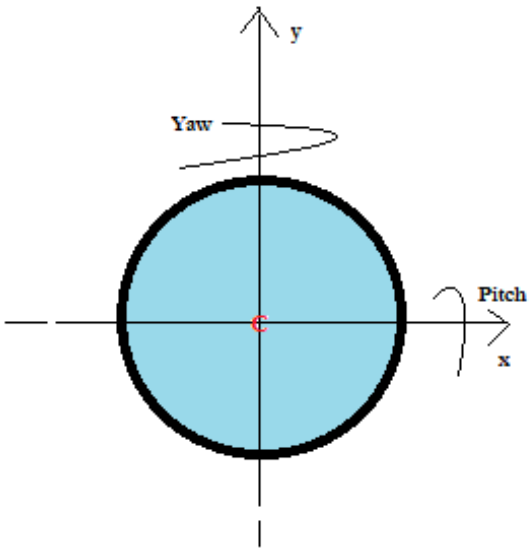

Figure 10.11: Schematic representation of (x,y) displacement from the center of the mirror. An angular motion in Pitch induce a decentring along y direction, while an angular motion in Yaw induce a decentring along x direction. When the beam is well centered means that the values (x,y) are smaller.

There calculation are implemented in a MATLAB script that produces, at given time, the PSD of the signal expressed by Eq.(10.9) and Eq.(10.23) for all Pitch and Yaw d.o.f of the test mass payloads (NI,NE,WE, WE) .The output of this script are a plot showing the PSDs before mentioned and a vector in which the value of c_{θ_i} are stored (see Tab. (10.4)). In the

	c_{θ_i} Pitch (m)		c_{θ_i} Yaw (m)
NI	0.7×10^{-4}		0.8×10^{-5}
NE	0.3×10^{-4}		0.4×10^{-5}
WI	0.1×10^{-4}		0.7×10^{-5}
WE	0.2×10^{-4}		0.4×10^{-5}

Table 10.4: Pitch and Yaw decentring (c_{θ_i}) measured at time of the event GW170814.

following we show an example of these calculation.In the following we show an example of this calculations. In Fig. 10.13 the angular control noise budget in the configuration adopted during O2 has been estimated. In this figure we can see also the nominal displacement sensitivity for both steel and fused silica suspensions. In the region $6.5 \div 7.2\,Hz$ the blue and yellow curve

are matching: this means that $\tilde{h}^{lf}$ is affected by the angular control noise provided by the NI_{θ_x} while other angular contribution are very low: during the the event GW170814 we was not limited by angular control noise. At about $9\,Hz$, the $\tilde{h}^{lf}$ computed with the Eq. (10.9) and PSD of the Hrec signal (red curve) become the same signal.

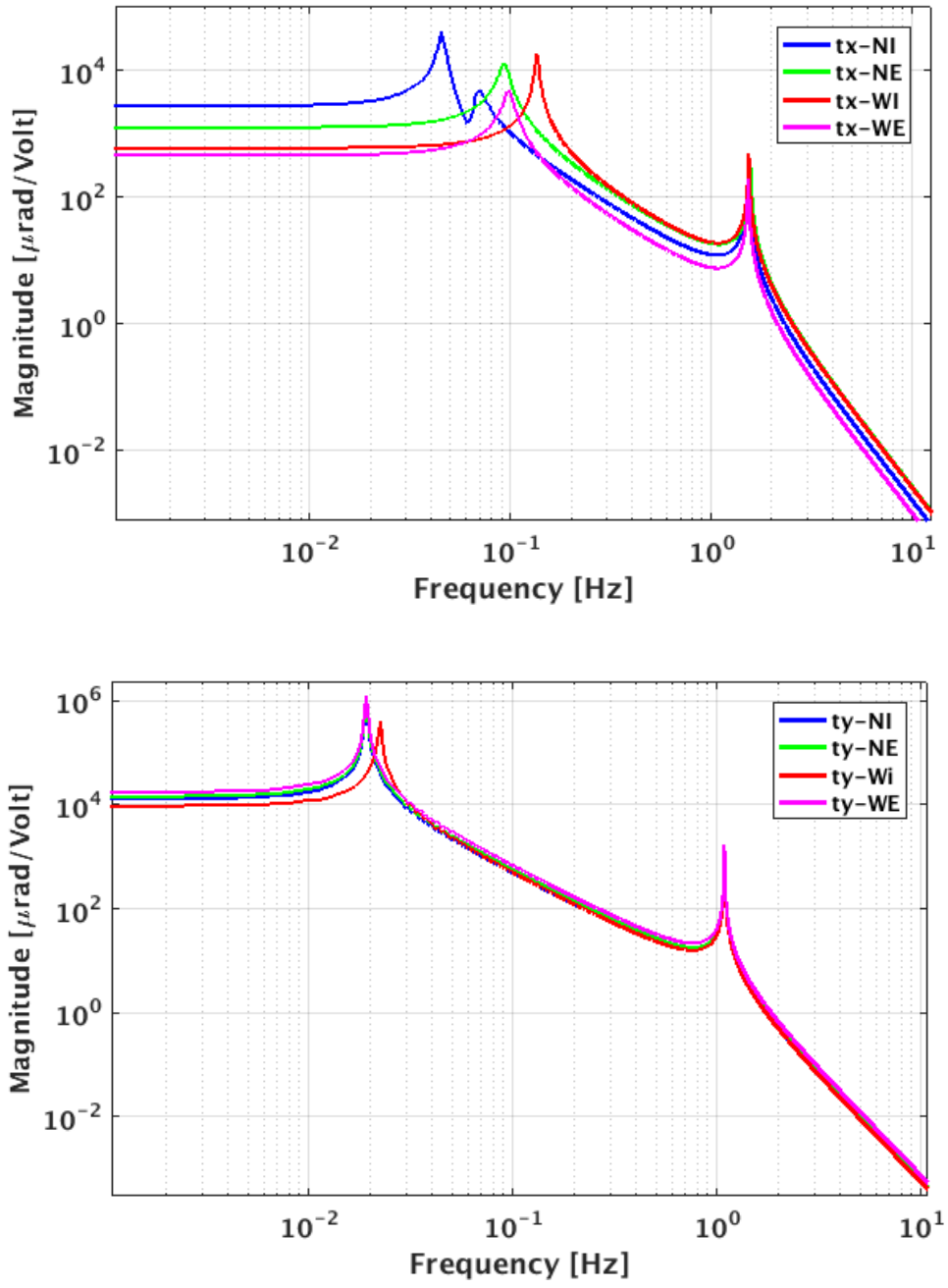

(a)

Figure 10.12: Upper figure: Experimental transfer function along θ_x d.o.f of marionette-mirror chain accommodated along the Fabry-Perot cavities (NI,NE,WE, WE). Bottom figure: Experimental transfer function along θ_y d.o.f of marionette-mirror chain accommodated along the Fabry-Perot cavities (NI,NE,WE, WE).

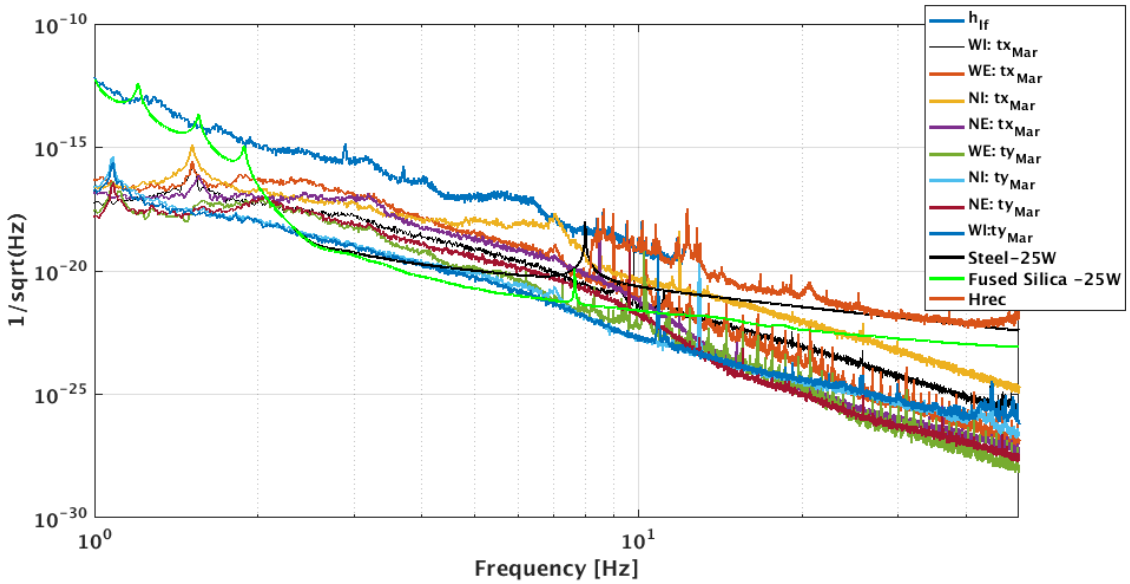

Figure 10.13: Impact of the angular feedback force on the Virgo detector sensitivity. In this plot the comparison between differential signal calculated with Eq.(10.9) (blue line) and all angular contribution calculated with .(10.23) measured at time of the event GW170814 are reported.

Conclusions

The advanced Virgo (AdV) upgrade of Virgo detector was concluded in November 2016. Advanced Virgo joined the Advanced LIGO detectors on the scientific data taking O2 the 1^{th} of August until the 25^{th} of August. Mostly thanks to the high-performance seismic isolation system, which allowed to keep the continuously the working point with good accuracy, during O2 the duty cycle was 83% and the average sensitivity figure for BNS [4] events with SNR 8 was 26 Mpc, a factor 2 better than the sensitivity of the first generation Virgo detector. On the 14^{th} of August the Virgo detector contributed to the first triple detection of a coalescing Binary Black Hole system, made together with LIGO.

Until November 2016 the commissioning activity related to the control of ten superattenuators and payloads was one of the main ones. To bring such a complex system to a level of performance compatible with the sensitivity demanded by AdV, a significant amount of work was required. One of the fundamental milestones to reach the working point is the so-called "alignment" of the seismic isolation system. In this phase, being physically close to the system, I had the opportunity to directly observe it, checking step by step all the he realization of all the requirements listed in Chapter 5, and appreciate its majestic beauty even from a purely aesthetic point of view.

The procedure to model the overall mechanical transfer function, from ground to the test masses, adopts the impedance matrix method had been systematically used such a method, first to describe the dynamics of the system then to further develop control strategies. In Chapter 6 the latest version is presented and finalized to estimate suspension control noise budget.

Obviously, the effective measurement of the transfer functions is the next step of the "on-site calibration" of all position sensors mounted on the apparatus to monitor its behavior. This work must be done with great precision. After this pre-calibration, we have a good monitor of the real displacement of the all mechanical components and the second commissioning phase can start. Then, all the operations performed remotely on the sensors and on the actuators are

[4] The standard figure of merit for the sensitivity of an interferometer is the binary neutron star (BNS) range: the volume- and orientation-averaged distance at which a compact binary coalescence consisting of two $1.4 M_{\odot}$ neutron stars gives a matched filter signal-to-noise ratio of 8 in a single detector. [20]

aimed at making the system suitable to reach its maximum efficiency. Galileo teaches us that in order to understand a physical phenomenon the obligatory step is observation. Also in our case, we expect the achievement of our goal goes through the continuous observation of the system. The monitoring of the local seismic spectra provided by a large number of vibration sensors disseminated on EGO site and the spectra provided by the sensors set on the suspension stages suggests us that the most convenient reference frame to implement the “active mode damping control" is the Virgo Reference Frame (VRF), with respect to which also the micro-seism noise is referred.

As shown in Chapter 7, all the operations done on the sensors and actuators are finalized to build up the sets of virtual sensors and actuators in that reference frame. Indeed, the performance of the controlled suspension is guaranteed in primis by those choices, related to the mechanics, and then by the meticulous attention adopted in combining the sensors.

Another important point to have a good performance of an active mode damping, is to use a good inertial sensors. We remind that the accelerometer must monitor very small displacements and for this reason its intrinsic noise must be very low. This required the implementation of a robust and stable feedback, that was suitably re-calibrated and shaped. This preliminary work helps us to acquire confidence with the system and it was essential to achieve the exceptional performance of the whole seismic isolation system.

Real data, in combination with simulation and modeling results, help us to identify the suitable active mode control, as explained in Chapter 8. In order to reach a good performance, the sensor blending filters, the controller filters and the background noise sources must be all accurately considered. Combining this data we are able to simulate the expected PSD related to the residual motion and define a projection method. Then, we can compare the efficiency of different strategies, under specific background seismic conditions. The method developed has been quite useful during the commissioning work and was finalized to the strategy to be adopted the scientific run O2.

Some simulations had been done in the past, in order to improve the control strategy for AdV seismic attenuator using a different approaches, but none of them had been tested on the real system [8, 29]. In this perspective, for future developments, the resulting test related to the Kalman filter and LQG control, shown in the Chapter 9, represents a first attempt in that direction. It should be emphasized that the development of this technique requires a detailed knowledge of both the system and of all possible sources of disturbance acting on it, as well as an accurate mathematical modeling. This results can be used as starting point towards more complex system like AdV suspensions.

This thesis cannot be considered complete without the estimation of the impact of suspension controls on the AdV sensitivity curve.

In Chapter 10 a procedure to calculate the suspension control noise budget in the micro-seismic range is presented and show that the performance of the AdV seismic isolation system was excellent:

- in the region $0.1 \div 2 Hz$ where the active mode damping control acts the rms of the test mass speed (v), in good background conditions (low microseism), is compatible with the value $v \sim 10^{-7} \frac{m}{s}$ and, in high microseimic conditions, is still low enough to acquire the lock ($v < 0.5 \times 10^{-7} \frac{m}{s}$);
- above 2 Hz the effect of the passive mechanical attenuation, how expected, assure us good seismic isolation and at about 3 Hz, where the thermal noise effects are dominant, the seismic contribution cross with the theoretical sensitivity curves. At about $7 Hz$ the effective passive attenuation of the system allow us to have a residual motion of $3 \times 10^{-22} \frac{m}{\sqrt{Hz}}$;
- in the region $2 \div 50 Hz$, the angular control noise contributions are very low: this means the signal $\tilde{h}^{lf}$ is not affected by the angular control noise.

The commissioning activity of the suspension system was continued also after the O2 run. Regarding this period, most simulations and adjustments were done in order further improve the recombined operation of suspensions, Global Inverted Pendulum Control (GIPC), exploiting also the interferometer signals.

Actually the overall performance reached by Virgo seismic isolation system, using the method reported in Chapter 8, has not been overcome and not even equaled by other control techniques. Indeed, even though the distinctive features of the superattenuator, the effectiveness of such a complex seismic suspension system strongly rely upon the control strategy design. However, it should be evident that Virgo suspension design and control strategy are nor merely a reliable part for the current detector, but also a solid playground for future developments and seismic isolation architectures for 3G gravitational wave detectors.

References

[1] *The Fourier Transform and Its Application*. McGraw-Hill, 1986.

[2] et al. Abbot B. P. An upper limit on the stochastic gravitational-wave background of cosmology origin. *Nature*, 2009.

[3] A.Einstein. Die grundlage der allgemeinen relativitatstheorie. *Annalen der Physik*, 49, 1916.

[4] Annalisa Allocca. *Thermal projection system for surface figure correction of core optics in Gravitational Waves interferometers*. PhD thesis, Dipartimento di Scienze Fisiche, delle Terra e dell' ambiente Sezione di Fisica, Università degli studi di Siena, 2015.

[5] K.J. Aström and R. M. Murrey. *Feedback Systems:an introduction forscientists and engineers*. Princeton University Press,Princeton, 2011.

[6] M. Bassan, editor. *Advanced Interferometers and the Search for Gravitational Waves*. Springer, 2014.

[7] Matteo Beccaria, Giancarlo Cella, Giuseppe Curci, and A.Vicerè. Model of the super attenuator dynamics. *https://labcit.ligo.caltech.edu/e2e/*, 1999.

[8] Valerio Boschi. *Modeling and simulation of Seismic Isolation System for Gravitational Waves Interferometers*. PhD thesis, Universitá degli studi di Pisa.

[9] K. C. B. New C. L. Fryer. Gravitational waves from gravitational collapse. *Living Reviews in Relativity*, 14(2), 2011.

[10] R.H. Cannon. *Dynamics of Physical Systems*. 1967.

[11] C. Casciano. *Seismic Isolation for the Test Masses of the VIRGO Gravitational Wave Antenna*. PhD thesis, Università degli studi di Pisa, Dottorato di Ricerca in Fisica - XIV Ciclo.

[12] C. M. Caves. Quantum mechanica noise in an interferometrer. *Phys. Rev. D, 23*, 1981.

[13] Giovanni Cerretani. Performance improvement of the inertial sensor of advanced virgo seismic isolators with digital tecniques. Master's thesis, Universitá di Pisa, Dipartimento di Fisica Enrico Fermi, 2013.

[14] C.M. Close, D.K. Frederick, and J.C. Newell. *Modeling and Analysis of Dynamic Systems*. 2001.

[15] I. Cochin and W. Cadwallender. *Analysis and Design of Dynamic Systems*. 1997.

[16] Virgo Collaboration. Advanced virgo technical design report. Technical report, Virgo Collaboration, 2012.

[17] R. Courant and D. Hilbert. *Methods of Mathematical Physics*. 1989.

[18] Julia Casanueva Diaz. *Control of the Gravitational Waves Interferometric Detector Advanced Virgo*. PhD thesis, Université Paris-Saclay preparé á l' Université Paris-Sud, 2017.

[19] A. Einstein. Die grundlage der allgemeinen relativitätstheorie. *Annalen der Physik*, 354: 769–822, 1916.

[20] Abbot B. P. et al. Prospects for localization of gravitational waves transient by the advanced ligo and advanced virgo observatories. *arxiv: 1304.0670v1*, 2013.

[21] F. Acernese et al. Virgo collaboration. *Class. Quantum Grav. 25*, 2008.

[22] F. Acernese et al. Advanced virgo: a 2nd generation of interferometric gravitational waves detector. *Class. Quantum Grav. 32 024001*, 2015.

[23] G.Ballardin et al. Measurement of the virgo superattenuator performance for seismic noise suppression. *Review of scientific instrument, Vol. 72, N. 9*, 2001.

[24] K. Yamamoto et al. Measurement of seismic motion at large-scale cryogenic gravitational wave telescope project site. 2010.

[25] Mauceli et al. The allegro gravitational wave detector: Data acquisition and analysis. *Phys. Rev. D*, 54(2), 1996. doi: doi:10.1103/PhysRevD.54.1264.

[26] R.De Salvo et al. Filter 0 performance as a vertical pre-isolator stadium for virgo superattenuator. *Nucl. Instrument*, 1998.

[27] S. Braccini et al. The maraging-steel blades of the virgo super attenuator. *Meas. Sci. Technol. 11, 467-476*, 2000.

[28] S.Braccini et al. Measurement of the seismic attenuation performance of the virgo superattenuator. *Astroparticle Physics 23, 557-565*, 2005.

[29] Valerio Bochi et al. A state observer for the virgo inverted pendulum. *Rewiew of Scientific intruments 82*, 2011.

[30] B. P. Abbott et al. (LIGO Scientific Collaboration and Virgo Collaboration). Gw170817: Observation of gravitational waves from a binary neutron star inspiral. *Phys. Rev. Lett. 119, 161101*, 16 October 2017.

[31] B. P. Abbott et al. (LIGO Scientific Collaboration and Virgo Collaboration). Gw170814 : A three-detector observation of gravitational waves from a binary black hole coalescence. *Phys. Rev. Lett. 119, 141101*, 6 October 2017.

[32] B. P.Abbott et al. (LIGO Scientific Collaboration and Virgo Collaboration). Observation of gravitational waves from a binary black hole merger. *Phys. Rev. Lett. 116,061102*, 2016.

[33] Irene Fiori. *Reference Seismic Data for Virgo*. Private Communication, 2015.

[34] B. Friedland. *Control systemdesign:anintroduction to state-space models*. Dover Publications, New York, 2005.

[35] A. Giazotto. The virgo experiment: status of art. In *First Edoardo Amaldi Conference on Gravitational Waves*, 1995.

[36] G.Losurdo. *Ultra-Low Frequeny Inverted Pendulum for the VIRGO Test Mass Suspension*. PhD thesis, Classe di Sienze, Suola Normale Superiore di Pisa, 1998.

[37] T. A. Welton H. B. Callen. Irreversibility an generalized noise. *Phys. Rev. 83, 34-40*, 1951.

[38] Leo H Holthuijsen. *Waves in oceanic and coastal waters.* Cambridge University Press., 2007.

[39] S. A. Hughes and K. Thorne. Seismic gravity-gradient noise in interferometric gravitational-wave detectors. *Phys. Rev. D*, 58(122002), 1998.

[40] R. A. Hulse and J. H. Taylor. Discovery of a pulsar in a binary system. *Astrophys. J.*, 195 (L51), 1975.

[41] RA Hulse and JH Taylor. Discovery of a pulsar in a binary system. *Neutron stars, black holes, and binary X-ray sources, 48:433*, 1975.

[42] D. J. Inman. *Engineering Vibration*. Boston, 4 edition, 2013.

[43] B. Francis J. Doyle and A. Tannenbaum. *Feedback control theory*. (1990).

[44] J. H. Taylor J. M. Weisberg. Relativistic binary pulsar b1913+16: Thirty years of observations and analysis. *ASP Conference Series*, 328(25), 2005.

[45] Peter Janssen. *The interaction of ocean waves and wind.* Cambridge University Press., 2004.

[46] C. W. Misner K. S. Thorne and J. A. Wheeler. *Gravitation*. W. H. Freeman, 1973.

[47] E. Kappos. *Classical Control Theory: A Course in the Linear Mathematics of Systems and Control*. University of Sheffield, School of Mathematics and Statistics, 2002.

[48] Roy P Kerr. Gravitational field of a spinning mass as an example of algebraically special metrics. *Physical review letters, 11(5):237*, 1963.

[49] Donald E. Kirk. *Optimal Control Theory: An Introduction*. Dover Publications, 2004.

[50] Martin D Kruskal. Maximal extension of schwarzschild metric. *Physical review, 119(5):1743*, 1960.

[51] V. Boschi L. Trozzo. Lqg control tests of advirgo ip. *Presentation, GWADW 2017, https://dcc.ligo.org/LIGO-G1700426*, 2017.

[52] M. Lalanne, P. Berthier, and J. Der Hagopian. *Mechanical Vibrations for Engineers*. Chichester West Sussex ; New York, 1983.

[53] LIGO and Virgo Scientific Collaborations. An upper limit on the stochastic gravitational-wave background of cosmological origin. *Nature*, 460:990–994, 2009.

[54] Michele Maggiore. *Gravitational Waves: Volume 1: Theory and Experiments*. Oxford Univeristy Press, USA, 2007.

[55] M.Beccaria, M.Bernardini, E.Bougleux, S.Braccini, C.Bradaschia, C.Casciano, G.Cella, E.Cuoco, E.D'Ambrosio, G.De Carolis, R.Del Fabbro, R.De Salvo, A.DiVirgilio, I.Ferrante, F.Fidecaro, R.Flaminio, A.Gaddi, A.Gennai, G.Gennaro, A.Giazotto, L.Holloway, P.La Penna, G.Losurdo, S.Malik, S.Mancini, J.Nicolas, F.Palla, H.B.Pan,

F.Paoletti, A.Pasqualetti, D.Passuello, R.Poggiani, P.Popolizio, F.Raffaelli, A.Vicerè, F.Waharte, and Z.Zhang. *Nucl. Instrum. Meth. in Phys. Res. A, 394, 397-408*, 1997.

[56] M.Beccaria, M.Bernardini, S.Braccini, C.Bradaschia, G.Cagnoli, C.Casciano, G.Cella, E.Cuoco, V.Dattilo, G.De Carolis, R.De Salvo, A.Di Virgilio, G.T.Feng, I.Ferrante, F.Fidearo, F.Frasconi, A.Gaddi, L.Gammaitoni, A.Gennai, A.Giazotto, L.Holloway, J.Kovalik, P.La Penna, G.Losurdo, S.Malik, S.Mancini, F.Marchesoni, J.Nicolas, F.Palla, H.B.Pan, F.Paoletti, A.Pasqualetti, D.Passuello, R.Poggiani, P.Popolizio, M.Punturo, F.Raffaelli, V.Rubino, R.Valentini, A.Vicerè, F.Waharte, and Z.Zhang. *Nucl. Instrum. Meth. in Phys. Res. A, 455-469*, 1998.

[57] U. Meneghetti, A. Maggiore, , and E. Funaioli. *Lezioni di meccanica applicata alle macchine - Terza parte - Dinamica e vibrazioni delle macchine*. Bologna, 2011.

[58] Scott Miller and Donald Childer. *Probability and Random Processes*. Academic Press, 2012.

[59] ANGUS P. ANDREWS MOHINDER S. GREWAL. *KALMAN FILTERING: Theory and Practice Using MATLAB, Third Edition*. John Wiley & Sons, Inc., New Jersey, 2008.

[60] Katsuhiko Ogata. *Modern Control Engineering,5TH ED*. Prentice Hall, 2010.

[61] J. Peterson. Observations and modeling of seismic background noise. *USGS Report 93-322*, 1993.

[62] PHILIPS. *Datasheet of Ferroxdure 330 (FXD 330)*. 1991.

[63] P.Ruggi. L' attenuazione del rumore sismico nel rivelatore di onde gravitazionale virgo. Master's thesis, Dipartimento di Fisica, Università di Pisa, 2003.

[64] R. J. Raab. The ligo project: progress and prospects. In *First Edoardo Amaldi Conference on Gravitational Waves*, 1995.

[65] S. S. Rao. *Mechanical Vibrations*. N.J: Prentice Hall, 5th edition ed., 2010.

[66] P. Ruggi. Modeling multipendulum suspension. *Private comunication, https://tds.virgo-gw.eu/ql/?c=6714*, 2009.

[67] Paolo Ruggi. Unpublished results. *Private communication*, 2017.

[68] K. Thorne S.A.Hughes. Seismic gravity-gradient noise in interferometric gravitational-waves detectors. *Phys. Rev. D, 122002*, 1998.

[69] P. R. Saulson. *Fundamentals of interferometric gravitational wave detectors*. World Scientic, 1994.

[70] S.Braccini. *Tesi di Perfezionamento*. PhD thesis, Scuola Normale Superiore di Pisa, 1996.

[71] S.Braccini, C.Bradashia, R.Del Fabbro, A.Di Virgilio, I.Ferrante, F.Fidecaro, R.Flaminio, A.Gennai, A.Giassi, A.Giazotto, G.Gorini, G.Losurdo, F.Palla, A.Pasqualetti, D.Passuello, R.Poggiani, G.Torelli, and Z.Zhang. *Rev. Sci. Instrum., 67, (8),2899-2902*, 1996.

[72] S.Braccini, C.Casciano, R.De Salvo, R.Del Fabbro, and F.Fidecaro. *VIRGO Note NTS 096/045*, 1996.

[73] S.Braccini, C.Casciano, R.De Salvo, and F.Fidecaro. *VIRGO Note NTS 096/032*, 1996.

[74] Daniele Scaglione. Effetti del rumore sismico sulle sospensioni del rivelatore virgo. Master's thesis, Facolta' di scienze Matematiche Fisiche e Naturali,Corso di Laurea in Fisica, Universita' degli studi di Pisa, 2006.

[75] B. De Schutter. Minimal state-space realization in linear system theory: An overview. *Journal of Computational and Applied Mathematics, Special Issue on Numerical ANalysis in the 20th Century - Vol. I: Approximation Theory, vol. 121, no. 1-2, pp. 331-354*, Sept. 2000.

[76] Michael Wysession Seth Stein. *An Introduction to Seismology, Earthquakes, and Earth Structure*. John Wiley & Sons, 2009.

[77] Peter M. Shearer. *Introduction to Seismology.* Cambridge University Press, 2009.

[78] A.E. Siegman. *Lasers*. University Science Books, 1986.

[79] Vladimir Ivanovic Smirnov. *Corso di Matematica Superiore Vol. II*. Editori Riuniti, 2011.

[80] Joseph H Taylor and Joel M Weisberg. A new test of general relativity-gravitational radiation and the binary pulsar psr 1913+ 16. *The Astrophysical Journal, 253:908-920*, 1982.

[81] The Virgo Collaboration The LIGO scientifc Collaboration. Sensitivity achieved by the ligo and virgo gravitational wave detectors during ligo's sixth and virgo's second and third science runs. *arXiv:1203.2674 [gr-qc]*, 2012.

[82] L. Trozzo. Suspension control in adv: noise projection methods and strategy design. *Presentation GWADW 2017, https://dcc.ligo.org/LIGO-G1700878, https://tds.virgo-gw.eu/ql/?c=12292*, 2017.

[83] L. Trozzo V. Boschi. Lqg control of advirgo ip, presentation lvc meeting, https://dcc.ligo.org/ligo-g1700426. 2017.

[84] G. Vajente. Interferometer configuration. *Virgo Note*, 2012.

[85] V.Boschi. Present and future of superattenuator control system,. *GWADW 2016 Presentation, https://dcc.ligo.org/LIGO-G1601197*, 2016.

[86] J. Weber. Gravitational wave detector events. *Phy.Rev.Lett. 20, 1307*, 3 June 1968.

[87] S. Weinberg. *Gravitation and cosmology*. Wiley, New York, 1993.